T H E U N I V E R S I T Y O F T U L S A
THE GRADUATE SCHOOL

A WELL TEST FOR IN-SITU DETERMINATION OF RELATIVE PERMEABILITY CURVES

by
Shi Chen

A dissertation submitted in partial fulfillment of
the requirements for the degree of Doctor of Philosophy
in the Discipline of Petroleum Engineering

The Graduate School
The University of Tulsa

2007

T H E U N I V E R S I T Y O F T U L S A

THE GRADUATE SCHOOL

A WELL TEST FOR IN-SITU DETERMINATION
OF RELATIVE PERMEABILITY CURVES

by
Shi Chen

A DISSERTATION
APPROVED FOR THE DISCIPLINE OF
PETROLEUM ENGINEERING

By Dissertation Committee

_____ , Chairperson
Dr. Albert C. Reynolds

_____
Dr. Gaoming Li

_____
Dr. Christian Constanda

_____
Dr. Leslie G. Thompson

ABSTRACT

Shi Chen (Doctor of Philosophy in Petroleum Engineering)

A Well Test for In-Situ Determination of Relative Permeability Curves

Directed by Dr. Albert C. Reynolds

206 pp. Chapter 7

(195 words)

In this research, a new pressure transient test consisting of a traditional injection/falloff followed by a flow period when we produce oil and injected water, an injection/falloff/production test (IFPT), is proposed to estimate relative permeabilities, reservoir permeability and well skin factor for the water-oil two-phase problem. An automatic history match code has been developed to estimate parameters defining relative permeabilities, absolute permeability and well skin factor by matching measured data from the test. Two parameterizations of relative permeability curves are considered, a power law model and a more flexible B-spline representation. In this research, an analytical solution for the pressure response was obtained for the case where capillary pressure was negligible. For the case where capillary pressure is significant, we were forced to combine analytical method with a finite difference solution of the Buckley-Leverett equation to obtain the pressure solution during the flow back period. We show that the new IFPT yields more accurate estimates of relative permeabilities than can be obtained with a conventional injection/falloff test. The analytical solution assumes constant injection rate, but we show that good parameter estimates can still be obtained by the analysis method under reasonable flow rate fluctuations.

ACKNOWLEDGEMENTS

Though only my name appears on the cover of this dissertation, a great many people have contributed to its production. I owe my gratitude to all those people who have made this dissertation possible.

My deepest gratitude is to my advisor, Dr. Albert C. Reynolds, Jr., Professor of Petroleum Engineering and Mathematical Sciences at the University of Tulsa. I have been amazingly fortunate to have an advisor who gave me his guidance, patience, support and encouragement during my Ph.D study and research in the University of Tulsa.

My co-advisor and dissertation committee member, Dr. Gaoming Li, has been there to listen and give advices. I am deeply grateful to him for the discussions that helped me sort out the technical details of my work. I am also thankful to Dr. Christian Constanda and Dr. Leslie G. Thompson for serving on my committee. Their instructions, comments, suggestions and reviews of my dissertation are deeply appreciated. I would like to thank Dr. Guohua Gao for his help and suggestions during my study and Mr. Alan Steinle for the proofreading of my dissertation.

I gratefully acknowledge financial support from the Department of Petroleum Engineering of the University of Tulsa. I appreciate Mrs. Judy L. Teal and Mrs. Loreta M. Watkins for their help during my study.

I am thankful to my wife Dongfang Zhao for her unconditional love, support and patience over the last few years.

This work is dedicated to my parents, Wensen Chen and Huilan Cao for their unconditional love and support.

.

TABLE OF CONTENTS

LIST OF TABLES

LIST OF FIGURES

CHAPTER 1

INTRODUCTION

1.1 Literature Review of Estimate of Relative Permeability Curves

Relative permeability curves are critical for many reservoir engineering calculations. these corves have a major on water flood performance. Conventionally, relative permeabilities are obtained from laboratory core analysis. But this method has its limitations. It is hard for conventional laboratory core analysis to perfectly simulate reservoir conditions. Moreover, estimates of relative permeability curves from reservoir core samples represent only a very small portion of the reservoir (see [60]). Our objective is to design an in-situ test for the estimate of relative permeability curves.

Although estimation of relative permeability curves is not often done in pressure transient analysis, it has a long history in the history matching literature. Numerous papers from the 1970's and 1980's discuss techniques for the estimation of relative permeability curves by matching pressure and rate (or displaced volume) data from laboratory core floods using an optimization algorithm to minimize a least squares type objective function. It appears that Archer and Wong [4] were the first authors to consider the estimation of relative permeability curves by applying a reservoir simulator to history match laboratory core flood. They estimated only parameters that define the shape of relative permeability curves by a trial and error method during the history match. Sigmund and McCaffery [51] used power law expressions to model relative permeability curves and estimated only the two exponential parameters in the formulas. Kerig and Watson [30] used cubic splines to parameterize relative permeability curves and found that cubic splines with a small number of knots appear to be sufficiently flexible to yield more accurate estimates of true relative permeability curves, however, they assumed absolute permeability is known. Lee and Seinfeld [35] considered the simultaneous estimation of the absolute

permeability field and relative permeability for a two-dimensional, two-phase flow oil-water system. They used power law relative permeability and assumed that the end point values of relative permeabilities were known. Thus, only the two exponents in the power law relative permeability functions were estimated. In the specific examples considered, they matched pressure and water cut data at wells producing from an oil reservoir under water flood. Watson et al. [57] considered the simultaneous estimation of porosity, absolute permeability and relative permeability by automatic history matching of production data. In these examples, they used power law relative permeabilities and estimated only the two exponents in these two power law functions and assumed end-point values were known. Kulkarni et al. [32] also considered the estimation of relative permeabilities from water-cut and pressure data for a two-phase flow oil-water system. They modeled relative permeabilities with both B-splines and power law functions. Reynolds et al. [49] first discussed the simultaneous estimation of absolute permeability fields and relative permeability curves under three-phase flow conditions. A power law form of relative permeability curves was used. Their paper gives an overview of attempts made to estimate relative permeability curves over the past thirty or so years.

The Wireline Formation Tester (WFT) has been applied in pressure measurements since the 1950's. WFT, which provides direct flow tests and analysis, has been largely confined to the determination of single-phase permeability and anisotropy. Since 2001, however, some authors have made efforts to obtain relative permeabilities using information from the WFT. Zeybek et al. [61] presented a methodology to integrate the formation-tester pressure and water-fraction measurements with openhole array resistivity measurements to obtain zonal relative permeabilities of oil and water. This approach aims to obtain relative permeabilities that honor the pressure drop and the fraction of water observed in the flowline by trial and error. The details of the inversion of conductivity logs in terms of fractional flow are given by Ramarkrishnan and Wilkinson [48]. The WFT states that saturation change around a wellbore provides useful information for estimation of relative permeability curves.

Although many papers have also proposed using history matching techniques (see

reference [49]) to adjust relative permeability curves by matching long-time production data, the objective of this research is to generate a procedure to estimate relative permeability curves from a well test that has a duration of a few hours to a very few days. Intuitively, to do this successfully, one should generate data that is sensitive to a wide range of saturations, i.e., generate data similar to that which can be obtained in a laboratory core flood. To do so, an injection/falloff test followed by a production period is proposed. The idea is that, during the flow back period, the sandface will be exposed to a wide range of water saturations and the associated pressure and phase rate data or water cut data should be sufficient to obtain good estimates of relative permeability curves.

1.2 Injection/Falloff/Production Test (IFPT)

1.2.1 Pressure Response of IFPT

The IFPT consists of three periods: (i) injection of water into an oil reservoir, (ii) a falloff test, and (iii) a producing period. Fig. 1.1 shows the total flow rate and bottomhole pressure response of an IFPT with a sequence of 5-hour injection, 5-hour falloff and 14-hour production. Fig. 1.1 shows the bottomhole pressure responses of the IFPT with constant rates of water injection and production, respectively. The initial pressure is 2500 psi. At a very early times, the pressure increases rapidly at first because of a damaged skin zone with low permeability around the wellbore. Then the bottomhole pressure drops, mainly because of the mobility ratio effect, i.e water more mobile than oil. Following injection, the pressure drops during falloff approaching the initial pressure of 2500 psi. During production, the bottomhole pressure demonstrates a special behavior due to the total mobility changing around the wellbore. The total mobility is defined as

$$\lambda_t = \lambda_w + \lambda_o, \tag{1.1}$$

where $\lambda_w = k_{rw}(S_w)/\mu_w$ and $\lambda_o = k_{ro}(S_w)/\mu_o$ represent water phase and oil phase mobilities, respectively; k_{rw} and k_{ro} represent relative permeabilities of water and oil phases respectively; and μ_w and μ_o are water and oil mobilities. In the case shown here, the

pressure drops sharply around 14 hours when the sandface oil saturation increases very rapidly, because the oil mobility is smaller than the water mobility. The pressure response may have a different behavior, depending on the endpoint mobility ratio between the water phase and oil phase, which is expressed as

$$\hat{M} = \frac{\hat{\lambda}_w}{\hat{\lambda}_o}, \tag{1.2}$$

where $\hat{\lambda}_w = k_{rw}(1 - S_{or})/\mu_w$ is endpoint water mobility and $\hat{\lambda}_o = k_{ro}(S_{iw})/\mu_o$ is endpoint oil mobility.

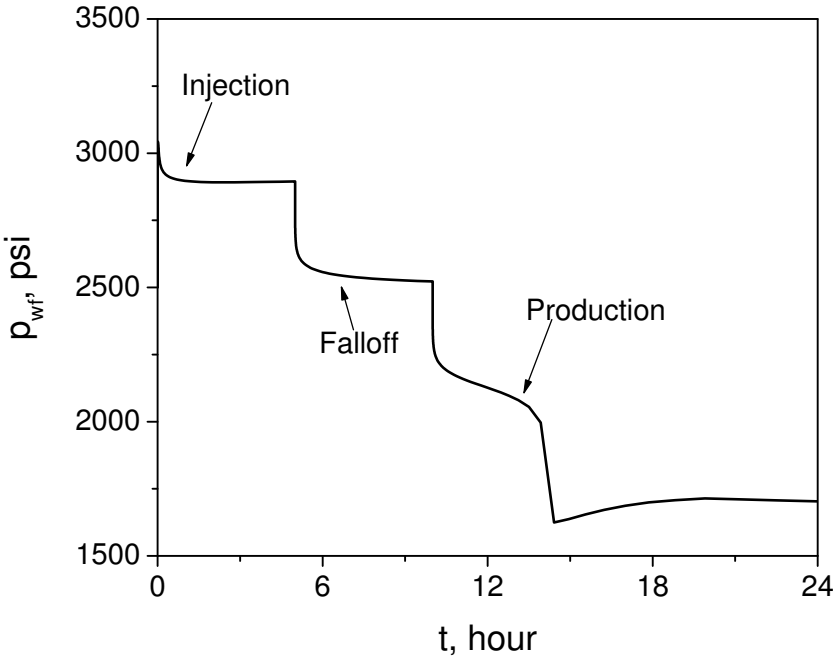

Figure 1.1: Bottomhole pressure response of injection/falloff/production test.

1.2.2 Diagnostic Plots of IFPT

Diagnostic plots are widely applied to determine the reservoir properties in conventional welltesting. Using diagnostic plots, this section introduces information provided by an IFPT. Fig. 1.2 shows a diagnostic plot of the pressure change, the circles, and its derivative, the solid curves, for the injection period. At indicated in Bratvold and Horne [12] and Boughrara [9], at extremely early times during the injection period, the derivative

of the pressure difference should be nearly constant and be proportional to endpoint oil mobility, i.e.,

$$\frac{d\Delta p}{d\ln(t)} = \frac{70.6 q_{inj}}{kh\hat{\lambda}_o}. \tag{1.3}$$

In practice we do not expect to see this semilog line because the data are contaminated by wellbore storage effects at early times. At the end of the injection period, the derivative of the pressure difference is close to a constant value (see references [56, 12, 46]) given by

$$\frac{d\Delta p}{d\ln(t)} = \frac{70.6 q_{inj}}{kh\hat{\lambda}_w}. \tag{1.4}$$

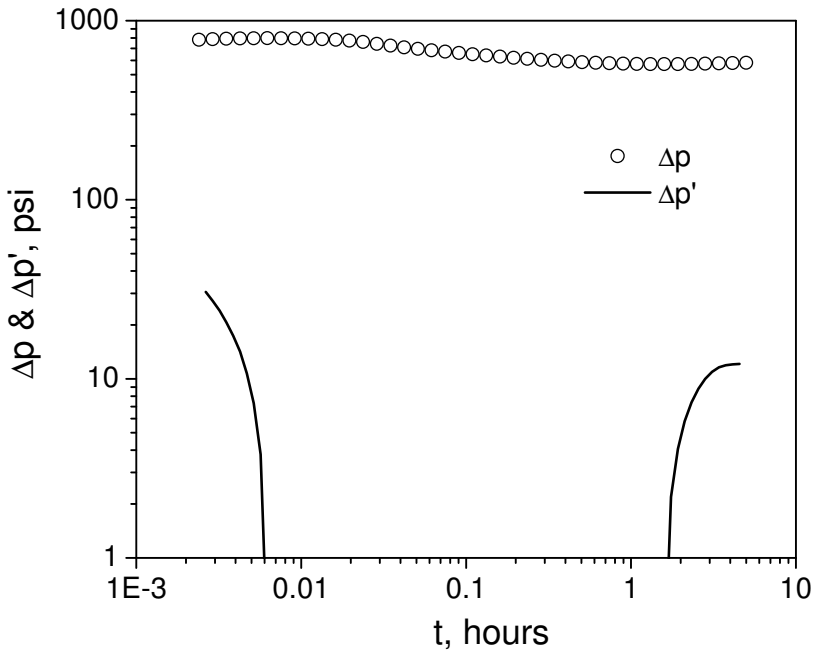

Figure 1.2: Diagnostic plot of pressure difference during water injection.

Between 0.01 and 1 hours, the pressure derivative in Fig. 1.2 is negative as expected for the case of a positive skin factor and an unfavorable mobility ratio [8]. Throughout, $\hat{\lambda}_w$ is the endpoint water mobility, i.e., the water mobility evaluated at residual oil saturation. Similarly, $\hat{\lambda}_o$ denotes the endpoint oil mobility, i.e., the oil mobility evaluated at irreducible water saturation.

Fig. 1.3 shows the log-log diagnostic plot of pressure data from the subsequent falloff period. The falloff derivative represents the log-derivative of $\Delta p = p_{wf,s} - p_{ws}(\Delta t)$ with respect to Agarwal's equivalent time[3], defined by

$$t_e = \frac{t_p \Delta t}{t_p + \Delta t}, \tag{1.5}$$

plotted versus shutin time Δt. Here, $p_{wf,s}$ is the pressure at the end of the injection period. t_p is total injection time. Since the injection period was short, the derivative of the falloff data reflects the oil mobility in the uninvaded zone almost immediately after the beginning of the falloff test and is equal to its theoretical value given by the right side of Eq. 1.3.

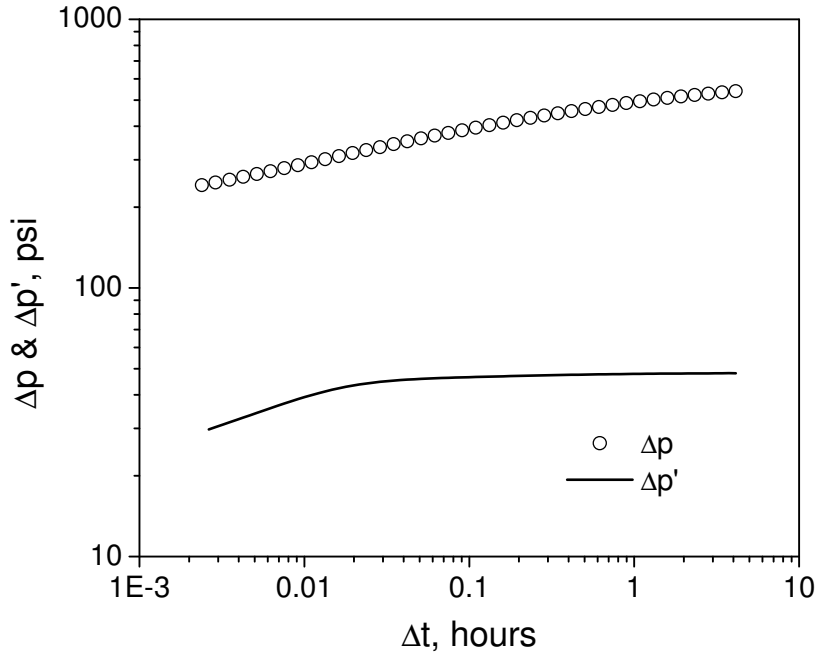

Figure 1.3: Diagnostic plot of pressure difference during falloff.

The pressure change during flow back period is defined by

$$\Delta p = p_{wf,s} - p_{wf}(\Delta t), \tag{1.6}$$

where $p_{wf,s}$ is the final shutin pressure for the falloff test and Δt is time measured from

the beginning of the flow back period.

Fig. 1.4 shows a log-log plot of Δp and its derivative with respect to Δt during the flow back period. The behavior of the pressure derivative during the flow back period is more complicated. The pressure derivative behavior is determined by the values of total mobility in the region where the total rate is changing as well as reservoir properties in the region where the total mobility is changing. It is obvious that the derivative should represent water property first at very early production time because of a water bank surrounding the wellbore after the injection/falloff period. In a short time, in which the water saturation around wellbore doesn't change much, the constant flow rate passes through the water bank and goes into the single oil phase zone according to the steady-state theory [55]. During the period from 0.1 to 1.0 hours, the pressure diffusion (region where rate is changing with time) is essentially confined to the single phase oil zone whereas the total mobility is changing only in the vicinity of the flood front location at the end of injection. This change in total mobility has only a small effect on the wellbore pressure during the period from 0.1 to 1.0 hours. The pressure derivative of Δp is close to the single phase oil result given by the right side of Eq. 1.3. When oil begins to flow back to the wellbore, the oil saturation increases and the total mobility around the wellbore sandface decreases significantly. Correspondingly, the derivative shows a sharp increase beginning at about 2 hours (solid curve as shown in Fig. 1.4). At the very essentially injected water has been produced and the derivative of the pressure difference appearances a constant value, reflecting the single phase oil property, at late time of production.

The above statements suggest that the data during late time of injection and falloff production provide us with information to estimate endpoint mobilities or relative permeabilities and the data during production present information on the saturation and total mobility around the wellbore, i.e., information on relative permeability curves. In later chapters, we present information to change this objective into a conclusions by considering sensitivities and synthetic examples.

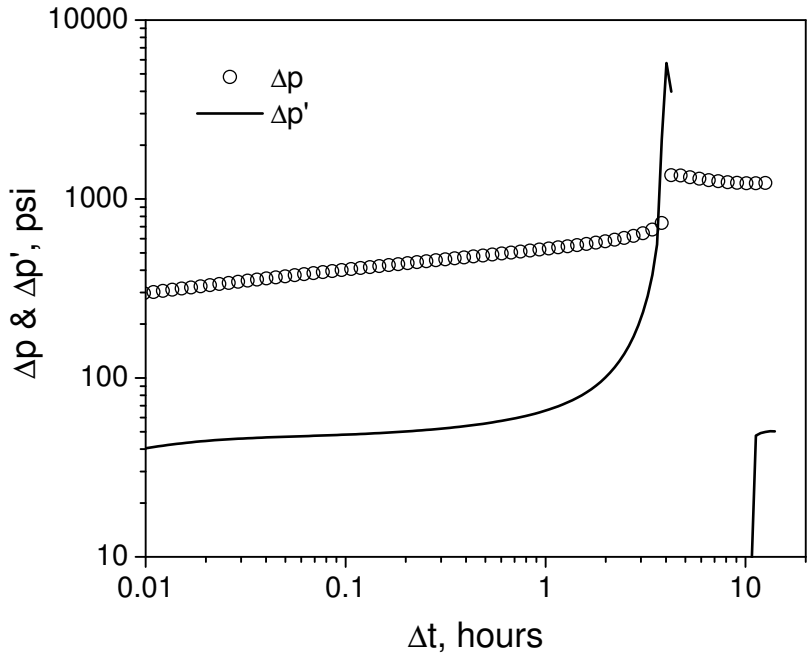

Figure 1.4: Diagnostic plot of pressure difference during production.

1.3 Literature Review, Analytical Solution

As noted previously, our focus is to estimate relative permeability curves using data from an IFPT. The producing period is critical, as it yields production data that reflects changes in sandface mobility and is thus highly sensitive to the parameters used to model relative permeability curves. We provide a nonlinear regression algorithm to use to estimate the parameters defining the relative permeabilities by matching pressure data both by using a numerical reservoir simulator and by applying our analytical solution for the IFPT.

Beginning at least as early as 1952 (Verigin [56]), various analytical or approximate analytical solutions for the pressure response during injection and/or falloff tests have been presented in the literature. In general, these solutions require a model for generating the saturation distribution as a function of time (piston displacement or Buckley-Leverett) during injection and assume that the front does not move during falloff so that the falloff

solution is equivalent to solving a multicomposite single-phase reservoir problem where the pressure at the end of the injection solution period provides the initial condition for the falloff problem. Abbaszadeh and Kamal [2] show that the pressure solution at the end of injection can itself be obtained from an equivalent multicomposite problem, whereas, Bratvold and Horne [12] assume the validity of the Boltzman transform to generate the injection solution. Most solutions available consider only injection at a constant rate followed by a falloff test, the major exception being the work of Levitan [37] who was able to generate a solution for multirate tests. Most solutions, including all those mentioned above, consider only one-dimensional radial flow problems, the major exceptions being Thambynayagam [53] who presented injection/falloff solutions for a vertical restricted-entry well assuming piston displacement. Recent papers [8, 46, 7] used the Thompson-Reynolds steady-state theory [55, 54] to generate approximate analytical solutions for complete-penetration and restricted-entry vertical wells as well as for horizontal wells. We use a similar approach in our work.

Peres and Reynolds [8] showed that incorporation of the skin factor using the infinitesimally thin skin is not valid during the injection period; for example, for one-dimensional radial flow problems, they showed that a skin zone with a width of a few inches can have a pronounced effect on the injection pressure and its derivative for several hours. For a damaged well and an unfavorable mobility ratio, they showed that the injection pressure derivative may be negative for a considerable period of time. Because of this result, we use a finite-radius skin zone [28] for the injection/falloff/production test (IFPT) considered here.

This paper focuses on obtaining the analytical solution during the multiphase production portion of the IFPT for one-dimensional radial flow problems. By combining this solution with the analytical solutions for injection and falloff periods [46, 8], the pressure solution for the IFPT test is obtained. The difficult part is generating the solution for the water saturation profile during the production period of the IFPT. Once this is done, it is easy to use the steady-state theory [55, 54] to generate the pressure solution.

For water injection, the saturation distribution can be easily calculated using the Buckley-Leverett theory [15]. However, the Buckley-Leverett theory is not directly applicable to calculate the saturation distribution during production, mainly due to the fact that the initial saturation distribution is not uniform. The front tracking method (see [23, 52, 10, 11]) seems to be an appropriate way to generate the saturation distribution. In the front tracking method, the saturation is discretized into small intervals and each saturation discontinuity interval is treated as a shock. Different shocks travel at different speeds according to the Rankine-Hugoniot equation. The faster shocks catch up with slower ones and merge into new shocks. To accurately capture the propagation and merging of shocks, Juanes and T.W. Patzek [29] implemented an iterative procedure, but this is a slow computational procedure. For the special case of production starting with a nonuniform saturation distribution, a modified front tracking approach is presented in this research, which does not formally discretize the saturation profile and does not require iteration to generate the evolution of the saturation profile during production. After the saturation distribution is generated, the pressure response can be obtained easily. By comparing the saturation and pressure results generated with the solution procedure with those from a simulator using a very fine radial grid system, the accuracy of the solution is validated.

It is shown that pressure data from an IFPT can be matched with our analytical solution using nonlinear regression to obtain reliable estimates of absolute permeability, skin factor and relative permeability curves. Our initial work on this estimation procedure is summarized in papers of Chen et. al. [19, 20].

1.4 Assumptions

For the synthetic examples presented in this work, the parameters that we estimate are reservoir permeability, skin factor (or permeability in the skin zone) and the parameters defining relative permeability curves. All other rock and fluid properties are assumed to be known. Wellbore storage is neglected, but we delete very early time data from the analysis under the assumption that it would be influenced by wellbore storage

effects. The skin zone is modeled as a circular region concentric with the wellbore using Hawkins' formula [28]. When matching data for the examples presented, we fix the radius of the skin zone and estimate the skin zone permeability and then estimate the skin factor by applying the formula of Hawkins [28]. Hysteresis effects are neglected after we gave investigation on different models from literatures. Experiments by Carlson [18] and Bedrikovetsky et al. show that the hysteresis of the wetting phase relative permeability curve is generally small. Killough [31] considered the hysteresis on the wetting and non-wetting phase relative permeability curves. Ramakrishnan and Wasan [47] also support the above quote from Killough. Recently, Zeybek et al. [61] also used Killough's model [31] to argue flow test data obtained with a formation tester (drainage process) reflects the imbibition relative permeability curves that govern filtrate invasion (imbibition). For the non-wetting phase relative permeability curves, hysteresis models generally assume that the scanning curves are reversible, which bears some theoretical rationale [13]. All results considered here are based on the two-phase radial flow of oil and water where, during the first time period, water is injected into a homogeneous oil reservoir of uniform thickness at a constant rate through a completely-penetrating vertical well. In this research, the Thompson-Reynolds steady-state theory [55, 54] is applied during the water injection and production (oil flow back) periods.

Although in some examples, constant flow rates during water injection and production are assumed in practice, it is difficult to maintain constant injection and production rates, in practice, thus the effects of flow rate fluctuation are investigated. We used some time interval with a average flow rate to represent the fluctuation of flow rate when we do the nonlinear regression. The results suggest that the IFPT analysis can still be applied. We also considered IFPT analysis for a heterogeneous permeability field by a homogeneous model of permeability. The results show that the IFPT can provide a reasonable average estimates of model parameters for the heterogeneous field.

CHAPTER 2

ANALYTICAL SOLUTION OF PRESSURE RESPONSE DURING IFPT

In this chapter, some theoretical results about two phase oil-water system flow in reservoir porous media are presented. In the first section, the steady-state theory presented by Thompson and Reynolds [55] is introduced. The steady-state theory is an important assumption and one of the theoretical foundations for the IFPT. In the second section, the Buckley-Leverett theory for radial flow is discussed. Buckley-Leverett theory predicts the saturation profile versus time during water injection. In the third section, an approximate analytical solution for pressure for the injection/falloff/production test is presented for the case where the capillary pressure effects are negligible. This solution relies on computing the saturation evolution during production based on the Buckley-Leverett theory and the front tracking method. The analytical results are verified with simulation results obtained from a black oil simulator in the third section. Finally, the validation of this saturation evolution model and pressure response is also validated with simulation results by comparison with synthetic cases.

2.1 Steady-state Theory for Water Injection

It is assumed that water is injected into an infinite and homogeneous reservoir through a completely-penetrating vertical well. The initial water saturation for water injection is uniform and equal to the irreducible water saturation, S_{iw}. Thompson and Reynolds [55] showed that, during water injection, a constant rate zone increasing in radius with time, propagates from the wellbore into the reservoir and the extent of this growing "steady-state" zone due to water injection always encompasses the water bank.

Fig. 2.1 shows an example obtained from a simulation result where the relationship between the total injection rate q_t and water saturation, S_w, at one particular time is shown clearly. In this figure, the total flow rate, the constant flow rate part of q_t (the dashed curve), is always larger than the zone where water saturation is varying. Let $r_{ss}(t)$ be the radius of the steady-state zone of constant flow rate at injection time t. We always have $r_{ss}(t) > r_{wf}(t)$, where $r_{wf}(t)$ is the radius of the water front during water injection for any reasonable values of reservoir properties, see Peres and Reynolds [46]. Within the steady-state region, for $r < r_{ss}$, $q_t(r,t)$ is equal to q_{inj}.

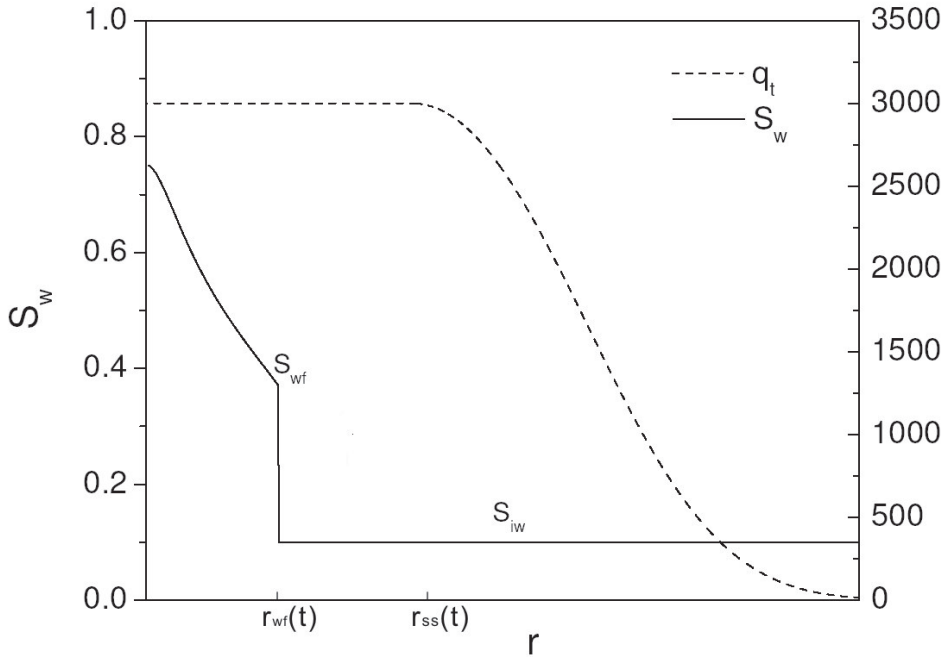

Figure 2.1: Relationship between water saturation and total flow rate in steady-state of water injection.

2.2 Buckley-Leverett Theory for Radial Flow

Water injection is assumed to be implemented in a one-layer reservoir with a uniform thickness by a completely penetrating vertical well. Gravity effects are neglected. Therefore, the flow in the reservoir can be treated as an oil-water two-phase one dimensional radial flow. When we consider capillary pressure, we assume a water wet system so that capillary pressure is given by

$$p_c = p_o - p_w, \tag{2.1}$$

where p_o is pressure in the oil phase, p_w is pressure in the water phase, and p_c is the capillary pressure. Applying Darcy's law, for this one dimensional radial flow problem with gravity ignored, the rates of oil and water in field units are given by

$$q_o = -1.127 \times 10^{-3} \frac{k k_{ro}}{\mu_o} 2\pi h r \frac{\partial p_o}{\partial r} \tag{2.2}$$

and

$$q_w = -1.127 \times 10^{-3} \frac{k k_{rw}}{\mu_w} 2\pi h r \frac{\partial p_w}{\partial r}, \tag{2.3}$$

where for injection, $q_w \geq 0$ and $q_o \geq 0$. Multiplying by $\frac{k_{rw}}{\mu_w}$ on both sides of Eq. 2.2 and $\frac{k_{ro}}{\mu_o}$ on both sides of Eq. 2.3, and subtracting subtracting the results, we have

$$q_w \frac{k_{ro}}{\mu_o} - q_o \frac{k_{rw}}{\mu_w} = -1.127 \times 10^{-3} \cdot 2\pi h k \frac{k_{ro}}{\mu_o} \frac{k_{rw}}{\mu_w} r \left(\frac{\partial p_w}{\partial r} - \frac{\partial p_o}{\partial r} \right). \tag{2.4}$$

From Eq. 2.1, we have

$$\frac{\partial p_w}{\partial r} - \frac{\partial p_o}{\partial r} = -\frac{\partial p_c}{\partial r}. \tag{2.5}$$

Substituting Eq. 2.5 and $q_o = q_t - q_w$ into Eq. 2.4, one can rearrange to get

$$q_w \left(\frac{k_{ro}}{\mu_o} + \frac{k_{rw}}{\mu_w} \right) = q_t \frac{k_{rw}}{\mu_w} + 1.127 \times 10^{-3} \cdot 2\pi h k \frac{k_{ro}}{\mu_o} \frac{k_{rw}}{\mu_w} r \frac{\partial p_c}{\partial r}, \tag{2.6}$$

where q_t is the total flow rate. When both sides of Eq. 2.6 are divided by

$$q_t \left(\frac{k_{ro}}{\mu_o} + \frac{k_{rw}}{\mu_w} \right),$$

we have the general fractional flow equation for F_w which includes the influence of capillary pressure and is given by

$$
\begin{aligned}
F_w &= \frac{q_w}{q_t} \\
&= f_w + 1.127 \times 10^{-3} \cdot 2\pi hk \frac{1}{q_t} f_w \lambda_o r \frac{\partial p_c}{\partial r},
\end{aligned}
\tag{2.7}
$$

where, in this work, f_w and λ_o are always defined by

$$
f_w(S_w) = \frac{\frac{k_{rw}(S_w)}{\mu_w}}{\frac{k_{rw}(S_w)}{\mu_w} + \frac{k_{ro}(S_w)}{\mu_o}},
\tag{2.8}
$$

and

$$
\lambda_o(S_w) = \frac{k_{ro}(S_w)}{\mu_o}.
\tag{2.9}
$$

While water is being injected into an infinite reservoir, the reservoir can be considered to be a combination of an infinite set of rings centered at the wellbore, as shown in Fig. 2.2. A grid block, S_{w_j}, represents a ring with water saturation S_{w_j} between its left boundary, $r_{j-\frac{1}{2}}$, and right boundary, $r_{j+\frac{1}{2}}$. The first grid bock, S_{w_1}, has a left boundary of $r_{\frac{1}{2}} = r_w$. During water injection, the conservation of mass of water in each grid block should be satisfied. Here, it is assumed that water density is constant and the flow rate is at reservoir conditions, which means the volume factor is equal to 1. The mass conservation of water on the j^{th} gridblock, assuming incompressible flow, can be expressed by

$$
\begin{pmatrix} \text{Increase in water due} \\ \text{to } S_w \text{ change with} \\ \text{a time interval } \Delta t \end{pmatrix} = \begin{pmatrix} \text{Volume of water flowing into} \\ \text{the control volume - volume of} \\ \text{water flowing out the control volume} \end{pmatrix}
$$

or

$$
\frac{\pi h \phi \left(r_{j+\frac{1}{2}}^2 - r_{j-\frac{1}{2}}^2\right)}{\theta} \Delta S_w = \Delta t \left(q_w \Big|_{r_{j-\frac{1}{2}}} - q_w \Big|_{r_{j+\frac{1}{2}}} \right),
\tag{2.10}
$$

where θ is a unit conversion constant in field units with time in hours, $\theta = 5.165/24$. Here

ΔS_w defines the change in saturation over the time step of length Δt, and we assume the rates in and out are constant over this time step. From Eq. 2.7, the equations of water rate at the two boundaries of the control volume are

$$q_w\Big|_{r_{j-\frac{1}{2}}} = q_t F_{w_{j-\frac{1}{2}}}, \tag{2.11}$$

and

$$q_w\Big|_{r_{j+\frac{1}{2}}} = q_t F_{w_{j+\frac{1}{2}}}. \tag{2.12}$$

Using Eqs. 2.11 and 2.12 in Eq. 2.10 and dividing the resulting equation by $\Delta t(r_{j+\frac{1}{2}})$ gives

$$\frac{\pi h\phi(r_{j+\frac{1}{2}} + r_{j-\frac{1}{2}})}{\theta}\frac{\Delta S_w}{\Delta t} = -q_t\left[\frac{F_{w_{r_{j+\frac{1}{2}}}} - F_{w_{r_{j-\frac{1}{2}}}}}{r_{j+\frac{1}{2}} - r_{j-\frac{1}{2}}}\right]. \tag{2.13}$$

Since this applies for all gridblocks, we simply let

$$r = r_j = \frac{r_{j+\frac{1}{2}} + r_{j-\frac{1}{2}}}{2}. \tag{2.14}$$

So Eq. 2.13 can be written as

$$\frac{2\pi h\phi}{\theta}\frac{\Delta S_w}{\Delta t} = -\frac{q_t}{r}\left[\frac{F_{w_{r_{j+\frac{1}{2}}}} - F_{w_{r_{j-\frac{1}{2}}}}}{r_{j+\frac{1}{2}} - r_{j-\frac{1}{2}}}\right]. \tag{2.15}$$

Taking the limit of as $\Delta t \to 0$ and $\Delta r = r_{j+\frac{1}{2}} - r_{j-\frac{1}{2}} \to 0$ gives

$$\frac{2\pi h\phi}{\theta}\frac{\partial S_w}{\partial t} = -\frac{1}{r}q_t\frac{\partial F_w}{\partial r}. \tag{2.16}$$

Because F_w is a function of S_w, using the chain rule $\frac{\partial F_w}{\partial r} = \frac{dF_w}{dS_w}\frac{\partial S_w}{\partial r}$, Eq. 2.16 can be expressed by

$$\frac{2\pi h\phi}{\theta}\frac{\partial S_w}{\partial t} = -\frac{1}{r}q_t\frac{dF_w}{dS_w}\frac{\partial S_w}{\partial r}, \tag{2.17}$$

with the initial condition and boundary condition for water injection given by

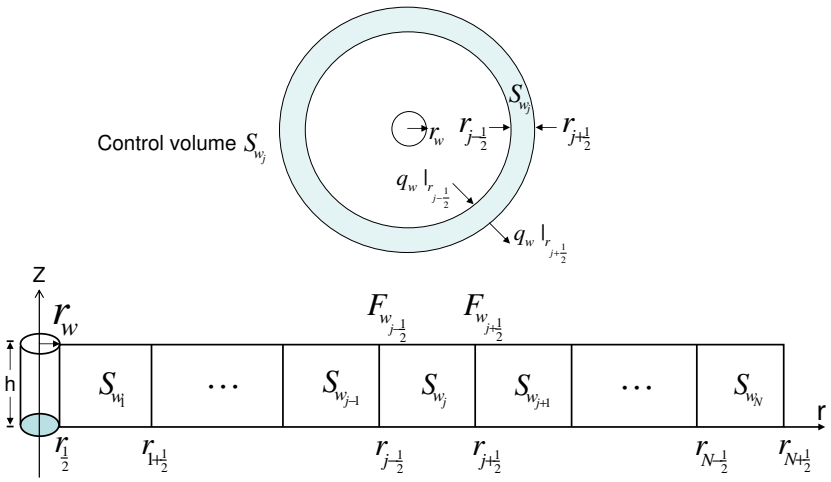

Figure 2.2: Block center grid system of S_w change for water injection.

$$\begin{cases} \text{I.C.} & S_w(r, t=0) = S_{iw}; \\ \text{B.C.} & S_w(r=r_w, t) = 1 - S_{or}; \\ & S_w(r=\infty, t) = S_{iw}. \end{cases} \tag{2.18}$$

In this chapter, capillary pressure is ignored, so Eq. 2.17 can be simplified to

$$\frac{\partial S_w}{\partial t} + \frac{1}{r}\frac{\theta q_t}{2\pi h\phi}\frac{df_w}{dS_w}\frac{\partial S_w}{\partial r} = 0. \tag{2.19}$$

This is a nonlinear hyperbolic PDE. The characteristic method indicates that water saturation, S_w, is constant along a characteristic curve. Thus, along any characteristic curve, the total differential of the water saturation is zero, i.e.,

$$dS_w = \frac{\partial S_w}{\partial r}dr + \frac{\partial S_w}{\partial t}dt = 0, \tag{2.20}$$

which means

$$\frac{\partial S_w}{\partial t} = -\frac{dr}{dt}\frac{\partial S_w}{\partial r}. \tag{2.21}$$

Substituting Eq. 2.21 into Eq. 2.19 results in

$$\frac{dr(S_w)}{dt} = \frac{1}{r}\frac{\theta q_t}{2\pi h\phi}\frac{df_w(S_w)}{dS_w}. \tag{2.22}$$

Then the Buckley-Leverett equation for radial flow can be represented by rewriting Eq. 2.22 as

$$\frac{dr^2}{dt} = \frac{\theta q_t}{\pi h\phi}\frac{df_w(S_w)}{dS_w}. \tag{2.23}$$

All saturations between S_w and $1 - S_{or}$ exist at $t = 0$, we can integrate Eq. 2.23 to obtain

$$r^2(S_w) = r_w^2 + \frac{\theta}{\pi h\phi}\frac{df_w(S_w)}{dS_w}\int_0^t q_t dt. \tag{2.24}$$

Eq. 2.24 gives an equation for locating the radial location ($r(S_w)$) of the saturation S_w at time t and applies for any S_w such that $S_{iw} \leq S_w \leq 1 - S_{or}$. In the case that q_t is constant for all time and capillary pressure is negligible, Eq. 2.24 becomes

$$r^2(S_w) = r_w^2 + \frac{\theta q_t}{\pi h\phi}t\frac{df_w(S_w)}{dS_w}. \tag{2.25}$$

As in one-dimensional linear flow, the solution of Buckley-Leverett has a shock, a jump discontinuity in the saturation profile at location of the water front. Where S_{wf} denotes the saturation at the flood front. The water balance across the shock front indicates that the shock speed (the speed of water front) can be expressed by the Rankine-Hugoniot shock condition,

$$\frac{dr^2}{dt} = \frac{\theta q_t}{\pi h\phi}\frac{f_w^+(S_w^+) - f_w^-(S_w^-)}{S_w^+ - S_w^-}, \tag{2.26}$$

where, on the two sides of the shock, $S_w^+ = S_{iw}$ and $S_w^- = S_{wf}$, as shown in Fig. 2.1. So according to Eq. 2.26 (speed of water front) the shock speed becomes

$$\frac{dr^2}{dt} = \frac{\theta q_t}{\pi h\phi}\frac{f_w(S_{wf}) - f_w(S_{iw})}{S_{wf} - S_{iw}}. \tag{2.27}$$

Using $S_w = S_{wf}$ in Eq. 2.22 and comparing the resulting equation with Eq. 2.27 gives

$$\frac{df_w(S_{wf})}{S_{wf}} = \frac{f_w(S_{wf}) - f_w(S_{iw})}{S_{wf} - S_{iw}} \tag{2.28}$$

This equation represents the equation for calculating S_{wf}. Welge [58] showed that S_{wf} can be calculated graphically as shown in Fig. 2.3, which shows the fractional flow curve and its derivative. Note the shock speed of the water front movement is represented by the slope of the tangent line, i.e., the straight dashed line through $(S_{iw}, f_w(S_{iw}))$ and $(S_{wf}, f_w(S_{wf}))$.

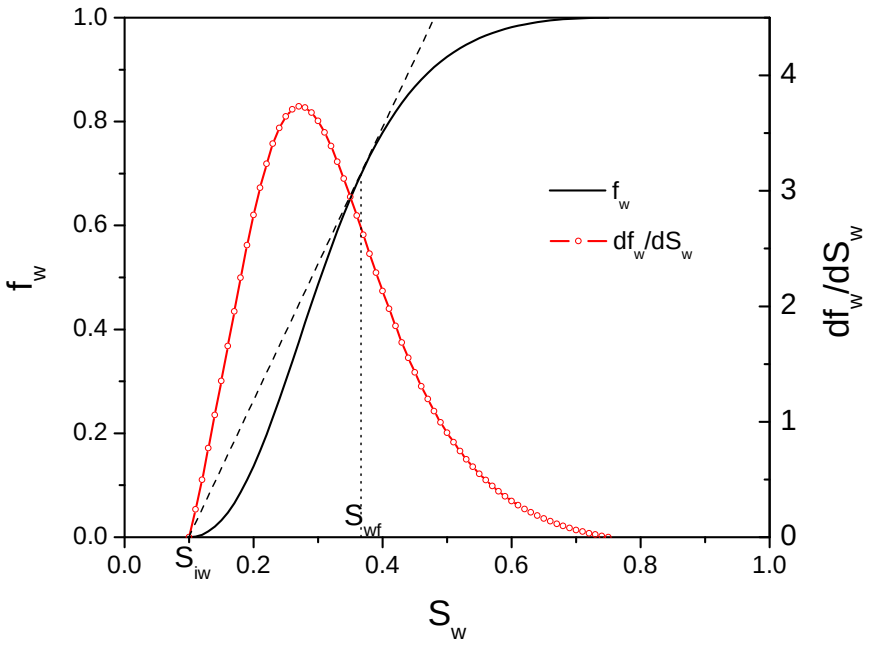

Figure 2.3: Fractional flow and its derivative.

Buckley-Leverett theory states that, for water injection into an oil reservoir with uniform initial water saturation, the water front separates the oil reservoir into two parts: ahead of the water front is the single phase oil with initial water saturation, S_{iw}; and behind the water front is the two-phase zone. In the two-phase zone, water saturation is between $1 - S_{or}$ and S_{wf} from the wellbore to the water front.

2.3 Approximate Analytical Solution for Pressure Response

The following sections discuss the bottomhole pressure responses during the water injection, falloff and production periods (capillary pressure is ignored) based on Buckley-Leverett theory and front tracking method. When water is injected into an infinite reservoir through a completely-penetrating water injection well, according to the Darcy's law expressed in Eqs. 2.3 and 2.2, total flow rate, q_t, can be expressed by

$$q_t(r,t) = -1.127 \times 10^3 \cdot 2\pi hk\lambda_t \frac{dp(r,t)}{dr}, \qquad q_t > 0, \tag{2.29}$$

where

$$\lambda_t(S_w) = \frac{k_{rw}(S_w)}{\mu_w} + \frac{k_{ro}(S_w)}{\mu_o}. \tag{2.30}$$

Rearranging and integrating Eq. 2.29, we have

$$\int_{p(r_w,t)}^{p(r=\infty,t)} dp(r,t) = -\frac{1}{1.127 \times 10^3 \cdot 2\pi h} \int_{r_w}^{\infty} \frac{q_t(r,t)}{\lambda_t(r,t)k(r)} \frac{dr}{r}, \tag{2.31}$$

where $p(r=\infty,t) = p_i$ and $p(r_w,t) = p_{wf}(t)$. Then the pressure difference between the bottomhole pressure, $p_{wf}(t)$, and the reservoir initial pressure, p_i, is defined by

$$\Delta p(t) = p_{wf}(t) - p_i = \frac{\alpha}{h} \int_{r_w}^{\infty} \frac{q_t(r,t)}{\lambda_t(r,t)k(r)} \frac{dr}{r}, \tag{2.32}$$

where α is a unit conversion constant. In field units,

$$\alpha = \frac{1}{1.127 \times 10^3 \cdot 2\pi} = 141.2. \tag{2.33}$$

In this research, it is assumed that water is injected into a homogeneous reservoir, but a damaged zone with known radius, r_s, around the wellbore is also considered. The damaged zone has its own permeability, k_s, to denote mechanical skin factor. So the permeability distribution can be expressed by

$$k(r) = \begin{cases} k_s, & \text{for } r_w < r \leq r_s; \\ k, & \text{for } r > r_s. \end{cases} \tag{2.34}$$

2.4 Approximate Analytical Solution of Pressure Response during Injection

In the previous section, it was stated that a reservoir is divided into two parts by the water saturation front during water injection through a completely-penetrating vertical well in an infinite reservoir. Ahead of the front, $S_w = S_{iw}$ and $\lambda_t = \hat{\lambda}_o$ for single-phase oil. Separating the integral in Eq. 2.32 into two parts by location of the water front, $r_f(t)$, and adding two terms which sum to zero, i.e.,

$$\frac{\alpha}{h}\int_{r_w}^{r_{f(t)}} \frac{q_t(r,t)}{\hat{\lambda}_o k(r)}\frac{dr}{r} - \frac{\alpha}{h}\int_{r_w}^{r_{f(t)}} \frac{q_t(r,t)}{\hat{\lambda}_o k(r)}\frac{dr}{r}, \tag{2.35}$$

Eq. 2.32 can be rewritten as

$$\begin{aligned} \Delta p(t) &= p_{wf}(t) - p_i \\ &= \frac{\alpha}{h}\int_{r_w}^{r_{f(t)}} \frac{q_t(r,t)}{\lambda_t(r,t)k(r)}\frac{dr}{r} + \frac{\alpha}{h}\int_{r_{f(t)}}^{\infty} \frac{q_t(r,t)}{\lambda_t(r,t)k(r)}\frac{dr}{r} \\ &\quad + \frac{\alpha}{h}\int_{r_w}^{r_{f(t)}} \frac{q_t(r,t)}{\hat{\lambda}_o k(r)}\frac{dr}{r} - \frac{\alpha}{h}\int_{r_w}^{r_{f(t)}} \frac{q_t(r,t)}{\hat{\lambda}_o k(r)}\frac{dr}{r}. \end{aligned} \tag{2.36}$$

Combining the first and the forth terms in Eq. 2.36, we have

$$\begin{aligned} \Delta p(t) = \frac{\alpha}{h\hat{\lambda}_o}\int_{r_w}^{r_{f(t)}} \frac{q_t(r,t)}{k(r)}\left(\frac{\hat{\lambda}_o}{\lambda_t(r,t)} - 1\right)\frac{dr}{r} \\ + \frac{\alpha}{h}\int_{r_{f(t)}}^{\infty} \frac{q_t(r,t)}{\lambda_t(r,t)k(r)}\frac{dr}{r} + \frac{\alpha}{h}\int_{r_w}^{r_{f(t)}} \frac{q_t(r,t)}{\hat{\lambda}_o k(r)}\frac{dr}{r}. \end{aligned} \tag{2.37}$$

It is known that ahead of the water front, $r > r_f$, we have $\lambda_t(r,t) = \hat{\lambda}_o$. In section 2.1, the steady-state theory of Thompson and Reynolds [55] states that the steady-state zone, $r_{ss}(t)$, always covers the water front zone, $r_f(t)$, i.e. $r_f < r_{ss}$. And, within the steady-state zone, the total flow rate, $q_{(r<r_{ss},t)}$, equals the constant injection rate, q_{inj}. So

Eq. 2.37 becomes

$$\Delta p(t) = \frac{\alpha q_{inj}}{h\hat{\lambda}_o} \int_{r_w}^{r_{f(t)}} \left(\frac{\hat{\lambda}_o}{\lambda_t(r,t)} - 1 \right) \frac{1}{k(r)} \frac{dr}{r} + \frac{\alpha}{h\hat{\lambda}_o} \int_{r_w}^{\infty} \frac{q_t(r,t)}{k(r)} \frac{dr}{r}. \tag{2.38}$$

It's clear that the second term in Eq. 2.38 is the pressure change in the single-phase oil at irreducible water saturation, denoted by $\Delta\hat{p}_o$. Then Eq. 2.38 can be simplified as

$$\Delta p(t) = \Delta\hat{p}_o(t) + \frac{\alpha q_{inj}}{h\hat{\lambda}_o} \int_{r_w}^{r_{f(t)}} \left(\frac{\hat{\lambda}_o}{\lambda_t(r,t)} - 1 \right) \frac{1}{k(r)} \frac{dr}{r}. \tag{2.39}$$

The techniques stated above were first presented by Peres and Reynolds (see reference [46]) for the generation of approximate analytical solutions for the water injection response. Based on the Buckley-Leverett theory and the Steady-state theory of Thompson and Reynolds, the pressure response of water injection into an infinite reservoir is denoted by a combination of the pressure response of single-phase oil and the pressure change in a limited two-phase zone. The single-phase oil pressure is obtained with the effective permeability, $kk_{ro}(S_{iw})$, and the total oil compressibility, which is expressed by

$$\hat{c}_{to} = c_w S_{iw} + c_o(1 - S_{iw}) + c_r, \tag{2.40}$$

where c_w, c_o and c_r represent the compressibilities of water, oil and rock, respectively. They are assumed to be constant in this research. For a given constant injection rate, the pressure change in the two-phase region is dominated by the total mobility distribution, which is calculated by the Buckley-Leverett theory. The single-phase oil solution based on oil mobility at irreducible water saturation is give by

$$\Delta p_o = p_{wf} - p_i = \frac{\alpha q_t}{kh\hat{\lambda}_o} \left[\frac{1}{2} \ln \left(\frac{\beta k \hat{\lambda}_o t}{\phi \hat{c}_{to} r_w^2} \right) + 0.4045 + s \right], \tag{2.41}$$

where β is a constant which depends on the system of units used. $\beta = 2.637 \times 10^{-4}$ if oil field units with time in hours are used. s is the skin factor of the damaged zone.

2.5 Approximate Analytical Solution of Pressure Response during Falloff

This section introduces the approximate analytical solution of pressure response during falloff based on the steady-state theory of Thompson and Reynolds [55] combined with rate superposition. This method is used in this research for predicting the pressure response during falloff. In the previous discussion, it was shown that our research is a two-phase flow problem in a homogeneous reservoir with uniform distribution of water saturation. Since gravity segregation and capillary pressure are ignored, the water saturation can be safely assumed to remain unchanged during falloff. The study of Abbaszadeh et al. [2] shows that this assumption is true only if the fluids are incompressible. In this research, numerical experiments also show the change in water saturation distribution is negligible during falloff provided capillary pressure is zero. Before falloff, there is a water bank after a time t_p of water injection with a constant flow rate, q_{inj}. The water saturation distribution is described by the Buckley-Leverett theory at the end of water injection, t_p. During falloff, the total compressibility of the system does not change. For a given location, r, in the reservoir and at any shut-in time, Δt, during falloff, the total compressibility can be expressed by

$$\begin{aligned} c_t(r,\Delta t) = c_t(r,t_p) &= c_r + c_o S_o(r,t_p) + c_w S_w(r,t_p) \\ &= c_r + c_o + (c_w - c_o) S_w(r,t_p). \end{aligned} \tag{2.42}$$

The total mobility, which does not change either during falloff, can be expressed by

$$\lambda_t(r,\Delta t) = \lambda_t(r,t_p) = \frac{k_{rw}(S_w(r,t_p))}{\mu_w} + \frac{k_{ro}(S_w(r,t_p))}{\mu_o}. \tag{2.43}$$

During falloff, Darcy's law is still valid. Similar to the water injection equation, the pressure difference during falloff can be represented by

$$\Delta p_{ws}(\Delta t) = p_{ws}(\Delta t) - p_i = \frac{\alpha}{h} \int_{r_w}^{\infty} \frac{q_s(r,\Delta t)}{\lambda_t(r,\Delta t) k(r)} \frac{dr}{r}, \tag{2.44}$$

where $q_s(r,\Delta t)$ is the total flow rate profile at shut-in time Δt. During falloff the total flow rate can not be zero immediately after shut-in because of the fluids' compressibilities.

Modified in the same way as was done for the pressure difference during water injection, Eq. 2.44 can be written as

$$\Delta p_{ws}(\Delta t) = \frac{\alpha}{h}\int_{r_w}^{r_f(t_p)} \frac{q_s(r,\Delta t)}{\lambda_t(r,\Delta t)k(r)}\frac{dr}{r} + \frac{\alpha}{h}\int_{r_f(t_p)}^{\infty} \frac{q_s(r,\Delta t)}{\lambda_t(r,\Delta t)k(r)}\frac{dr}{r}, \tag{2.45}$$

where $r_f(t_p)$ represents the water front at the instant of shut-in. Then adding and subtracting an integral from r_w to $r_f(t_p)$ to Eq. 2.45, we have

$$\begin{aligned}\Delta p_{ws}(\Delta t) = \frac{\alpha}{h}\int_{r_w}^{r_f(t_p)} \frac{q_s(r,\Delta t)}{\lambda_t(r,\Delta t)k(r)}\frac{dr}{r} + \frac{\alpha}{h}\int_{r_f(t_p)}^{\infty} \frac{q_s(r,\Delta t)}{\lambda_t(r,\Delta t)k(r)}\frac{dr}{r} \\ + \frac{\alpha}{h}\int_{r_w}^{r_f(t_p)} \frac{q_{os}(r,\Delta t)}{\hat{\lambda}_o k(r)}\frac{dr}{r} - \frac{\alpha}{h}\int_{r_w}^{r_f(t_p)} \frac{q_{os}(r,\Delta t)}{\hat{\lambda}_o k(r)}\frac{dr}{r}.\end{aligned} \tag{2.46}$$

In Eq. 2.46, $q_{os}(r,\Delta t)$ is the oil flow rate distribution in the reservoir obtained under single-phase oil flow conditions at the shut-in time Δt, i.e., it is the flow rate would be obtained if we inject oil at a rate of q_{inj} RB/D. For $r > r_f(t_p)$, it is assumed that $q_s(r,\Delta t) = q_{os}(r,\Delta t)$ and $\lambda_t(r,t_p) = \hat{\lambda}_o$, so that Eq. 2.46 becomes

$$\begin{aligned}\Delta p_{ws}(\Delta t) = \frac{\alpha}{h\hat{\lambda}_o}\int_{r_w}^{\infty} \frac{q_{os}(r,\Delta t)}{k(r)}\frac{dr}{r} \\ + \frac{\alpha}{h}\int_{r_w}^{r_f(t_p)} \left(\frac{q_s(r,\Delta t)}{\lambda_t(r,\Delta t)k(r)} - \frac{q_{os}(r,\Delta t)}{\hat{\lambda}_o k(r)}\right)\frac{dr}{r}.\end{aligned} \tag{2.47}$$

The first term on the right side of Eq. 2.47 is the pressure change for single-phase oil during falloff, which is denoted by $\Delta\hat{p}_{os}(\Delta t)$ and defined by

$$\Delta\hat{p}_{os}(\Delta t) = p_{ws}(\Delta t) - p_i = \frac{\alpha q_t}{2kh\hat{\lambda}_o}\ln\left(\frac{t_{pD}+\Delta t_D}{\Delta t_D}\right). \tag{2.48}$$

Then Eq. 2.47 can be simplified as

$$\Delta p_{ws}(\Delta t) = \Delta\hat{p}_{os}(\Delta t) + \frac{\alpha}{h\hat{\lambda}_o}\int_{r_w}^{r_f(t_p)} \left(\frac{\hat{\lambda}_o}{\lambda_t(r,\Delta t)}q_s(r,\Delta t) - q_{os}(r,\Delta t)\right)\frac{1}{k(r)}\frac{dr}{r}. \tag{2.49}$$

During falloff, the flow rate does not become zero through out reservoir immediately after the well is shut-in. Based on Duhamel's principle and rate superposition (see the reference [7]), the single-phase oil flow rate can be expressed by

$$q_{os}(r, \Delta t) = q_{inj} \left[\exp\left(-\frac{r_D^2}{4(t_{pD} + \Delta t_D)} \right) - \exp\left(-\frac{r_D^2}{4\Delta t_D} \right) \right], \tag{2.50}$$

where r_D and t_D are dimensionless radial distance and time, respectively, defined by

$$r_D = \frac{r}{r_w} \tag{2.51}$$

and

$$t_D = \frac{2.637 \times 10^{-4} k\lambda t}{\phi c_t r_w^2}. \tag{2.52}$$

t_{pD} is the dimensionless injection time of injection time t_p. The oil single-phase solution is based on oil properties at irreducible water saturation, S_{iw}. The dimensionless time should be based on the single-phase oil mobility $\hat{\lambda}_o$ and the single-phase oil compressibility expressed by

$$c_{to} = c_w S_{iw} + c_o(1 - S_{iw}) + c_r. \tag{2.53}$$

Then, Eq. 2.50 becomes

$$q_{os}(r, \Delta t) = q_{inj} \left[\exp\left(-\frac{\phi c_{to} r^2}{4\beta k \hat{\lambda}_o (t_p + \Delta t)} \right) - \exp\left(-\frac{\phi c_{to} r^2}{4\beta k \hat{\lambda}_o \Delta t} \right) \right]. \tag{2.54}$$

where in oil field units with time in hours $4\beta = 10.548 \times 10^{-4}$.

In this research, the total flow rate, $q_s(r, \Delta t)$, in the two-phase flow region is also evaluated by applying the single-phase rate superposition equation, so $q_s(r, \Delta t)$ is also expressed by

$$q_s(r,\Delta t) = q_{inj}\left[\exp\left(-\frac{r_D^2}{4(t_{pD}+\Delta t_D)}\right) - \exp\left(-\frac{r_D^2}{4\Delta t_D}\right)\right]. \tag{2.55}$$

But in Eq. 2.55, obviously the mobility and total compressibility should not be based on single-phase oil in the two-phase flow region. The research of Peres, Boughrara and Reynolds (see [45, 7, 9]) shows that a more accurate solution would be obtained if the values of these two properties are based on those that exist at the instant of shut-in time and at r. Therefore, we can set

$$\frac{r_D^2}{t_{pD}+\Delta t_D} = \frac{\phi c_t(r,t_p)r^2}{\beta k\lambda_t(r,t_p)(t_p+\Delta t)}, \tag{2.56}$$

and

$$\frac{r_D^2}{\Delta t_D} = \frac{\phi c_t(r,t_p)r^2}{\beta k\lambda_t(r,t_p)\Delta t} \tag{2.57}$$

in Eq. 2.55 to get

$$q_s(r,\Delta t) = q_{inj}\left[\exp\left(-\frac{\phi c_t(r,t_p)r^2}{4\beta k\lambda_t(r,t_p)(t_p+\Delta t)}\right) - \exp\left(-\frac{\phi c_t(r,t_p)r^2}{4\beta k\lambda_t(r,t_p)\Delta t}\right)\right]. \tag{2.58}$$

In this research, the approximate analytical solution of pressure response during falloff is computed using Eq. 2.49 with flow rates evaluated by Eqs. 2.54 and 2.58.

2.6 Approximate Analytical Solution of Pressure Response during Production

Based on the steady-state theory of Thompson and Reynolds [55] and the Buckley-Leverett theory [15], approximate analytical solutions for pressure response during water injection/falloff were achieved successfully. In this research, we also derive the approximate analytical solution of the pressure response during production based on the steady-state theory, the Buckley-Leverett theory and the front tracking method. During production, when water and oil flow back towards the well, the initial saturation distribution is

not uniform as it is during water injection and not static as it is during falloff. In the previous section, it was shown that the pressure change for a two phase problem can be treated as a sum of the pressure change in the single-phase oil and the pressure change in a limited two-phase region if the saturation distribution is known. So if we know how the saturation evolves during production, we may obtain the approximate analytical solution for the pressure response.

2.6.1 Water Saturation Evolution during Production

The fluid flow during production follows the same governing equation (Eq. 2.19) as for the water injection. However, the initial condition for production is represented by the saturation distribution at the end of falloff, i.e., it is not uniform (see Fig. 2.1). Thus the Buckley-Leverett theory cannot be directly applied to obtain the saturation distribution during production. However as mentioned in the introduction, the front tracking method [29] can be applied to generate the saturation profile as a function of time.

The front tracking method discretizes the saturation profile into small steps and treats these small saturation intervals as shocks (discontinuities). Shocks corresponding to different saturation ranges travel at different speeds according to Eq. 2.26. For two neighboring shocks, the faster one will catch up the slower one and the two shocks will merge into one new shock. To keep track of how the shocks propagate and merge as a function of time, an iterative process can be implemented [11], but this makes the algorithm slow. Furthermore, to be able to have an accurate representation of the water saturation distribution, small saturation intervals are required. To overcome these difficulties, we present a modified algorithm to calculate the saturation distribution. In this algorithm, the traditional Buckley-Leverett theory and the front tracking method are combined. This procedure avoids discretization of the saturation and does not require iteration.

During production, oil invades the water bank, and the initial oil saturation is variable. In this section, we use the oil saturation to illustrate the saturation evolution in the two-phase zone during production. Fig. 2.4, an exaggerated figure showing saturation

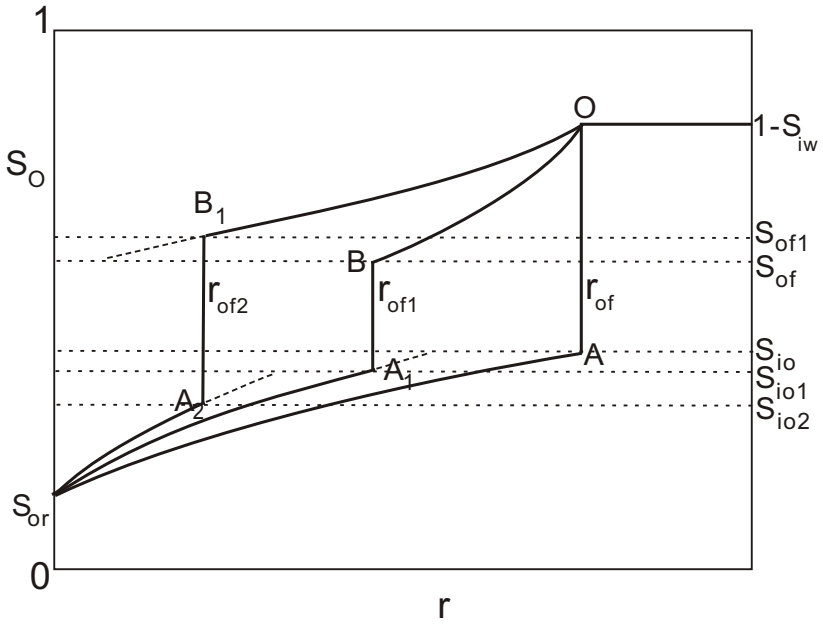

Figure 2.4: Illustration of oil saturation evolution during the production.

distributions after small time steps, illustrates the oil saturation profile at the end of falloff and at the first two time steps during production. We assume the well is at the left side in Fig. 2.4. The oil saturation at wellbore sandface $r = r_w$ is the residual oil saturation S_{or} and the water front is located at $r_{of} = r_{wf}(t_{inj})$, where t_{inj} is the end time of water injection. So at very beginning of production, the initial oil saturation for oil invading the two-phase zone at r_{of} is $S_{io} = 1 - S_{wf}$. To the right of r_{of} is the single phase oil zone and oil saturation equals to $1 - S_{iw}$. After falloff the initial oil saturation distribution is represented by curve $\widehat{OAS_{or}}$. Starting from initial oil saturation condition, using Fig. 2.4 and Fig. 2.5 (the oil fraction flow curve), we give the first two time steps, Δt_1 and Δt_2, to illustrate our model of water saturation evolution during production with an nonuniform initial oil saturation distribution.

1^{st} **time step,** Δt_1: According the initial oil saturation condition stated above, in Fig. 2.5, we can find point A on the oil fraction flow curve, which is corresponding to the initial oil saturation S_{io} when oil begins to invade water bank. In the same method as we normally had water front saturation for water injection using Welge's model [58], starting

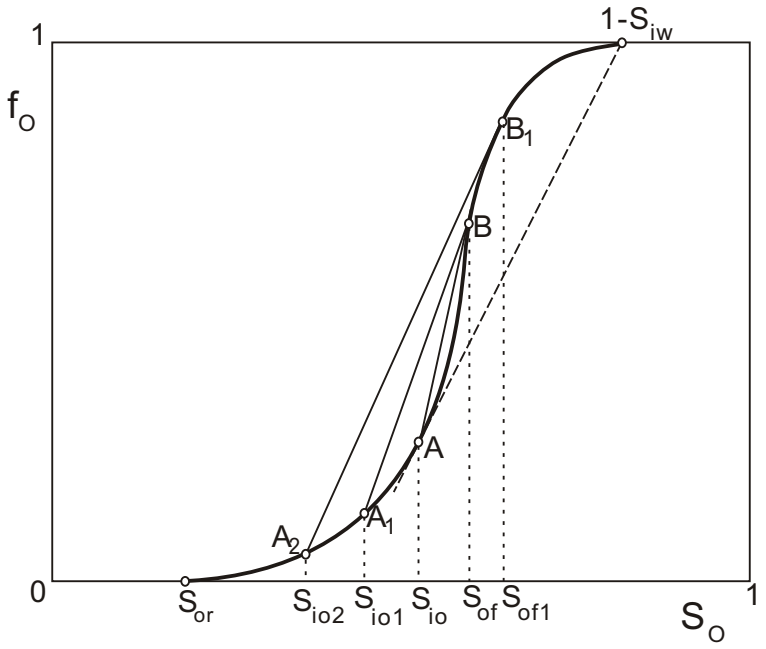

Figure 2.5: Oil fractional flow curve.

from the point A and drawing the tangent to the oil fractional flow curve, we obtained the point B with the initial oil front saturation S_{of}. The slope of line $\overline{AB}$, representing the initial oil shock front speed, is expressed by

$$\frac{df_o(S_{of})}{dS_o} = \frac{f_o(S_{of}) - f_o(S_{io})}{S_{of} - S_{io}}. \tag{2.59}$$

Then the initial shock speed is denoted by

$$\frac{dr^2(S_{of})}{dt} = -\frac{\theta q_t}{\pi\phi h}\left[\frac{f_o(S_{of}) - f_o(S_{io})}{S_{of} - S_{io}}\right], \tag{2.60}$$

where total flow rate q_t is assumed to be a positive constant value during production. Here, we assume in each time step, the shock speed is contant. We integrate Eq. 2.60 based on the production time Δt_1 and have

$$\int_{r_{of}}^{r_{of1}(\Delta t_1)} dr^2(S_{of}) = -\int_0^{\Delta t_1} \frac{\theta q_t}{\pi\phi h}\left[\frac{f_o(S_{of}) - f_o(S_{io})}{S_{of} - S_{io}}\right] dt. \tag{2.61}$$

Then, we have

$$r_{of1}(\Delta t_1)^2 - {r_{of}}^2 = -\frac{\theta q_t}{\pi\phi h}\left[\frac{f_o(S_{of}) - f_o(S_{io})}{S_{of} - S_{io}}\right]\Delta t_1. \tag{2.62}$$

where $r_{of}(\Delta t_1)$ is the oil front location after the first time step Δt_1. Finally, the front location after Δt_1 can be expressed by

$$r_{of1}(\Delta t_1) = \sqrt{r_{of} - \frac{\theta q_t}{\pi\phi h}\left[\frac{f_o(S_{of}) - f_o(S_{io})}{S_{of} - S_{io}}\right]\Delta t_1}. \tag{2.63}$$

After first time step Δt_1, the initial oil front moved from r_{of} to r_{of1} represented by moving of lines from $\overline{AO}$ to $\overline{A_1B}$, as shown in Fig. 2.4. In practice, we have a small time step of Δt_1, the distance between r_{of} and r_{of1} is very small. In Fig. 2.5, we can see the derivatives of oil fraction flow to the oil saturations $S_{io} < S_o \leq 1 - S_{iw}$ are lower than that to the initial oil front saturation S_{io} expressed by Eq. 2.59, i.e., the initial oil front saturation has the highest speed among those oil saturations between the initial oil front saturation S_{io} and oil saturation $1 - S_{iw}$. Noting that all saturation between S_{io} and $1 - S_{iw}$ exist at r_{of} at $\Delta t = 0$ similar to water injection at wellbore sandface. So after time Δt_1, the location of oil front moves from r_{of} to r_{of1} and oil distributions of saturations between S_{io} and $1 - S_{iw}$ exactly follows the Buckley-Leverett theory given by

$$\frac{dr^2(S_o)}{dt} = \frac{\theta q_t(t)}{\pi\phi h}\cdot\frac{df_o(S_o)}{dS_o}, \quad \text{for } S_{of} \leq S_o \leq 1 - S_{iw}. \tag{2.64}$$

For a constant rate production, we have $q_t(t) = q_t$. Rearranging and integrating Eq. 2.64, we have

$$\int_{r_{of}}^{r(S_o,\Delta t)} dr^2(S_o) = \int_0^{\Delta t}\frac{\theta q_t}{\pi\phi h}\cdot\frac{df_o(S_o)}{dS_o}dt, \quad \text{for } S_{of} \leq S_o \leq 1 - S_{iw}. \tag{2.65}$$

Then, after first time step, $\Delta t = \Delta t_1$, the oil distribution of oil saturation behind the oil front r_{of} is given by

$$r^2(S_o, \Delta t_1) = r_{of}^2 - \frac{\theta q_t}{\pi \phi h} \Delta t_1 \cdot \frac{df_o(S_o)}{dS_o}, \quad \text{for } S_{of} \leq S_o \leq 1 - S_{iw}; \tag{2.66}$$

and

$$r(S_o, \Delta t_1) = \sqrt{r_{of}^2 - \frac{\theta q_t(t)}{\pi \phi h} \Delta t_1 \cdot \frac{df_o(S_o)}{dS_o}}, \quad \text{for } S_{of} \leq S_o \leq 1 - S_{iw}. \tag{2.67}$$

The distribution of the oil saturation ahead of the oil front, $S_{or} \leq S_o \leq S_{io}$, is the reverse process of water injection before oil "breakthrough" during production and also follows the Buckley-Leverett theory, i.e., the distribution of oil saturations ahead of oil front after the first time step Δt_1, according to Eq. 2.25, is given by

$$\begin{aligned} r^2(S_o, \Delta t_1) &= r_{inj}^2(S_w = 1 - S_o, t = t_{inj} - \Delta t_1) \\ &= r_w^2 + \frac{\theta q_t}{\pi h \phi}\big(t_{inj} - \Delta t_1\big) \frac{df_w(S_w = 1 - S_o)}{dS_w}, \\ &\text{for } S_{or} \leq S_o < S_{io}, \end{aligned} \tag{2.68}$$

where $r_{inj}(S_w, t)$ represents, during injection, the location of water saturation of S_w at time of t and q_t is the positive water injection rate. In Fig. 2.5, we also note that the slope of the line $\overline{AB}$ is higher than derivatives of oil fractional flow to all oil saturations ($S_{or} \leq S_o < S_{io}$) ahead of the oil front saturation S_{io} at fractional flow curve, i.e,

$$\frac{df_o(S_o)}{dS_o} < \frac{f_o(S_{of}) - f_o(S_{io})}{S_{of} - S_{io}}, \quad \text{for } S_{or} \leq S_o < S_{io}. \tag{2.69}$$

That means the speed of initial oil front is higher than the speeds of all oil saturation ahead of it. Then after the first production time step, according to the front tracking method, we have that oil front catches up and merges some saturations ahead of the oil front as shown in Fig. 2.4 by a dashed line at right of new oil front line $\overline{A_1 B}$. Using Eq. 2.68, the saturation just ahead of the oil front, S_{io1}, is determined by calculating the derivative of water fractional flow to water saturation at the location of new oil front r_{of1},

i.e.,

$$\frac{df_w(S_w)}{dS_w} = \left[r_{of1}^2(S_{of1}) - r_w^2\right] \frac{\pi h\phi}{\theta q_t\big(t_{inj} - \Delta t_1\big)} \tag{2.70}$$

first. Then using the numerical interpolation, we can obtain the water saturation S_w just ahead of the new oil front r_{of1} after Δt_1. Thus the oil saturation ahead of r_{of1} is $S_{io1} = 1 - S_w$. Because the first time step Δt_1 is very small in practice, the material lost in first time step is small enough to be ignored. Then, after the first time step Δt_1, the finial distribution of oil saturation is represented by curve $O\widehat{BA_1}S_{or}$.

2^{nd} **time step,** Δt_2: After the first time step, the saturation just ahead and behind the new oil front (shock) r_{of1} are S_{io1} and S_{of}, respectively, as shown in Fig. 2.4. According to Rankine-Hugoniot shock condition Eq. 2.26, assumed a constant value, the speed of the oil front in the second time step Δt_2, represented by the slope of line $\overline{A_1B}$, is given by

$$\frac{dr^2}{dt} = -\frac{\theta q_t}{\pi h\phi} \frac{f_o(S_{of}) - f_o(S_{io1})}{S_{of} - S_{io1}}. \tag{2.71}$$

By Integrating, we have

$$\int_{r_{of1}}^{r_{of2}} dr^2 = -\int_0^{\Delta t_2} \frac{\theta q_t}{\pi h\phi} \frac{f_o(S_{of}) - f_o(S_{io1})}{S_{of} - S_{io1}}, \tag{2.72}$$

where q_t is positive value during production r_{of2} is new oil front location after the second time step Δt_2 and is given by

$$r_{of2} = \sqrt{r_{of1}^2 + \frac{\theta q_t}{\pi h\phi}\Delta t_2 \frac{f_o(S_{of}) - f_o(S_{io1})}{S_{of} - S_{io1}}}. \tag{2.73}$$

During the second time step Δt_2, the distribution of the saturations behind the oil front r_{of1}, $S_{of} \le S_o \le 1 - S_{iw}$, follows Buckley-Leverett theory and is given by

$$\frac{dr^2(S_o)}{dt} = -\frac{\theta q_t}{\pi h\phi} \frac{df_o(S_o)}{dS_o}, \text{ for } S_{of} \le S_o \le 1 - S_{iw}. \tag{2.74}$$

At the second time step, after production time of $\Delta t_1 + \Delta t_2$, rearranging and integrating Eq. 2.74, the distribution of saturations behind the oil front can be expressed as

$$\int_{r_{of}}^{r(S_o)} dr^2 = -\int_0^{\Delta t_1+\Delta t_2} \frac{\theta q_t}{\pi h\phi}\frac{df_o(S_o)}{dS_o}dt, \quad \text{for } S_{of} \le S_o \le 1 - S_{iw}. \tag{2.75}$$

Then we have

$$r(S_o)^2 = r_{of}^2 - \frac{\theta q_t}{\pi h\phi}\Big(\Delta t_1 + \Delta t_2\Big)\frac{df_o(S_o)}{dS_o}dt, \quad \text{for } S_{of} \le S_o \le 1 - S_{iw}, \tag{2.76}$$

and

$$r(S_o) = \sqrt{r_{of}^2 - \frac{\theta q_t}{\pi h\phi}\Big(\Delta t_1 + \Delta t_2\Big)\frac{df_o(S_o)}{dS_o}dt}, \quad \text{for } S_{of} \le S_o \le 1 - S_{iw}, \tag{2.77}$$

In Fig. 2.5, we note that the slope of line $\overline{A_1B}$ representing the oil front speed in second time step Δt_2 is smaller than the slope of $\overline{AB}$, denoting the speed of oil front in the first time step Δt_1. So in the second time step Δt_2, some oil saturations behind the oil front r_{of1} catch up and merge with the second oil front r_{of2} based on front tracking method, see the dashed curve on the left side of point B_1 as shown in Fig. 2.4. We lost some oil during this merge. Similar to the first time step, using Eq. 2.76, the saturation just behind the oil front (S_{of1}) at point B_1 can be obtained by calculating

$$\frac{df_o(S_{of1})}{dS_o}dt = \Big(r_{of}^2 - r_{of1}^2\Big)\frac{\pi h\phi}{\theta q_t\big(\Delta t_1 + \Delta t_2\big)} \tag{2.78}$$

first, then the S_{of1} is obtained next by the numerical interpolation from the table of df_o/dS_o vs. S_o.

As we stated before, our model of saturation evolution during production assumes that saturation ahead of the oil front is a reverse process of water injection before the oil "breakthrough". So according to Eq. 2.25, the distributions of the oil saturations ahead

the oil front r_{of1} ($S_{or} \leq S_o \leq S_{io1}$) after the second time step Δt_2 is given by

$$\begin{aligned} r^2(S_o, \Delta t_1 + \Delta t_2) &= r_{inj}^2(S_w = 1 - S_o, t = t_{inj} - \Delta t_1 - \Delta t_2) \\ &= r_w^2 + \frac{\theta q_t}{\pi h \phi}\big(t_{inj} - \Delta t_1 - \Delta t_2\big)\frac{df_w(S_w = 1 - S_o)}{dS_w}, \\ &\text{for } S_{or} \leq S_o < S_{io1}. \end{aligned} \tag{2.79}$$

From Fig. 2.5, we also can note that derivatives of oil fractional flow to oil saturation, $S_{or} \leq S_o \leq S_{io1}$, is smaller than the slope of line $\overline{A_1 B}$, which represents the speed of oil front r_{of1}. So during the second time step Δt_2, the oil front r_{of1} still moves faster than oil saturations ahead of it. The oil front r_{of1} catches and merges some saturations to the location r_{of2} denoted by Eq. 2.73. We gained some oil saturation during this catching up. That balances we lost from the catching up behind the oil front. As we did before, the oil saturation just ahead of new oil front r_{of2} after the second time step Δt_2 can be calculated by numerical interpolating

$$\frac{df_w(S_w)}{dS_w} = \left[r_{of2}^2(S_{of2}) - r_w^2\right]\frac{\pi h \phi}{\theta q_t\big(t_{inj} - \Delta t_1 - \Delta t_2\big)} \tag{2.80}$$

and obtaining water saturation S_w just ahead the oil front r_{of2}. Thus, the corresponding oil saturation can be achieved $S_{of2} = 1 - S_w$. So after the second time step Δt_2, oil saturation distribution is saturation curve $O\widehat{B_1 A_2 S_{or}}$ as shown in Fig. 2.4.

For the subsequent time steps, There are two types of saturation evolution: one is before the oil "breakthrough", the saturation evolution just repeats the second time step stated above. The oil front moves more slowly. The other is after oil "breakthrough", the saturation evolution only involves some saturations behind the oil front. Then oil saturation is increasing gradually at the sand face wellbore, which is shown in the section of validation. In the practice, the size of time step at early time is much smaller than the size of time step at late time. We use the time table for the reservoir simulator when we calculate the saturation evolution based on our analytical model. The time sequence is a logarithmic series, and typically, first time step size is 1×10^{-4} hours and the size of

time step could be 0.1 hours around the oil "breakthrough" time. The results from cases in following sections show that the sizes of time steps are good enough to obtain good estimates of saturation evolution during production.

2.6.2 Pressure Response during Production

The pressure response during production can be derived using the steady-state theory and, similar to the derivation of the expression for injection and falloff pressure, is also be expressed by combination of pressure response in single phase oil and pressure change in two-phase zone. Then bottomhole pressure change during production is given by

$$\begin{aligned}\Delta p(\Delta t) &\equiv p_i - p_{wf}(\Delta t) \\ &= \Delta\hat{p}_o(\Delta t) + \frac{\alpha}{h\hat{\lambda}_o}\int_{r_w}^{r_{wf}(t_p)} \frac{q_t(r,\Delta t)}{k(r)}\left(\frac{\hat{\lambda}_o}{\lambda_t(r,\Delta t)} - 1\right)\frac{dr}{r}\end{aligned} \tag{2.81}$$

where $q_t(\Delta t)$ is a positive production rate at reservoir conditions; Δt corresponds to the time of production so $\Delta t = 0$ corresponds to the end of the falloff period and $p_{wf}(\Delta t)$ now represents the wellbore pressure during production period; r_{wf} is the water front location at the end time of falloff, t_p. Similar to injection and falloff, $\Delta\hat{p}_o(\Delta t) = p_i - p_o(\Delta t)$, where $p_o(\Delta t)$ is the wellbore pressure during single-phase oil production and is obtained by the superposition of three constant rate solutions, injection at a constant rate, followed by shutin (zero rate), then followed by production at a constant rate. For multirate production introduced in later section, the single-phase oil pressure is also obtained by rate superposition method. In the previous section, we stated that the oil front, r_{of}, separates the water bank into two parts. One is the saturation behind the oil front; the other is the saturation ahead of the oil front. Therefore, Eq. 2.81 can be changed to

$$\begin{aligned}\Delta p(\Delta t) &\equiv p_i - p_{wf}(\Delta t) \\ &= \Delta\hat{p}_o(\Delta t) + \frac{\alpha}{h\hat{\lambda}_o}\int_{r_w}^{r_{of}(\Delta t)} \frac{q_t(r,\Delta t)}{k(r)}\left(\frac{\hat{\lambda}_o}{\lambda_t(r,\Delta t)} - 1\right)\frac{dr}{r} \\ &\quad + \frac{\alpha}{h\hat{\lambda}_o}\int_{r_{of}(\Delta t)}^{r_{wf}(t_p)} \frac{q_t(r,\Delta t)}{k(r)}\left(\frac{\hat{\lambda}_o}{\lambda_t(r,\Delta t)} - 1\right)\frac{dr}{r},\end{aligned} \tag{2.82}$$

where the first integral represents the pressure changes in ahead of the oil front r_{of} and the second integral represents the pressure changes behind the oil front in the two-phase water bank. After oil "breakthrough", the oil front reaches the wellbore and all saturation in the two-phase zone are behind the oil front following Buckley-Leverett theory for oil invading water zone as we stated before.

To evaluate the integrals in Eq. 2.81, the total mobility profile at a given time is computed using the saturation profile and oil front radius $r_{of}(t)$ obtained from the procedure described previously. After oil breakthrough (the oil front reaches the wellbore), $r_{of} = r_w$ and the first integral is equal to zero in Eq. 2.82.

As mentioned earlier, the steady-state assumption is valid throughout the injection period. However, during production, the total flow rate in the two phase region is not constant at very early times. Thus, the use of the steady-state assumption, which allowed us to take q_t outside the integrals in Eq. 2.81, causes a small difference in pressure response between the analytical solution and the numerical simulation at early production time. But this difference disappears shortly after production begins, unless the water bank is very large, and does not affect the later time pressure response. For example, Fig. 2.6 shows a case with 5-hour water injection. The water bank extends to about 15 feet at the end of the injection/falloff periods. After 0.0003 hours of production, the flow rate profile (the dashed curve) within the two-phase zone is not constant. However, the total flow rate is essentially constant in the two-phase zone after 0.1 hours. For a larger water bank, the constant flow rate propagation takes longer to cover the two-phase region. Here, Fig. 2.7 shows the saturation profile and total flow rate distributions of the

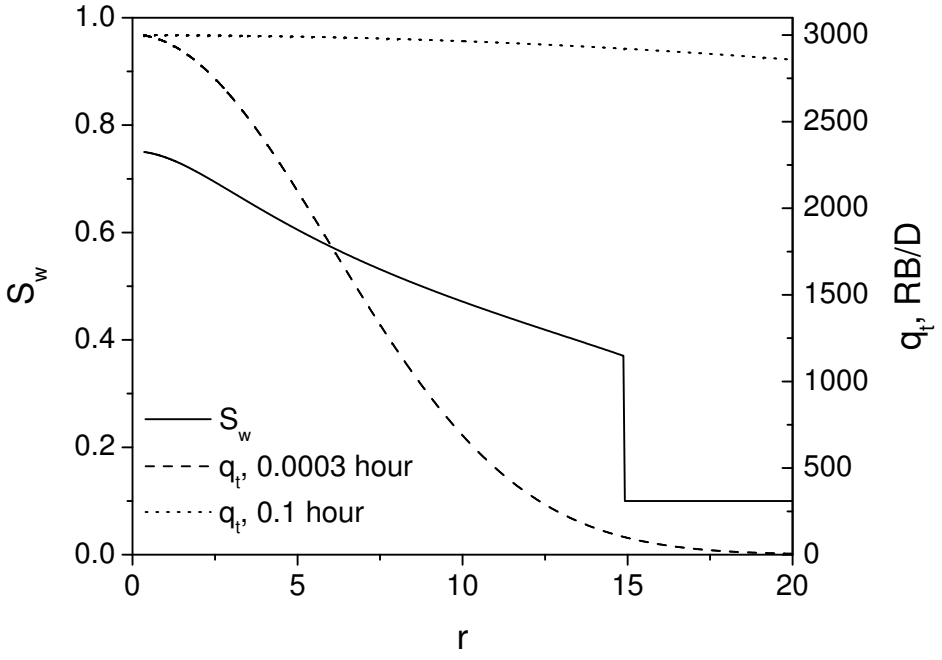

Figure 2.6: Relationship between water saturation and total flow rate profile during production with an initial water bank for case with a 5-hour injection ($\hat{M} = 3.0$).

case with a 48-hour water injection. The radius of two-phase water bank is 43.3 ft after injection, solid curve as shown in Fig. 2.7. In Fig. 2.7, the total flow rates at times of 0.01 hour, 0.4 hour and 1.0 hour are also shown respectively. In the region of the water bank, we note that the total flow rate at 0.4 hours (doted curve) is close to the constant total flow rate of 3000 RB/Day. We also know that the farther from the wellbore, the total mobility change has the less effect on the pressure change in the water phase in the two-phase zone. So for an initial injection test of less than a few days in length, the inaccuracies in the pressure solution for production period are negligible for $\Delta t > 1$ hour.

2.7 Validation of Approximate Analytical Solution of IFPT

In this section, we first considered two cases with different mobility ratios, favorable and unfavorable calculated based on the endpoint saturations by Eq. 1.2, to study the validity of our approximate analytical solution of the IFPT with a constant water injection rate and a same constant production rate during production. Multirate production is also

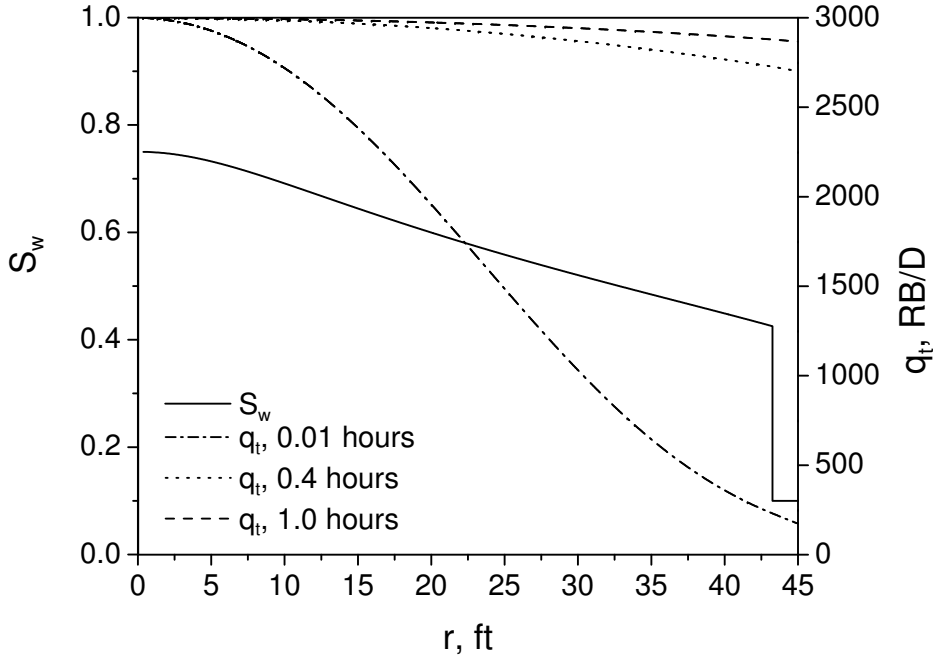

Figure 2.7: Relationship between water saturation and total flow rate profile during production with an initial water bank for case with a 48-hour injection ($\hat{M} = 3.0$).

Property	Value	
q_{inj}	3000	RB/Day
h	60	ft
r_w	0.350	ft
r_e	6800	ft
k	300	md
S_{iw}	0.1	
S_{or}	0.25	
p_i	2500	psi
ϕ	0.22	
B_o	1.003	RB/STB
B_w	1.002	RB/STB
c_o	8.0×10^{-6}	psi^{-1}
c_w	3.02×10^{-6}	psi^{-1}
c_r	5.0×10^{-6}	psi^{-1}

Table 2.1: Reservoir, rock and fluid properties for simulation and analytical solution.

evaluated in this research. For the multirate production, we investigated the multirate effect on our analytical solution. We also studied effects of a large water bank after a long water injection on the our analytical solution of pressure response during production. The

reservoir is infinite-acting throughout the test. Table 2.1 shows the parameters used for simulation as well as for analytical calculations. The true data is generated by running the reservoir simulator. The true relative permeability curves are generated from a power law model. The definition of the power law model of relative permeabilities are defined as

$$k_{rw}(S_w) = a_w \left(\frac{S_w - S_{iw}}{1 - S_{iw} - S_{or}} \right)^{n_w}, \tag{2.83}$$

and

$$k_{ro}(S_w) = a_o \left(\frac{1 - S_w - S_{or}}{1 - S_{iw} - S_{or}}. \right)^{n_o} \tag{2.84}$$

A detailed explanation of power law relative permeability curves is given in Chapter 4. Note we assume that relative permeability is obtained by normalizing effective permeabilities by effective oil permeability at irreducible water saturation, so $k_{ro}(S_{iw}) = 1$.

2.7.1 Unfavorable Mobility Ratio ($\hat{M} = 3.0$)

In this case, the IFPT is a test sequence of 16-hour injection, 16-hour falloff and 24-hour production. We will mainly focus on the comparison between the approximate analytical solution and the numerical simulation result during the production. The relative permeability is based on power law model with $k_{rw}(S_w = 1 - S_{or}) = 0.5$ and $n_w = n_o = 2.0$. The viscosities of oil and water are $\mu_o = 3.0$ cp and $\mu_w = 0.5$ cp, respectively. The endpoint mobility ratio is 3.0. At the end of water injection, $r_{wf}(t_p) = 25.0$ ft based on the Buckley-Leverett calculation.

Fig. 2.8 compares the analytical solution (solid curve) with the simulation result (circular data points) from simulator IMEX. The analytical solution mirrors the numerical result. Because water mobility is higher than oil mobility, the total pressure response during injection is lower than the single phase oil injection pressure (dashed curve). During production, while oil is flowing back to the well, the pressure shows a sharp drop due to a rapid decrease in total mobility. Fig. 2.9 shows a comparison of the water saturation profile

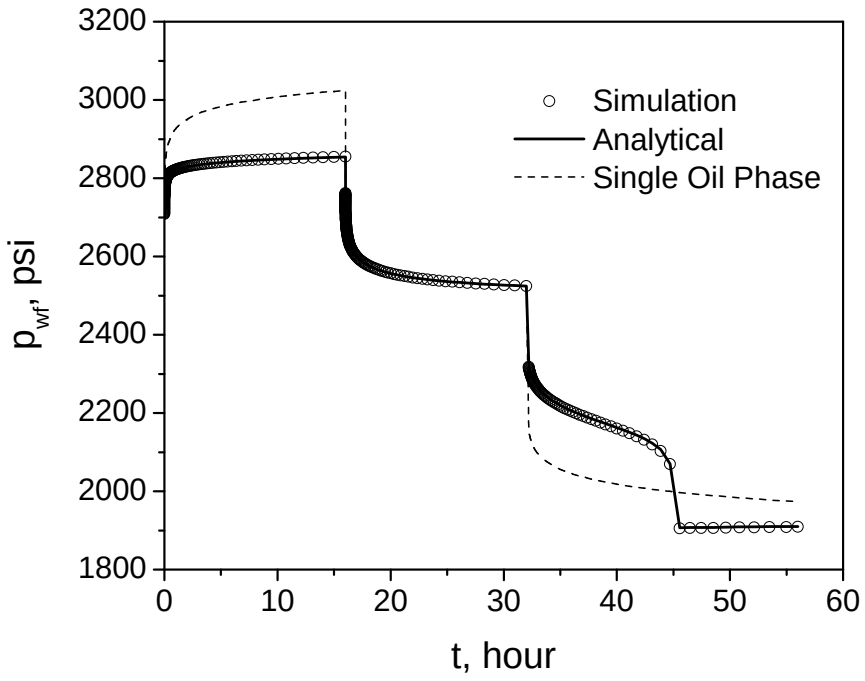

Figure 2.8: Bottomhole pressure, analytical solution versus simulation result for unfavorable mobility ratio ($\hat{M} = 3.0$).

from the analytical and numerical simulations at different times during the production period. In this figure, the solid curves correspond to the analytical solution and the dashed curves correspond to the numerical simulation. The analytical solution and the simulation results are in good agreement. For the unfavorable mobility ratio, production is more like piston displacement because when oil is displacing water, the mobility ratio is favorable.

When we apply the analytical solution as the forward model to estimate relative permeability curves, we only use the pressure data 0.5 hours after the last rate change which is generally enough to avoid the inaccuracies from the steady-state assumption and account for the fact that in practice, early time data will normally be corrupted by wellbore storage effects. The behavior of the wellbore pressure change during production, $\Delta p = p_{wf,f}(t_p) - p_{wf}(t)$, and the absolute value of its derivative with respective to $\ln(\Delta t)$ versus Δt are illustrated in the diagnostic plot, Fig. 2.10. Because of the effect of total mobility change, the derivative in Fig. 2.10 is negative in the time after oil "breakthrough",

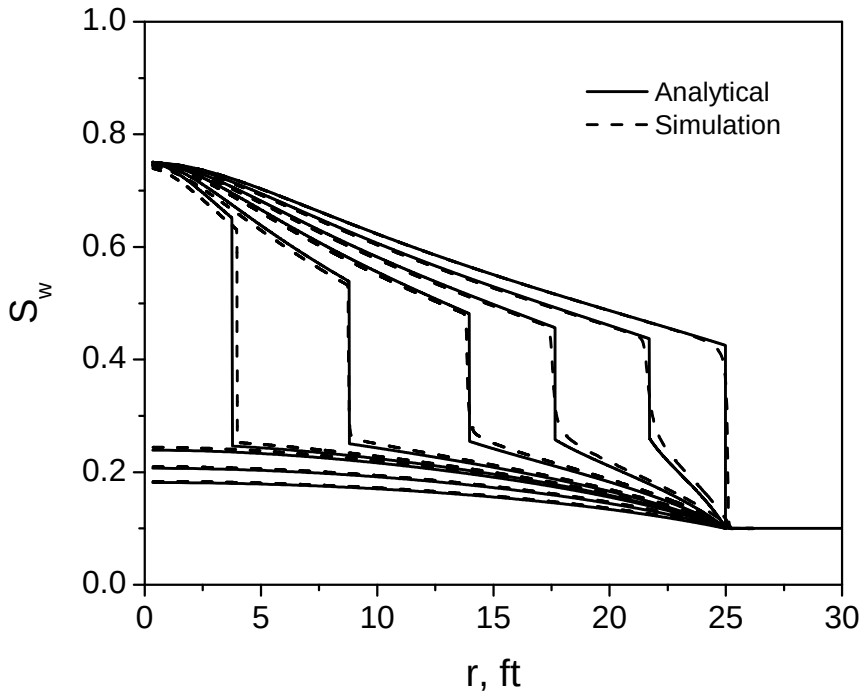

Figure 2.9: Comparison of water saturation profile between analytical model and simulation results for unfavorable mobility ratio ($\hat{M} = 3.0$).

we have used the absolute value of the log-derivative to show that the analytical solution matches the simulation results very well. Fig. 2.11 shows the normal diagnostic plot of the pressure and its log-derivative.

2.7.2 Favorable Mobility Ratio ($\hat{M} = 0.25$)

Next, we consider a favorable mobility ratio case with an endpoint mobility ratio of $\hat{M} = 0.25$. In this case, the IFPT is also a test sequence of 16-hour injection, 16-hour falloff and 24-hour production. The relative permeabilities are based on power law model with $k_{rw}(S_w = 1 - S_{or}) = 0.5$ and $n_w = n_o = 2.0$. Viscosities of oil and water are $\mu_w = 1.0$ cp and $\mu_o = 0.5$ cp, respectively. The test sequence is the same as for the unfavorable case. After 16 hours of water injection, the water front is located at 21.5 ft from the wellbore based on the Buckley-Leverett calculation. Fig. 2.12 shows the water saturation evolution during production and compares results from the analytical solution (solid curves) with results from the simulator solution (the dashed curve). We

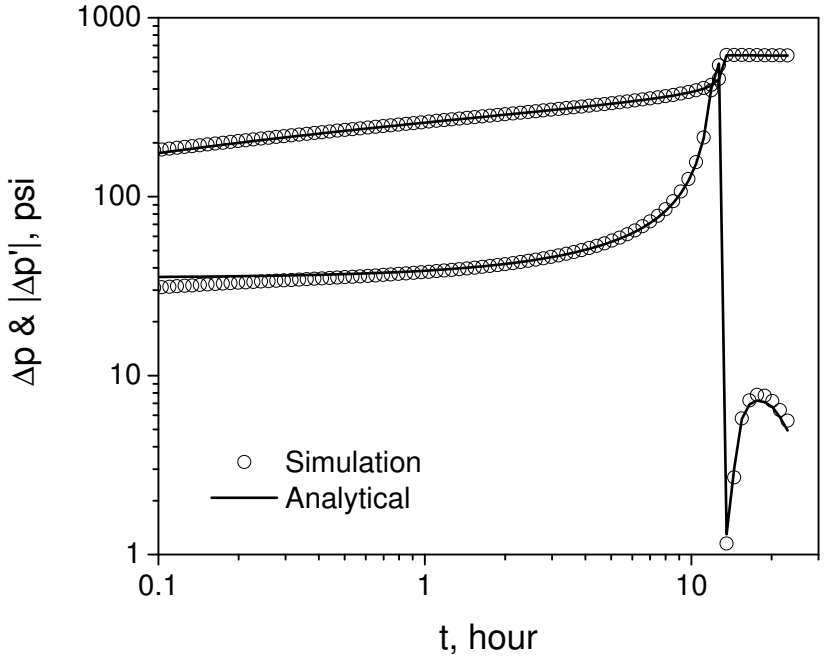

Figure 2.10: Plot of production pressure difference and its absolute derivative for unfavorable mobility ratio ($\hat{M} = 3.0$).

obtain good matches for all times, although at late times, the oil front seems to move very slightly faster for the simulation results. In Fig. 2.13, the bottomhole pressure computed with the approximate analytical solution (solid curve) shows a very good agreement with the numerical simulation result (circles). After oil flows back to the wellbore, $t > 40$ hours in Fig. 2.13, the bottomhole pressure increases because total mobility is increasing. Fig. 2.14 shows the production pressure change and the absolute value of its log-derivative as defined in the previous subsection. In this figure, we also use the absolute derivative value, because the total mobility is increasing, the derivative of the pressure change is negative value while oil is flowing back in the wellbore, $\Delta t > 4.1$ hours. Fig. 2.15 shows the corresponding semi-log plot pressure difference Δp and its log-derivative.

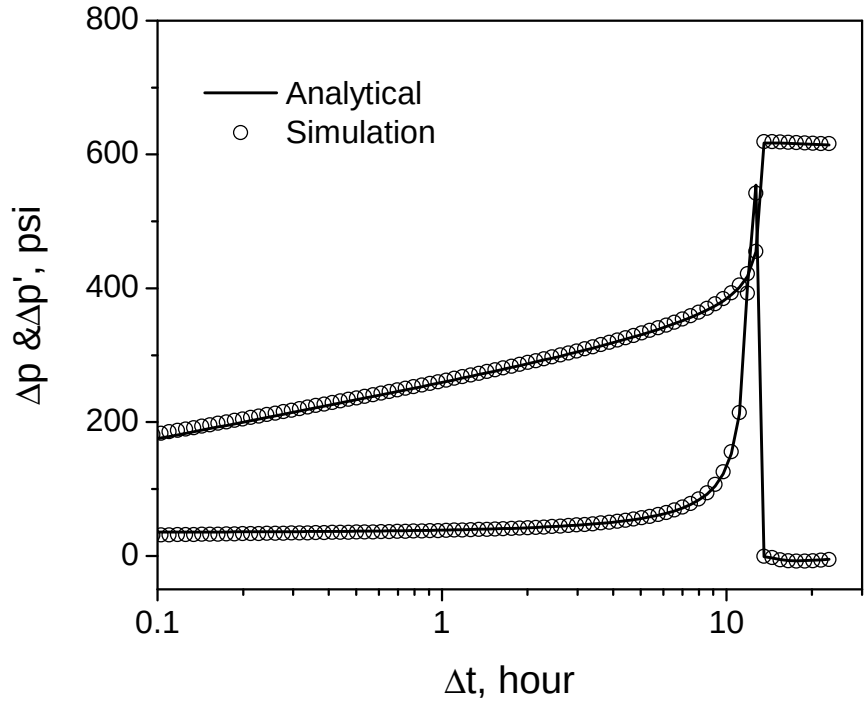

Figure 2.11: Plot of production pressure difference and its derivative for unfavorable mobility ratio ($\hat{M} = 3.0$).

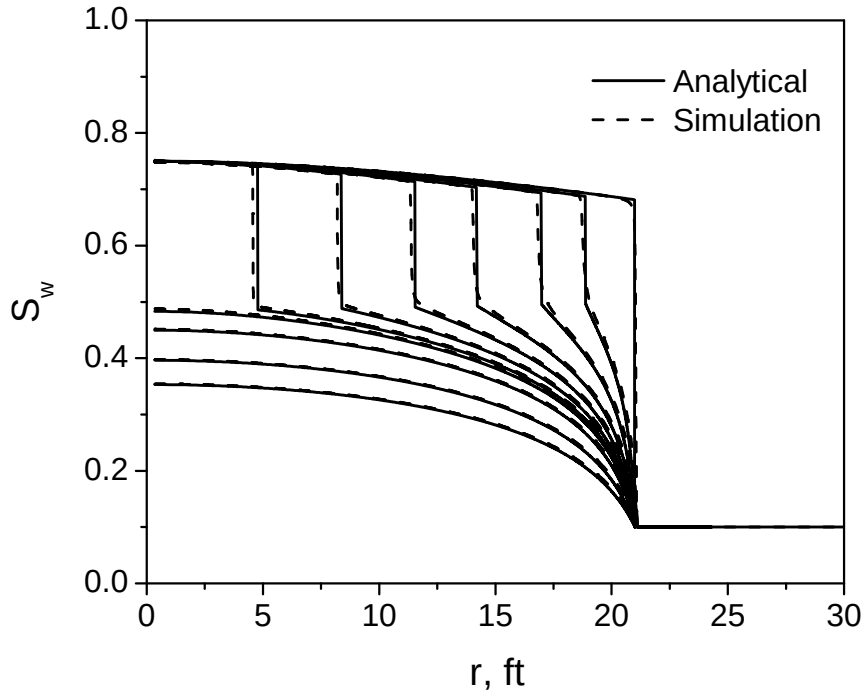

Figure 2.12: Comparison of water saturation profile between analytical model and simulation results for favorable mobility ratio ($\hat{M} = 0.25$).

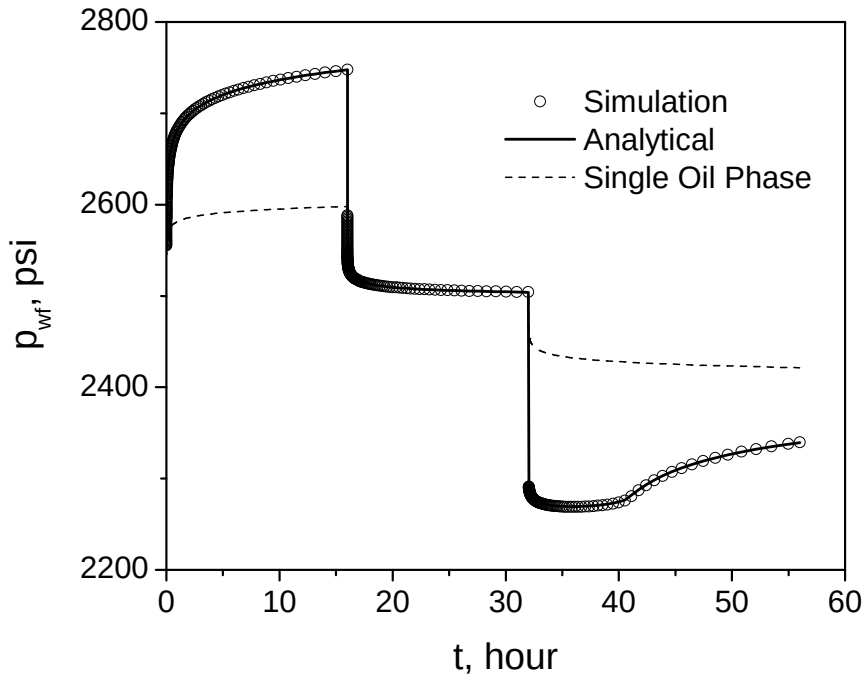

Figure 2.13: Bottomhole pressure, analytical solution versus simulation result for favorable mobility ratio ($\hat{M} = 0.25$).

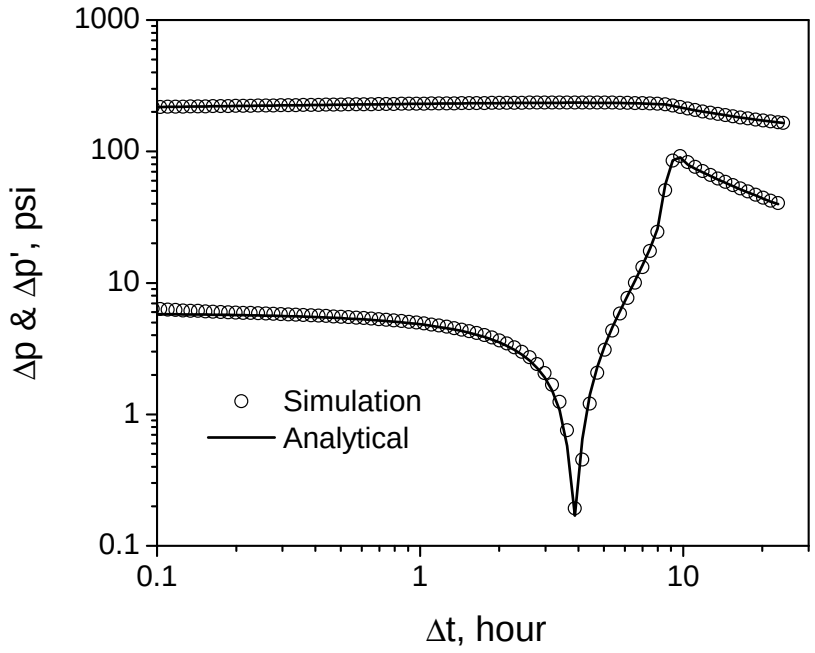

Figure 2.14: Plot of production pressure difference and its absolute derivative for favorable mobility ratio ($\hat{M} = 0.25$).

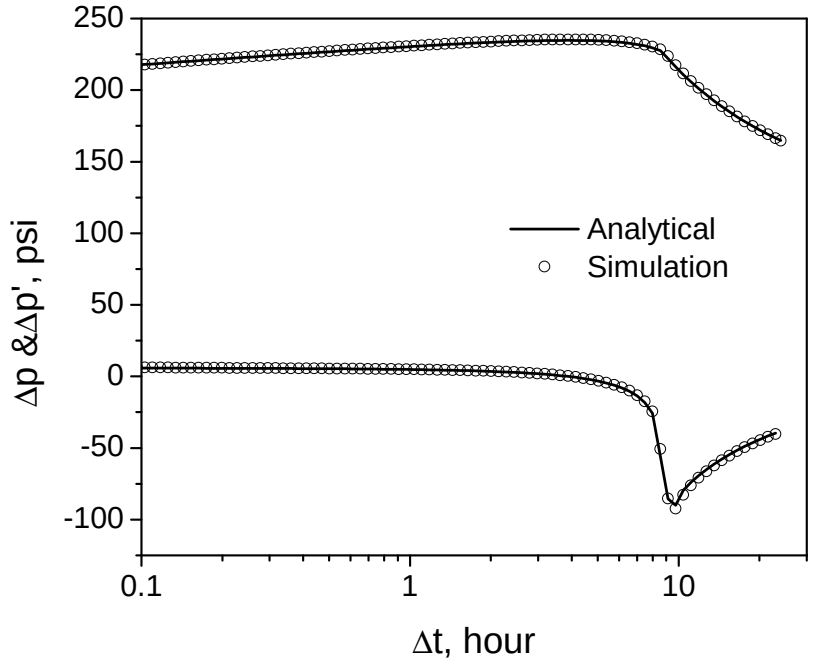

Figure 2.15: Plot of production pressure difference and its derivative for favorable mobility ratio ($\hat{M} = 0.25$).

2.7.3 Multi-rate Production

In practice, it is always difficult to maintain a constant production rate. The following provides some examples with multirate production to show the applicability of our analytical pressure solution. For multirate production, three situations were considered based on the size of the water bank after water injection and frequency of fluctuation of flow rate in this research.

We first present cases with a small water bank after a short period of water injection. We study cases with both unfavorable and favorable mobility ratios. The water banks are obtained after 5 hours of water injection. Fig. 2.16 shows the production rate history of the well. The production rate changes from 3000 RB/Day to 1800 RB/Day in 5 steps and the difference between two sequential rates is 300 RB/Day. Each rate, except the last one, is maintained for a period of 3 hours. Figs. 2.17 and 2.18 show the comparison between the analytical solution and the simulation result of the bottomhole

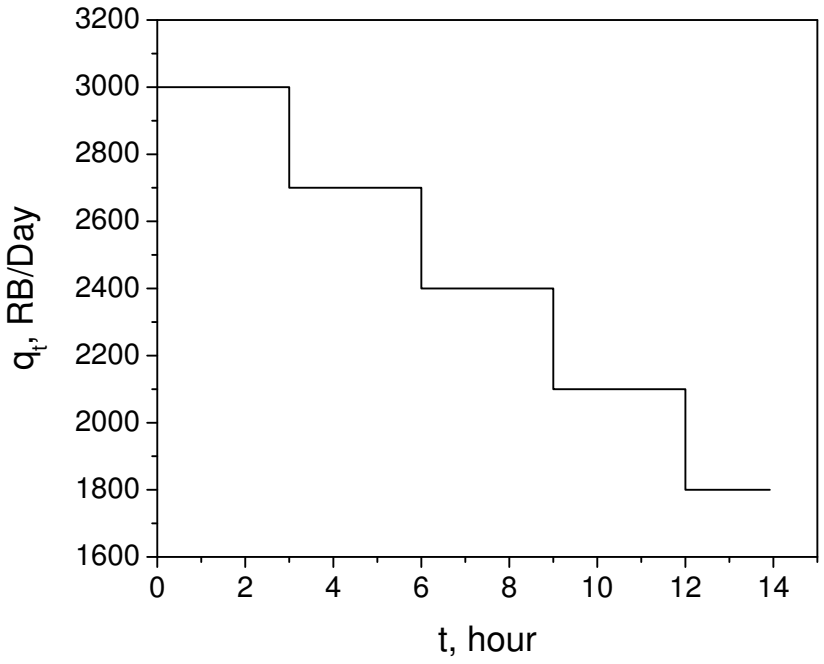

Figure 2.16: Multirate production step function for the case of an initial water bank after 5 hours of water injection.

pressure for unfavorable and favorable mobility ratios, respectively. Very good agreement is obtained in both cases. In both cases, the pressure behavior is complicated by the

production rate changes. When the production rate decreases, the pressure usually increases. However, in this case as the production rate changes from the first rate to the second smaller rate, the pressure shows a sharp drop because oil breaks through. For the unfavorable case, the oil flows back to to the well around 4.2 hours in the second rate region, which is shown as a sharp decrease on the pressure curve in Fig. 2.17.

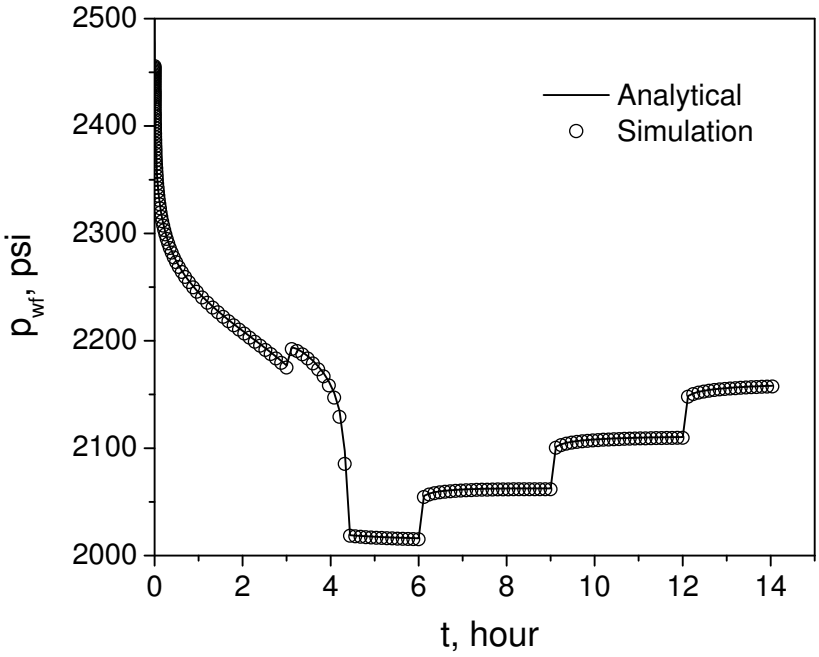

Figure 2.17: Bottomhole pressure of multirate production step function for the case of unfavorable mobility ratio ($\hat{M} = 4.8$).

It is not easy to determine the time of oil breakthrough from the bottomhole pressure for the favorable mobility ratio case as shown in Fig. 2.18, but it occurs within the first 3 hour flow period. The comparison of the analytical and simulation results shows very good agreement in both cases. From an earlier discussion, we know that the analytical solution deviates from the simulation at very early time due to the steady-state assumption. A similar deviation can also occur whenever the production rate changes. Fig. 2.19 shows the total flow rate profile at different production times for the case of an unfavorable mobility ratio case. During the first rate step, from 0 to 3000 RB/Day, it takes about 0.5 hours to reach a constant total flow rate within 14.9 ft to the wellbore (at the end of injection $r_f = 14.9$ ft). However, it takes less time (about 0.1 hours)

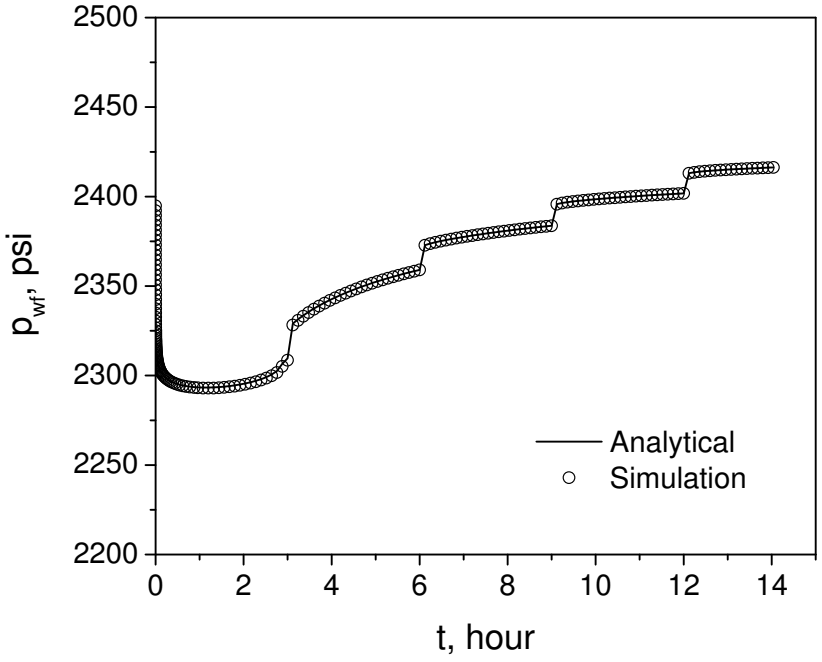

Figure 2.18: Bottomhole pressure of multirate production step function for case of favorable mobility ratio ($\hat{M} = 0.25$).

to form the constant flow rate in that range of the reservoir for subsequent production rate changes. The favorable mobility case shows essentially the same behavior and is not presented here.

A more complicated production rate profile is shown in Fig. 2.20. This case ($\hat{M} = 4.8$) is based on a 5-hour injection with injection rate of 3000 Rb/Day followed by a 5-hour falloff and a 14-hour production. After injection, the radius of water bank is 14.9 ft. During production, the change of rate is randomly generated with the maximum flow rate change between two neighboring times equal to 200 RB/Day. Fig. 2.21 shows the comparison of the analytical solution (solid curve) to the numerical results (dash curve). which is obtained from reservoir simulation based on the parameters in Table 2.1. Surprisingly good agreement between the two curves is obtained and no visual distinction can be made from the figure. This case shows that the analytical solution is quite stable for the multirate case, and that the steady-state assumption is appropriate. The bottomhole pressure looks noisy due to the high frequency change on the production rate. Oil breaks into the well around 5 hours after production as revealed by the sharp pressure decrease.

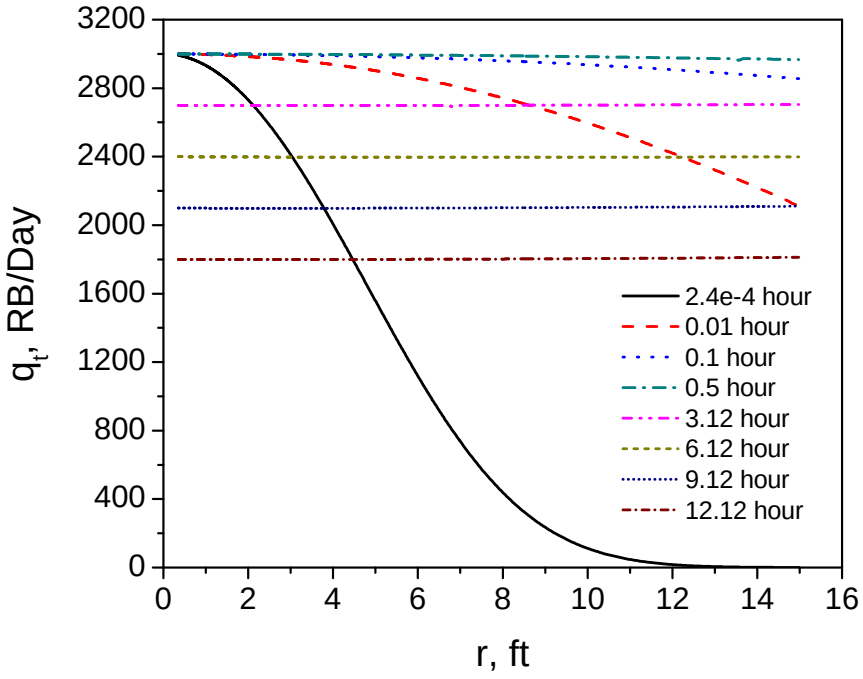

Figure 2.19: Production rate distributions in the two-phase zone at different time ($\hat{M} = 4.8$).

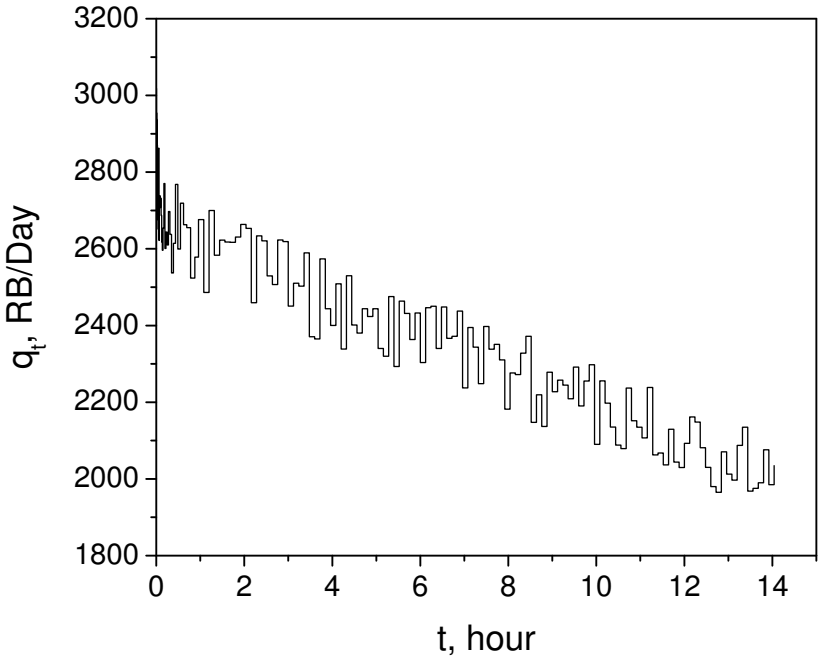

Figure 2.20: A variable flow rate production schedule.

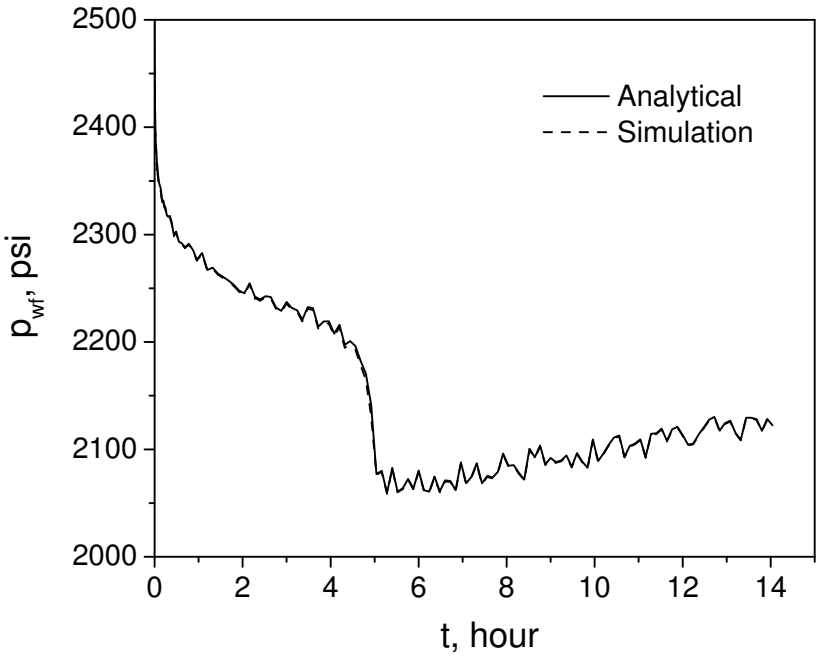

Figure 2.21: Bottomhole pressure under the random production flow rate schedule for the case of unfavorable mobility ratio ($\hat{M} = 4.8$).

The cases shown above indicated that with a small two phase zone, the steady-state assumption is reasonable. This section presents some cases with a much larger water bank (two phase region) formed after a long time of water injection. The main purpose for this case is to test the validity of the steady-state assumption with a large water bank for variable production rate.

Following case is an IFPT with a sequence of 48-hour injection, 24-hour falloff and 72-hour production. Some parameters for reservoir simulation and analytical solution are shown in Table 2.1. We use power law model for the relative permeabilities with $k_{rw}(S_w = 1 - S_{or}) = 0.5$ and $n_w = n_o = 2.0$. The viscosities of oil and water are, respectively, $\mu_w = 0.5$ cp and $\mu_o = 3.0$ cp. The endpoint mobility ratio is $\hat{M} = 3.0$. During production, we use also a multirate production as shown in Fig. 2.22. The multirate production is combined with 36 decreasing production rate steps. The time of each step is two hours. The production rates of the first step and the last one are 2950 RB/Day and 1200 RB/Day respectively. The rate difference between two neighbor uniform time interval steps is 50 RB/Day. At the end of the water injection, the water front location is

$r_{wf}(t_p) = 43.3$ ft based on the Buckely-Leverett theory as shown in Fig. 2.23, a comparison of water saturation evolution between reservoir simulation and our analytical solution during production. In Fig. 2.23, we compared the water saturation snapshots at the end of water injection, before oil "breakthrough" and after oil "breakthrough", respectively. For all saturation snapshot, the solutions of our analytical model (solid curves) and the results of reservoir simulation (dashed curves) have a good agreement. Fig. 2.24 shows the comparison bottomhole pressure between the solution of our analytical model (solid curve) and the result of reservoir simulation (dashed curve). They have a good match with each other again, even for the oscillation of pressure during production because of the multirate production. The oil "breakthrough" time is around 120 hours and makes a sharp drop on pressure response. After oil "breakthrough", the pressure response is essentially dominated by single-phase oil and shows increasing pressure steps because of the decreasing production rate steps.

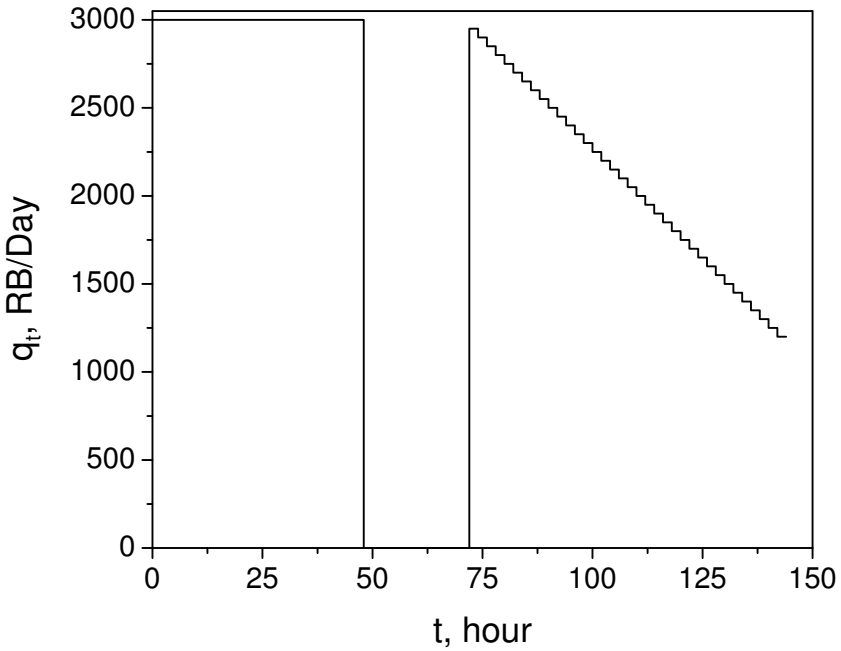

Figure 2.22: Total flow rate for case of 48-hour injection, 24-hour falloff and 72-hour production ($\hat{M} = 3.0$).

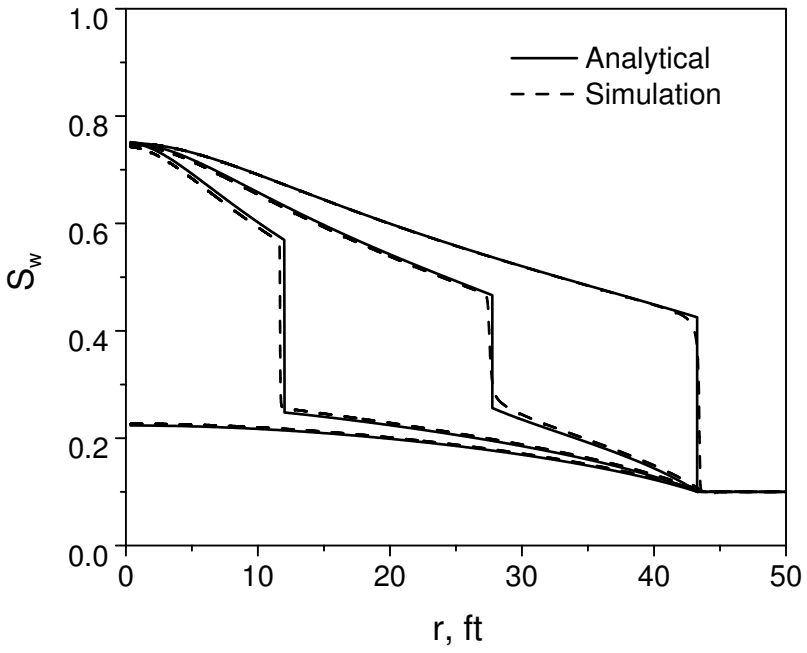

Figure 2.23: Comparison of water saturation evolution during production for case of 48-hour injection, 24-hour falloff and 72-hour production ($\hat{M} = 3.0$).

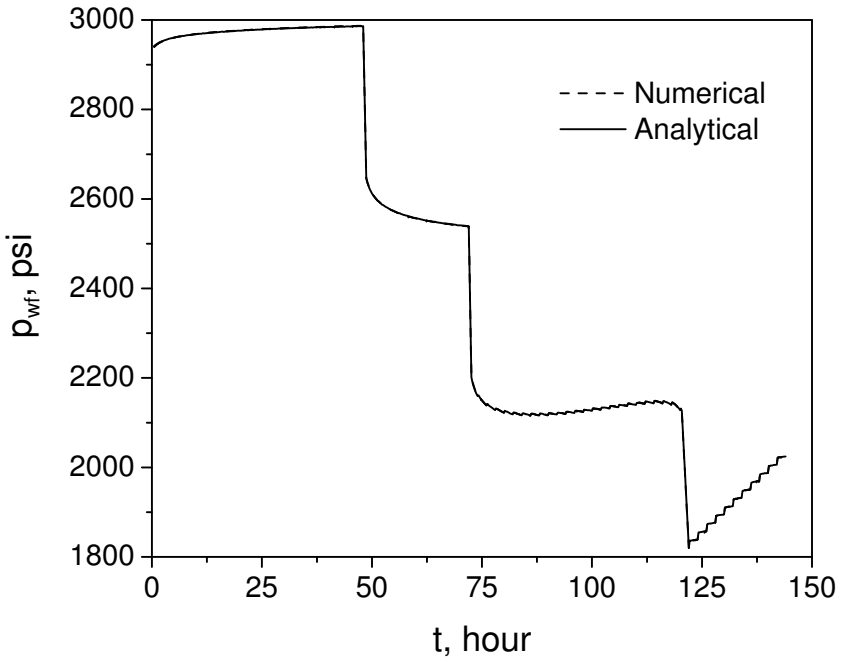

Figure 2.24: Comparison of bottomhole pressure for case of 48-hour injection, 24-hour falloff and 72-hour production ($\hat{M} = 3.0$).

Next case is an IFPT with a sequence of 100-hour injection, 100-hour falloff and 150-hour production. All other parameters of reservoir and fluids are the same as in the cases, previous. The water front is located at 66.7 ft from the wellbore after 100 hours of water injection for the unfavorable mobility ratio ($\hat{M} = 4.8$) case. Fig. 2.25 shows the production rate changes. Each production rate is maintained for 30 hours. Fig. 2.26

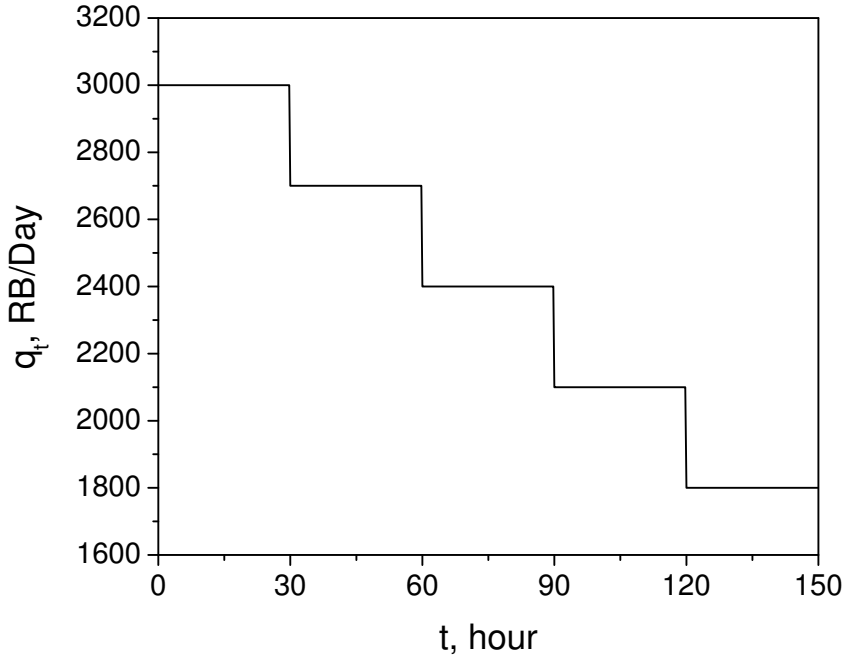

Figure 2.25: Step of production flow rate for case after 100 hours water injection.

shows the comparison of bottomhole pressure between the analytical solution (solid curve) and the simulation result (dashed curve) for both the single phase oil and two-phase pressure response. The analytical solution has a good agreement with the simulation result. Generally, the difference between the bottomhole pressure of the analytical solution and simulation result of two phase is less than 1 psi except during early production time, where the steady state assumption is not valid. However, the data points at oil breakthrough (around 95 hours) show a maximum pressure difference of 15 psi between the analytical solution and simulation result at only one time point. In practice of nonlinear regression, we need to avoid using this type of singular point as the observed data. This is mainly due to fact that at oil breakthrough the pressure decreases sharply (Fig. 2.26)

and a small difference in oil breakthrough time makes a big pressure difference. As in the small water bank cases, the steady-state assumption has limited impact on the analytical solution during production rate change, except at very early time of production when the production rate changes from 0 to 3000 RB/Day. The diagnostic plot in Fig. 2.27 shows that the pressure difference between analytical solution and simulation result is greater than 5 psi before 1 hour and decreases to less than 2 psi around 5 hours. Compared with the previous cases with a short injection time and a smaller water bank, it takes a longer time to overcome the non-constant rate effect for the analytical solution.

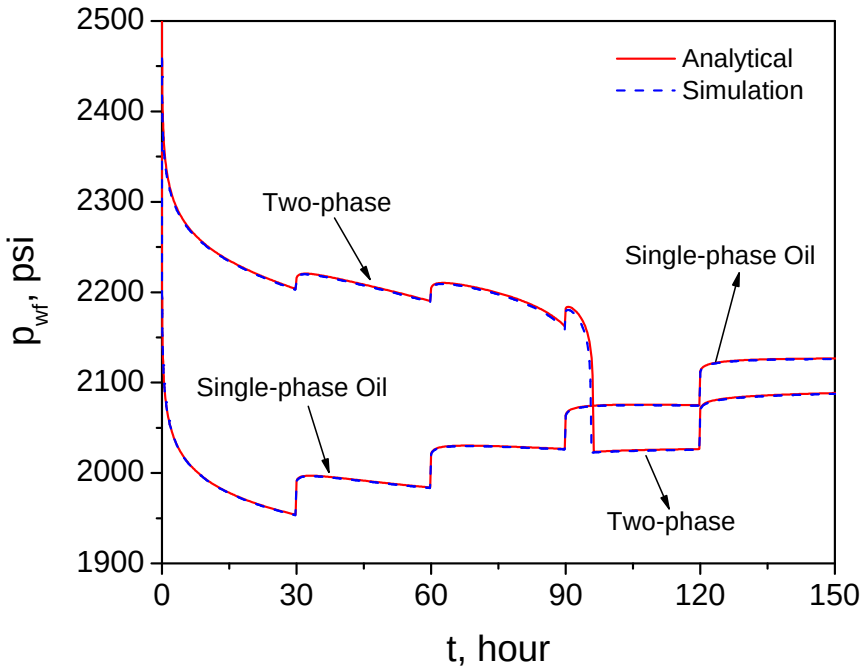

Figure 2.26: Bottomhole pressure under the production flow rate step after 100 hours water injection for case of unfavorable mobility ratio ($\hat{M} = 4.8$).

Figs. 2.28 and 2.29 show the results for a favorable mobility ratio case ($\hat{M} = 0.25$) case. After 100 hours of water injection, the water front location is 55.4 ft away from the wellbore. The pressure match between the analytical solution and simulation is as good as the unfavorable case shown in Fig. 2.26. The semi-log plot of pressure in Fig. 2.29

shows that the non-constant production rate effect disappears around 0.2 hour, which is much shorter than for the unfavorable case because of a slightly smaller water bank and a higher oil mobility.

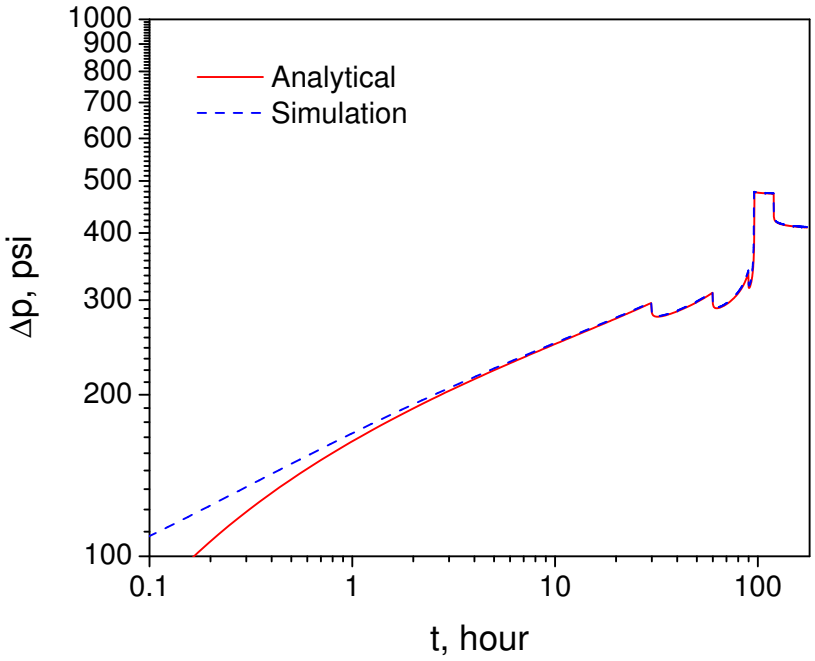

Figure 2.27: Pressure difference under the production flow rate step after 100 hours water injection for case of unfavorable mobility ratio ($\hat{M} = 4.8$).

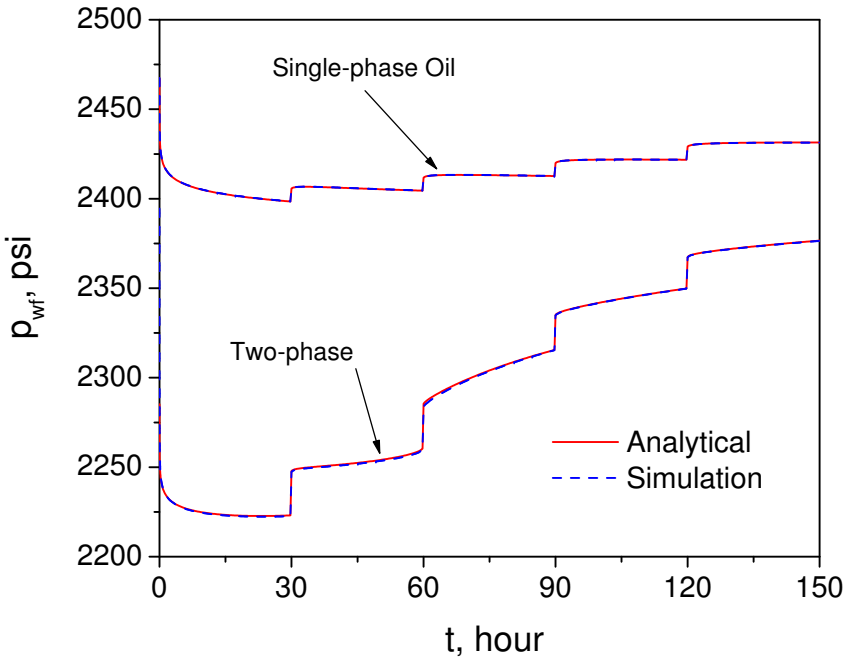

Figure 2.28: Bottomhole pressure under the production flow rate step after 100 hours water injection for case of favorable mobility ratio ($\hat{M} = 0.25$).

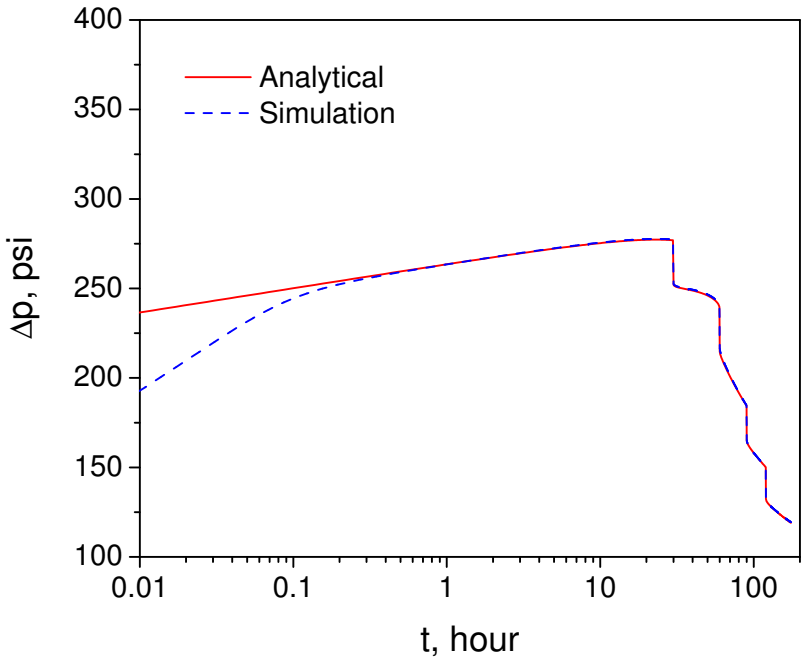

Figure 2.29: Pressure difference under the production flow rate step after 100 hours water injection for case of favorable mobility ratio ($\hat{M} = 0.25$).

CHAPTER 3

PRESSURE RESPONSE OF THE IFPT WITH CAPILLARY PRESSURE

In this chapter, the capillary pressure effect on the Injection/Falloff/Production test is studied. In the previous chapter, the pressure response of two-phase oil-water flow was obtained as a sum of pressure responses in single-phase oil and in a water bank around the wellbore. In this chapter, the nonlinear partial differential equation (PDE) for water saturation evolutions including capillary pressure is solved using a finite difference method. Then the pressure responses of the IFPT with capillary pressure were also obtained using the steady-state theory of Thompson and Reynolds [55]. The numerical results are compared with the results from a reservoir simulator with capillary pressure effect and shown to be in good agreement.

3.1 Saturation Evolutions with the Capillary Pressure Effect

In Chapter 2, Eq. 2.16 gives the nonlinear hyperbolic PDE system based on mass conservation of water with the capillary pressure effect. By substituting Eq. 2.7 into Eq. 2.16 and rearranging, we get

$$\frac{2\pi h\phi}{\theta}\frac{\partial S_w}{\partial t} + \frac{1}{r}q_t\frac{\partial}{\partial r}\Bigg[f_w(S_w) + 1.127\times 10^{-3}\frac{1}{q_t}2\pi hk f_w(S_w)\lambda_o(S_w)r\frac{\partial p_c(S_w)}{\partial r}\Bigg] = 0, \tag{3.1}$$

or equivalently, as

$$\frac{2\pi h\phi}{\theta}\frac{\partial S_w}{\partial t}+\frac{1}{r}q_t\frac{\partial f_w(S_w)}{\partial r} + 1.127\times 10^{-3}\cdot 2\pi hk\frac{1}{r}\frac{\partial}{\partial r}\left[f_w(S_w)\lambda_o(S_w)r\frac{\partial p_c(S_w)}{\partial r}\right]=0, \tag{3.2}$$

For injection, falloff and production, Eq. 3.2 has different initial conditions (IC) and boundary conditions (BC). During injection and production, the total flow rate, q_t, is not equal to zero, and convection dominates the physical behavior at high rates. During falloff, it is assumed that the total flow rate, q_t, is zero in the water bank almost immediately after the shut-in, so diffusion shows the dominant behavior. We were unable to find an analytical solution for this PDE system using perturbation theory. Thus we use a finite difference method to solve this nonlinear PDE.

3.1.1 Saturation Evolution during Water Injection

We assume water is injected into an infinite homogeneous reservoir with an initial uniform distribution equal to irreducible water saturation, S_{iw}. Then the PDE has its initial condition and boundary condition as

$$\begin{cases} \text{I.C.} & S_w(r,t=0)=S_{iw}; \\ \text{B.C.} & S_w(r=r_w,t)=1-S_{or}, \quad t>0; \\ & S_w(r=\infty,t)=S_{iw}, \quad t\geq 0. \end{cases} \tag{3.3}$$

When the finite difference method is used to solve the PDE, we solve the problem in a cylindrical reservoir of radius r_e, where r_e is sufficiently large to ensure that the water front at the end of injection does not reach r_e. In practice, we set r_e equal to 2 times the radius of the water front at the end time of water injection, t_p, i.e.,

$$r_e=2\sqrt{r_w^2+\frac{\theta q_t}{\pi h\phi}t_p\frac{df_w(S_{wf})}{dS_{wf}}}. \tag{3.4}$$

which also should clearly be greater than the maximum distance of the capillarity diffusion

during falloff. Considering mass conservation, we take a uniform block center grid system for the finite difference as shown in Fig. 3.1.

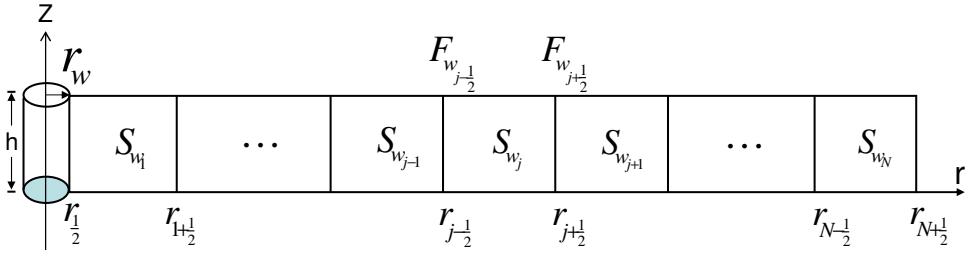

Figure 3.1: Block center grid of water saturation distribution.

There are N blocks in the r-direction. Each grid block represents a water saturation ring, S_{w_j}, $1 \leq j \leq N$, centered at the wellbore. The grid block has a uniform thickness defined by

$$\Delta r = r_{j+\frac{1}{2}} - r_{j-\frac{1}{2}} = \frac{r_e}{N}, \qquad \text{for} \quad 1 \leq j \leq N, \tag{3.5}$$

The initial condition and boundary conditions for the finite difference method can be expressed by

$$\begin{cases} \text{I.C.} \quad S^0_{w_j}, \qquad 1 \leq j \leq N; \\ \text{B.C.} \quad S^n_{w_{\frac{1}{2}}} = 1 - S_{or}, \qquad n = 1, 2, 3, \cdots; \\ \qquad\quad S^n_{w_{N+\frac{1}{2}}} = S_{iw}, \qquad n = 1, 2, 3, \cdots, \end{cases} \tag{3.6}$$

where the superscript n refer to the time step.

In order to obtain the numerical solution of the partial differential equation of mass conservation by a finite difference method, finite difference quotients are used to replace the partial derivatives. Using the implicit backward-difference equation and assuming a total injection rate $q_t > 0$, the mass conservation can be expressed by

$$\frac{\pi h \phi \left(r^2_{j+\frac{1}{2}} - r^2_{j-\frac{1}{2}}\right)}{\theta} \frac{S^{n+1}_{w_j} - S^n_{w_j}}{\Delta t} + q_t \left(F^{n+1}_{w_{j+\frac{1}{2}}} - F^{n+1}_{w_{j-\frac{1}{2}}} \right) = 0, \tag{3.7}$$

where, according to the definition of fractional flow considering the capillary pressure, we have

$$F_{w_{j-\frac{1}{2}}}^{n+1} = f_{w_{j-\frac{1}{2}}}^{n+1} + 1.127 \times 10^{-3} \frac{1}{q_t} 2\pi h k_{j-\frac{1}{2}} r_{j-\frac{1}{2}} f_{w_{j-\frac{1}{2}}}^{n+1} \lambda_{o_{j-\frac{1}{2}}}^{n+1} \left.\frac{\partial p_c}{\partial r}\right|_{j-\frac{1}{2}}^{n+1} \tag{3.8}$$

and

$$F_{w_{j+\frac{1}{2}}}^{n+1} = f_{w_{j+\frac{1}{2}}}^{n+1} + 1.127 \times 10^{-3} \frac{1}{q_t} 2\pi h k_{j+\frac{1}{2}} r_{j+\frac{1}{2}} f_{w_{j+\frac{1}{2}}}^{n+1} \lambda_{o_{j+\frac{1}{2}}}^{n+1} \left.\frac{\partial p_c}{\partial r}\right|_{j+\frac{1}{2}}^{n+1}. \tag{3.9}$$

For the uniform grid, we have

$$\begin{aligned} r_{j+\frac{1}{2}}^2 - r_{j-\frac{1}{2}}^2 &= (r_j + \Delta r)^2 - (r_j - \Delta r)^2 \\ &= (r_j + \Delta r + r_j - \Delta r)(r_j + \Delta r - r_j + \Delta r) \\ &= 2 r_j \Delta r. \end{aligned} \tag{3.10}$$

Substituting Eqs. 3.8, 3.9 and 3.10 into Eq. 3.7 and reorganizing, we have

$$\begin{aligned} &\frac{2\pi h}{\theta\phi} r_j \frac{\Delta r}{\Delta t}\left(S_{w_j}^{n+1} - S_{w_j}^{n}\right) + q_t\left(f_{w_{j+\frac{1}{2}}}^{n+1} - f_{w_{j-\frac{1}{2}}}^{n+1}\right) \\ &\quad + 1.127 \times 10^{-3} 2\pi h \left(k_{j+\frac{1}{2}} r_{j+\frac{1}{2}} f_{w_{j+\frac{1}{2}}}^{n+1} \lambda_{o_{j+\frac{1}{2}}}^{n+1} \left.\frac{\partial p_c}{\partial r}\right|_{j+\frac{1}{2}}^{n+1} \right. \\ &\quad \left. - k_{j-\frac{1}{2}} r_{j-\frac{1}{2}} f_{w_{j-\frac{1}{2}}}^{n+1} \lambda_{o_{j-\frac{1}{2}}}^{n+1} \left.\frac{\partial p_c}{\partial r}\right|_{j-\frac{1}{2}}^{n+1} \right) = 0. \end{aligned} \tag{3.11}$$

Using the backward difference to replace the partial difference of capillary pressure p_c with respect to distance, r, i.e.,

$$\left.\frac{\partial p_c}{\partial r}\right|_{j-\frac{1}{2}}^{n+1} = \frac{p_{c_j}^{n+1} - p_{c_{j-1}}^{n+1}}{r_j - r_{j-1}} = \frac{p_{c_j}^{n+1} - p_{c_{j-1}}^{n+1}}{\Delta r} \tag{3.12}$$

and

$$\left.\frac{\partial p_c}{\partial r}\right|_{j+\frac{1}{2}}^{n+1} = \frac{p_{c_{j+1}}^{n+1} - p_{c_j}^{n+1}}{r_{j+1} - r_j} = \frac{p_{c_{j+1}}^{n+1} - p_{c_j}^{n+1}}{\Delta r}, \tag{3.13}$$

then Eq 3.11 can be written as

$$\frac{2\pi h}{\theta\phi} r_j \frac{\Delta r}{\Delta t}\left(S_{w_j}^{n+1} - S_{w_j}^{n}\right) + q_t\left(f_{w_{j+\frac{1}{2}}}^{n+1} - f_{w_{j-\frac{1}{2}}}^{n+1}\right) + 1.127 \times 10^{-3} 2\pi h\left(k_{j+\frac{1}{2}} r_{j+\frac{1}{2}} f_{w_{j+\frac{1}{2}}}^{n+1} \lambda_{o_{j+\frac{1}{2}}}^{n+1} \frac{p_{c_{j+1}}^{n+1} - p_{c_j}^{n+1}}{\Delta r} - k_{j-\frac{1}{2}} r_{j-\frac{1}{2}} f_{w_{j-\frac{1}{2}}}^{n+1} \lambda_{o_{j-\frac{1}{2}}}^{n+1} \frac{p_{c_j}^{n+1} - p_{c_{j-1}}^{n+1}}{\Delta r}\right) = 0. \tag{3.14}$$

In virtually all cases, we consider homogeneous permeability and porosity fields. If permeability values from gridblock to gridblock, we use the standard and harmonic average to evaluate $k_{j+\frac{1}{2}}$ $0 \le j \le N$ with $k_{\frac{1}{2}} = k_1$ and $k_{N+\frac{1}{2}} = k_N$. We use upstream weighting [44] to evaluate the values at the grid block boundaries, so, for water injection, we have

$$\begin{aligned} f_{w_{j+\frac{1}{2}}} &= f_{w_j}; \\ \lambda_{o_{j+\frac{1}{2}}} &= \lambda_{o_j}; \\ f_{w_{j-\frac{1}{2}}} &= f_{w_{j-1}}; \\ \lambda_{o_{j-\frac{1}{2}}} &= \lambda_{o_{j-1}}. \end{aligned} \tag{3.15}$$

Thus, setting $k_{j+\frac{1}{2}} = k_{j-\frac{1}{2}} = k$, and using upstream weighting, Eq. 3.14 can be replaced by

$$\begin{aligned} &\frac{2\pi h}{\theta\phi} r_j \frac{\Delta r}{\Delta t}\left(S_{w_j}^{n+1} - S_{w_j}^{n}\right) + q_t\left(f_{w_j}^{n+1} - f_{w_{j-1}}^{n+1}\right) \\ &\quad + 1.127 \times 10^{-3} 2\pi h\left(r_{j+\frac{1}{2}} k f_{w_j}^{n+1} \lambda_{o_j}^{n+1} \frac{p_{c_{j+1}}^{n+1} - p_{c_j}^{n+1}}{\Delta r} - r_{j-\frac{1}{2}} k f_{w_{j-1}}^{n+1} \lambda_{o_{j-1}}^{n+1} \frac{p_{c_j}^{n+1} - p_{c_{j-1}}^{n+1}}{\Delta r}\right) = 0, \\ &\quad 1 \le j \le N. \end{aligned} \tag{3.16}$$

For spacial values at boundaries $j = 0$ and $j = N + 1$, we have values of

$$\left.\frac{\partial p_c}{\partial r}\right|_{N+\frac{1}{2}}^{n+1} = \frac{p_{c_1}^{n+1} - p_{c_{\frac{1}{2}}}^{n+1}}{r_1 - r_{\frac{1}{2}}} = \frac{p_c^{n+1}(S_{w_1}) - p_c^{n+1}(1 - S_{or})}{\frac{1}{2}\Delta r} \tag{3.17}$$

and

$$\left.\frac{\partial p_c}{\partial r}\right|_{N+\frac{1}{2}}^{n+1} = \frac{p_{c_{N+\frac{1}{2}}}^{n+1} - p_{c_N}^{n+1}}{r_{N+\frac{1}{2}} - r_N} = \frac{p_c^{n+1}(S_{iw}) - p_c^{n+1}(S_{w_N})}{\frac{1}{2}\Delta r} \tag{3.18}$$

Because $f_w(S_w)$, $\lambda_o(S_w)$ and $p_c(S_w)$ are functions of water saturation, the preceding system equations represent N nonlinear equations in the N unknowns, $S_{w_j}^{n+1}$, $1 \le j \le N$. For a new time step, $n+1$, denote the nonlinear finite difference equation centered at grid block j as g_j^{n+1}:

$$g_j^{n+1}\left(S_{w_1}^{n+1}, S_{w_2}^{n+1}, \cdots, S_{w_N}^{n+1}\right) = 0. \tag{3.19}$$

The solution of this system is denoted by a vector:

$$S_w^{n+1} = \left(S_{w_1}^{n+1}, S_{w_2}^{n+1}, \cdots, S_{w_N}^{n+1}\right)^T. \tag{3.20}$$

The Newton-Raphson method is used to system equations g_i. Let $S_w^{n+1,k}$ be the most recent iteration's estimate of S_w^{n+1}, and $S_w^{n+1,k+1}$ be the next iteration's estimate. Let $\delta S_w^{n+1,k+1} = S_w^{n+1,k+1} - S_w^{n+1,k}$. Then by a Taylor's series expansion, we have

$$\begin{aligned} g_j^{n+1,k+1} \equiv g_j^{n+1}(S_w^{n+1,k+1}) = g_j^{n+1}(S_w^{n+1,k}) + \left[\nabla(g_j^{n+1,k})\right]^T \delta S_w^{n+1,k+1} \\ + \mathcal{O}(\delta S_w^{n+1,k+1^T} \delta S_w^{n+1,k+1}) = 0, \end{aligned} \tag{3.21}$$

Keeping only the first-order term, we have

$$g_j^{n+1}(S_w^{n+1,k}) + \left[\nabla(g_j^{n+1,k})\right]^T \delta S_w^{n+1,k+1} \cong 0, \tag{3.22}$$

where

$$g_j^{n+1,k} \equiv g_j\left(S_{w_j}^{n+1,k}\right). \tag{3.23}$$

Eq. 3.22 is for a single equation g_j^{n+1}. Assembling all the equations gives

$$\begin{pmatrix} \frac{\partial g_1^{n+1,k}}{\partial S_{w_1}^{n+1,k}} & \frac{\partial g_1^{n+1,k}}{\partial S_{w_2}^{n+1,k}} & \cdots & \frac{\partial g_1^{n+1,k}}{\partial S_{w_N}^{n+1,k}} \\ \frac{\partial g_2^{n+1,k}}{\partial S_{w_1}^{n+1,k}} & \frac{\partial g_2^{n+1,k}}{\partial S_{w_2}^{n+1,k}} & \cdots & \frac{\partial g_2^{n+1,k}}{\partial S_{w_N}^{n+1,k}} \\ \vdots & \vdots & \ddots & \vdots \\ \frac{\partial g_N^{n+1,k}}{\partial S_{w_1}^{n+1,k}} & \frac{\partial g_N^{n+1,k}}{\partial S_{w_2}^{n+1,k}} & \cdots & \frac{\partial g_N^{n+1,k}}{\partial S_{w_N}^{n+1,k}} \end{pmatrix} \begin{pmatrix} \delta S_{w_1}^{n+1,k+1} \\ \delta S_{w_2}^{n+1,k+1} \\ \vdots \\ \delta S_{w_N}^{n+1,k+1} \end{pmatrix} = - \begin{pmatrix} g_1^{n+1,k} \\ g_2^{n+1,k} \\ \vdots \\ g_N^{n+1,k} \end{pmatrix}. \tag{3.24}$$

The coefficient matrix is the Jacobian, $\left(\frac{\partial g_i}{\partial S_{w_j}^{n+1,k}}\right)$. When the linear equations, Eq. 3.24, is solved, the update, $\left(\delta S_{w_j}^{n+1,k+1}\right)_{N\times 1}$, is obtained for iteration k. the updated saturations at t_{n+1} are given by

$$S_{w_j}^{n+1,k+1} = S_{w_j}^{n+1,k} + \delta S_{w_j}^{n+1,k+1}, \text{ for } 1 \le j \le N. \tag{3.25}$$

When an update satisfies the convergence criteria,

$$\max \left\| \delta S_w^{n+1,k+1} \right\|_\infty \le \epsilon, \tag{3.26}$$

the iteration stops, where $\epsilon = 0.001$ in this work. Then the calculation of S_{w_j} goes to the next time step. The initial guess for next time step Newton-Raphson is the solution for saturation at the previous time step.

For the problem of water saturation evolution during water injection, Eq. 3.16, the finite difference equation can be written as

$$\begin{aligned} g_1^{n+1} = q_t \left(f_{w_1}^{n+1} - f_{w_{\frac{1}{2}}}^{n+1} \right) \\ + 1.127 \times 10^{-3} 2\pi h \Bigg(r_{1+\frac{1}{2}} k f_{w_1}^{n+1} \lambda_{o_1}^{n+1} \frac{p_{c_2}^{n+1} - p_{c_1}^{n+1}}{\Delta r} \\ - r_{\frac{1}{2}} k f_{w_{\frac{1}{2}}}^{n+1} \lambda_{o_{\frac{1}{2}}}^{n+1} \frac{p_{c_1}^{n+1} - p_{c_{\frac{1}{2}}}^{n+1}}{\frac{1}{2}\Delta r} \Bigg) \\ + \frac{2\pi h}{\theta \phi} r_1 \frac{\Delta r}{\Delta t} \left(S_{w_1}^{n+1} - S_{w_1}^{n} \right) = 0 \end{aligned} \tag{3.27}$$

$$
\begin{aligned}
g_j^{n+1} = q_t\Big(f_{w_j}^{n+1} - f_{w_{j-1}}^{n+1}\Big) \\
+ 1.127\times 10^{-3} 2\pi h\Big(r_{j+\frac{1}{2}} k f_{w_j}^{n+1}\lambda_{o_j}^{n+1}\frac{p_{c_{j+1}}^{n+1} - p_{c_j}^{n+1}}{\Delta r} \\
- r_{j-\frac{1}{2}} k f_{w_{j-1}}^{n+1}\lambda_{o_{j-1}}^{n+1}\frac{p_{c_j}^{n+1} - p_{c_{j-1}}^{n+1}}{\Delta r}\Big) \\
+ \frac{2\pi h}{\theta\phi} r_j \frac{\Delta r}{\Delta t}\big(S_{w_j}^{n+1} - S_{w_j}^{n}\big) = 0, \\
\text{for} \quad 2 \le j \le N-1;
\end{aligned}
\tag{3.28}
$$

and

$$
\begin{aligned}
g_N^{n+1} = q_t\Big(f_{w_N}^{n+1} - f_{w_{N-1}}^{n+1}\Big) \\
+ 1.127\times 10^{-3} 2\pi h\Big(r_{N+\frac{1}{2}} k f_{w_N}^{n+1}\lambda_{o_N}^{n+1}\frac{p_{c_{N+\frac{1}{2}}}^{n+1} - p_{c_N}^{n+1}}{\frac{1}{2}\Delta r} \\
- r_{N-\frac{1}{2}} k f_{w_{N-1}}^{n+1}\lambda_{o_{N-1}}^{n+1}\frac{p_{c_N}^{n+1} - p_{c_{N-1}}^{n+1}}{\Delta r}\Big) \\
+ \frac{2\pi h}{\theta\phi} r_N \frac{\Delta r}{\Delta t}\big(S_{w_N}^{n+1} - S_{w_N}^{n}\big) = 0.
\end{aligned}
\tag{3.29}
$$

In Eq. 3.28, for $2 \le j \le N-1$, note that one finite difference equation, g_j^{n+1}, only involves three water saturations, $S_{w_{j-1}}^{n+1}$, $S_{w_j}^{n+1}$ and $S_{w_{j+1}}^{n+1}$. Thus we have

$$
\frac{\partial g_j^{n+1}}{\partial S_{w_l}^{n+1}} = 0, \quad \text{for} \quad l \neq, j-1, j \text{ and } j+1 \tag{3.30}
$$

and

$$
\begin{aligned}
\frac{\partial g_j^{n+1}}{\partial S_{w_{j-1}}^{n+1}} = -q_t f_{w_{j-1}}^{'n+1} + 1.127\times 10^{-3} 2\pi h r_{j-\frac{1}{2}} k\Big(- f_{w_{j-1}}^{'n+1}\lambda_{o_{j-1}}^{n+1}\frac{p_{c_j}^{n+1} - p_{c_{j-1}}^{n+1}}{\Delta r} \\
- f_{w_{j-1}}^{n+1}\lambda_{o_{j-1}}^{'n+1}\frac{p_{c_j}^{n+1} - p_{c_{j-1}}^{n+1}}{\Delta r} + f_{w_{j-1}}^{n+1}\lambda_{o_{j-1}}^{n+1}\frac{p_{c_{j-1}}^{'n+1}}{\Delta r}\Big),
\end{aligned}
\tag{3.31}
$$

$$\frac{\partial g_j^{n+1}}{\partial S_{w_j}^{n+1}} = q_t f_{w_j}^{'n+1} + 1.127\times10^{-3}2\pi h\Bigg[r_{j+\frac{1}{2}}k\Bigg(f_{w_j}^{'n+1}\lambda_{o_j}^{n+1}\frac{p_{c_{j+1}}^{n+1}-p_{c_j}^{n+1}}{\Delta r} + f_{w_j}^{n+1}\lambda_{o_j}^{'n+1}\frac{p_{c_{j+1}}^{n+1}-p_{c_j}^{n+1}}{\Delta r} - f_{w_j}^{n+1}\lambda_{o_j}^{n+1}\frac{p_{c_j}^{'n+1}}{\Delta r}\Bigg) - r_{j-\frac{1}{2}}kf_{w_{j-1}}^{n+1}\lambda_{o_{j-1}}^{n+1}\frac{p_{c_j}^{'n+1}}{\Delta r}\Bigg] + \frac{2\pi h}{\theta\phi}r_j\frac{\Delta r}{\Delta t} \tag{3.32}$$

and

$$\frac{\partial g_j^{n+1}}{\partial S_{w_{j+1}}^{n+1}} = 1.127\times10^{-3}2\pi h r_{j+\frac{1}{2}}kf_{w_j}^{n+1}\lambda_{o_j}^{n+1}\frac{p_{c_{j+1}}^{'n+1}}{\Delta r}, \tag{3.33}$$

where

$$\begin{aligned} f_{w_j}^{'} &= \frac{df_w(S_{w_j})}{dS_w}, \\ \lambda_{o_j}^{'} &= \frac{d\lambda_o(S_{w_j})}{dS_w}, \\ p_{c_j}^{'} &= \frac{dp_c(S_{w_j})}{dS_w}. \end{aligned} \tag{3.34}$$

According to Eq. 3.27, for $j = 1$, we have

$$\frac{\partial g_1^{n+1}}{\partial S_{w_{\frac{1}{2}}}^{n+1}} = -q_t f_{w_{\frac{1}{2}}}^{'n+1} + 1.127\times10^{-3}2\pi h r_{\frac{1}{2}}k\Bigg(-f_{w_{\frac{1}{2}}}^{'n+1}\lambda_{o_{\frac{1}{2}}}^{n+1}\frac{p_{c_1}^{n+1}-p_{c_{\frac{1}{2}}}^{n+1}}{\frac{1}{2}\Delta r} - f_{w_{\frac{1}{2}}}^{n+1}\lambda_{o_{\frac{1}{2}}}^{'n+1}\frac{p_{c_1}^{n+1}-p_{c_{\frac{1}{2}}}^{n+1}}{\frac{1}{2}\Delta r} + f_{w_{\frac{1}{2}}}^{n+1}\lambda_{o_{\frac{1}{2}}}^{n+1}\frac{p_{c_{\frac{1}{2}}}^{'n+1}}{\frac{1}{2}\Delta r}\Bigg) \tag{3.35}$$

$$\frac{\partial g_1^{n+1}}{\partial S_{w_1}^{n+1}} = q_t f_{w_1}^{'n+1} + 1.127\times10^{-3}2\pi h\Bigg[r_{1+\frac{1}{2}}k\Bigg(f_{w_1}^{'n+1}\lambda_{o_1}^{n+1}\frac{p_{c_2}^{n+1}-p_{c_1^{n+1}}}{\Delta r} + f_{w_1}^{n+1}\lambda_{o_1}^{'n+1}\frac{p_{c_2}^{n+1}-p_{c_1}^{n+1}}{\Delta r} - f_{w_1}^{n+1}\lambda_{o_1}^{n+1}\frac{p_{c_1}^{'n+1}}{\Delta r}\Bigg) - r_{\frac{1}{2}}kf_{w_{\frac{1}{2}}}^{n+1}\lambda_{o_{\frac{1}{2}}}^{n+1}\frac{p_{c_1}^{'n+1}}{\frac{1}{2}\Delta r}\Bigg] + \frac{2\pi h}{\theta\phi}r_1\frac{\Delta r}{\Delta t} \tag{3.36}$$

and

$$\frac{\partial g_1^{n+1}}{\partial S_{w_2}} = 1.127 \times 10^{-3} 2\pi h r_{1+\frac{1}{2}} k f_{w_1}^{n+1} \lambda_{o_1}^{n+1} \frac{p_{c_2}^{'n+1}}{\frac{1}{2}\Delta r}, \tag{3.37}$$

where

$$\begin{aligned} f_{w_{\frac{1}{2}}}^{'} &= \frac{df_w(S_{w_{\frac{1}{2}}})}{dS_w}, \\ \lambda_{o_{\frac{1}{2}}}^{'} &= \frac{d\lambda_o(S_{w_{\frac{1}{2}}})}{dS_w}, \\ p_{c_{\frac{1}{2}}}^{'} &= \frac{dp_c(S_{w_{\frac{1}{2}}})}{dS_w}. \end{aligned} \tag{3.38}$$

From Eq. 3.29, for $j = N$, we have

$$\begin{aligned} \frac{\partial g_1^{n+1}}{\partial S_{w_{N-1}}^{n+1}} = -q_t f_{w_{N-1}}^{'n+1} + 1.127 \times 10^{-3} 2\pi h r_{N-\frac{1}{2}} k \Bigg(& - f_{w_{N-1}}^{'n+1} \lambda_{o_{N-1}}^{n+1} \frac{p_{c_N}^{n+1} - p_{c_{N-1}}^{n+1}}{\Delta r} \\ & - f_{w_{N-1}}^{n+1} \lambda_{o_{N-1}}^{'n+1} \frac{p_{c_N}^{n+1} - p_{c_{N-1}}^{n+1}}{\Delta r} + f_{w_{N-1}}^{n+1} \lambda_{o_{N-1}}^{n+1} \frac{p_{c_{N-1}}^{'n+1}}{\Delta r} \Bigg) \end{aligned} \tag{3.39}$$

$$\begin{aligned} \frac{\partial g_1^{n+1}}{\partial S_{w_N}^{n+1}} = q_t f_{w_N}^{'n+1} + 1.127 \times 10^{-3} 2\pi h \Bigg[r_{N+\frac{1}{2}} k \Bigg(& f_{w_N}^{'n+1} \lambda_{o_N}^{n+1} \frac{p_{c_{N+\frac{1}{2}}}^{n+1} - p_{c_N^{n+1}}}{\frac{1}{2}\Delta r} \\ & + f_{w_N}^{n+1} \lambda_{o_N}^{'n+1} \frac{p_{c_{N+\frac{1}{2}}}^{n+1} - p_{c_N}^{n+1}}{\frac{1}{2}\Delta r} - f_{w_N}^{n+1} \lambda_{o_N}^{n+1} \frac{p_{c_N}^{'n+1}}{\frac{1}{2}\Delta r} \Bigg) \\ & - r_{N-\frac{1}{2}} k f_{w_{N-\frac{1}{2}}}^{n+1} \lambda_{o_{N-\frac{1}{2}}}^{n+1} \frac{p_{c_N}^{'n+1}}{\Delta r} \Bigg] + \frac{2\pi h}{\theta\phi} r_N \frac{\Delta r}{\Delta t} \end{aligned} \tag{3.40}$$

and

$$\frac{\partial g_1^{n+1}}{\partial S_{w_{N+\frac{1}{2}}}} = 1.127 \times 10^{-3} 2\pi h r_{N+\frac{1}{2}} k f_{w_N}^{n+1} \lambda_{o_N}^{n+1} \frac{p_{c_{N+\frac{1}{2}}}^{'n+1}}{\frac{1}{2}\Delta r}, \tag{3.41}$$

where

$$
\begin{aligned}
f'_{w_{N+\frac{1}{2}}} &= \frac{df_w(S_{w_{N+\frac{1}{2}}})}{dS_w}, \\
\lambda'_{o_{N+\frac{1}{2}}} &= \frac{d\lambda_o(S_{w_{N+\frac{1}{2}}})}{dS_w}, \\
p'_{c_{N+\frac{1}{2}}} &= \frac{dp_c(S_{w_{N+\frac{1}{2}}})}{dS_w}.
\end{aligned}
\tag{3.42}
$$

For the above problem, apply the Newton-Raphson method to the iteration estimate of the grid block value of $S_{w_j}^{n+1}$, $1 \le j \le N$. Then we have

$$
\big(J\big)
\begin{pmatrix}
\delta S_{w_{\frac{1}{2}}}^{n+1,i+1} \\
\delta S_{w_1}^{n+1,i+1} \\
\vdots \\
\delta S_{w_j}^{n+1,i+1} \\
\vdots \\
\delta S_{w_N}^{n+1,i+1} \\
\delta S_{w_{N+\frac{1}{2}}}^{n+1,i+1}
\end{pmatrix}
= -
\begin{pmatrix}
g_1^{n+1,i} \\
g_2^{n+1,i} \\
\vdots \\
g_j^{n+1,i} \\
\vdots \\
g_{N-1}^{n+1,i} \\
g_N^{n+1,i}
\end{pmatrix}
\tag{3.43}
$$

where $\big(J\big)_{N\times(N+2)}$ is the Jacobian coefficient matrix, which is equal to

$$
\big(J\big)_{N\times(N+2)} =
\begin{pmatrix}
\frac{\partial g_1^{n+1,i}}{\partial S_{w_{\frac{1}{2}}}^{n+1,i}} & \frac{\partial g_1^{n+1,i}}{\partial S_{w_1}^{n+1,i}} & \frac{\partial g_1^{n+1,i}}{\partial S_{w_2}^{n+1,i}} & 0 & \cdots & \cdots & \cdots & \cdots & 0 \\
0 & \frac{\partial g_2^{n+1,i}}{\partial S_{w_1}^{n+1,i}} & \frac{\partial g_2^{n+1,i}}{\partial S_{w_2}^{n+1,i}} & \frac{\partial g_2^{n+1,i}}{\partial S_{w_3}^{n+1,i}} & 0 & \cdots & \cdots & \cdots & 0 \\
\vdots & \ddots & \ddots & \ddots & \ddots & \ddots & \vdots & \vdots & \vdots \\
0 & \cdots & 0 & \frac{\partial g_j^{n+1,i}}{\partial S_{w_{j-1}}^{n+1,i}} & \frac{\partial g_j^{n+1,i}}{\partial S_{w_j}^{n+1,i}} & \frac{\partial g_j^{n+1,i}}{\partial S_{w_{j+1}}^{n+1,i}} & 0 & \cdots & 0 \\
\vdots & \vdots & \vdots & \ddots & \ddots & \ddots & \ddots & \ddots & 0 \\
0 & \cdots & \cdots & \cdots & 0 & \frac{\partial g_{N-1}^{n+1,i}}{\partial S_{w_{N-2}}^{n+1,i}} & \frac{\partial g_{N-1}^{n+1,i}}{\partial S_{w_{N-1}}^{n+1,i}} & \frac{\partial g_{N-1}^{n+1,i}}{\partial S_{w_N}^{n+1,i}} & 0 \\
0 & \cdots & \cdots & \cdots & \cdots & 0 & \frac{\partial g_N^{n+1,i}}{\partial S_{w_{N-1}}^{n+1,i}} & \frac{\partial g_N^{n+1,i}}{\partial S_{w_N}^{n+1,i}} & \frac{\partial g_N^{n+1,i}}{\partial S_{w_{N+\frac{1}{2}}}^{n+1,i}}
\end{pmatrix}
$$

In Eq. 3.43, there are N equations, but $N+2$ unknowns. Boundary Condition, Eq. 3.6, provides $S_{w_{\frac{1}{2}}} = 1 - S_{or}$ and $S_{w_{N+\frac{1}{2}}} = S_{iw}$, which mean $\delta S_{w_{\frac{1}{2}}} = 0$ and $\delta S_{w_{N+\frac{1}{2}}} = 0$. Then the Jacobian matrix above can be simplified as

$$
(J) = \begin{pmatrix}
\frac{\partial g_1^{n+1,i}}{\partial S_{w_1}^{n+1,i}} & \frac{\partial g_1^{n+1,i}}{\partial S_{w_2}^{n+1,i}} & & & & & & \\
\frac{\partial g_2^{n+1,i}}{\partial S_{w_1}^{n+1,i}} & \frac{\partial g_2^{n+1,i}}{\partial S_{w_2}^{n+1,i}} & \frac{\partial g_2^{n+1,i}}{\partial S_{w_3}^{n+1,i}} & & & & & \\
 & \ddots & \ddots & \ddots & & & & \\
 & & \frac{\partial g_j^{n+1,i}}{\partial S_{w_{j-1}}^{n+1,i}} & \frac{\partial g_j^{n+1,i}}{\partial S_{w_j}^{n+1,i}} & \frac{\partial g_j^{n+1,i}}{\partial S_{w_{j+1}}^{n+1,i}} & & & \\
 & & & \ddots & \ddots & \ddots & & \\
 & & & & \frac{\partial g_{N-1}^{n+1,i}}{\partial S_{w_{N-2}}^{n+1,i}} & \frac{\partial g_{N-1}^{n+1,i}}{\partial S_{w_{N-1}}^{n+1,i}} & \frac{\partial g_{N-1}^{n+1,i}}{\partial S_{w_N}^{n+1,i}} \\
 & & & & & \frac{\partial g_N^{n+1,i}}{\partial S_{w_{N-1}}^{n+1,i}} & \frac{\partial g_N^{n+1,i}}{\partial S_{w_N}^{n+1,i}}
\end{pmatrix},
$$

which is an $N \times N$ tridiagonal matrix, and the Newton-Raphson iteration, Eq. 3.43, can be simplified as

$$
(J) \begin{pmatrix} \delta S_{w_1}^{n+1,i+1} \\ \delta S_{w_2}^{n+1,i+1} \\ \vdots \\ \delta S_{w_j}^{n+1,i+1} \\ \vdots \\ \delta S_{w_N-1}^{n+1,i+1} \\ \delta S_{w_N}^{n+1,i+1} \end{pmatrix} = - \begin{pmatrix} g_1^{n+1,i} \\ g_2^{n+1,i} \\ \vdots \\ g_j^{n+1,i} \\ \vdots \\ g_{N-1}^{n+1,i} \\ g_N^{n+1,i} \end{pmatrix} \tag{3.44}
$$

3.1.2 Saturation Evolution during Falloff

During falloff, it is assumed that total flow rate, q_t, is zero in this research, although as discussed previously in Chapter 2, this is not valid at very early times. Then in Eq. 3.2 the convection term disappears, i.e., diffusion dominates the physical behavior during falloff. Another assumption is that the diffusion does not propagate to the two boundaries during falloff. So during falloff, Eq. 3.2 gives the following partial differential equation and initial and boundary conditions:

$$PDE: \quad \frac{2\pi h\phi}{\theta}\frac{\partial S_w}{\partial t} + 1.127\times 10^{-3}\cdot 2\pi hk\frac{1}{r}\frac{\partial}{\partial r}\left[f_w(S_w)\lambda_o(S_w)r\frac{\partial p_c(S_w)}{\partial r}\right] = 0, \quad (3.45)$$

and

$$\begin{cases} \text{I.C.} & S_w(r, t=0) = S_w(r, t_p); \\ \text{B.C.} & S_w(r=r_w, t) = 1 - S_{or}, \quad t > 0; \\ & S_w(r=r_e, t) = S_{iw},, \quad t > 0, \end{cases} \quad (3.46)$$

where the initial condition $S_w(r, t=0) = S_w(r, t_p)$ is the water saturation distribution obtained at the end of water injection. The upstream weight is also used for the finite difference equations during falloff. For a given time step, $n+1$, the finite difference equations of mass conservation of grid blocks and the initial and boundary conditions can be expressed by

$$\begin{aligned} g_1^{n+1} = 1.127\times 10^{-3}2\pi h\Bigg(& r_{1+\frac{1}{2}}kf_{w_1}^{n+1}\lambda_{o_1}^{n+1}\frac{p_{c_2}^{n+1} - p_{c_1}^{n+1}}{\Delta r} \\ & - r_{\frac{1}{2}}kf_{w_{\frac{1}{2}}}^{n+1}\lambda_{o_{\frac{1}{2}}}^{n+1}\frac{p_{c_1}^{n+1} - p_{c_{\frac{1}{2}}}^{n+1}}{\frac{1}{2}\Delta r}\Bigg) \\ & + \frac{2\pi h}{\theta\phi}r_1\frac{\Delta r}{\Delta t}\left(S_{w_1}^{n+1} - S_{w_1}^{n}\right) = 0, \end{aligned} \quad (3.47)$$

$$\begin{aligned} g_j^{n+1} = 1.127\times 10^{-3}2\pi h\Bigg(& r_{j+\frac{1}{2}}kf_{w_j}^{n+1}\lambda_{o_j}^{n+1}\frac{p_{c_{j+1}}^{n+1} - p_{c_j}^{n+1}}{\Delta r} \\ & - r_{j-\frac{1}{2}}kf_{w_{j-1}}^{n+1}\lambda_{o_{j-1}}^{n+1}\frac{p_{c_j}^{n+1} - p_{c_{j-1}}^{n+1}}{\Delta r}\Bigg) \\ & + \frac{2\pi h}{\theta\phi}r_j\frac{\Delta r}{\Delta t}\left(S_{w_j}^{n+1} - S_{w_j}^{n}\right) = 0; \\ \text{for} \quad & 2 \le j \le N-1, \end{aligned} \quad (3.48)$$

$$g_N^{n+1} = 1.127\times10^{-3}2\pi h\Bigg(r_{N+\frac{1}{2}}kf_{w_N}^{n+1}\lambda_{o_N}^{n+1}\frac{p_{c_{N+\frac{1}{2}}}^{n+1}-p_{c_N}^{n+1}}{\frac{1}{2}\Delta r} - r_{N-\frac{1}{2}}kf_{w_{N-1}}^{n+1}\lambda_{o_{N-1}}^{n+1}\frac{p_{c_N}^{n+1}-p_{c_{N-1}}^{n+1}}{\Delta r}\Bigg) + \frac{2\pi h}{\theta\phi}r_N\frac{\Delta r}{\Delta t}\left(S_{w_N}^{n+1}-S_{w_N}^{n}\right)=0 \tag{3.49}$$

and

$$\begin{cases} \text{I.C.} & S_{w_j}^0 = S_{w_j}(r_j,t_p), \qquad 1\le j\le N; \\ \text{B.C.} & S_{w_{\frac{1}{2}}} = 1-S_{or}; \\ & S_{w_{N+\frac{1}{2}}} = S_{iw}. \end{cases} \tag{3.50}$$

When we use the Newton-Raphson iteration to solve the equations, the elements of the Jacobian matrix for g_j^{n+1} to water saturation of blocks can be evaluated by following equations: for $j=1$, we have

$$\frac{\partial g_1^{n+1}}{\partial S_{w_{\frac{1}{2}}}} = 1.127\times10^{-3}2\pi hr_{\frac{1}{2}}k\Bigg(-f_{w_{\frac{1}{2}}}^{'n+1}\lambda_{o_{\frac{1}{2}}}^{n+1}\frac{p_{c_1}^{n+1}-p_{c_{\frac{1}{2}}}^{n+1}}{\frac{1}{2}\Delta r} - f_{w_{\frac{1}{2}}}^{n+1}\lambda_{o_{\frac{1}{2}}}^{'n+1}\frac{p_{c_1}^{n+1}-p_{c_{\frac{1}{2}}}^{n+1}}{\frac{1}{2}\Delta r} + f_{w_{\frac{1}{2}}}^{n+1}\lambda_{o_{\frac{1}{2}}}^{n+1}\frac{p_{c_{\frac{1}{2}}}^{'n+1}}{\frac{1}{2}\Delta r}\Bigg), \tag{3.51}$$

$$\frac{\partial g_1^{n+1}}{\partial S_{w_1}} = 1.127\times10^{-3}2\pi h\Bigg[r_{1+\frac{1}{2}}k\Bigg(f_{w_1}^{'n+1}\lambda_{o_1}^{n+1}\frac{p_{c_2}^{n+1}-p_{c_1}^{n+1}}{\Delta r} + f_{w_1}^{n+1}\lambda_{o_1}^{'n+1}\frac{p_{c_2}^{n+1}-p_{c_1}^{n+1}}{\Delta r} - f_{w_1}^{n+1}\lambda_{o_1}^{n+1}\frac{p_{c_1}^{'n+1}}{\Delta r}\Bigg) - r_{\frac{1}{2}}kf_{w_1}^{n+1}\lambda_{o_{\frac{1}{2}}}^{n+1}\frac{p_{c_1}^{'n+1}}{\Delta r}\Bigg] + \frac{2\pi h}{\theta\phi}r_1\frac{\Delta r}{\Delta t} \tag{3.52}$$

and

$$\frac{\partial g_1^{n+1}}{\partial S_{w_2}} = 1.127\times10^{-3}2\pi hr_{1+\frac{1}{2}}kf_{w_1}^{n+1}\lambda_{o_1}^{n+1}\frac{p_{c_2}^{'n+1}}{\Delta r}. \tag{3.53}$$

For $2\le j\le N-1$, we have

$$\frac{\partial g_j^{n+1}}{\partial S_{w_{j-1}}} = 1.127\times10^{-3}2\pi h r_{j-\frac{1}{2}}k\bigg(- f_{w_{j-1}}^{'n+1}\lambda_{o_{j-1}}^{n+1}\frac{p_{c_j}^{n+1}-p_{c_{j-1}}^{n+1}}{\Delta r} - f_{w_{j-1}}^{n+1}\lambda_{o_{j-1}}^{'n+1}\frac{p_{c_j}^{n+1}-p_{c_{j-1}}^{n+1}}{\Delta r} + f_{w_{j-1}}^{n+1}\lambda_{o_{j-1}}^{n+1}\frac{p_{c_{j-1}}^{'n+1}}{\Delta r}\bigg), \tag{3.54}$$

$$\frac{\partial g_j^{n+1}}{\partial S_{w_j}} = 1.127\times10^{-3}2\pi h\bigg[r_{j+\frac{1}{2}}k_j\bigg(f_{w_j}^{'n+1}\lambda_{o_j}^{n+1}\frac{p_{c_{j+1}}^{n+1}-p_{c_j}^{n+1}}{\Delta r} + f_{w_j}^{n+1}\lambda_{o_j}^{'n+1}\frac{p_{c_{j+1}}^{n+1}-p_{c_j}^{n+1}}{\Delta r} - f_{w_j}^{n+1}\lambda_{o_j}^{n+1}\frac{p_{c_j}^{'n+1}}{\Delta r}\bigg) - r_{j-\frac{1}{2}}k_{j-1}f_{w_{j-1}}^{n+1}\lambda_{o_{j-1}}^{n+1}\frac{p_{c_j}^{'n+1}}{\Delta r}\bigg] + \frac{2\pi h}{\theta\phi}r_j\frac{\Delta r}{\Delta t} \tag{3.55}$$

and

$$\frac{\partial g_j^{n+1}}{\partial S_{w_{j+1}}} = 1.127\times10^{-3}2\pi h r_{j+\frac{1}{2}}k f_{w_j}^{n+1}\lambda_{o_j}^{n+1}\frac{p_{c_{j+1}}^{'n+1}}{\Delta r}. \tag{3.56}$$

For $j = N$, we have

$$\frac{\partial g_N^{n+1}}{\partial S_{w_{N-1}}} = 1.127\times10^{-3}2\pi h r_{N-\frac{1}{2}}k\bigg(- f_{w_{N-1}}^{'n+1}\lambda_{o_{N-1}}^{n+1}\frac{p_{c_N}^{n+1}-p_{c_{N-1}}^{n+1}}{\Delta r} - f_{w_{N-1}}^{n+1}\lambda_{o_{N-1}}^{'n+1}\frac{p_{c_N}^{n+1}-p_{c_{N-1}}^{n+1}}{\Delta r} + f_{w_{N-1}}^{n+1}\lambda_{o_{N-1}}^{n+1}\frac{p_{c_{N-1}}^{'n+1}}{\Delta r}\bigg), \tag{3.57}$$

$$\frac{\partial g_N^{n+1}}{\partial S_{w_N}} = 1.127\times10^{-3}2\pi h\bigg[r_{N+\frac{1}{2}}k\bigg(f_{w_N}^{'n+1}\lambda_{o_N}^{n+1}\frac{p_{c_{N+\frac{1}{2}}}^{n+1}-p_{c_N}^{n+1}}{\frac{1}{2}\Delta r} + f_{w_N}^{n+1}\lambda_{o_N}^{'n+1}\frac{p_{c_{N+\frac{1}{2}}}^{n+1}-p_{c_N}^{n+1}}{\frac{1}{2}\Delta r} - f_{w_N}^{n+1}\lambda_{o_N}^{n+1}\frac{p_{c_N}^{'n+1}}{\frac{1}{2}\Delta r}\bigg) - r_{N-\frac{1}{2}}k f_{w_{N-1}}^{n+1}\lambda_{o_{N-1}}^{n+1}\frac{p_{c_N}^{'n+1}}{\Delta r}\bigg] + \frac{2\pi h}{\theta\phi}r_N\frac{\Delta r}{\Delta t} \tag{3.58}$$

and

$$\frac{\partial g_N^{n+1}}{\partial S_{w_{N+\frac{1}{2}}}} = 1.127\times10^{-3}2\pi h r_{N+\frac{1}{2}}k f_{w_N}^{n+1}\lambda_{o_N}^{n+1}\frac{p_{c_{N+\frac{1}{2}}}^{'n+1}}{\Delta r}. \tag{3.59}$$

The process of obtaining iteration estimates of grid block saturations by Newton-Raphson has been described in Eq. 3.44.

3.1.3 Saturation Evolution during Production

After water injection and falloff, there is a water bank which gives the initial saturation distribution at the beginning of production. During production, oil flows back to the well and water saturation decreases in the water bank. If we used the total flow rate as positive, $q_t > 0$, then the mass conservation of water during production can be expressed by the following partial differential equation:

$$\frac{2\pi h\phi}{\theta}\frac{\partial S_w}{\partial t} - \frac{1}{r}q_t\frac{\partial}{\partial r}\Bigg[f_w(S_w) + 1.127\times 10^{-3}\frac{1}{q_t}2\pi hk f_w(S_w)\lambda_o(S_w)r\frac{\partial p_c(S_w)}{\partial r}\Bigg] = 0, \tag{3.60}$$

During production, the initial condition of water saturation distribution is obtained at the time at the end time of falloff, t_s. In the solution for the saturation during the flow back (production) period, we let $t = 0$ correspond to the beginning of production. The outer boundary saturation is still the irreducible water saturation, $S_w(r = r_e, t) = S_{iw}$. The water saturation at the well changes when oil begins to be produced. In this research a zero saturation gradient is assumed for the production boundary. The assumption $\partial S_w/\partial r|_{r=r_w} = 0$ makes the solution unique (see reference [5]). So the initial and boundary conditions during production can be expressed as

$$\begin{cases} \text{I.C.} & S_w(r, t = 0) = S_w(r, t_s), \quad r_w \le r \le r_e; \\ \text{B.C.} & \left.\frac{\partial S_w(r,t)}{\partial r}\right|_{r=r_w} = 0, \text{ for } t > 0; \\ & S_w(r = \infty, \Delta t) = S_{iw}, \text{ for } t > 0. \end{cases} \tag{3.61}$$

When the finite difference method is used to solve the PDE, the finite difference equation of mass conservation of water during production is given by

$$\frac{2\pi h}{\theta\phi} r_j \frac{\Delta r}{\Delta t}\left(S_{w_j}^{n+1} - S_{w_j}^{n}\right) - q_t\left(f_{w_{j+\frac{1}{2}}}^{n+1} - f_{w_{j-\frac{1}{2}}}^{n+1}\right) - 1.127\times 10^{-3} 2\pi h\left(k_{j+\frac{1}{2}} r_{j+\frac{1}{2}} f_{w_{j+\frac{1}{2}}}^{n+1} \lambda_{o_{j+\frac{1}{2}}}^{n+1} \left.\frac{\partial p_c}{\partial r}\right|_{j+\frac{1}{2}}^{n+1} - k_{j-\frac{1}{2}} r_{j-\frac{1}{2}} f_{w_{j-\frac{1}{2}}}^{n+1} \lambda_{o_{j-\frac{1}{2}}}^{n+1} \left.\frac{\partial p_c}{\partial r}\right|_{j-\frac{1}{2}}^{n+1}\right) = 0. \tag{3.62}$$

The upstream weighting for the values at the boundaries of the blocks is also applied. During production the direction of upstream is the direction away from the wellbore. Using the upstream weighting, we have

$$\begin{aligned} f_{w_{j+\frac{1}{2}}} &= f_{w_{j+1}}; \\ \lambda_{o_{j+\frac{1}{2}}} &= \lambda_{o_{j+1}}; \\ f_{w_{j-\frac{1}{2}}} &= f_{w_j}; \\ \lambda_{o_{j-\frac{1}{2}}} &= \lambda_{o_j}. \end{aligned} \tag{3.63}$$

The backward finite difference is also employed for the partial derivative of p_c, as shown in Eqs. 3.12 and 3.13. So, assuming constant permeability k, the implicit finite difference equations during production can be represented by

$$\begin{aligned} g_j^{n+1} = -q_t\left(f_{w_{j+1}}^{n+1} - f_{w_j}^{n+1}\right) &- 1.127\times 10^{-3} 2\pi h\left(r_{j+\frac{1}{2}} k f_{w_{j+1}}^{n+1} \lambda_{o_{j+1}}^{n+1} \frac{p_{c_{j+1}}^{n+1} - p_{c_j}^{n+1}}{\Delta r} - r_{j-\frac{1}{2}} k f_{w_j}^{n+1} \lambda_{o_j}^{n+1} \frac{p_{c_j}^{n+1} - p_{c_{j-1}}^{n+1}}{\Delta r}\right) \\ &+ \frac{2\pi h}{\theta\phi} r_j \frac{\Delta r}{\Delta t}\left(S_{w_j}^{n+1} - S_{w_j}^{n}\right) = 0, \end{aligned} \tag{3.64}$$

$$2 \le j \le N-1.$$

The initial and boundary conditions for finite difference can be expressed as

$$\begin{cases} \text{I.C.} & S^0_{w_j} = S_w(r_j, t_s), \qquad 1 \le j \le N; \\ \text{B.C.} & S^n_{w_{\frac{1}{2}}} = S^n_{w_1}; \\ & S^n_{w_{N+\frac{1}{2}}} = S_{iw}. \end{cases} \tag{3.65}$$

For $j = 1$, we have

$$\begin{aligned} g_1^{n+1} = -q_t\Big(f_{w_2}^{n+1} - f_{w_1}^{n+1}\Big) \\ - 1.127 \times 10^{-3} 2\pi h \Bigg(r_{1+\frac{1}{2}} k f_{w_2}^{n+1} \lambda_{o_2}^{n+1} \frac{p_{c_2}^{n+1} - p_{c_1}^{n+1}}{\Delta r} \\ - r_{\frac{1}{2}} k f_{w_1}^{n+1} \lambda_{o_1}^{n+1} \frac{p_{c_1}^{n+1} - p_{c_{\frac{1}{2}}}^{n+1}}{\frac{1}{2}\Delta r} \Bigg) \\ + \frac{2\pi h}{\theta\phi} r_1 \frac{\Delta r}{\Delta t} \big(S_{w_1}^{n+1} - S_{w_1}^n\big) = 0. \end{aligned} \tag{3.66}$$

Boundary condition $S^n_{w_{\frac{1}{2}}} = S^n_{w_1}$ makes $p^{n+1}_{c_1} - p^{n+1}_{c_{\frac{1}{2}}} = 0$, so Eq. 3.66 can be simplified as

$$\begin{aligned} g_1^{n+1} = -q_t\Big(f_{w_2}^{n+1} - f_{w_1}^{n+1}\Big) \\ - 1.127 \times 10^{-3} 2\pi h r_{1+\frac{1}{2}} k f_{w_2}^{n+1} \lambda_{o_2}^{n+1} \frac{p_{c_2}^{n+1} - p_{c_1}^{n+1}}{\Delta r} \\ + \frac{2\pi h}{\theta\phi} r_1 \frac{\Delta r}{\Delta t} \big(S_{w_1}^{n+1} - S_{w_1}^n\big) = 0. \end{aligned} \tag{3.67}$$

For $j = N$, we have

$$\begin{aligned} g_N^{n+1} = -q_t\Big(f_{w_{N+\frac{1}{2}}}^{n+1} - f_{w_N}^{n+1}\Big) \\ - 1.127 \times 10^{-3} 2\pi h \Bigg(r_{N+\frac{1}{2}} k f_{w_{N+\frac{1}{2}}}^{n+1} \lambda_{o_{N+\frac{1}{2}}}^{n+1} \frac{p_{c_{N+\frac{1}{2}}}^{n+1} - p_{c_N}^{n+1}}{\frac{1}{2}\Delta r} \\ - r_{N-\frac{1}{2}} k f_{w_N}^{n+1} \lambda_{o_N}^{n+1} \frac{p_{c_N}^{n+1} - p_{c_{N-1}}^{n+1}}{\Delta r} \Bigg) \\ + \frac{2\pi h}{\theta\phi} r_N \frac{\Delta r}{\Delta t} \big(S_{w_N}^{n+1} - S_{w_N}^n\big) = 0. \end{aligned} \tag{3.68}$$

As before, the Newton-Raphson method is applied to solve the finite difference equations in Eq. 3.64. The elements in the Jacobian matrix of equation g_i^{n+1} to S_{w_j} for $2 \le j \le N-1$ can be expressed by

$$\frac{\partial g_j^{n+1}}{\partial S_{w_{j-1}}^{n+1}} = -1.127 \times 10^{-3} 2\pi h r_{j-\frac{1}{2}} k_j f_{w_j^{n+1}} \lambda_{o_j}^{n+1} \frac{p_{c_{j-1}}^{'n+1}}{\Delta r}, \tag{3.69}$$

$$\begin{aligned}\frac{\partial g_j^{n+1}}{\partial S_{w_j}} = q_t f_{w_j}^{'n+1} - 1.127 \times 10^{-3} 2\pi h \Bigg[& - r_{j+\frac{1}{2}} k_{j+1} f_{w_{j+1}}^{n+1} \lambda_{o_{j+1}}^{n+1} \frac{p_{c_j}^{'n+1}}{\Delta r} \\ & - r_{j-\frac{1}{2}} k_j \Bigg(f_{w_j}^{'n+1} \lambda_{o_j}^{n+1} \frac{p_{c_{j+1}}^{n+1} - p_{c_j}^{n+1}}{\Delta r} + f_{w_j}^{n+1} \lambda_{o_j}^{'n+1} \frac{p_{c_{j+1}}^{n+1} - p_{c_j}^{n+1}}{\Delta r} \\ & + f_{w_j}^{n+1} \lambda_{o_j}^{n+1} \frac{p_{c_{j+1}}^{'n+1}}{\Delta r} \Bigg) \Bigg] + \frac{2\pi h}{\theta \phi} r_j \frac{\Delta r}{\Delta t}\end{aligned} \tag{3.70}$$

and

$$\begin{aligned}\frac{\partial g_j^{n+1}}{\partial S_{w_{j+1}}} = -q_t f_{w_{j+1}}^{'n+1} - 1.127 \times 10^{-3} 2\pi h r_{j+\frac{1}{2}} k_{j+1} \Bigg(& f_{w_{j+1}}^{'n+1} \lambda_{o_{j+1}}^{n+1} \frac{p_{c_{j+1}}^{n+1} - p_{c_j}^{n+1}}{\Delta r} \\ & + f_{w_{j+1}}^{n+1} \lambda_{o_{j+1}}^{'n+1} \frac{p_{c_{j+1}}^{n+1} - p_{c_j}^{n+1}}{\Delta r} + f_{w_{j+1}}^{n+1} \lambda_{o_{j+1}}^{n+1} \frac{p_{c_{j+1}}^{'n+1}}{\Delta r} \Bigg).\end{aligned} \tag{3.71}$$

For $j = 1$, we have

$$\frac{\partial g_1^{n+1}}{\partial S_{w_{\frac{1}{2}}}^{n+1}} = 0, \tag{3.72}$$

$$\frac{\partial g_1^{n+1}}{\partial S_{w_1}} = q_t f_{w_1}^{'n+1} 1.127 \times 10^{-3} 2\pi h r_{1+\frac{1}{2}} k f_{w_1}^{n+1} \lambda_{o_2}^{n+1} \frac{p_{c_1}^{'n+1}}{\Delta r} + \frac{2\pi h}{\theta \phi} r_1 \frac{\Delta r}{\Delta t} \tag{3.73}$$

and

$$\begin{aligned}\frac{\partial g_1^{n+1}}{\partial S_{w_2}} = -q_t f_{w_2}^{'n+1} - 1.127 \times 10^{-3} 2\pi h r_{1+\frac{1}{2}} k \Bigg(& f_{w_2}^{'n+1} \lambda_{o_2}^{n+1} \frac{p_{c_2}^{n+1} - p_{c_1}^{n+1}}{\Delta r} \\ & + f_{w_2}^{n+1} \lambda_{o_1}^{'n+1} \frac{p_{c_2}^{n+1} - p_{c_1}^{n+1}}{\Delta r} + f_{w_2}^{n+1} \lambda_{o_2}^{n+1} \frac{p_{c_2}^{'n+1}}{\Delta r} \Bigg).\end{aligned} \tag{3.74}$$

For $j = N$, we have

$$\frac{\partial g_N^{n+1}}{\partial S_{w_{N-1}}^{n+1}} = -1.127\times 10^{-3} 2\pi h r_{N-\frac{1}{2}} k f_{w_N}^{n+1} \lambda_{o_N}^{n+1} \frac{p_{c_{N-1}}^{'n+1}}{\Delta r}, \tag{3.75}$$

$$\begin{aligned}\frac{\partial g_N^{n+1}}{\partial S_{w_N}} = q_t f_{w_N}^{'n+1} - 1.127\times 10^{-3} 2\pi h \Bigg[& - r_{N+\frac{1}{2}} k f_{w_{N+\frac{1}{2}}}^{n+1} \lambda_{o_{N+\frac{1}{2}}}^{n+1} \frac{p_{c_N}^{'n+1}}{\frac{1}{2}\Delta r} \\ & - r_{N-\frac{1}{2}} k \Bigg(f_{w_N}^{'n+1} \lambda_{o_N}^{n+1} \frac{p_{c_N}^{n+1} - p_{c_{N-1}}^{n+1}}{\Delta r} + f_{w_N}^{n+1} \lambda_{o_N}^{'n+1} \frac{p_{c_N}^{n+1} - p_{c_{N-1}}^{n+1}}{\Delta r} \\ & + f_{w_N}^{n+1} \lambda_{o_N}^{n+1} \frac{p_{c_N}^{'n+1}}{\Delta r} \Bigg) \Bigg] + \frac{2\pi h}{\theta\phi} r_N \frac{\Delta r}{\Delta t}\end{aligned} \tag{3.76}$$

and

$$\begin{aligned}\frac{\partial g_N^{n+1}}{\partial S_{w_{N+\frac{1}{2}}}} = -q_t f_{w_{N+\frac{1}{2}}}^{'n+1} & -1.127\times 10^{-3} 2\pi h r_{N+\frac{1}{2}} k \Bigg(f_{w_{N+\frac{1}{2}}}^{'n+1} \lambda_{o_{N+\frac{1}{2}}}^{n+1} \frac{p_{c_{N+\frac{1}{2}}}^{n+1} - p_{c_N}^{n+1}}{\frac{1}{2}\Delta r} \\ & + f_{w_{N+\frac{1}{2}}}^{n+1} \lambda_{o_{N+\frac{1}{2}}}^{'n+1} \frac{p_{c_{N+\frac{1}{2}}}^{n+1} - p_{c_j}^{n+1}}{\frac{1}{2}\Delta r} + f_{w_{N+\frac{1}{2}}}^{n+1} \lambda_{o_{N+\frac{1}{2}}}^{n+1} \frac{p_{c_{N+\frac{1}{2}}}^{'n+1}}{\frac{1}{2}\Delta r} \Bigg).\end{aligned} \tag{3.77}$$

Because $S_{w_{N+\frac{1}{2}}} = S_{iw}$, we have $\delta S_{w_{N+\frac{1}{2}}} = 0$. Thus, during production, the process of obtaining iteration estimates of grid block saturations by Newton-Raphson has been described in Eq. 3.44.

3.2 Validation of the Capillary Pressure Effect

In this section, some examples are given to illustrate the validity of water saturation evolutions and pressure responses during the injection/falloff/production test. Comparisons were made between the results from our method and the results from the reservoir simulator IMEX.

3.2.1 Examples of Saturation Evolution

Two cases with different mobility ratios are considered, one unfavorable mobility ratio and one favorable mobility ratio. Some parameters for the calculation and the

reservoir simulation are shown in Table. 2.1. An IFPT with 5-hour injection, 5-hour falloff and 14-hour production was used to illustrate the capillary pressure effects. The relative permeability curves are defined by the power law model, Eqs. 2.83 and 2.84, and the capillary pressure in Corey's model, Eq. 4.44. Table 3.1 gives the model parameters defining relative permeability curves and capillary pressure in the examples. For the unfavorable mobility ratio case, $\mu_w = 0.516$ cp and $\mu_o = 5.1$ cp. The endpoint mobility ratio between water and oil is $\hat{M} = 7.9$. For the favorable mobility ratio case, $\mu_w = 1.0$ cp and $\mu_o = 0.5$ cp. The endpoint mobility ratio is 0.4. Based on the parameters in Table 3.1, the relative permeability and capillary pressure curve are as shown in Fig. 3.2 and 3.3, respectively. In Fig. 3.3 the maximum of capillary pressure is 20 psi at irreducible water saturation $S_{iw} = 0.15$. Fig. 3.4 shows total mobility curves for favorable and unfavorable mobility ratio cases respectively.

Parameter	S_{iw}	S_{or}	a_w	a_o	n_o	n_w	P_e (psi)	λ
value	0.15	0.25	0.8	1.0	2.0	2.0	0.5	2.0

Table 3.1: Parameters of relative permeabilities (power law model) and capillary pressure (Corey's model).

Fig. 3.5 displays the nonlinear function, $f_w S_w \lambda_o(S_w) \frac{\mathrm{d}P_c(S_w)}{\mathrm{d}S_w}$, which affects the diffusion due to capillary force. This nonlinear equation has a peak at a middle water saturation and becomes zero at two end-point water saturations because it has $f_w(S_{iw}) = 0$ and $\lambda_o(1 - S_{or}) = 0$. Thus, as one gets closer to the end-point saturations, the effect of the capillary pressure diffusion decreases.

Figs. 3.6 shows the water saturation distribution at the end of water injection and falloff, respectively, for the unfavorable mobility ratio case ($\hat{M} = 7.9$). During water injection, the movement of water is governed by the convection term in the PDE of Eq. 3.2, viscous forces dominate the behavior. The water front is essentially behaving a shock. Capillary force only results a very small smearing of the sharp front. The radius of the water bank is around 17 ft after water injection. During falloff, the flow rate goes to zero very soon after shut in the water the water bank and capillary pressure governs the

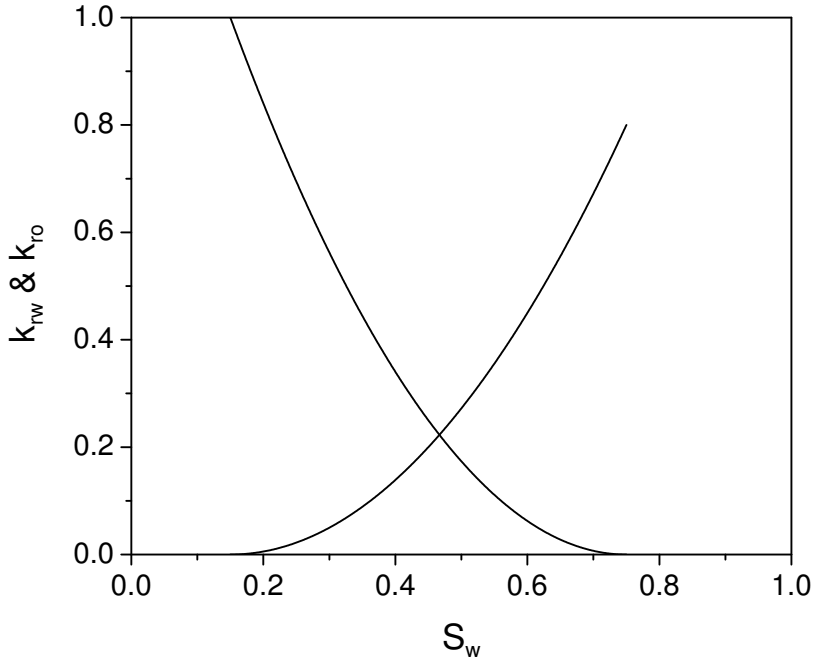

Figure 3.2: Power law relative permeabilities.

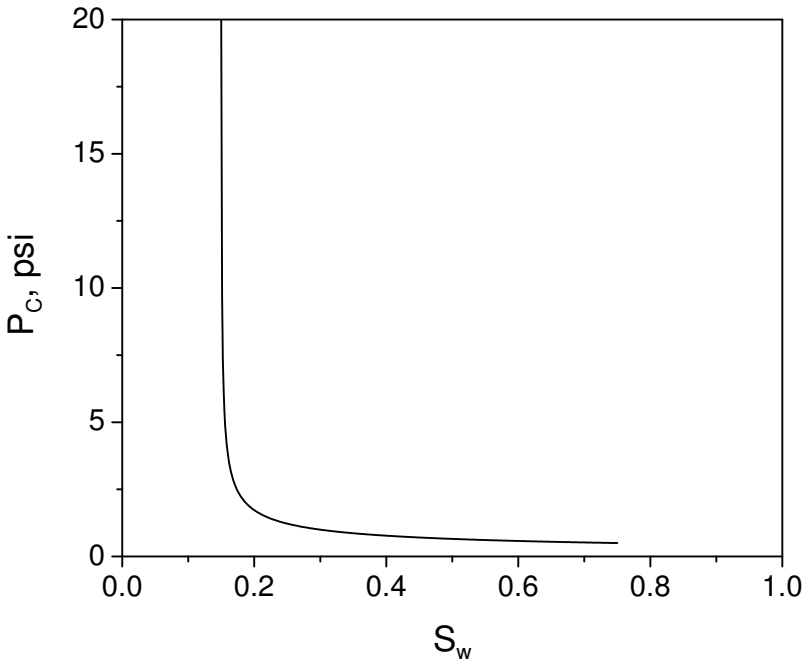

Figure 3.3: Capillary pressure from Corey's model.

saturation behavior and the water front is noticeably smeared. This smearing is stronger near the water saturation where the nonlinear function in the capillary pressure term

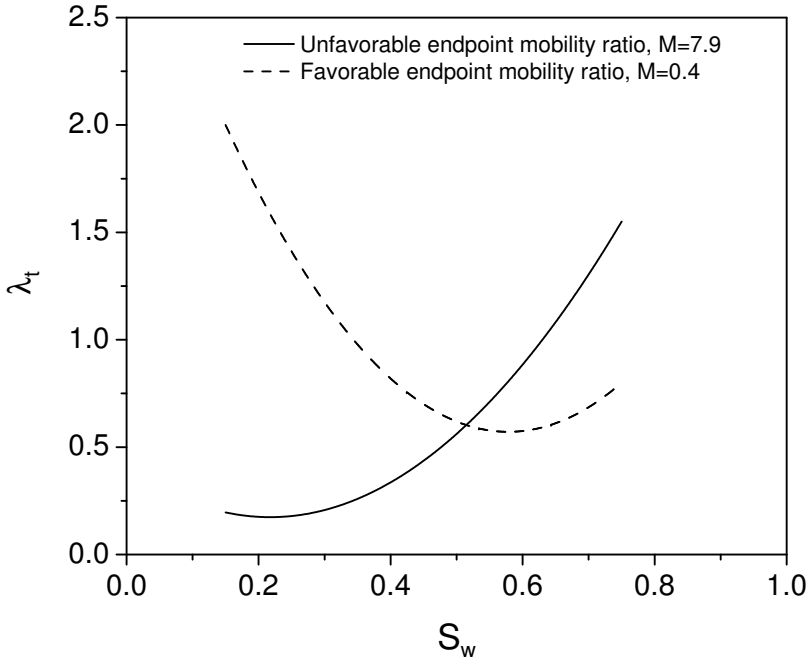

Figure 3.4: Total mobility curves for unfavorable and favorable endpoint mobility ratio cases

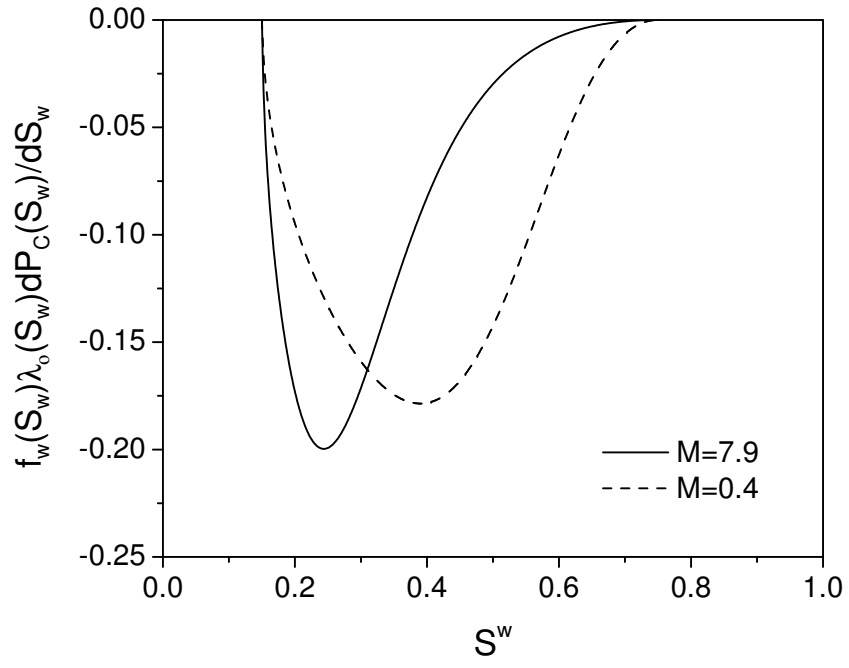

Figure 3.5: Nonlinear equation of capillary pressure diffusion term vs. water saturation.

has a large value as shown in Fig. 3.5. In Fig. 3.6, the solid curves are obtained by using the numerical solution of water conservation equation and the dashed curves are the results from commercial reservoir simulator IMEX. Our numerical results have a very good agreement with the reservoir simulation results for both water saturation evolutions during water injection and falloff. In Fig. 3.5 and similar figures, "Simulation" refers to results from CMG IMEX reservoir simulator and "Numerical" refers to results generated from our finite difference scheme. Note the reservoir simulator solves for both saturation and pressure, whereas in our numerical procedure, we solve only for water saturation.

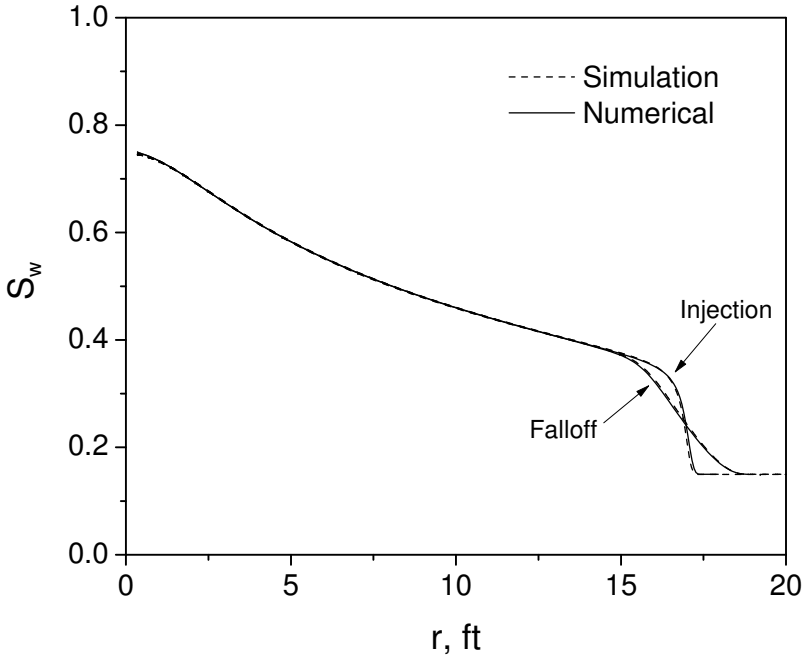

Figure 3.6: Water saturation distribution at end time of injection and falloff the for unfavorable endpoint mobility ratio $\hat{M} = 7.9$.

Fig. 3.7 displays the water saturation evolution during production. Each pair of curve is a snapshot of water saturation distribution at a given time. The saturation distribution curve that extends farthest to the right is the saturation profile at the end time of the falloff test. One can note that after falloff, the water saturation distribution has a strong smearing around the water front, but during production, when oil flows back to the well, a sharp oil front gradually develops, as the convection term (viscous forces) overwhelm the diffusion term (capillary force). In Fig. 3.7, the results of our numerical

solution of the water conservation equation (the solid curves) match the results from the simulator (the dashed curves) very well. As stated in the previous chapter, at very early production time, the total flow rate is not a constant in the water bank. Because we used the assumption of steady-state theory of Thompson and Reynolds in this work, our results move a little bit faster than the simulation results. As shown later, the saturation

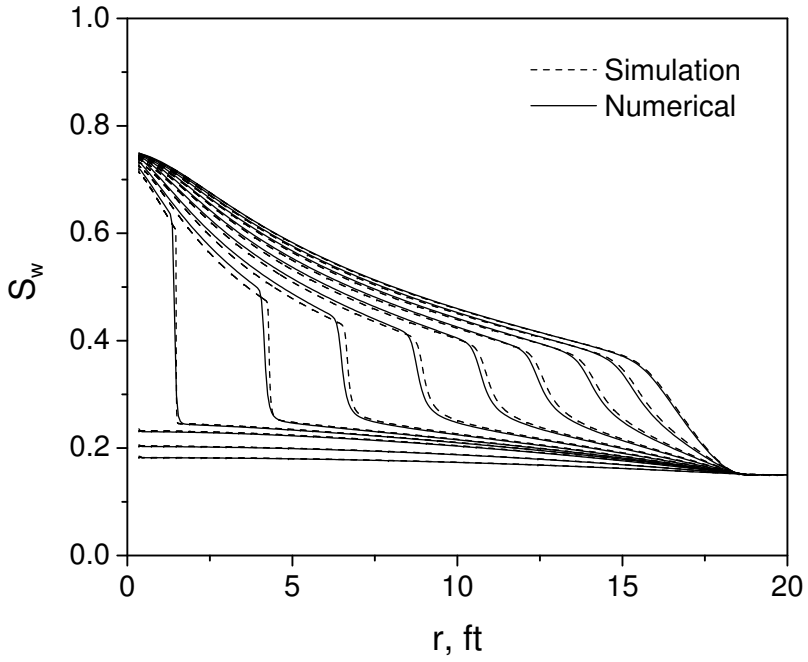

Figure 3.7: Water saturation evolution during production for the unfavorable endpoint mobility ratio $\hat{M} = 7.9$.

profiles are sufficiently accurate to generate an accurate pressure solution. Fig. 3.8 shows the comparison of saturation profiles without and with capillary pressure effects for unfavorable endpoint mobility ratio $\hat{M} = 7.9$. In this figure, two time snapshots are shown: one is at the end of falloff and the other is at a time before oil "breakthrough" during production. Around the location of water front, the saturation profiles with capillary pressure effects (solid points from reservoir simulation and solid curves from our numerical solution) show deviations from the saturation profile without the capillary pressure effect (the dashed curves from reservoir simulation). During production, there is a significant gap between the saturation profile with capillary pressure effect and the saturation profile without capillary pressure effect. With the capillary pressure effect, the oil "break-

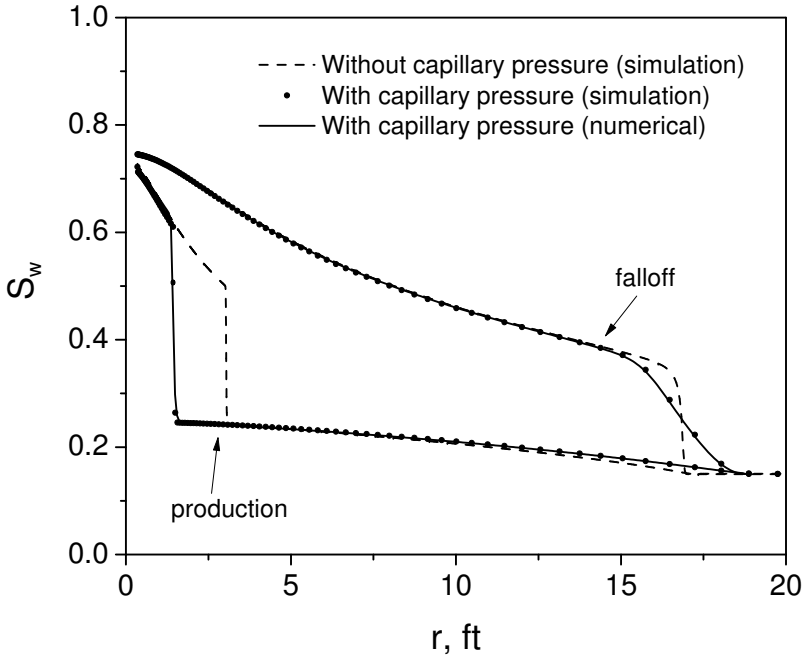

Figure 3.8: Comparison of saturation profiles for the unfavorable endpoint mobility ratio $\hat{M} = 7.9$.

through" comes earlier than that without the capillary pressure effect. That makes a huge pressure difference when oil flows back to the wellbore as shown in later section.

Fig. 3.9 presents the water saturation distributions at the end time of water injection and falloff for a favorable mobility ratio ($\hat{M} = 0.4$). Here, during water injection, we have almost piston displacement. The radius of the water bank is around 12.5 ft. During falloff, the diffusion of capillary pressure shapes the water front significantly. As shown in Fig. 3.9, water saturation distribution generated from our numerical model match the results from the reservoir simulation. Fig. 3.10 displays the snapshots of water saturation distribution during production. The results of our numerical solution are again in good agreement with the results of the simulation. During production, when oil flows back to the well, the oil front is still generated. Fig. 3.11 shows a comparison of saturation profiles between with and without capillary pressure effect for favorable endpoint mobility ratio $\hat{M} = 0.4$. As shown in Fig. 3.11, two time snapshots are compared: one is at end time of falloff and other is at time of 12.27 hours before oil "breakthrough" during production. Due to the capillary pressure effect, the saturation profiles with capillary

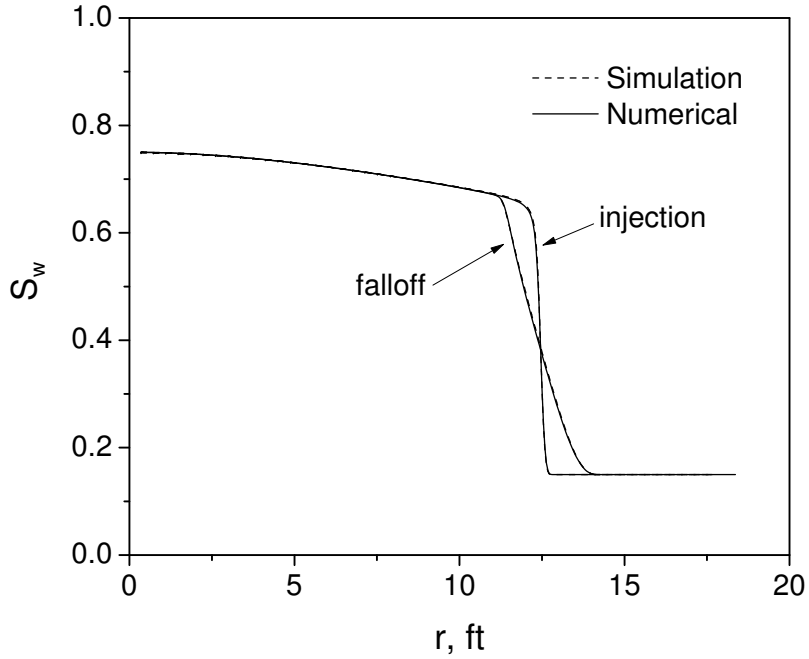

Figure 3.9: Water saturation distribution at end time of injection and falloff for the favorable endpoint mobility ratio $\hat{M} = 0.4$.

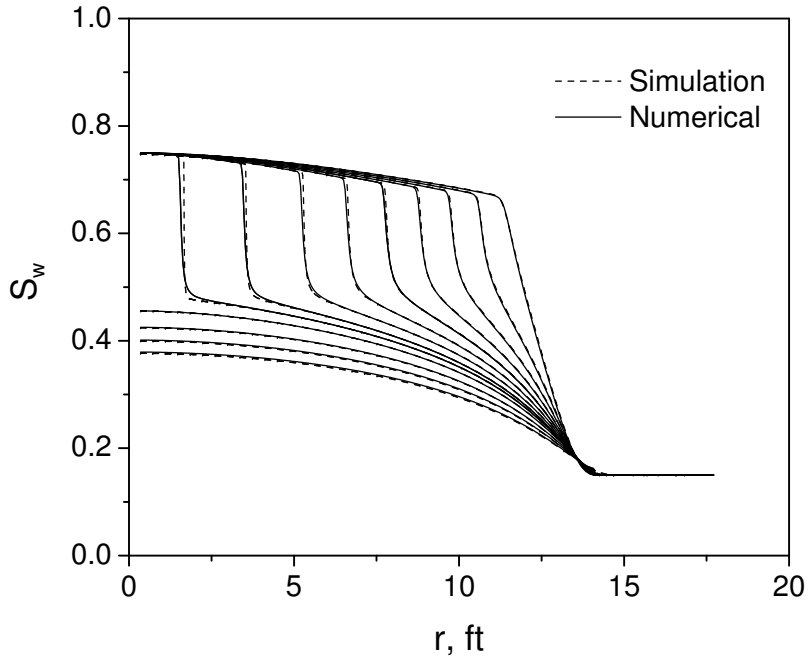

Figure 3.10: Water saturation evolution during production for the favorable endpoint mobility ratio $\hat{M} = 0.4$.

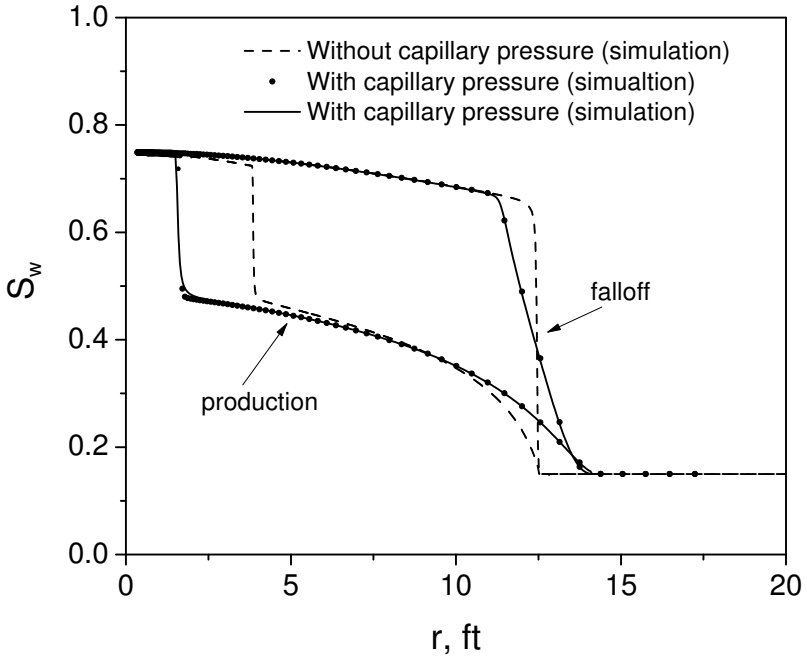

Figure 3.11: Comparison of saturation profiles for the favorable endpoint mobility ratio $\hat{M} = 0.4$.

pressure effect (solid points from reservoir simulation results and solid curves from our numerical results) have significant differences with the saturation profiles without the capillary pressure effect (dashed curves) both at end of falloff period and at 14.08 hours during production. For the case of favorable endpoint mobility ratio, the result also shows that capillary pressure makes an early oil "breakthrough" than without capillary pressure effect. The differences of saturation profiles cause the differences of the total mobility distributions around the wellbore, which generate the errors on pressure difference Δp in water phase as shown by the integral term in Eq. 2.39.

3.2.2 Examples of Pressure Response

Similar to zero capillary pressure case, the pressure responses of IFPT, considering capillary pressure effect, are obtained also based on the steady-state theory of Thompson and Reynolds [55] and the solution of Peres and Reynolds [46]. In Chapter 2, it was stated that the total pressure change can be expressed by a combination of the pressure change in the single phase oil and the pressure change in the two-phase zone. When the saturation

evolution considering the capillary pressure effect during the IFPT is resolved, the pressure responses considering the capillary pressure effect are also obtained by the Peres and Reynolds model in this research. Compared with the no-capillarity effect, the saturation distribution front is deformed after falloff by the capillary pressure diffusion, which gives a different initial condition for saturation evolution during production. Correspondingly, the pressure response cannot be the same as that obtained from no-capillary pressure effect. In the following section, pressure responses from the two cases are demonstrated.

Fig. 3.12 shows the bottomhole pressure response of a case of IFPT with an unfavorable mobility ratio, $\hat{M} = 7.9$. In Fig. 3.12, the results from our approximate solution for the pressure response (the dashed the curve) match the pressure responses from the reservoir simulation with capillary pressure (the circular data points) very well. But the results from simulation without the capillary pressure diffusion (the solid curve) have a deviation from the results with the capillary pressure effect around time of 14 hours (the oil "breakthrough" time). This deviation is due to the fact that the capillary pressure diffusion gives a different initial condition for water saturation evolution during production compared with no capillary pressure effect (see Fig. 3.8). During injection and falloff, the pressure responses are not affected too much by capillary pressure because the diffusion only affects a limited saturation region around the front, and the farther the region is from the wellbore, the less the capillary pressure affects the total pressure response (see Eq. 2.39). Fig. 3.13 demonstrates a log-log plot of pressure difference and its derivative during production. Here, the pressure difference $\Delta p(\Delta t) = p_{ws}(t_s) - p_{wf}(\Delta t)$, where $p_{ws}(t_s)$ is the bottomhole pressure at the end time of falloff; Δt is zero at beginning of production. Both from the pressure differences (Δp) and the derivatives ($\Delta p'$) the shift between the cases with and without the capillary pressure effect during the oil breakthrough time is apparent. The shift looks small in Fig. 3.12 due to the display scale. But when we compared the pressure responses at time of 14.08 hours, corresponding saturation profiles compared in Fig. 3.8, we found that the pressure difference is over 80 psi. In this case, the pressure differences between bottomhole pressure with and without capillary pressure effect vary from several psi to around 190 psi. So the large pressure difference

may ruin the estimate of relative permeabilities and other model parameters when we do the analysis with model of pressure response without capillary pressure effect to match the pressure response with capillary pressure effect.

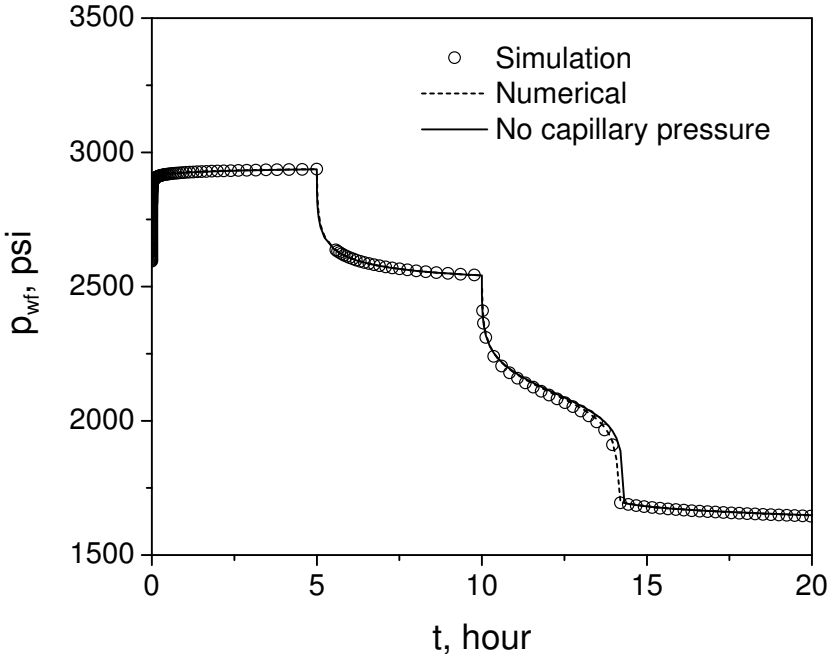

Figure 3.12: Bottomhole pressure of IFPT for the unfavorable endpoint mobility ratio $\hat{M} = 7.9$.

Figs. 3.14 and 3.15 show the results from a case with a favorable mobility ratio, $\hat{M} = 0.4$. In Fig. 3.14, the pressure response from our approximate analytical solution (the dashed curve) matches the simulation results with capillary pressure effect (the circles). The result without capillary pressure effect still gives a deviation around the time of oil "breakthrough", 13 hours. This deviation is shown clearly in Fig. 3.15, the log-log plot of pressure difference and its derivative. Corresponding to the saturation profiles at time 12.67 hours during production as shown in Fig. 3.11, the pressure error between with and without capillary pressure effect is over 5 psi. The largest error is 12 psi for this favorable endpoint mobility ratio case. In Chapter 1, it is stated that the pressure response provides information to estimate the shape of the relative permeability curves when oil flows back to the wellbore during production. Because of the sharp oil front and the total mobility change of oil flowing back to the well, the total pressure response

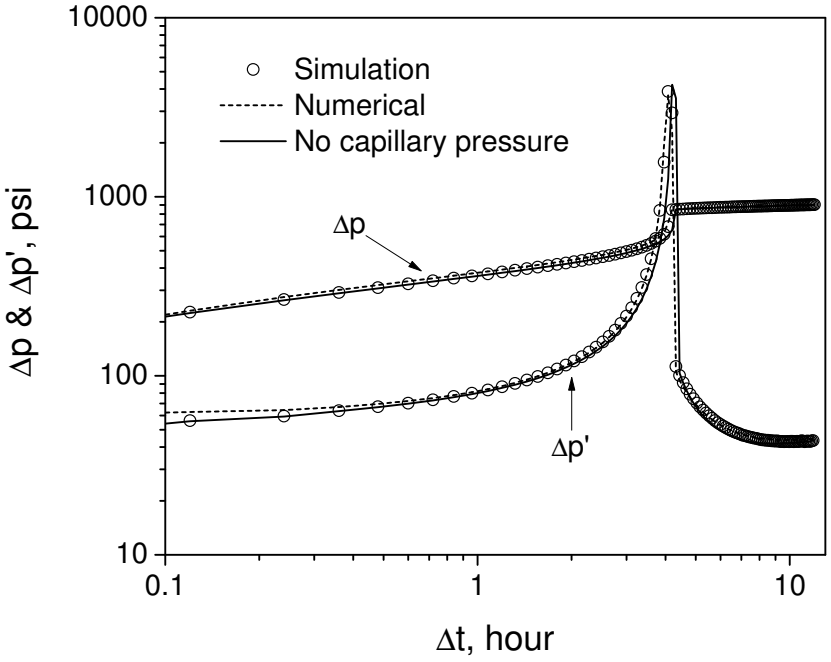

Figure 3.13: Pressure difference and its derivative during production, unfavorable endpoint mobility ratio $\hat{M} = 7.9$.

changes rapidly. Therefore, the deviation in the pressure response could ruin the estimate of the relative permeabilities and other model parameters during the process of inverse regression.

The results of these two cases with different mobility ratios demonstrate that the capillary pressure diffusion smears the water front during water injection and makes a significant change in the water saturation distribution around the front during the falloff. From the cases with favorable and unfavorable endpoint mobility ratios, we note that the diffusion during falloff gives an earlier oil "breakthrough" than that without the capillary pressure effect during production. Our approximate analytical solution in this research provides valid results for the capillary pressure effect. As shown in Figs. 3.8 and 3.11, most water saturations on the smeared front distribute between S_{iw} and S_{wf}. So a saturation among those saturations has the highest value of $df_w(S_w)/dS_w$ as shown in Fig. 2.3. Moreover, some saturations among those saturation between S_{iw} and S_{wf} have higher values of $df_w(S_w)/dS_w$ than value of $df_w(1 - S_{of})/dS_w$ which represents the front speed of oil invading water bank during production without capillary pressure effect.

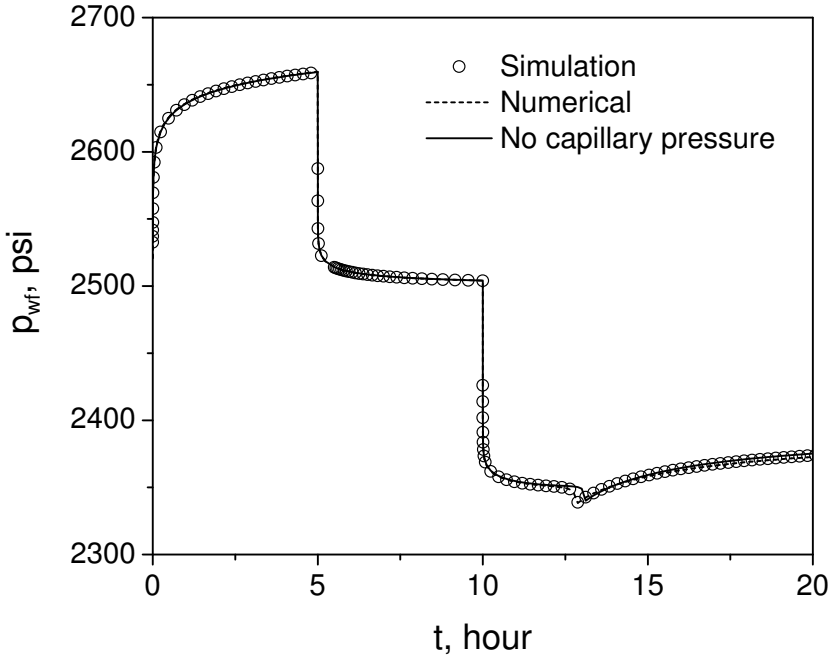

Figure 3.14: Bottomhole pressure of IFPT for the favorable endpoint mobility ratio $\hat{M} = 0.4$.

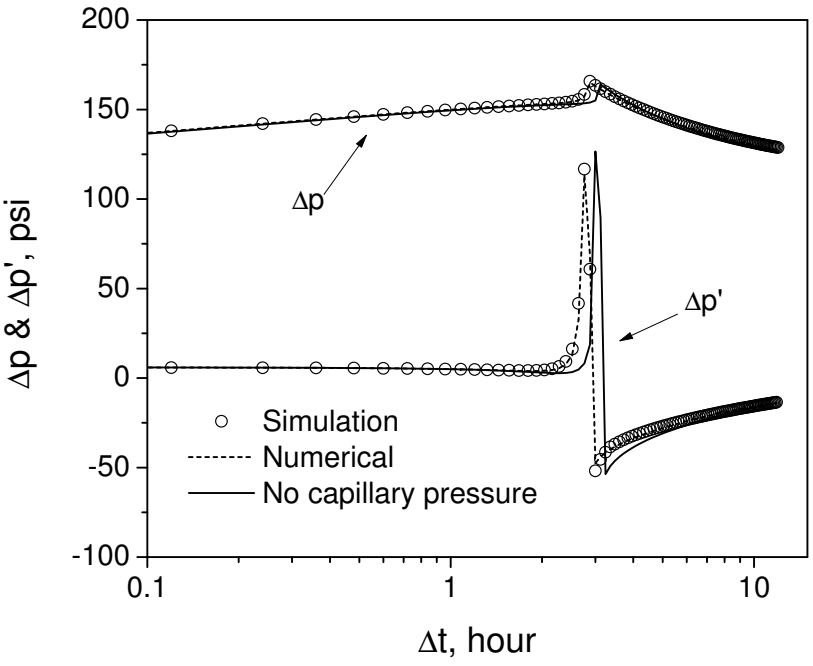

Figure 3.15: Pressure difference and its derivative during production for the favorable endpoint mobility ratio $\hat{M} = 0.4$.

Thus, due to capillary force, some water saturations on the smeared front move faster than the oil front speed without capillary pressure effect from beginning of production. That makes an early oil "breakthrough". The stronger capillary force gives a further diffusion smearing front at end time of falloff period and the earlier oil "breakthrough" time. Here, we used three different levels of capillary pressure to demonstrate the effects of capillary pressure. Fig. 3.16 – Fig. 3.18 demonstrate the results from the effect of the three different capillary pressure. In Fig. 3.16, the three different capillary pressure are shown with different maximum capillary pressure ($p_{c,\max}$) and entry capillary pressure (p_e). Apparently, the strongest capillary pressure is shown by the doted curve with the largest value of $p_{c,\max}$ and p_e, and the weakest capillary pressure is shown by the solid curve. Correspondingly, Fig. 3.17 shows the water saturation distributions with the three capillary pressure effects at the end time of falloff period. In Fig. 3.17, we can note that the strongest capillary pressure makes the worst smearing (the doted curve) around the water front saturation compared with others. Fig. 3.18 shows the bottomhole pressure response under the three capillary pressure effect. We found that the strongest capillary pressure makes the earliest oil "breakthrough" on the bottomhole pressure during production as shown by the doted curve and the pressure response with the weakest capillary pressure (solid curve) is closest to the pressure response without capillary pressure effect (the solid curve with circle).

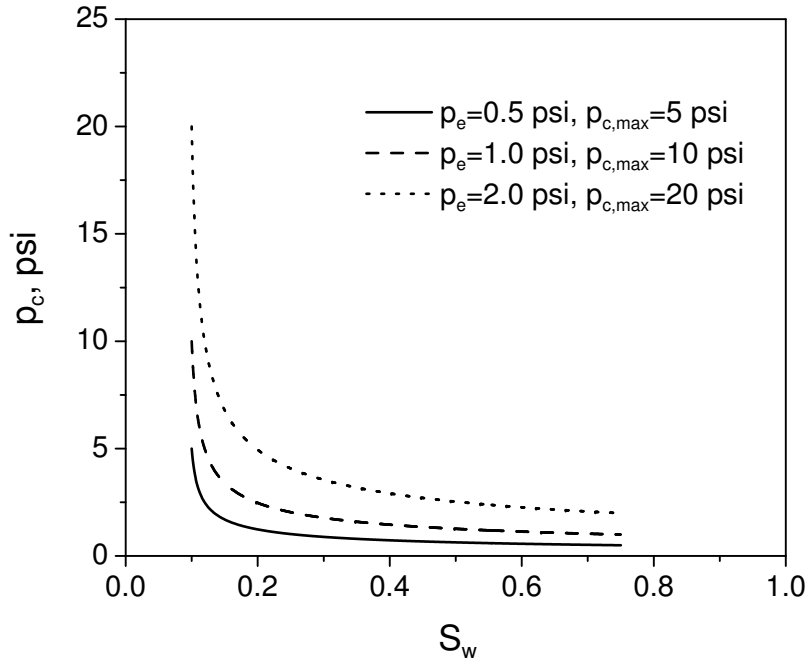

Figure 3.16: Capillary pressure curves.

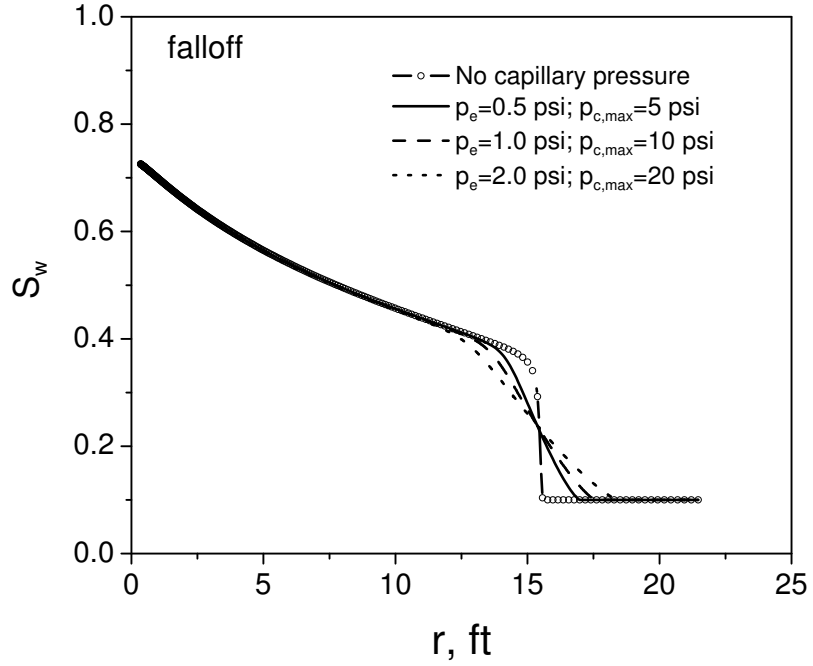

Figure 3.17: Different capillary pressure effects on saturation distributions at the end time of falloff period for the unfavorable endpoint mobility ratio $\hat{M} = 7.9$.

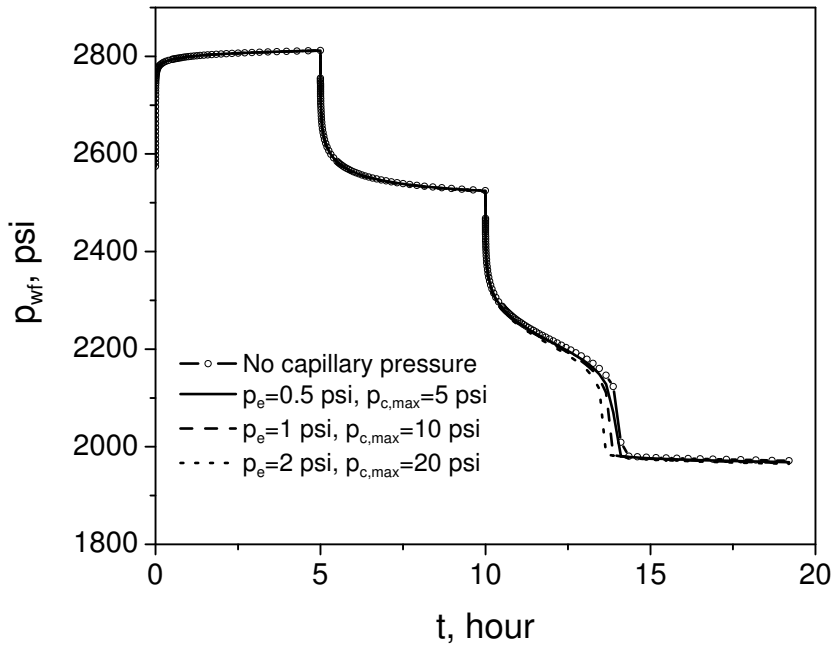

Figure 3.18: Bottomhole pressure with different capillary pressure effects for the unfavorable endpoint mobility ratio $\hat{M} = 7.9$.

CHAPTER 4

REPRESENTATION OF RELATIVE PERMEABILITIES

In this chapter, the three different representations of relative permeability curves and model parameters representing the relative permeability curves are discussed. In the first section, the power law model of water-oil two-phase relative permeability curves, which have been widely applied in reservoir engineering, is presented. In the second section, a more flexible B-spline curves representing relative permeability and the algorithms for monotonic and convex relative permeability curves are presented. The third method for modeling relative permeability curves relates relative permeability to capillary pressure.

4.1 Power Law Model Relative Permeability Curves

The standard representation of power law relative permeability curves is as follows:

$$k_{rw}(S_w) = a_w \left(\frac{S_w - S_{iw}}{1 - S_{iw} - S_{or}} \right)^{n_w}, \tag{4.1}$$

and

$$k_{ro}(S_w) = a_o \left(\frac{1 - S_w - S_{or}}{1 - S_{iw} - S_{or}} \right)^{n_o}, \tag{4.2}$$

where S_{iw} represents irreducible water saturation, S_{or} represents residual oil saturation,

$$a_w = k_{rw}(S_w = 1 - S_{or}), \tag{4.3}$$

is the end point water relative permeability and

$$a_o = k_{ro}(S_w = S_{iw}), \tag{4.4}$$

is the end point oil relative permeability. As the flow equations describing flow in a porous medium depend only on oil and water effective permeabilities, denoted respectively by k_o and k_w, production data is not sufficient to resolve absolute and relative permeabilities. To avoid this ambiguity, we define relative permeabilities by normalizing effective permeabilities using effective oil relative permeability at irreducible water saturation. Thus, at any S_w, effective oil permeability is written as

$$k_o(S_w) = \frac{k_o(S_{iw})}{k_o(S_{iw})} k_o(S_w) = k k_{ro}(S_w), \tag{4.5}$$

where absolute permeability is defined as

$$k = k_o(S_{iw}), \tag{4.6}$$

and relative permeability is defined as

$$k_{ro}(S_w) = \frac{k_o(S_w)}{k_o(S_{iw})}. \tag{4.7}$$

Thus, oil relative permeability must be equal to unity when water saturation is equal to irreducible water saturation, i.e., $a_o = 1$. Then, defining dimensionless water saturation by

$$S_{wD} = \frac{S_w - S_{iw}}{1 - S_{or} - S_{iw}}, \tag{4.8}$$

the power law representation of the oil relative permeability curve can be written as

$$k_{ro}(S_w) = \left(\frac{1 - S_w - S_{or}}{1 - S_{iw} - S_{or}} \right)^{n_o} = (1 - S_{wD})^{n_o}, \tag{4.9}$$

whereas, the water relative permeability curve is

$$k_{rw}(S_w) = a_w \left(\frac{S_w - S_{iw}}{1 - S_{iw} - S_{or}} \right)^{n_w} = a_w \left(S_{wD} \right)^{n_w}. \tag{4.10}$$

Eqs. 4.9 and 4.10 give the power law relative permeability curves used in the examples

presented here.

In Eqs. 4.9 and 4.10, there are only five possible parameters, a_w, n_w, n_o, irreducible water saturation (S_{iw}) and residual oil saturation (S_{or}) to define the power law relative permeabilities. From the definition of power law relative permeability curves, one can note that the curves are automatically monotonic and convex if the exponent values, n_o and n_w, are greater than 1. But the power law is not sufficiently flexible to describe the local variation in the shape of the relative permeability curves.

4.2 B-spline Model Relative Permeability Curves

Points on a power law relative permeability curve follow the same equation, so they can not describe local variations in a relative permeability curves. On the other hand, the use of power law curves in history matching is convenient in that the number of parameters to be adjusted is small, which tends to reduce the inherent non-uniqueness in history matching; moreover, if production data is sufficient to resolve only a small part of the curve, all of the curve is resolved. As power law models are not sufficiently flexible to accurately model all relative permeability curves, a more general representation is sought. Here, we consider using cubic B-splines to represent the relative permeability curves.

Although the results presented here focus on the case in which irreducible water saturation and residual oil saturation are known, when these endpoint saturations are considered as parameters, it is convenient to work in terms of dimensionless saturation so that one can use uniform knots and one-dimensional control points (see references [24, 50, 25]). To make the notation general, let u be the dependent variable and assume one wants to construct a B-spline approximation of a function $f(u)$ defined on $[a, b]$. To do so, one needs to define knots on this interval. Computational algorithms are more efficient if uniform knots are used [50]. For a given positive integer n, let

$$\Delta u = \frac{b-a}{n}, \tag{4.11}$$

and define uniform knots by

$$u_j = a + j\Delta u \text{ for } j = -3, -2, \cdots, n+3. \tag{4.12}$$

Note that $u_n = b$ and the knots u_j for $j < 0$ and u_j for $j > n$ are outside the interval of interest $[a, b] = [u_0, u_n]$. Relative to these knots, $B_j(u)$ is the standard B-spline basis function which is nonzero only on the interval $[u_j, u_{j+4}]$; see deBoor[24] and Appendix A.

For the case considered here, dimensionless water saturation is defined by Eq. 4.8, and the interval of interest for $u = S_{wD}$ is $[0, 1]$. Knots represent values of dimensionless water saturation with uniform knots on $[0, 1]$ given by

$$u_j = S_{wD,j} = j\Delta u \text{ for } j = 0, 1, 2, \cdots, n, \tag{4.13}$$

where $\Delta u = 1/n$ and knots outside $[0, 1]$ are defined by $u_j = S_{wD,-j} = j\Delta u$ for $j = -1, -2, -3$ and $u_j = S_{wD,j} = j\Delta u$ for $j = n+1, n+2, n+3$.

The approximating cubic B-splines for the oil and water relative permeability curves (see Appendix A), respectively, are given by

$$k_{ro}(S_{wD}) = \sum_{j=-3}^{n-1} C^o_{j+2} B_j(S_{wD}), \tag{4.14}$$

and

$$k_{rw}(S_{wD}) = \sum_{j=-3}^{n-1} C^w_{j+2} B_j(S_{wD}), \tag{4.15}$$

where the C^o_k's and C^w_k's, respectively, denote the control points for the B-spline approximations of the oil and water relative permeability curves. The control points C^o_{-1} and C^o_{n+1} are not independent but are defined to ensure that k_{ro} passes through C^o_0 and C^o_n. (The approximating spline, k_{ro} does not in general pass through any of the other control points.) Because we have chosen to normalize effective permeabilities by $k_o(S_{iw})$ to define relative permeabilities, it follows that $C^o_0 = 1$ so it is not a model parameter. Moveover, oil relative permeability is zero at $S_{wD} = 1$ so we must have $C^o_n = 0$. Similarly, the control points, C^w_{-1} and C^w_{n+1}, are not independent but are defined to ensure that k_{rw} passes

through C_0^w and C_n^w. Because water relative permeability is equal to zero at $S_{wD} = 0$, it follows that $C_0^w = 0$. It now follows that the parameters that must be estimated to obtain the B-spline approximations are C_j^o, for $j = 1, 2 \cdots n-1$ and C_j^w for $j = 1, 2, \cdots n$, i.e., there are $2n - 1$ parameters to estimate.

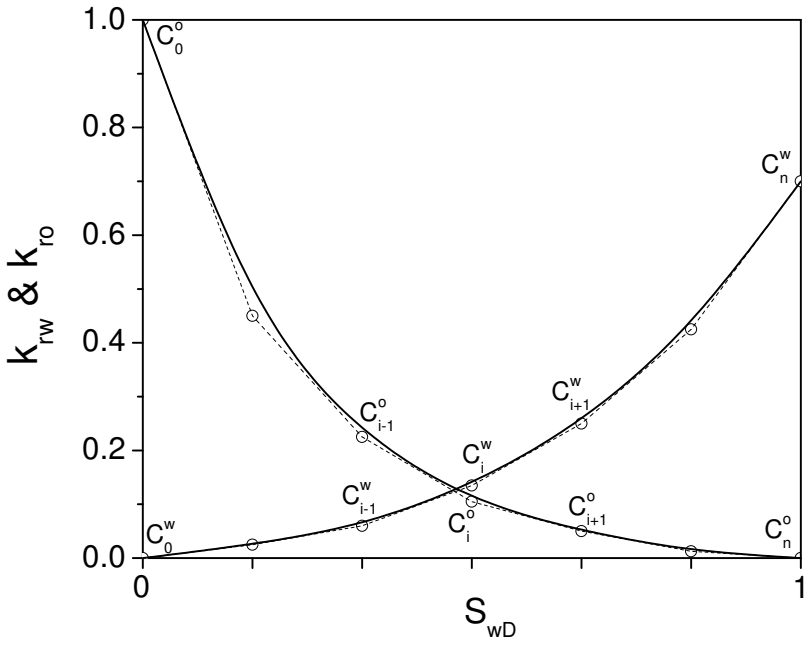

Figure 4.1: Relative permeability curves generated from specified control points.

Fig. 4.1 shows two B-spline approximations of relative permeability curves for the two sets of control points shown on the figure. In Fig. 4.1, the circles are the control points, C_i^m for $m = o, w$; the solid curves are the B-spline relative permeability curves, and the dashed lines passing through the control points form the control polyline. The B-spline is always within the control polyline, which means that the all points on the B-spline curve are always in the area generated by connecting all control points. Note that each B-spline curve passes through only two of its control points, the one labelled with the subscript zero and the one labelled with the subscript n. The cubic spline is "attracted" to the other control points but does not normally pass through them. For each curve, there are two control points which are not shown. For $m = o, w$ these points are defined by

$$C_{-1}^m = 2C_0^m - C_1^m, \tag{4.16}$$

and

$$C_{n+1}^m = 2C_n^m - C_{n-1}^m. \tag{4.17}$$

The last two definitions ensure that the B-spline curve for k_{rm} will pass through C_0^m and C_n^m (see Appendix A).

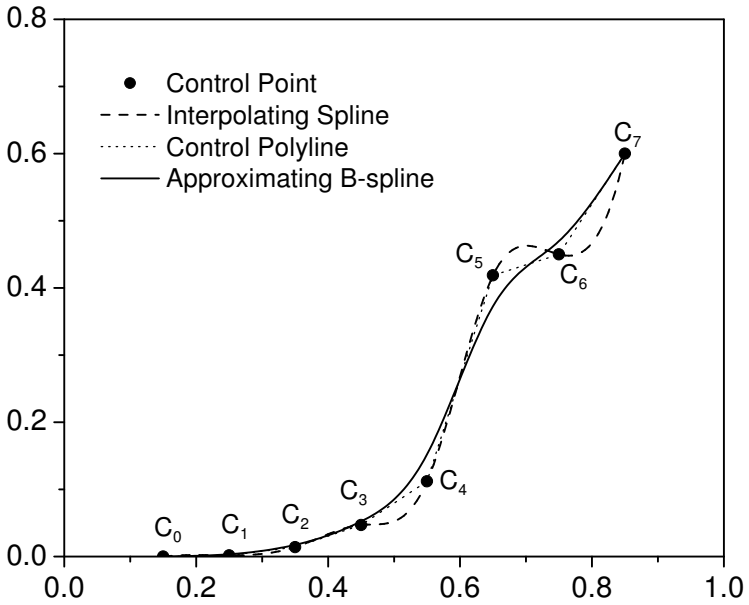

Figure 4.2: Approximating B-spline curve and interpolating spline curve.

The B-spline curve is a combination of a set of weighted control points. The adjustment of the control points makes it is easy to adjust the local shape of the relative permeability curves. When nonlinear regression is used to automatically estimate the relative permeabilities, it is easy to place conditions on the control points. This requirement to keep the relative permeability curves monotonic or convex conditions are naturally satisfied by the power law model of relative permeability curves for $n_o > 1$ and $n_w > 1$. For the B-spline model with the uniform knots, the monotonically increasing (decreasing)

control points implies that the approximating B-spline is monotonically increasing (decreasing) and convex control points implies that the approximating B-spline is convex. Using results from Lane and Resienfeld [34], it is possible to establish these results even when the knots are not uniform; see [25]. In Appendix A, the properties of monotony and convexity of B-spline relative permeability curves are proved based on the cubic B-spline. Fig. 4.2 shows a comparison of the approximating B-spline and interpolating spline. In this figure, the solid points are the control points. They are monotonically increasing. Correspondingly, their B-spline curve (solid curve) is also monotonically increasing. However, passing through the control points, the interpolating spline (the dashed curve) is not monotonically increasing as shown near the control point C_6 in Fig. 4.2.

4.2.1 Monotonicity and Convexity Constraints

If the relative permeability curves are not monotonic, then they are not meaningful, and will not be accepted for use in reservoir engineering or as input to a reservoir simulator. Thus, one wishes to introduce constraints to keep the B-spline approximations to relative permeability curves monotonic. This can be done by requiring that the control points are monotonic. Similarly, if desired, one can force the B-spline representation of a relative permeability curve to be convex by requiring the control points to be convex. This is a major advantage of B-spline approximations. If an interpolating cubic spline were used, the spline would not be guaranteed to be monotonic even when the function values at interpolation points are monotonic.

First, for the monotonic water relative permeability curve, it is required that the control points are monotonically increasing, i.e.,

$$C_0^w < C_1^w < \cdots < C_{i-1}^w < C_i^w < C_{i+1}^w < \cdots < C_n^w. \tag{4.18}$$

For the oil relative permeability curves, one wishes to require that the control points are monotonically decreasing, i.e.,

$$C_0^o > C_1^o > \cdots > C_{i-1}^o > C_i^o > C_{i+1}^o > \cdots > C_n^o. \tag{4.19}$$

To enforce these conditions, using the logarithm transform (see Chapter 5 and Section 5.5.2), the parameters C_i^w are transformed to a new set of parameters, x_i, $i = 1, 2, \cdots n$, which are defined by

$$\begin{cases} x_1 = \ln\left(\frac{C_1^w}{C_2^w - C_1^w}\right), \\ \\ x_i = \ln\left(\frac{C_i^w - C_{i-1}^w}{C_{i+1}^w - C_i^w}\right), \text{ for } 2 \leq i \leq n-1, \\ \\ x_n = \ln\left(\frac{C_n^w - C_{n-1}^w}{1 - C_n^w}\right). \end{cases} \tag{4.20}$$

This transformation maps C_i to the variable x_i. Optimization (matching of data) is done in terms of the transformed variables. Note that the inverse transformation is represented by the following system of equations:

$$e^{x_1} = \frac{C_1^w}{C_2^w - C_1^w}, 1 \leq i \leq n-1, \tag{4.21}$$

$$e^{x_i} = \frac{C_i^w - C_{i-1}^w}{C_{i+1}^m - C_i^w}, \text{ for } 1 \leq i \leq n-1, \tag{4.22}$$

and

$$e^{x_n} = \frac{C_n^w - C_{n-1}^w}{1 - C_n^w}. \tag{4.23}$$

Eqs. 4.21, 4.22, and 4.23, respectively, give

$$C_1^w = \frac{e^{x_1}}{1 + e^{x_1}} C_2^w, \tag{4.24}$$

$$C_i^w = \frac{e^{x_i}}{1+e^{x_i}} C_{i+1}^w + \frac{1}{1+e^{x_i}} C_{i-1}^w, \text{ for } 2 \leq i \leq n-1, \tag{4.25}$$

and

$$C_n^w = \frac{e^{x_n}}{1+e^{x_n}} + \frac{1}{1+e^{x_n}} C_{n-1}^w. \tag{4.26}$$

Since all the x_i's must be between $-\infty$ and ∞, it follows from Eqs. 4.24, 4.25 and 4.26, respectively, that

$$0 < C_1^w < C_2^w, \tag{4.27}$$

$$C_{i-1}^w < C_i^w < C_{i+1}^w, \text{ for } 2 \leq i \leq n-1, \tag{4.28}$$

and

$$C_{n-1}^w < C_n^w < 1. \tag{4.29}$$

Thus, the control points are monotonically increasing, which guarantees that the resulting B-spline approximation for k_{rw} is monotonically increasing.

Once we obtain new values of the x_i's at one iteration of the optimization process, we find the associated values of the control points by solving the system of equations given by Eqs. 4.24–4.26 which can be written in matrix form as

$$\begin{pmatrix} e^{x_1}+1 & -e^{x_1} & & & & \\ -1 & e^{x_2}+1 & -e^{x_2} & & & \\ & \ddots & \ddots & \ddots & & \\ & -1 & e^{x_i}+1 & -e^{x_i} & & \\ & & \ddots & \ddots & \ddots & \\ & & & -1 & e^{x_n}+1 \end{pmatrix} \begin{pmatrix} C_1^w \\ C_2^w \\ \vdots \\ C_i^w \\ \vdots \\ C_n^w \end{pmatrix} = \begin{pmatrix} 0 \\ 0 \\ \vdots \\ 0 \\ \vdots \\ e^{x_n} \end{pmatrix}. \tag{4.30}$$

As the coefficient matrix in the preceding equation is irreducibly diagonally dominant, the system of equations has a unique solution.

Treatment of the control points for the B-spline approximation of the oil relative permeability curve is similar except for the fact that the control points must be monotonically decreasing. Thus, the appropriate transformation of variables is defined by

$$\begin{cases} y_1 = \ln\left(\frac{C_1^o - C_2^o}{1.0 - C_1^o}\right); \\ \\ y_i = \ln\left(\frac{C_i^o - C_{i+1}^o}{C_{i-1}^o - C_i^o}\right), \qquad 2 \le i \le n-2; \\ \\ y_{n-1} = \ln\left(\frac{C_{n-1}^o - 0}{C_{n-2}^o - C_{n-1}^o}\right). \end{cases} \tag{4.31}$$

Thus, the inverse process of solving C_i^o based on a set of given y_i for knots of oil relative permeability curve can be done by solving Eq. 4.31 as

$$\begin{pmatrix} e^{y_1}+1 & -1 & & & & \\ -e^{y_2} & e^{y_2}+1 & -1 & & & \\ & \ddots & \ddots & \ddots & & \\ & -e^{y_i} & e^{y_i}+1 & -1 & & \\ & & \ddots & \ddots & \ddots & \\ & & & -e^{y_{n-1}} & e^{y_{n-1}}+1 \end{pmatrix} \begin{pmatrix} C_1^o \\ C_2^o \\ \vdots \\ C_i^o \\ \vdots \\ C_{n-1}^o \end{pmatrix} = \begin{pmatrix} e^{y_1} \\ 0 \\ \vdots \\ 0 \\ \vdots \\ 0 \end{pmatrix}. \tag{4.32}$$

Second, for convex relative permeability curves, control points must be convex or concave up, which means

$$\frac{C_{i+1}^m - C_i^m}{S_{wD,i+1} - S_{wD,i}} > \frac{C_i^m - C_{i-1}^m}{S_{wD,i} - S_{wD,i-1}}. \tag{4.33}$$

If the knots are uniform,

$$C_{i+1}^m - C_i^m > C_i^m - C_{i-1}^m, \tag{4.34}$$

for $m = o, w$, $i = 1, 2, \cdots, n-1$. Note that if we divide Eq. 4.34 by the uniform knot spacing, $\Delta u = S_{wD,i} - S_{wD,i-1}$, then the resulting equation represents the requirement that the slope of the line segment through the two points $(S_{wD,i-1}, C_{i-1}^m)$ and $(S_{wD,i}, C_i^m)$ is an increasing function of i. Thus, Eq. 4.34 is equivalent to the requirement that the slope of the polyline (in Fig. 4.1, the connected curve consisting of the dashed line segments through the control points) is monotonically increasing.

Eq. 4.34 can be used to obtain the following upper and lower bounds for C_i^m:

$$C_i^m < \frac{1}{2}(C_{i+1}^m + C_{i-1}^m), \text{ for } i = 1, 2, \cdots n-1, \tag{4.35}$$

and

$$C_i^m > 2C_{i-1}^m - C_{i-2}^m, \text{ for } i = 2, 3, \cdots n. \tag{4.36}$$

The preceding two equations effectively provide constraints for the control parameters that must be satisfied to ensure that the resulting B-splines are convex curves. For the water relative permeability curve, we set $C_0^w = 0$, set the lower bound for C_1^w to 0 and set the upper bound for C_n^w equal to 1. For oil relative permeability, we wish to fix the endpoint relative permeability equal to 1, which we do by fixing $C_0^o = 1$. We also set $C_n^o = 0$, set the upper bound for C_1^o equal to 1 and set the lower bound for C_{n-1}^o equal to zero.

To enforce convex relative permeability curves, it is required that the inequalities of Eqs. 4.35 and 4.36 are satisfied. As with the monotonicity condition, we can make a transformation to a new coordinate system can be make to ensure that the control points are convex. In this case, the appropriate transformation is

$$\begin{cases} x_1 = \ln\left(\frac{C_1^w}{\frac{1}{2}(C_2^w+0)-C_1^w}\right); \\ \\ x_i = \ln\left(\frac{C_i^w-(2C_{i-1}^w-C_{i-2}^w)}{\frac{1}{2}(C_{i+1}^w+C_{i-1}^w)-C_i^w}\right), \quad 2 \le i \le n-1; \\ \\ x_n = \ln\left(\frac{C_n^w-(2C_{n-1}^w-C_{n-2}^w)}{1-C_n^w}\right). \end{cases} \tag{4.37}$$

The equation for x_n can be obtained by setting $i = n$ and $C_{n+1}^w = 1$ in the second equation when $i = n$. Setting the value of $C_{n+1}^w = 1$ is used simply to provide an upper bound for the slope and is not the correct value of C_{n+1}^w. In fact, in order to force the approximating spline to pass through the control point C_n^w, the following must be satisfied:

$$C_{n+1}^w = 2C_n^w - C_{n-1}^w. \tag{4.38}$$

Similarly to ensure that the approximating spline pass through C_0^w, it is required that

$$C_{-1}^w = 2C_0^w - C_1^w. \tag{4.39}$$

These two requirements are valid for the cubic B-spline used in this research. Similar results apply to the control point parameterization of the oil relative permeability curve.

Optimization is applied to the transformed variables. After one iteration of the optimization algorithm, the new x_i values are transformed back to update the values of the control points by solving the following system of equations:

$$\begin{pmatrix} e^{x_1}+1 & -\frac{1}{2}e^{x_1} & & & & \\ -(\frac{1}{2}e^{x_2}+2) & e^{x_2}+1 & -\frac{1}{2}e^{x_2} & & & \\ 1 & -(\frac{1}{2}e^{x_3}+2) & e^{x_3}+1 & -\frac{1}{2}e^{x_3} & & \\ & \ddots & \ddots & \ddots & & \\ & 1 & -(\frac{1}{2}e^{x_i}+2) & e^{x_i}+1 & -\frac{1}{2}e^{x_i} & \\ & & \ddots & \ddots & \ddots & \\ & & 1 & -2 & e^{x_n}+1 \end{pmatrix} \begin{pmatrix} C_1^w \\ C_2^w \\ C_3^w \\ \vdots \\ C_i^w \\ \vdots \\ C_n^w \end{pmatrix} = \begin{pmatrix} 0 \\ 0 \\ 0 \\ \vdots \\ 0 \\ \vdots \\ e^{x_n} \end{pmatrix}. \quad (4.40)$$

For the oil relative permeability curve, C_0^o is set to 1, C_n^o is set to 0. Except for this change, the same log-transformation is used to define new variables in a way that guarantees that the approximating B-spline will be convex (concave up). The appropriate transformation is

$$\begin{cases} y_1 = \ln\left(\frac{C_1^o-(2C_2^o-C_3^o)}{\frac{1}{2}(C_2^o+1)-C_1^o}\right); \\ \\ y_i = \ln\left(\frac{C_i^o-(2C_{i+1}^o-C_{i+2}^o)}{\frac{1}{2}(C_{i+1}^o+C_{i-1}^o)-C_i^o}\right), \quad 2 \le i \le n-2; \\ \\ y_{n-1} = \ln\left(\frac{C_{n-1}^o-0}{\frac{1}{2}C_{n-2}^o-C_{n-1}^o}\right). \end{cases} \quad (4.41)$$

Given updated y_i's, updated values of the control points can be obtained by solving the following system of equations:

$$\begin{pmatrix} e^{y_1}+1 & -(\frac{1}{2}e^{y_1}+2) & 1 & & & \\ -\frac{1}{2}(e^{y_2}) & e^{y_2}+1 & -(\frac{1}{2}e^{y_2}+2) & 1 & & \\ & \ddots & \ddots & \ddots & & \\ & -\frac{1}{2}e^{y_i} & e^{y_i}+1 & -(\frac{1}{2}e^{y_i}+2) & 1 & \\ & & \ddots & \ddots & \ddots & \\ & & -\frac{1}{2}e^{y_{n-2}} & e^{y_{n-2}}+1 & -2 & \\ & & & -\frac{1}{2}e^{y_{n-1}} & e^{y_{n-1}}+1 \end{pmatrix} \begin{pmatrix} C_1^o \\ C_2^o \\ \vdots \\ C_i^o \\ \vdots \\ C_{n-2}^o \\ C_{n-1}^o \end{pmatrix} = \begin{pmatrix} \frac{1}{2}e^{y_1} \\ 0 \\ \vdots \\ 0 \\ \vdots \\ 0 \\ 0 \end{pmatrix}. \tag{4.42}$$

As noted previously, optimization is performed in terms of the x_i and y_i variables. Sensitivities are computed by a finite difference method. For example, to generate the sensitivity of a single predicted datum d_i to parameter x_j, we make a perturbation δx_j to x_j to obtain a new value $\hat{x}_j = x_j + \delta x_j$. If one wishes to generate monotonic relative permeability curves, one solves Eq. 4.30 for the new values of C_i^w corresponding to $\hat{x}_j$. If we require convexity, we solve Eqs. 4.40 and 4.42 instead of Eqs. 4.30 and 4.32. These control points give a new B-spline approximation for the water relative permeability curves, which is used to generate a new relative permeability table for running the reservoir simulator to generate new predicted data $d_i(\hat{x}_j)$ corresponding to the data $d_i = d_i(x_j)$ computed with the unperturbed value x_j. Then, the sensitivity of d_i to x_j is approximated by

$$s_{i,j} = \frac{d_i(\hat{x}_j) - d_i(x_j)}{\delta x_j}. \tag{4.43}$$

All sensitivities needed to compute the Gauss-Newton Hessian and the gradient of the objective function are computed in this way (see Chapter 5).

4.3 Relative Permeability Model from Capillary Pressure

Many studies (see references [17], [22], [14], [39] and [38]) indicate that there is a relationship between relative permeability and capillary pressure.

Based on the work of Corey [22] and Brooks [14] studies, the capillary pressure can be expressed as

$$p_c(S_w^*) = p_e(S_w^*)^{-1/\lambda}, \tag{4.44}$$

where, p_e is entry capillary pressure (threshold pressure) and λ is the pore size distribution index. The normalized water saturation, S_w^*, is defined by

$$S_w^* = \frac{S_w - S_{iw}}{1 - S_{or} - S_{iw}}. \tag{4.45}$$

The relative permeabilities of the water and oil phases are given by the following equations:

$$k_{rw}(S_w^*) = a_w(S_w^*)^{\frac{2+\lambda}{\lambda}}, \tag{4.46}$$

and

$$k_{ro}(S_w^*) = (1 - S_w^*)^2 \left[1 - (S_w^*)^{\frac{2+\lambda}{\lambda}}\right]. \tag{4.47}$$

From Eq. 4.44 we can note when S_w^* approaches to zero, the capillary pressure p_c could be infinite. So in practice, we introduce variable ϵ, a small value to adjust the maximum of p_c by

$$p_c(S_w^*) = p_e(S_w^* + \epsilon)^{-1/\lambda}. \tag{4.48}$$

The maximum of p_c should be $p_{c,max} = p_e(\epsilon)^{-1/\lambda}$. With ϵ fixed, the relative permeabilities and capillary pressure can be described by the model parameters S_{iw}, S_{or}, λ and p_e.

CHAPTER 5

MODEL PARAMETER AND HISTORY MATCHING

In this research the automatic history matching method (nonlinear regression) is applied to estimate model parameters, including the reservoir absolute permeability, well skin factor and parameters representing relative permeability curves. History matching is the process of changing model parameters to find a set of values that yield predicted data that matches observed data. The automatic history matching is accomplished by applying an optimization algorithm to minimize an objective function which is constructed by the data mismatch between predicted data and the observed data. In this chapter, the focus is on automatic history matching using the nonlinear regression. Model parameters will be discussed first and then the optimization method applied in this research will be introduced.

5.1 Model Parameter

For the synthetic examples presented here, the parameters that were estimated are absolute permeability, well skin factor and the parameters defining permeability curves. All other rock and fluid properties are assumed to be known. When estimating the skin factor at the wellbore, the radius of the skin zone is assumed to be known. Then the permeabilities in the reservoir and the damaged zone dominate the value of the skin factor. Based on the Hawkins' formula [28], the skin factor can be expressed as

$$s = \left(\frac{k}{k_s} - 1\right) \ln \frac{r_s}{r_w}, \tag{5.1}$$

where k and k_s are the permeabilities of reservoir and wellbore damaged zone, respectively; r_w and r_s are the radii of the wellbore and the damaged zone. During calculation, the permeability of the damaged zone is treated as a model parameter. At the end of the

estimation of model parameters, the skin factor is provided by Eq. 5.1.

In this research, different methods representing relative permeabilities are stated as in Chapter 4. According to the method used, different model parameters were used to describe the relative permeability curves. For the power law model (see Eqs. 4.1 and 4.2), the relative permeability curves are controlled by the end-point of water relative permeability, $a_w = k_{rw}(1 - S_{or})$, the exponent value of the water relative permeability curve, n_w, and the exponent value of oil relative permeability curve, n_o. As the flow equations involve only kk_{ro} and kk_{rw}, it is clear that data can only resolve effective permeabilities instead of absolute and relative permeabilies individually. The analysis of well test data can not uniquely resolve reservoir permeability k, the end-point relative permeability of the water phase a_w and the endpoint relative permeability of oil the phase $a_o = k_{ro}(S_{iw})$, but may be able to generate highly accurate estimates of ka_w and ka_o and effective permeability curves. Then the relative permeabilities could be obtained by normalizing the effective permeabilities by ka_o, endpoint oil effective permeability, which gives oil relative permeabilities equal to one at irreducible water saturation. So in this work, we simply set the end point of the oil phase relative permeabilities equal to 1, i.e., $a_o = 1$. We also attempted to consider irreducible water saturation, S_{iw}, and residual oil saturation, S_{or}, but we found that it is difficult to estimate them simultaneously. We give an explanation for that combining examples in Chapter 6. Thus we can have a total of seven model parameters for the power law model. The vector of model parameter, m, is given by

$$m = [k, s, a_w, n_w, n_o, S_{iw}, S_{or}]^T. \tag{5.2}$$

When the B-spline model is used to represent the relative permeability curves, a set of control points is used to adjust the shape of the relative permeability curves as stated in Chapter 4. The uniform cubic B-spline method is used to representing relative permeability curves in this research. For each relative permeability curve, the control points are distributed uniformly in a dimensionless water saturation domain, S_{wd},

defined in Eq. 4.8, and the control points adjust their values up or down in the relative permeability domain $k_r \in [0, 1]$. Obviously, the more control points we have, the more flexible it is for us to adjust the shape of the relative permeability curves, but it is more time consuming. Via extensive experimentation we have found that 7 control points represent each relative permeability curve well. Fig. 5.1 gives an example of the model parameter of control points that were used to represent the relative permeability by the B-spline model. As stated in the previous chapter, the B-spline curve is an approximate curve. It is not necessary that the B-spline curve passes through the control points, but we need to force the B-spline curves pass to through the end points of relative permeability, $k_{rw}(1 - S_{or})$ and $k_{ro}(S_{iw})$, and relative permeabilities of $k_{rw}(S_{iw}) = 0$ and $k_{ro}(1 - S_{or})$. In Fig. 5.1, One can see that the control points C_0^w and C_6^o are always equal zero in the relative permeability domain. Because it is assumed that the end point relative permeability of the oil phase equals 1, the control point C_0^o is always equal to 1 in this work. The adjustments of irreducible water saturation S_{iw} and residual oil saturation S_{or}

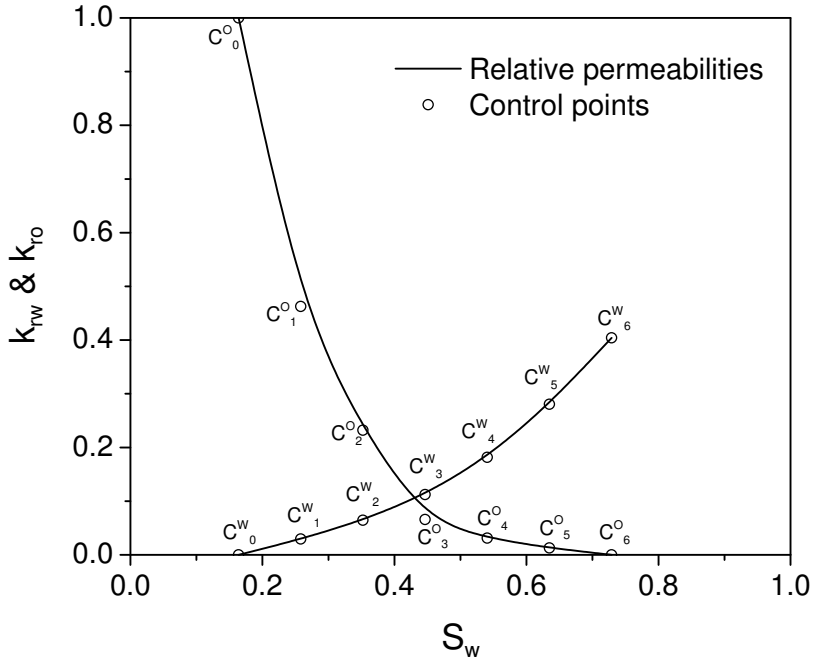

Figure 5.1: Model parameter of control points for B-spline relative permeability curves.

shift the control points left or right in the S_w domain although in the S_{wD} domain they

are fixed when the number of control points is given. So for the B-spline model of relative permeability curves, the total model parameters are expressed as

$$m = [k, s, C_1^o, C_2^o, C_3^o, C_4^o, C_5^o, C_1^w, C_2^w, C_3^w, C_4^w, C_5^w, C_6^w, S_{iw}, S_{or}]^T. \tag{5.3}$$

We introduced the relative permeability model generated from capillary pressure in Chapter 4. In this model, the parameters defining the capillary pressure curve and relative permeability curves are entry capillary pressure, p_e, rock pore size distribution index, λ, end point relative permeability of water phase, a_w, irreducible water saturation, S_{iw}, residual oil saturation, S_{or}, reservoir permeability, k, and skin factor, s. The model parameters of the relative permeabilities from capillary pressure are expressed by the vector m as

$$m = [k, s, a_w, p_e, \lambda, S_{iw}, S_{or}]^T. \tag{5.4}$$

5.2 Objective Function

In this research, the main aim is to find the model parameters m which generate the vector of predicted data

$$d_{\text{pred}} = g(m) \tag{5.5}$$

which is in good agreement with the observed data d_{obs}. If m is the true model, then the difference between d_{pred} and d_{obs} represents measurement error, i.e.,

$$e = d_{\text{obs}} - d_{\text{pred}}. \tag{5.6}$$

Assuming measurement error is random, $d_{\text{obs}} = d_{\text{pred}} - e$ is a random vector. If measurement errors are Gaussian, the probability density function (pdf) of d_{obs} for a given model m is expressed by

$$
\begin{aligned}
p(d_{\text{obs}}|m) &= a \exp\big(-\frac{1}{2}(d_{\text{pred}} - d_{\text{obs}})^T C_D^{-1}(d_{\text{pred}} - d_{\text{obs}})\big) \\
&= a \exp\big(-\frac{1}{2}(g(m) - d_{\text{obs}})^T C_D^{-1}(g(m) - d_{\text{obs}})\big),
\end{aligned}
\tag{5.7}
$$

where a is the normalizing constant defined by

$$
a = \frac{1}{(2\pi)^{\frac{N_d}{2}}\sqrt{\det C_D}}. \tag{5.8}
$$

C_D is an $N_d \times N_d$ data covariance matrix, d_{obs} is an N_d dimensional vector of observed data and d_{pred} is also an N_d dimensional vector representing the predicted data corresponding to the vector of model parameter m. Eq. 5.7 gives the likelihood of m given d_{obs}, which is expressed as

$$
l(m|d_{\text{obs}}) = a \exp\big(-\frac{1}{2}(g(m) - d_{\text{obs}})^T C_D^{-1}(g(m) - d_{\text{obs}})\big). \tag{5.9}
$$

The most likely estimate is the model that maximizes $l(m|d_{\text{obs}})$, i.e., the model that minimizes

$$
O(m) = \frac{1}{2}\big(g(m) - d_{\text{obs}})^T C_D^{-1}(g(m) - d_{\text{obs}})\big). \tag{5.10}
$$

In this work, it is assumed that bottom hole pressure measurements are the only data recorded during the injection and falloff periods, whereas, both bottom hole pressure and rate data are recorded as observed data for a production period conducted subsequent to the falloff period. Cumulative oil production as a function of time during the flow back or production period can also be used as observed data. In this case, the vector of observed data can be expressed by

$$d_{\text{obs}} = \begin{pmatrix} p_{\text{obs},1} \\ \vdots \\ p_{\text{obs},N_p} \\ Q_{\text{obs},1} \\ \vdots \\ Q_{\text{obs},N_q} \end{pmatrix}, \tag{5.11}$$

where Q_{obs} is observed cumulative oil production. When we consider both pressure and production data (cumulative oil production) are used as the observed data, data measurement errors are assumed to be independent random variables with mean zero and a prescribed variance, so the covariance matrix C_D is a diagonal matrix represented by

$$C_D = \begin{pmatrix} \sigma^2_{p,1} & & & & & & \\ & \ddots & & & & & \\ & & \sigma^2_{p,N_p} & & & & \\ & & & \sigma^2_{Q,1} & & & \\ & & & & \ddots & & \\ & & & & & \sigma^2_{Q,N_q} \end{pmatrix}. \tag{5.12}$$

The objective function, Eq. 5.10, to be minimized can be written as

$$\begin{aligned} O(m) = & \frac{1}{2} \sum_{i=1}^{N_p} \frac{\left(p_{\text{pred},i}(m) - p_{\text{obs},i}\right)^2}{\sigma^2_{p,i}} \\ & + \frac{1}{2} \sum_{j=1}^{N_q} \frac{\left(Q_{\text{pred},j}(m) - Q_{\text{obs},j}\right)^2}{\sigma^2_{Q,j}}. \end{aligned} \tag{5.13}$$

Throughout, $p_{\text{pred},i}$ is the "ith" predicted pressure data (based on a given vector of model parameters) corresponding to the ith observed pressure data $p_{\text{obs},i}$ and $Q_{\text{pred},j}$ represents the "jth" predicted production data (cumulative oil in STB) corresponding to $Q_{\text{obs},j}$, the jth "observed" value of cumulative oil production during the flow back period. The $\sigma_{p,i}$'s, and $\sigma_{Q,j}$'s represent, respectively, the standard deviations of pressure measurement errors

and cumulative oil production measurement errors. Measurement errors are assumed to be Gaussian. The means of all measurement errors are assumed to be equal to zero and uncorrelated. All σ_p's are in psi and all σ_Q's are in STB.

The examples presented here consider only synthetic data which are generated by adding noise (measurement error) to pressure and cumulative oil production data generated from a reservoir simulator with the true parameters as input. For these data, all $\sigma_{p,i}$ are equal. To model the measurement error in cumulative oil production, we assume that the noise is directly related to the magnitude of cumulative oil production, i.e., we specify a relative noise level by

$$\sigma_{Q,i} = \alpha Q_{o,i}, \tag{5.14}$$

for all i, where α is a constant and $Q_{o,i}$ is the true cumulative oil production. We also specify a minimum value $\sigma_{Q,min}$ and a maximum value for $\sigma_{Q,max}$. If the value of $\sigma_{Q,i}$ computed from Eq. 5.14 is less than $\sigma_{Q,min}$, $\sigma_{Q,i}$ is automatically set equal to $\sigma_{Q,min}$. If the value of $\sigma_{Q,i}$ computed from Eq. 5.14 is greater than $\sigma_{Q,max}$, $\sigma_{Q,i}$ is automatically set equal to $\sigma_{Q,max}$.

5.3 Optimization Algorithm

In this research, the gradient based optimization algorithms (see [59, 40, 62]), the Levenberg-Marquardt (LM) (see [36, 41, 26, 43]) method is applied to minimize the objective function of Eq. 5.10. The typical rapid convergence of the Gauss-Newton and the Levenberg-Marquardt methods results from using the curvature information represented by the second derivative of the objective function. In order to avoid an nonphysical meaning model parameter during the the optimization, a logarithm transform, changing the constrained optimization to unconstrained optimization, is also introduced.

5.3.1 Gradient Based Optimization–Levenberg-Marquardt Method

During iterations of the optimization process to minimize the objective function (Eq. 5.10), let m^k be the most recent estimate of the model m that minimizes $O(m)$.

When $O(m)$ is approximated by the second order truncated Taylor's expansion about m^k, we have

$$O(m) = O(m^k) + (\nabla O(m^k))^T \delta m + \frac{1}{2}\delta m^T \big[\nabla \cdot (\nabla O(m^k))^T\big]\delta m, \tag{5.15}$$

where,

$$\delta m = m - m^k. \tag{5.16}$$

The Hessian matrix, $H(m)$, is defined by

$$H(m) = \nabla \cdot (\nabla O(m))^T. \tag{5.17}$$

In Eq. 5.15, with the respect to m^k, the Hessian matrix can be expressed as

$$H^k = \nabla \cdot (\nabla O(m^k))^T. \tag{5.18}$$

Taking the gradient of $O(m)$ in Eq. 5.15 with respect to m, we have

$$\begin{aligned} \nabla O(m) &= \nabla \delta m^T \big[\nabla O(m^k)\big] + \frac{1}{2}\big[\nabla \delta m^T (H^k \delta m) + \nabla (m^T {H^k}^T)\delta m\big] \\ &= \nabla O(m^k) + \frac{1}{2}(H^k \delta m + {H^k}^T \delta m). \end{aligned} \tag{5.19}$$

H^k is a symmetric matrix, so Eq. 5.19 becomes

$$\nabla O(m) = \nabla O(m^k) + H^k \delta m. \tag{5.20}$$

If m minimizes $O(m)$, then

$$\nabla O(m) = 0. \tag{5.21}$$

Then Eq. 5.20 can be rearranged to yield

$$H^k \delta m = -\nabla O(m^k). \tag{5.22}$$

During the iteration of optimization, Eq. 5.22 is usually written as

$$H^k \delta m^{k+1} = -\nabla O(m^k), \tag{5.23}$$

and the update of model m is

$$m^{k+1} = m^k + \delta m^{k+1}. \tag{5.24}$$

This gradient based optimization is called Newton's method.

According to the objective function, Eq. 5.10, in this research, the gradient of the objective function can be easily obtained, and is given by

$$\nabla O(m) = G^T C_D^{-1}\big(g(m) - d_{\text{obs}}\big). \tag{5.25}$$

The second derivative of the objective function, the Hessian matrix of Eq. 5.17, can be written as

$$\begin{aligned} H(m) &= \nabla\big[G^T C_D^{-1}\big(g(m) - d_{\text{obs}}\big)\big]^T \\ &= \nabla\big[\big(g(m) - d_{\text{obs}}\big)^T C_D^{-1} G\big] \\ &= G^T C_D^{-1} G + \nabla G^T C_D^{-1}\big(g(m) - d_{obs}\big) \end{aligned} \tag{5.26}$$

where, in these equations, G denotes the matrix of sensitivity coefficients, i.e., the derivative of the predicted data $g(m)$ with respect to model parameters m. G^T is given by

$$G^T = \begin{pmatrix} \frac{\partial}{\partial m_1} \\ \vdots \\ \frac{\partial}{\partial m_{N_m}} \end{pmatrix} \begin{pmatrix} g_1 & \cdots & g_{N_d} \end{pmatrix} = \nabla g^T, \tag{5.27}$$

where N_m is the number of model parameters and N_d is the number of data to be matched. A sensitivity coefficient, $G_{i,j}$ is a measure of how strongly the change in the data, $d_{\text{pred},i} =$

$g_i(m)$, is affected by the change in the model parameter m_j. In Eq. 5.26, the calculation of gradient of G is impractical in practice. In the Gauss-Newton method, the second term in Eq. 5.26 is ignored and the Hessian matrix is approximated by

$$H(m) \approx G^T C_D^{-1} G. \tag{5.28}$$

Although $H(m)$ is theoretically positive semi-definite, with the numerical optimization process, the approximate Hessian matrix could be singular. The Levenberg-Marquardt method provides a way to handle these problems. Using the Levenberg-Marquardt method, the iteration of optimization in Eq. 5.23 is represented by

$$\big(\lambda I + H^k(m^k)\big)\delta m^{k+1} = -\nabla O(m^k), \tag{5.29}$$

where $\lambda > 0$ is the Levenberg-Marquardt parameter, and I is the identity matrix. λI alters the Hessian matrix H to be positive definite.

Depending on the magnitude of λ, the method varies smoothly between two algorithms: Newton's method as $\lambda \to 0$ and the steepest descent method as $\lambda \to \infty$. At the beginning of the optimization, we take the initial value of λ to be a large value. Some authors (see [1, 9]) consider the value of the objective function and the number of observed data and give the initial value of λ. In this research, it was found that the problem is strongly ill-conditioned by investigating the Euclidean condition number [42] of the Hessian H. For a real symmetric positive definite matrix A, the Euclidean condition number is defined by

$$\kappa(A) = \|A\|_2 \|A^{-1}\|_2 = \frac{\lambda_{\max}}{\lambda_{\min}}. \tag{5.30}$$

The Euclidean condition number of the Gauss Newton Hessian was found to typically be above 10^8 in the examples considered. We select the magnitude of the largest eigenvalue λ_1 as the initial Levenberg-Marquardt parameter λ_0 with a typical value of 10^7. In the iteration of optimization, for a new iteration model parameter m^{k+1}, such that $O(m^{k+1}) > O(m)$, then m^{k+1} is not accepted as the new estimate of the model parameter and the

Levenberg-Marquardt parameter λ is increased by a factor of 10 and the iteration of Eqs. 5.23 and 5.24 is recalculated. If $O(m^{k+1}) < O(m^k)$, then λ is divided by a factor of 10 and this new iteration model parameter m^{k+1} is accepted. The above process is repeated until convergence is reached.

5.3.2 Logarithm of Model Parameters

When minimizing $O(m)$, it is possible to obtain unreasonable or nonphysical values of model parameters if the Hessian is ill-conditioned, i.e., if λ_k becomes small, so that $\lambda_k I + H_k$ is poorly conditioned. To avoid this, one needs to impose constraints on the model parameters. For example, one wishes to require that permeabilities are positive if that S_{iw} and S_{or} are positive and less than unit, and that a_w is the power law for relative permeability is such that $0 < a_w \leq 1$. To do so, Gao and Reynolds [27] introduced a logarithmic transformation to replace each model parameter m_i by a new parameter x_i. If m_i is constrained between a minimum value $m_{i,min}$ and a maximum value $m_{i,max}$, then x_i is given by

$$x_i(m_i) = \ln\left(\frac{m_i - m_{i,min}}{m_{i,max} - m_i}\right). \tag{5.31}$$

As shown in Fig. 5.2, this means $m_i = m_{i,min}$ is mapped to $x_i = -\infty$ and $m_i = m_{i,max}$ corresponds to $x_i = +\infty$. Also note that we can solve Eq. 5.31 for m_i to obtain either of the two following equivalent expressions,

$$m_i(x_i) = \frac{\exp(x_i)m_{i,max} + m_{i,min}}{1 + \exp(x_i)}, \text{ for } x_i < 0, \tag{5.32}$$

and

$$m_i(x_i) = \frac{\exp(-x_i)m_{i,min} + m_{i,max}}{1 + \exp(-x_i)}, \text{ for } x_i > 0. \tag{5.33}$$

The choice between Eqs. 5.32 and 5.33 is made to control computational error. For the examples presented here, some of the maximum and minimum values of the model parameters are shown in Table 5.1. The maximum and minimum values of model parameters could be adjusted based on one's expectation of reasonable values. Using

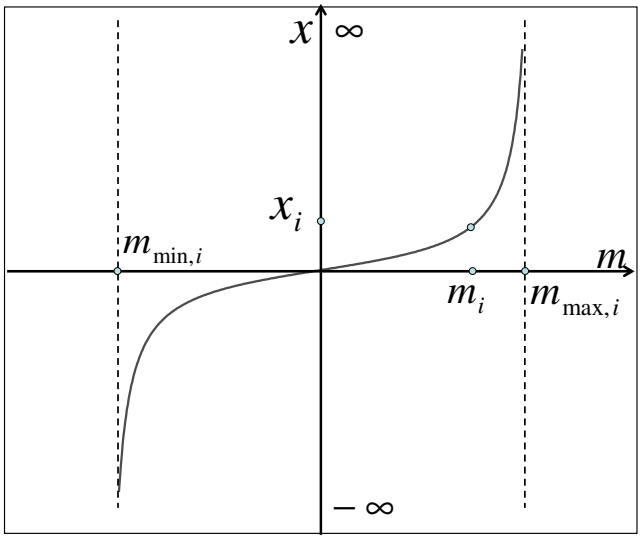

Figure 5.2: Logarithm transform from m domain to x domain.

the chain rule, one obtains the following relationship between sensitivities of a predicted datum, $g_i(m)$, to model parameters before and after the logarithmic transform as

$$\frac{\partial g_i(m)}{\partial m_i} = \frac{\partial g_i(m)}{\partial x_i}\frac{\partial x_i}{\partial m_i} = \frac{\partial g_i(m)}{\partial x_i}\frac{m_{i,max} - m_{i,min}}{(m_{i,max} - m_i)(m_i - m_{i,min})}, \tag{5.34}$$

and

$$\frac{\partial g_i(m)}{\partial x_i} = \frac{\partial g_i(m)}{\partial m_i}\frac{\partial m_i}{\partial x_i} = \frac{\partial g_i(m)}{\partial m_i}\frac{(m_{i,max} - m_i)(m_i - m_{i,min})}{m_{i,max} - m_{i,min}}. \tag{5.35}$$

After the logarithmic transform, the new model parameters are estimated by an optimization algorithm. At the end of each iteration of optimization, we apply the inverse logarithmic transform to calculate the original parameters for the simulator run.

Parameter	$k(md)$	$k_s(md)$	a_w	n_w	n_o	S_{iw}	S_{or}
Maximum	4000	4000	1.0	4.5	4.5	0.45	0.45
Minimum	5	5	0.05	0.5	0.5	0.05	0.05

Table 5.1: Maximum and minimum values of model parameters

In the process of using the Levenberg-Marquardt method to minimize the objective

function, because the new model parameters based on logarithmic transform are involved, one iteration of the Levenberg-Marquardt method can be represented by the following equations:

$$\left(\lambda I + H^k(x^k)\right)\delta x^{k+1} = -\nabla O(x^k), \tag{5.36}$$

$$x^{k+1} = x^k + \delta x^{k+1} \tag{5.37}$$

where H is the Hessian matrix. Using the new model parameter x in the logarithm transform domain, the Hessian matrix H and sensitivity coefficient G can be expressed by

$$H = G^T C_D^{-1} G, \tag{5.38}$$

and

$$G^T = \nabla_x(g^T(x)) = D_x \nabla_m \left([g(m)]^T \right), \tag{5.39}$$

$$G = \left(\nabla_x(g^T(x))\right)^T = \left(\nabla_m \left([g(m)]^T \right)\right)^T D_x, \tag{5.40}$$

where D_x is a $N_m \times N_m$ diagonal matrix with its entry equal to

$$\begin{aligned} d_{x,i} &= \frac{\partial m_i}{\partial x_i} \\ &= \frac{(m_{max,i} - m_i)(m_i - m_{min,i})}{m_{max,i} - m_{min,i}}. \end{aligned} \tag{5.41}$$

When the new parameter x is obtained, it can be transformed back to model parameter m by inverse transform Eqs. 5.32 and 5.33.

5.3.3 Sensitivity Analysis of Observed Data to Model Parameter

As stated above, the sensitivity coefficients reflect how strongly the change in the data is affected by the change in the model parameter. If one cannot calculate the sensitivity coefficients accurately enough, it is difficult to obtain the correct gradient (and

Hessian) for optimization. If it is possible, one should calculate the sensitivity coefficient analytically, but this is sometimes difficult to obtain the analytical sensitivity coefficient. For example, it is difficult for us to calculate the sensitivity coefficient of the pressure data to a control point of the relative permeability curves. In this work, the finite difference method is applied to calculate the sensitivity coefficient. For example, to generate the sensitivity of all predicted data $d_{\text{pred},i},\ i = 1, 2, \cdots, N_d$, to parameter m_j, we make a perturbation δm_j to m_j to obtain a new value $\hat{m}_j = m_j + \delta m_j$. Then the sensitivity of $d_{\text{pred},i}$ to m_j is approximated by

$$\frac{\partial d_{\text{pred},i}}{\partial m_j} = \frac{d_{\text{pred},i}(\hat{m}_j) - d_{\text{pred},i}(m_j)}{\delta m_j}, \quad 1 \leq i \leq N_d. \tag{5.42}$$

The appropriate size of the perturbation was chosen based on the previous experiments (see reference [21]). A relative perturbation size was used for model parameters. The following were used: 0.5 percent for permeability, 0.5 percent for end-point water relative permeability, 5 percent for exponent values of the power law model relative permeability curves and 20 percent for irreducible water saturation and residual oil saturation. It has been stated that the optimization is implemented in the unconstrained logarithm domain. So when the sensitivity coefficient is obtained, one can calculate the sensitivity coefficient in the logarithm domain by Eq. 5.35. All sensitivities needed to compute the Gauss-Newton Hessian and the gradient of the objective function are calculated in the same way. If convex (concave up) relative permeability curves are desired, the procedure is the same but the relation between control points and transformed variables is different, as discussed in Chapter 4.

The results show that the different types of observed data and the data from different periods (injection, falloff and production) have different sensitivities. Figs. 5.3-5.5 demonstrate the sensitivities of the pressure response to some model parameters based on a 5-hour injection, 5-hour falloff and 14-hour production test. The x-axis is the time t from the beginning of the test, so the falloff period corresponds to $5 < t < 10$. In Fig. 5.3, typical sensitivities of the pressure response to logarithm permeabilities are shown. The

sensitivities in the falloff are the smallest. At the end of injection and at the end of falloff, the sensitivities tend to flat constant values, because late time data reflect single phase properties as has been shown by the diagnostic plots (see Eqs. 1.1 and 1.2). So the later time pressure data from injection/falloff are able to resolve relative endpoint permeabilities and absolute permeabilities. At late production time, the sensitivities also show constant values because we have produced virtually all injected water.

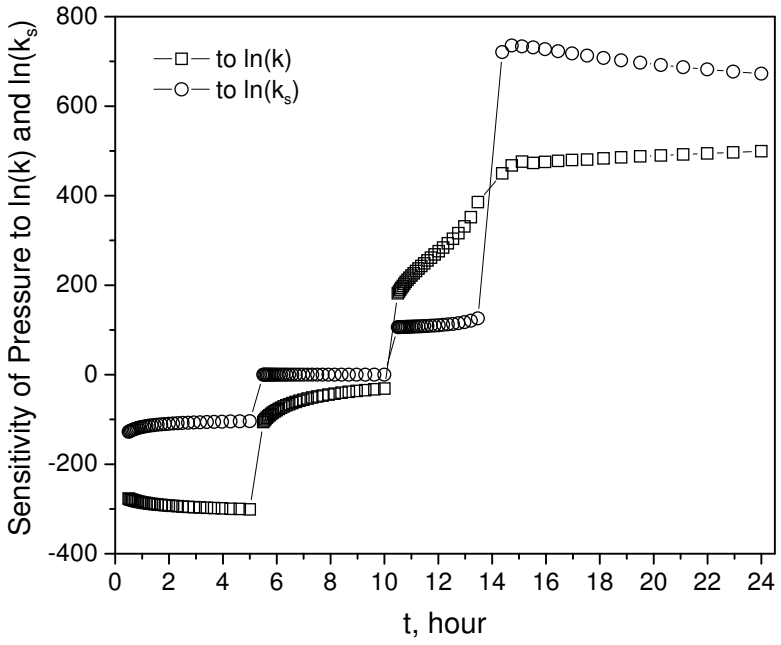

Figure 5.3: Sensitivity of pressure to permeabilities.

Fig. 5.4 displays the sensitivity of the pressure response to the logarithm exponent values of power law relative permeability curves. The exponent values control the shape of the relative permeability curves. In Fig. 5.4, the sensitivities have the largest values during the production and change greatly when oil flows back to the well from 13 hours to 15 hours. That indicates that the pressure data from production can significantly improve the estimates of the shape of relative permeability curves.

Fig. 5.5 shows the sensitivities of pressure to the control points in the log domain during the 24 hour injection/falloff/production test to the log-transformed parameters. Shortly after the beginning of falloff, all sensitivities become zero and remain zero through-

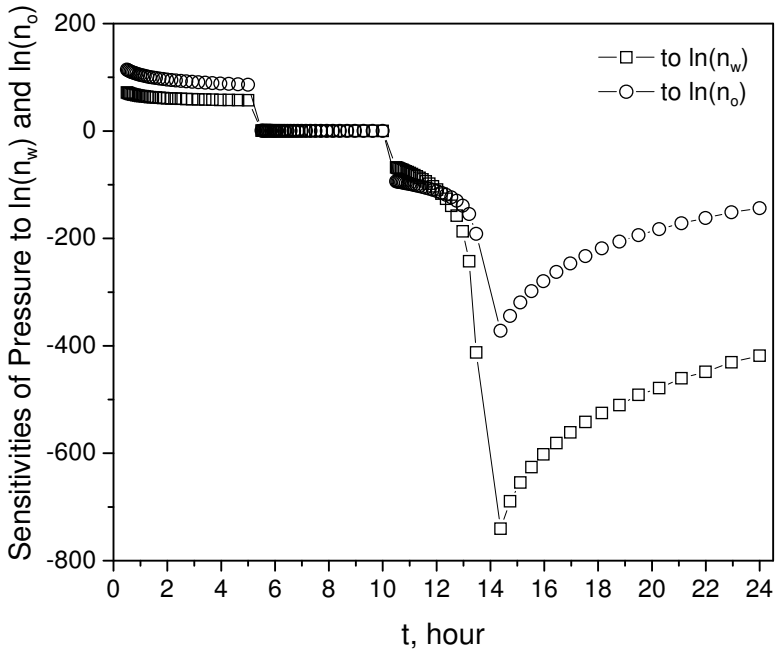

Figure 5.4: Sensitivity of pressure to exponent values of relative permeabilities, power law model.

out the shutin period. This is as expected from our previous discussion because falloff data resolves only k because oil relative permeability at S_{iw} is always equal to 1. Also the injection time was short, so the zero rate propagates through the water bank almost immediately after shutin. The dashed curves indicate sensitivities to the x_i's (log transforms of the control points for the water relative permeability curve) and the solid curves, the sensitivities to the y_i's (log transforms of the control points for the oil relative permeability curve). Perturbing an x_i (or y_i) in general changes all non-fixed control points for the water (oil) relative permeability curve and hence changes the whole curve. Because both end points of the oil relative permeability curve are fixed, the magnitude of the sensitivity of wellbore pressure to the x_i's is larger than its sensitivity to the y_i's throughout the injection period and throughout most of the production period. Near the end of the production period, the sensitivity of pressure to relative permeability becomes zero because at this time, only oil is flowing in the reservoir. Recall that the injection rate is fixed. Thus, sensitivities are negative during injection because increasing the total mobility enables the rate to be maintained with a lower injection pressure. During pro-

duction, increasing total mobility allows production at the specified constant total rate with a higher wellbore pressure (smaller pressure drop) so sensitivities are positive.

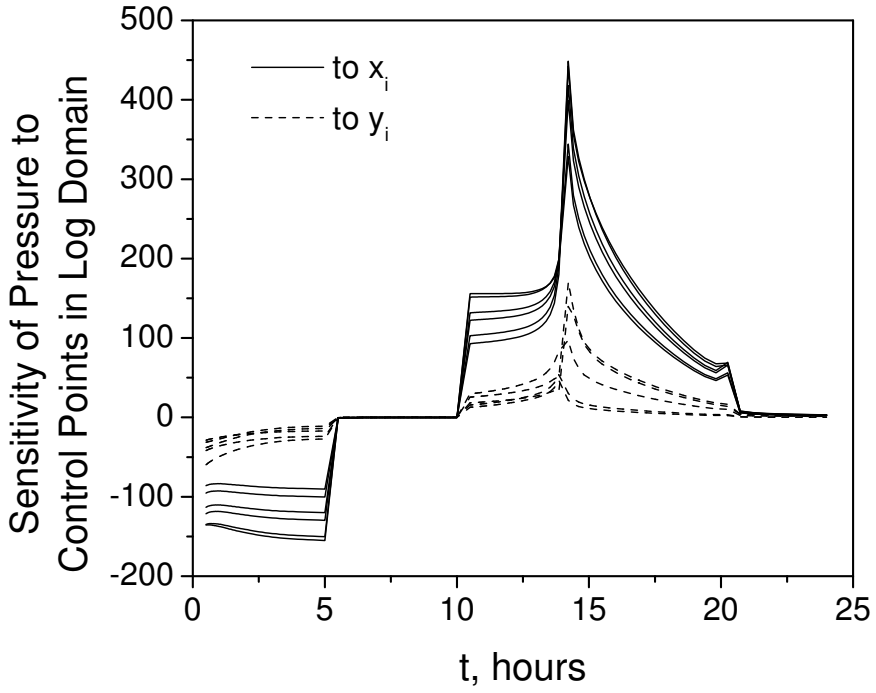

Figure 5.5: Sensitivity of pressure data to log-transformed control points, B-spline model.

In this research, the rate data during production are also considered for estimating the model parameters. Figs. 5.6-5.8 compare the sensitivities of oil production rate and cumulative oil production to the exponent values of power law relative permeability curves. In Chapter 3.2, we showed that there is still a saturation front (shock), which gives a singularity for $\frac{\partial \lambda_t(r,t)}{\partial \ln(\Delta t)}$, when oil flows back to the well during production. Correspondingly, the oil production rate has a sharp change (shown in Fig. 5.6) around the oil breakthrough time of 12.5 hours. On the other hand, the cumulative oil production changes smoothly in Fig. 5.6. The sharp change of oil production rate while oil is flowing back gives an extremely high value of the sensitivity of oil the production rate to logarithm exponent values of relative permeability curves at the time of oil breakthrough in Fig. 5.7. But sensitivities at other times are small. In the practice of inverse regression, this extremely high sensitivity is difficult to be computed accurately with a finite difference method and highly inaccurate values can introduce errors in the optimization

process. The sensitivities of cumulative oil production to exponent values of relative permeability curves show smoother variations than those of oil production rate as shown in Fig. 5.8. Thus, we employ the cumulative oil production rather than oil production or water cut during production as observed data in addition to bottomhole pressure data from injection, falloff and production.

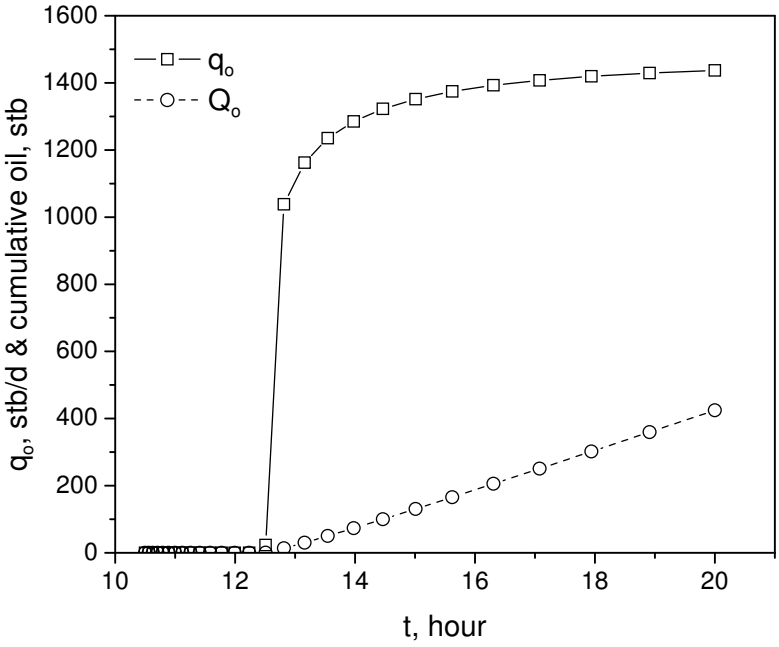

Figure 5.6: Oil production rate and cumulative production oil during production, power law relative permeabilities.

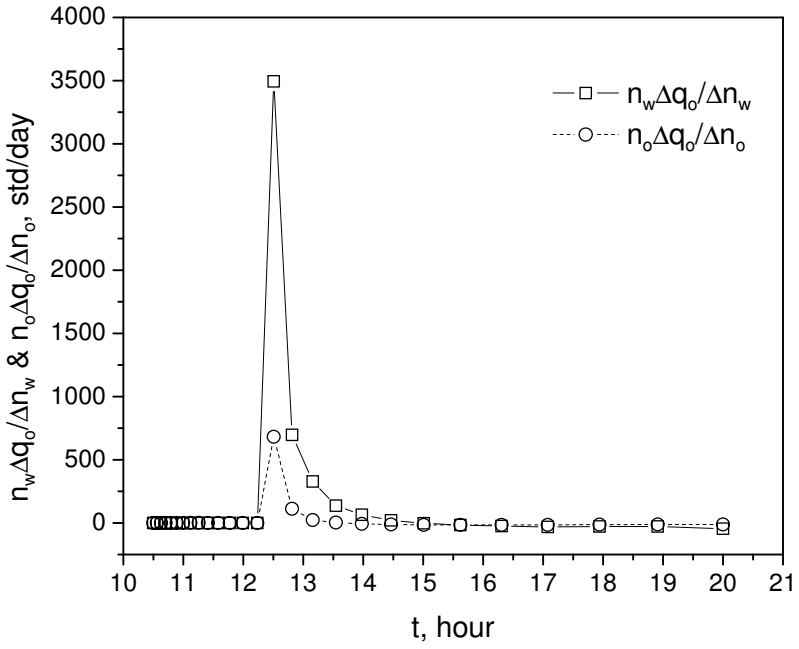

Figure 5.7: Sensitivity of oil production data to logarithm exponent value of power law relative permeabilities.

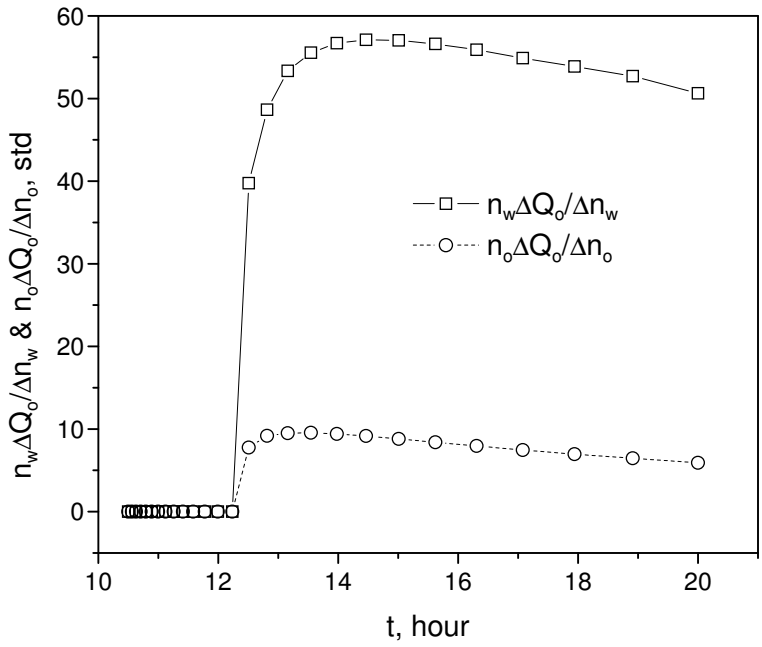

Figure 5.8: Sensitivity of cumulative oil production data to logarithm exponent value of power law relative permeabilities.

5.3.4 Convergence of Optimization

In this work, two criteria to determine the convergence of the optimization algorithm were applied. One is based on the change in the vector of model parameters and is given by

$$\max_i \frac{\left|m_i^{k+1} - m_i^k\right|}{\left|m_i^k\right| + 10^{-14}} < \epsilon_1, \tag{5.43}$$

and the other is based on the change in the objective function and is given by

$$\frac{\left|O(m^{k+1}) - O(m^k)\right|}{\max\left(\left|m_i^{k+1}\right|, 1\right)} < \epsilon_2. \tag{5.44}$$

where, the terms ϵ_1 and ϵ_2 are convergence tolerances, and we give them values of 0.001 and 0.1, respectively. In this work, both criteria must be satisfied for the optimization to converge. Also, a maximum of 100 iterations is allowed.

CHAPTER 6

EXAMPLES OF ESTIMATES OF RELATIVE PERMEABILITIES

This chapter shows some synthetic cases and the results of estimate of relative permeabilities and other model parameters, as stated in chapter 4, three models for representing relative permeabilities were applied in the synthetic cases. The data from different periods of the IFPT were studied with respect to the reliability of estimating the relative permeabilities by using data from different time periods. In this research, the nonlinear regression was used to estimate relative permeabilities and other model parameters based on either using the reservoir simulator (IMEX) as a forward model or our approximate analytical solution of the pressure response from different periods of the IFPT. Cases with different fluid mobility ratios, favorable and unfavorable, are also studied. Considering application of the IFPT in the field case, the effects from the horizontal heterogeneity of reservoir permeability, hysteresis of relative permeability and fluctuation of flow rate during the IFPT were simulated and studied for synthetic cases. For all synthetic cases, the observed data used in this research were after 0.5 hours after a rate change.

6.1 Estimate of Relative Permeabilities Based on the Power Law Model

Results from cases using the power law model to estimate the relative permeabilities and other model parameters are shown in this section. We investigated the flexibility of the power law model by matching the observed data generated by relative permeabilities that did not fit the power low model. The simulator IMEX is used as a forward model for all cases in this section.

6.1.1 *Estimate Based on Data from the IFPT*

Here, we used the power law relative permeability model in the nonlinear regression to match the observed pressure data generated using the power law model relative permeability curves as the true relative permeability curves. Table 6.1 gives the true values of k and s, and some parameters for reservoir simulation. For the true power law

Property	Value
r_e	6800 ft
h	60 ft
r_w	0.350 ft
r_s	1.264 ft
k	372 md
k_s	74.4 md
Skin factor, s	5.14
S_{iw}	0.164
S_{or}	0.271
μ_o	5.1 cp
μ_w	0.516 cp
$\hat{\lambda}_w$	0.73
$\hat{\lambda}_o$	0.18
Endpoint mobility ratio, $\hat{M}$	4.00
p_i	2500 psi
ϕ	0.2
B_o	1.03 RB/STB
B_w	1.02 RB/STB
c_o	8.0×10^{-6} psi^{-1}
c_w	3.02×10^{-6} psi^{-1}
Injection Rate, q_{inj}	3000 RB/Day
Production Rate, $q_t(r_w)$	3000 RB/Day

Table 6.1: Reservoir, rock and fluid properties for simulation of well test.

model relative permeability, endpoint value of water phase relative permeability curve is $a_w = 0.5$; exponent values of water and oil relative permeability curves are $n_w = 2.0$ and $n_o = 3.0$, respectively; irreducible water saturation is $S_{iw} = 0.164$ and residual oil saturation is $S_{or} = 0.271$.

Estimate Based on Bottomhole Pressure: In this case, the irreducible water saturation S_{iw} and residual oil saturation *are* assumed to be known. We used the pressure

data from all periods of injection(5 hours)/falloff(5 hours)/production(14 hours) as the observed data. The observed data was generated by added noise to data generated from the reservoir simulator with noise generated from a Gaussian distribution with mean zero and a standard deviation of 0.25 psi. The noise is uncorrelated in all examples. Unless stated otherwise all observed pressure data were generated with this noise model. After applying nonlinear regression, Fig. 6.1 shows that bottomhole pressure predicted with our estimated model parameters (solid curve) matches the observed pressure data (circular data points) well. As shown in Fig. 6.2, our estimates of relative permeability curves (curves through circular data points) mirror the true relative permeability curves (solid curves). Table 6.2 shows that the estimates of all model parameters provide good estimates of the true values.

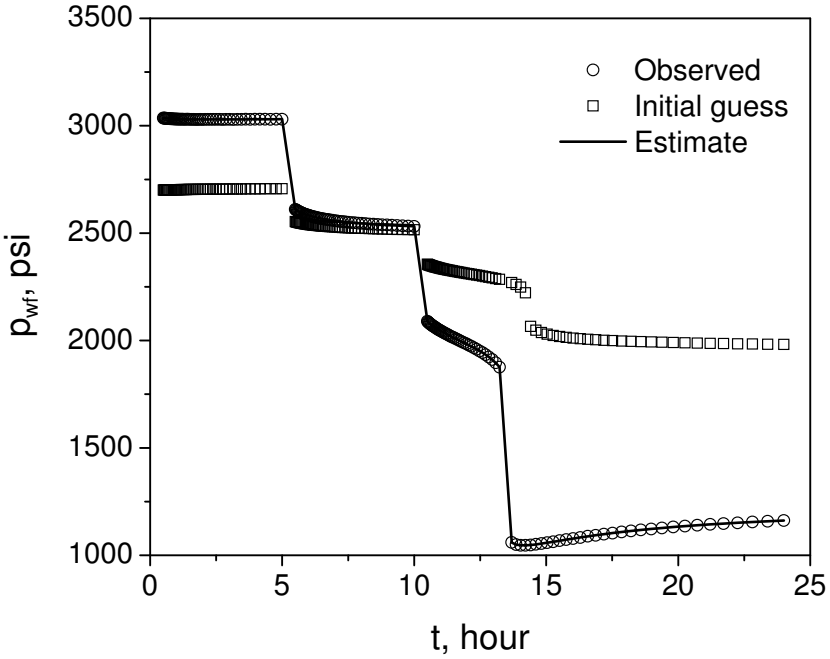

Figure 6.1: Pressure data match based on the power law model matching observed data from the true power law relative permeabilities, $\hat{M} = 4.0$.

Estimate Based on Pressure and Cumulative Oil: This case shows the results from matching observed pressure data and cumulative oil data. The pressure data are from all three periods of injection, falloff and production. The cumulative oil data during the

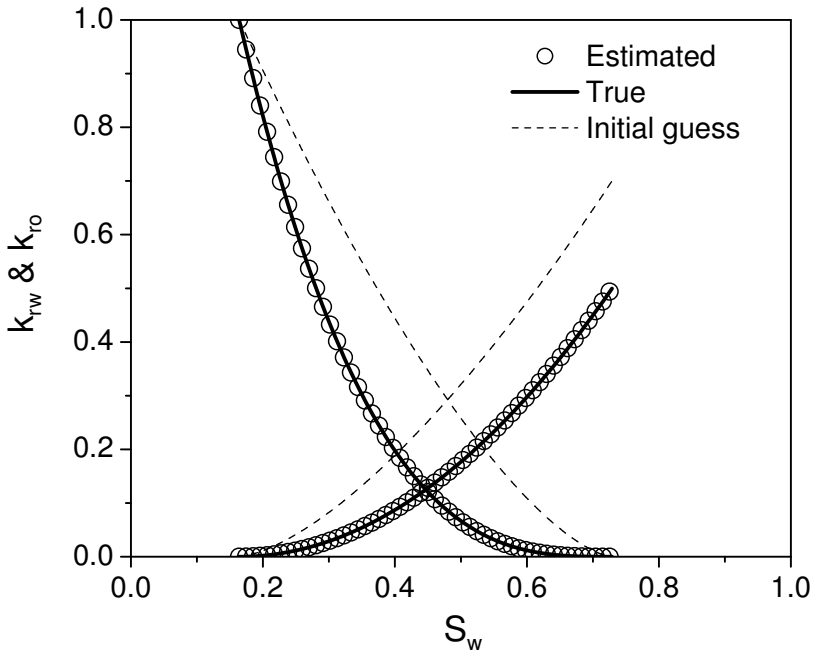

Figure 6.2: Estimate of relative permeabilities based on power law model matching observed data from the true power law relative permeabilities,, $\hat{M} = 4.0$.

Model Parameter	k (md)	k_s (md)	s	a_w	n_w	n_o
True	372	74.4	5.14	0.5	2.0	3.0
Estimate	389.6	74.9	5.39	0.5	2.0	3.0
Initial Guess	800	200	3.85	0.7	1.5	2.0

Table 6.2: Estimate of model parameters based on power law model matching pressure data from injection/falloff/production.

production were generated from the true data by adding noise based on $\sigma_{Q,min} = 0.1$ RB/Day and $\sigma_{Q,max} = 5$ RB/day as we stated in Chapter 5. In this case, the irreducible water saturation S_{iw} and residual oil saturation S_{or} are also estimated by the nonlinear regression. As in the previous case where we only matched the observed pressure data, we obtained a good match of pressure. Fig. 6.3 shows the match of cumulative oil, we note that our estimate of cumulative oil (solid curve) is in good agreement with the observed data (circular points). The initial guess of cumulative oil shows a different time of oil "breakthrough " compared with the observed data in Fig. 6.3. We also obtained the good estimate of relative permeability curves as shown in Fig. 6.4, our estimates of relative permeability curves (circle points) mirror the true relative permeability curves

(solid curves). All estimates of model parameter are shown in Table 6.3, and our estimates of model parameters are accurate.

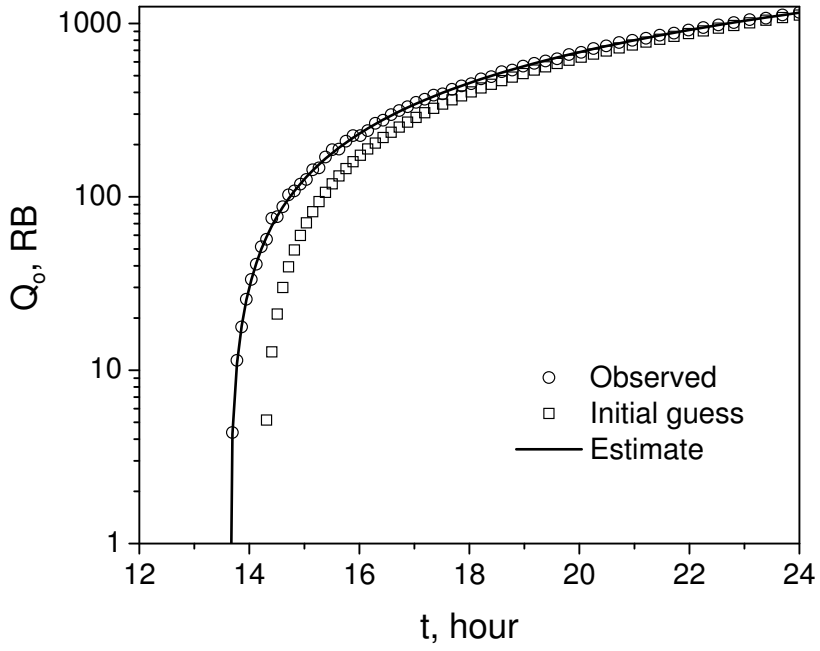

Figure 6.3: Cumulative oil data match based on power law model matching observed data from the true power law relative permeabilities, $\hat{M} = 4.0$.

Model Parameter	k (md)	k_s (md)	s	a_w	n_w	n_o	S_{iw}	S_{or}
True	372	74.4	5.14	0.5	2.0	3.0	0.164	0.271
Estimate	389.7	75.0	5.39	0.5	2.0	2.99	0.163	0.270
Initial Guess	800	200	3.85	0.7	1.5	2.0	0.1	0.1

Table 6.3: Estimate of model parameters based on the power law model matching pressure data from injection/falloff/production.

In this example we obtained good estimates of both the irreducible water saturation, S_{iw}, and residual oil saturation, S_{or}. But we found that it is very difficult to obtain reliable estimates of endpoint saturations. This difficulty can be explained as follows. If the sum $S_{or} + S_{iw}$ is kept equal to the true value and all other parameters are kept fixed, then varying the individual values of S_{or} and S_{iw} simply shifts the relative permeability curves and does not change the fractional flow curve. Thus, the only effect that the individual values of S_{or} and S_{iw} can have on the pressure response during the

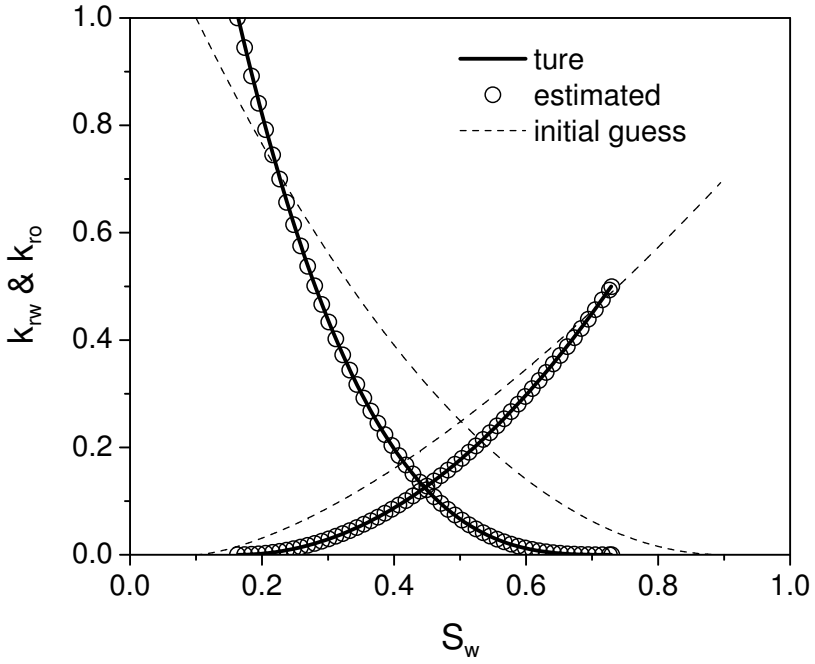

Figure 6.4: Estimate of relative permeabilities based on the power law model matching observed data from the true power law relative permeabilities, $\hat{M} = 4.0$.

injection/falloff/production test is due to the change in system compressibility, and if the water and oil compressibilities are equal, this effect is completely negligible.

6.1.2 Estimate of Polynomial Relative Permeabilities Based on the Power Law Model

It has been stated that the points on the power law relative permeabilities are controlled by the same model parameters, such as exponent values, which make it hard for the power law model to characterize the local shape of relative permeability curves. In this section, an example is given to show the validity of the power law relative permeability curves representing polynomial relative permeability curves. The true relative permeabilities are expressed by the following polynomials:

$$\begin{aligned} k_{rw}(S_{wD}) &= 0.182S_{wD} - 0.104S_{wD}^2 + 0.328S_{wD}^3 \\ k_{ro}(S_{wD}) &= 1.0 - 3.430S_{wD} \\ &\quad + 4.387S_{wD}^2 - 2.388S_{wD}^3 + 0.431S_{wD}^4 \end{aligned} \tag{6.1}$$

The above relative permeability curves do not follow the power law model. The end-point

values of relative permeabilities for water and oil phases are $k_{rw}(1 - S_{or}) = 0.406$ and $k_{ro}(S_{iw}) = 1.0$, respectively. The observed data are generated by running the simulator IMEX based on the true relative permeabilities, Eq. 6.1, and the parameters in Table 6.1. In this case, we assume the irreducible water saturation, S_{iw}, and residual oil saturation, S_{or}, are known. This test is a 5-hour injection, 5-hour falloff and 14-hour production test. The observed data are bottomhole pressure from all three periods. The noise is a Gaussian distribution with mean zero and standard deviation of 0.25 psi. The simulator is used as the forward model for calculating the predicted pressure response based on the estimate of model parameters.

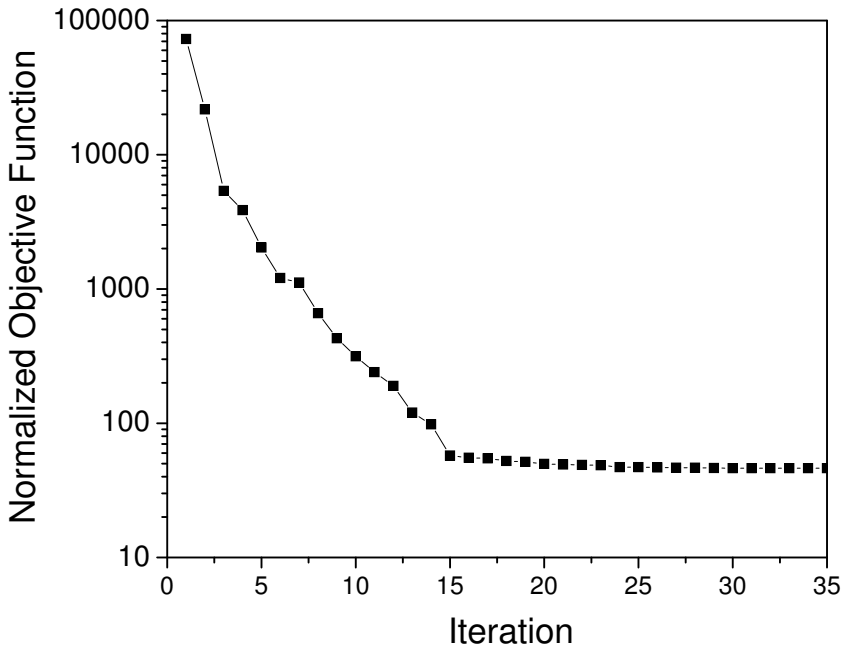

Figure 6.5: Normalized objective function (polynomial true relative permeabilities), $\hat{M} = 4.0$.

Fig. 6.5 shows the normalized objective function value change iteration by iteration. We can note that the Levenberg-Marquardt algorithm converged in 35 iterations but the normalized objective function, $2O(m)/N_d$, which should be around 1 normally, is over 60. The estimated relative permeability curves (the circle points) shown in Fig. 6.6 deviate from the true relative permeability curves (the solid curves). The dashed curves are the initial guesses of the relative permeability curves. In Fig. 6.7, the match of bottom-

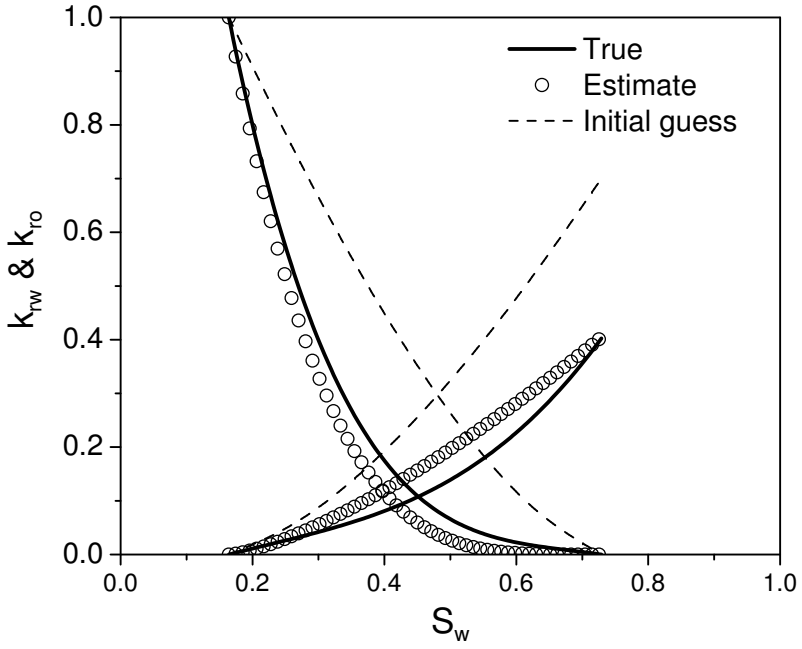

Figure 6.6: Estimate of relative permeabilities based on the power law model (polynomial true relative permeabilities), $\hat{M} = 4.0$.

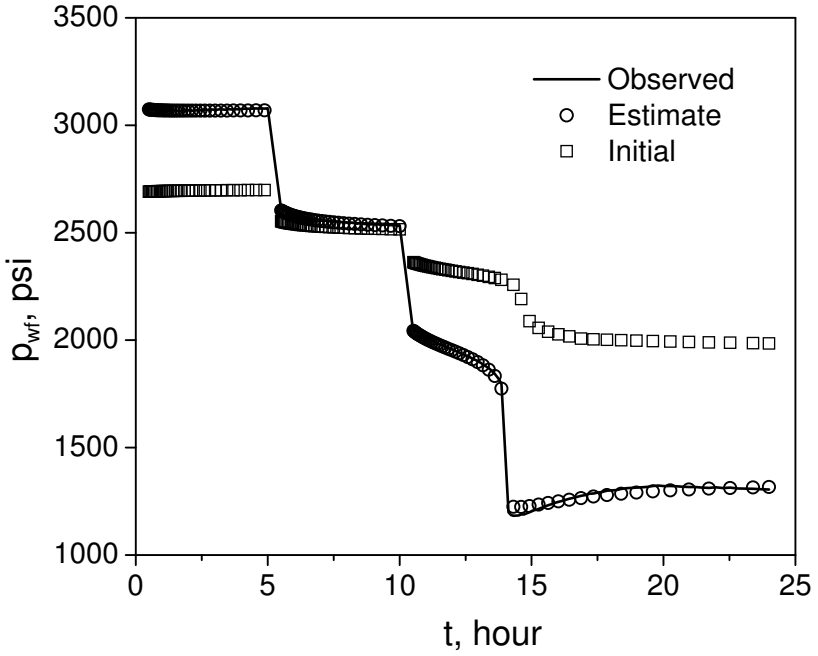

Figure 6.7: Estimate of bottomhole pressure (polynomial true relative permeabilities), $\hat{M} = 4.0$.

hole pressure, the estimate of bottomhole pressure (the circle points) follows the observed pressure data (the solid curve) although the initial guess (the squared points) are far from the observed data. But we can note the high data mismatch when oil flows back to the well during production. Less accurate estimates of absolute permeability and skin factor were also obtained. The estimated values are $k = 412.4$ md and $s = 6.0$ compared to the true values of $k = 372.0$ md and $s = 5.14$. The failure to obtain good estimates of relative permeability curves is due to the fact that the power law model is not flexible and is not appropriate for this example.

6.2 Estimate of Relative Permeabilities Based on the B-spline Model

Results from cases using the B-spline model to estimate the relative permeabilities and other model parameters are shown in this section. Reservoir simulator (IMEX) were used as the forward model in nonlinear regression. From the study of the sensitivity of observed data to model parameters representing relative permeability curves, we found that the data obtained during production are more sensitive to the model parameters than the data during injection and falloff periods. The estimates of relative permeabilities and other model parameters, based on the pressure data from injection/falloff and injection/falloff/production, are compared in this research. The flexible B-spline model, with 7 knots on each of the relative permeability curves, was used to represent the relative permeability curves.

6.2.1 Estimate Based on the Injection/Falloff Test

We used three cases to investigate the efficiency of the pressure data from an injection/falloff test. The observed pressure data of the three synthetic cases were obtained based on the value given in Table 6.1, and the true relative permeability curves defined by Eq. 6.1. The observed pressure data are added a Gaussian noise with mean zero and a standard deviation of 0.25 psi. The convex (concave up) B-spline model is used in the process of the nonlinear regression to estimate relative permeabilities. The irreducible water saturation S_{iw} and residual oil saturation S_{or} are assumed to be known.

In the first case, the observed pressure data are from a test with 5-hour injection and 5-hour falloff. We used pressure data after 0.5 hours for each period as the observed data. Fig. 6.8 shows the match of bottomhole pressure after nonlinear regression. The dashed curve is our initial guess of bottomhole pressure based on the given initial estimate of model parameters. We can see that bottomhole pressure calculated using the estimate parameters (solid curve) gives a good match of the observed pressure (circular points). However, we obtain a poor estimate of the model parameters. In Fig. 6.9, our finial estimate of relative permeability curves (the circled points) do not match the true relative permeability curves (the solid curves). The estimate of the endpoint value of water phase $a_w = 0.88$, which is far from the true value of $a_w = 0.406$. The estimates of the absolute permeabilities are $k = 368.1$ md and $k_s = 20.6$ md (s=21.7) compared to the true values of $k = 374.0$ md and $k_s = 74.4$ md (s=5.14). From the results, we note that this short time injection/falloff test only gave a good estimate of absolute permeability.

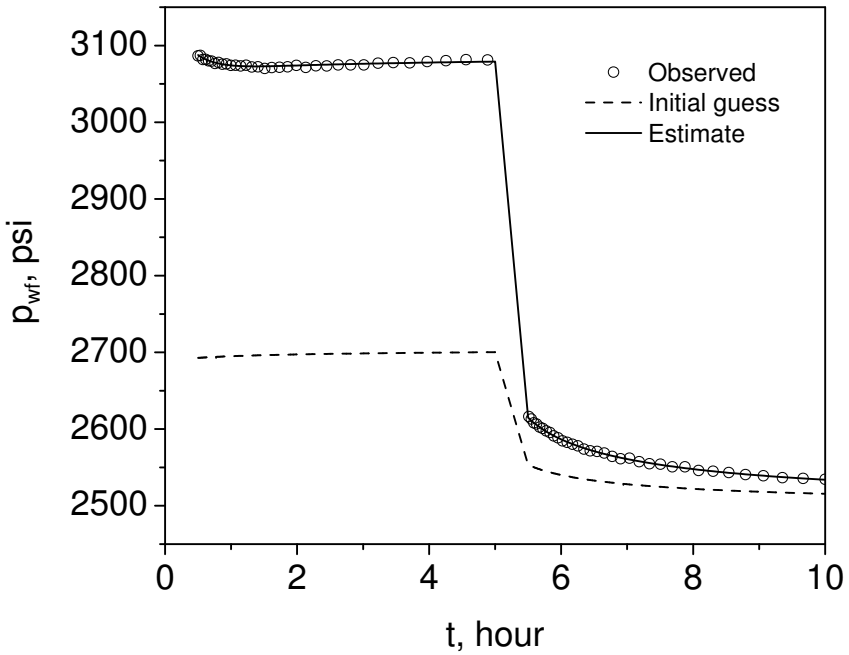

Figure 6.8: Match of bottomhole pressure based on 5-hour injection and 5-hour falloff, $\hat{M} = 4.0$.

When we matched only pressure data from the injection and falloff tests together (total of 10 hours of data) in the above case, we obtained very poor estimates of the relative

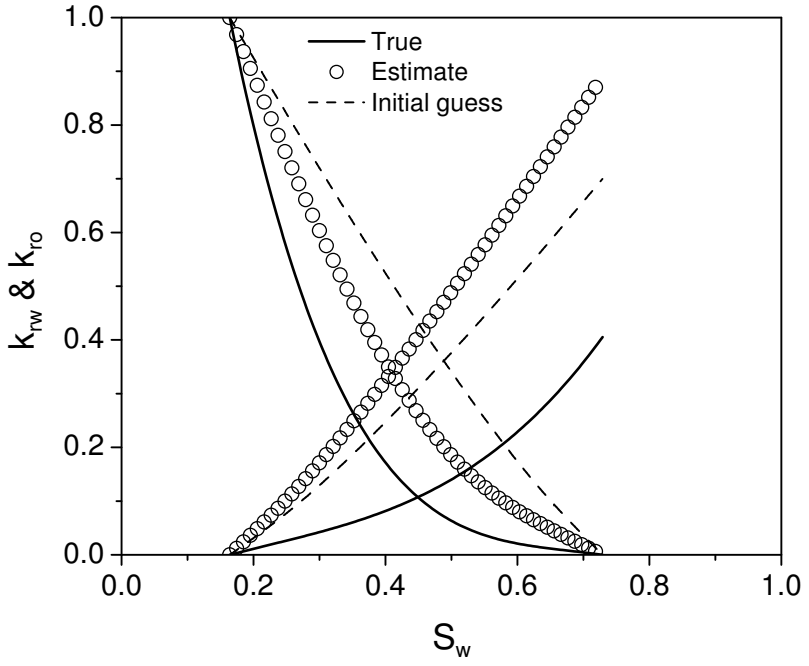

Figure 6.9: Estimate of relative permeabilities based on 5-hour injection and 5-hour falloff, $\hat{M} = 4.0$.

permeability curves. To obtain a fairer comparison, we generated comparable data for two longer tests with an 24-hour injection period followed by a 24-hour falloff period. In one case, parameters are estimated by matching observed pressure data from both injection and falloff periods after 0.5 hours; in the other case, to eliminate the information from early times of each period, we used observed data from the injection after 5 hours together with observed pressure data from the falloff period after 0.5 hours considering sensitivity of observed data to parameters are close to zero during falloff. Figs. 6.10–6.13 give the results of the case with observed pressure data after 0.5 hours for the injection and falloff periods. Fig. 6.10 shows that there is a good match between our estimate of bottomhole pressure and the observed pressure data. Fig. 6.11 shows the estimate of the relative permeability curves. Our estimate of relative permeability curves (circle points) obtained the main structure of the true relative permeability curves. The estimate has a good match of endpoint value of water phase with estimated $a_w = 0.40$ compared the the true value $a_w = 0.406$. But the shifts between the estimated relative permeability curves and the true relative permeability curves can be observed between irreducible water saturation

S_{iw} and the saturation $1 - S_{or}$ in Fig. 6.11. The estimates of absolute permeabilities are $k = 370.8$ md and $k_s = 70.1$ md ($s = 5.51$) compared to the true values of $k = 372.0$ md and $k_s = 74.4$ md ($s = 5.14$). Fig. 6.12 shows the diagnostic plot of pressure difference

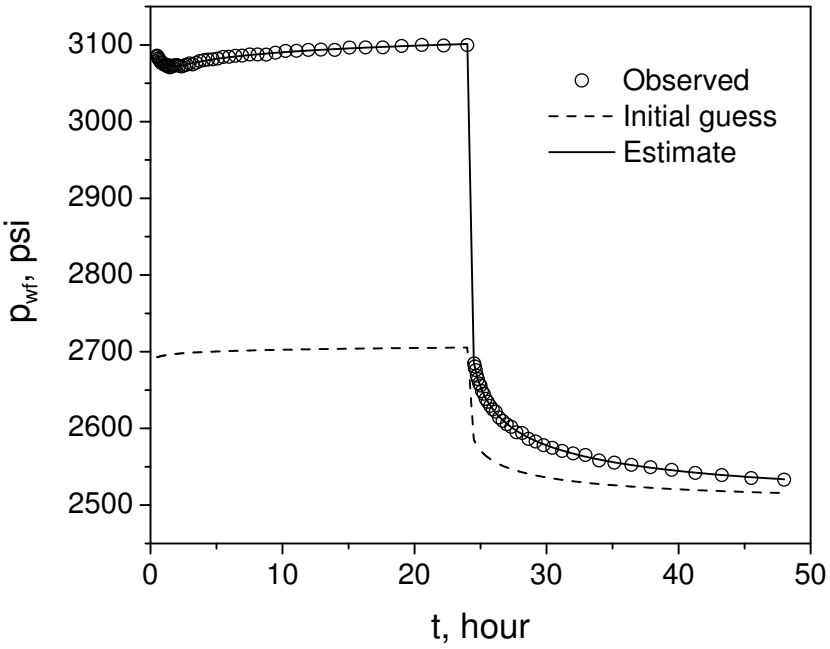

Figure 6.10: Match of bottomhole pressure based on 24-hour injection and 24-hour falloff with observed pressure data after 0.5 hours for each period, $\hat{M} = 4.0$.

and its derivative during production of the 24-hour injection and 24-hour falloff test. After nonlinear regression, although the derivative of the observed data (triangular data) is very noisy, the derivative of our estimate (solid curve) traces the derivative of the true pressure difference (circled data) well. Here, the true pressure data are obtained based on the true model parameters without adding noise. At late injection times, the derivative of the pressure difference shows a constant value 12.1 representing the water property defined by Eq. 1.4. From the derivative of pressure difference in Fig. 6.12, we also note that most data do not give the constant value representing water property for 5 hours of injection. So the pressure data from the short time test of the 5-hour injection do not provide enough information for estimating the endpoint value of water phase relative permeability curve. Fig. 6.13 shows the diagnostic plot of pressure data from the subsequent falloff period. The derivative of our estimate (solid curve) has a good agreement with the derivative of

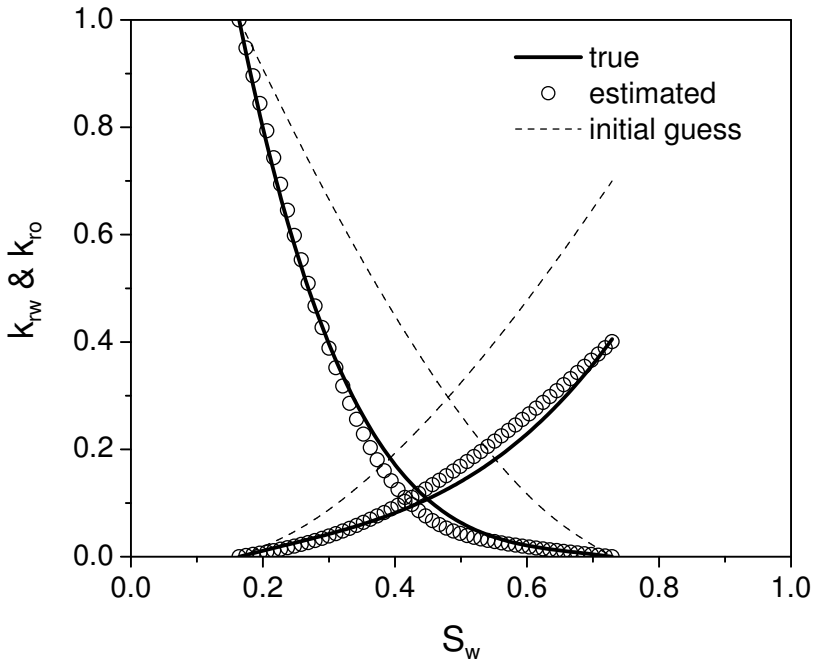

Figure 6.11: Estimate of relative permeability curves based on the test of 24-hour injection and 24-hour falloff with observed pressure data after 0.5 hours for each period, $\hat{M} = 4.0$.

true data (circled data). The all derivatives of pressure difference during falloff give a constant value of 48.7, representing the oil property given by

$$\frac{d\Delta p}{d\ln(t_e)} = \frac{70.6 q_t}{kh\hat{\lambda}_o} = \frac{70.6 q_t \mu_o}{kh} \tag{6.2}$$

The falloff derivative represents the log-derivative of $\Delta p = p_{wf,s} - p_{ws}(\Delta t)$ with respect to Agarwal's equivalent time (t_e) plotted versus shutin time.

In Chapter 1, we state that at end of the injection and falloff, the pressure data only provide the information representing endpoint water relative permeability and endpoint oil relative permeability, respectively. We note that the derivatives of pressure differences during falloff in Fig. 6.13 show an essentially constant value throughout the falloff. So here, we gave a case selecting the pressure data after 5 hours as the observed data for the injection period, i.e., the observed data for both the injection and falloff only show constant values of pressure difference as shown in Figs. 6.12 and 6.13. Although we obtained a good match between our estimate of pressure and observed data, the estimated

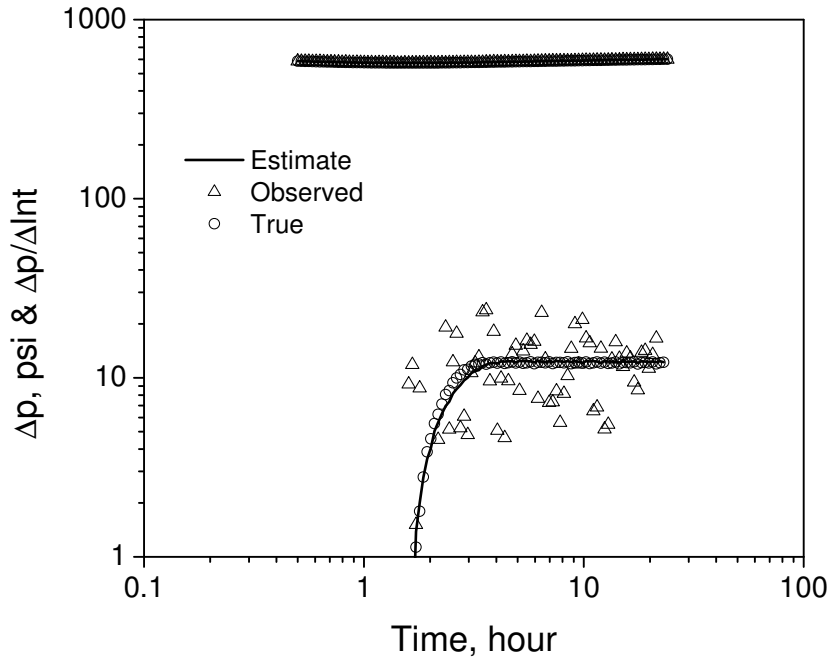

Figure 6.12: Match of bottomhole pressure based on 24-hour injection and 24-hour falloff, $\hat{M} = 4.0$.

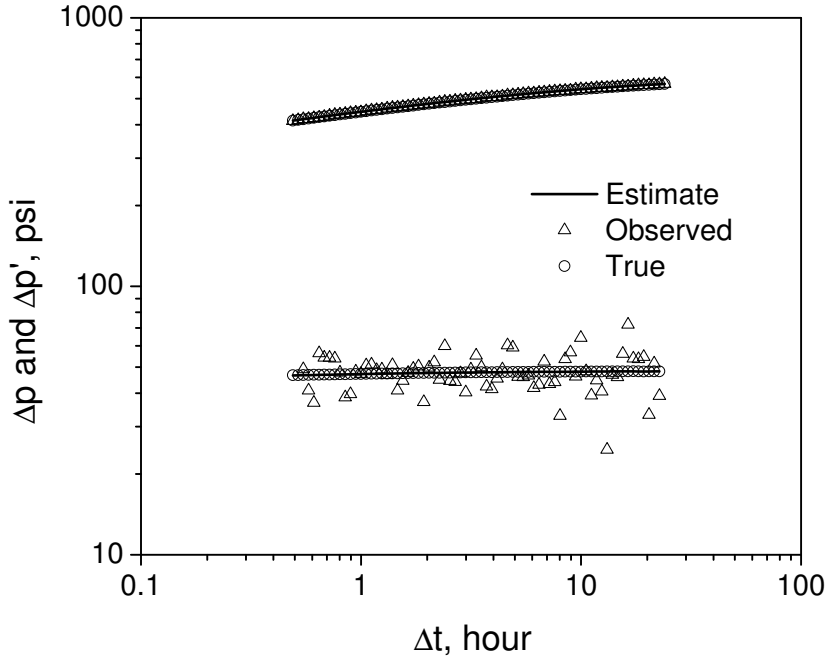

Figure 6.13: Estimate of relative permeabilities based on 24-hour injection and 24-hour falloff, $\hat{M} = 4.0$.

relative permeability curves as shown in Fig. 6.14 are not accurate because we did not use the earlier time injection data which reflects total mobility values between the two endpoint values. Our estimate of relative permeability curves (circle points) represents a good estimate of the endpoint value of water phase, $a_w = 0.401$ compared with true value $a_w = 0.405$. However, our estimate of relative permeability curves do not match the true curves (solid curves) in the region between irreducible water saturation S_{iw} and saturation $1 - S_{or}$. The estimates of absolute permeabilities are $k = 370.8$ md and $k_s = 70.1$ md ($s = 5.51$) compared to the true values of $k = 372.0$ md and $k_s = 74.4$ md ($s = 5.14$).

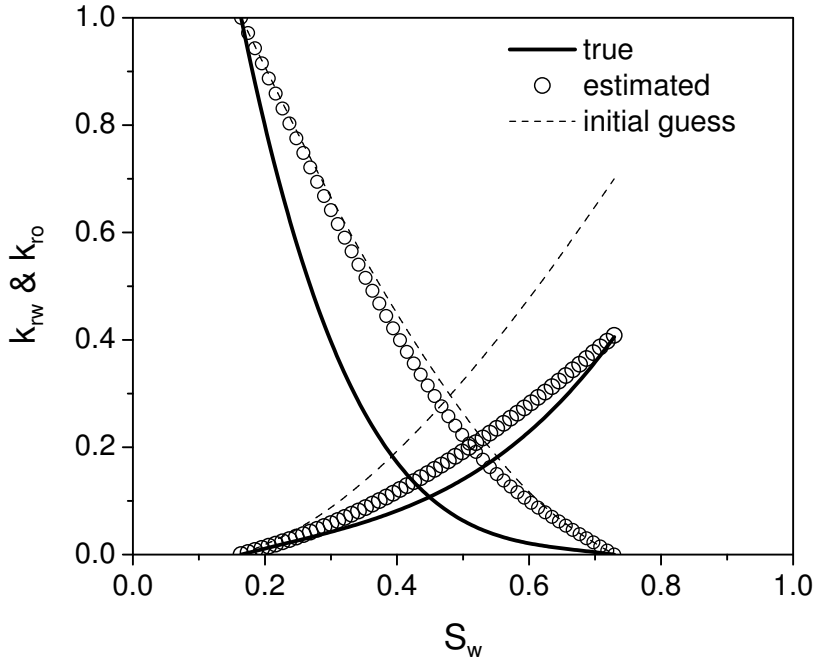

Figure 6.14: Estimate of relative permeabilities based on 24-hour injection and 24-hour falloff with observed pressure data after 5 hours for injection period, $\hat{M} = 4.0$.

Comparing the results and estimates from cases from injection/falloff, we found that in all cases, we obtain a good estimate of absolute permeability because the pressure data from falloff period provides enough information to resolve absolute permeability, injection test does not reflect both endpoint water relative permeability and total mobility at intermediate water saturations, we get relatively poor estimate of relative permeability curves. For the 24-hour injection/24-hour falloff case, we obtained good estimate of endpoint value of water relative permeability curve. However, we show next that we

obtain an much better estimate using data from 24 hours injection/falloff/production test with a 5-hour of injection, a 5-hour of falloff and a 14-hour flow back period.

6.2.2 Estimate Based on the IFPT

When we have injection/falloff/production test (IFPT) data, we have more information than only using injection/falloff test. Here, we show some nonlinear regression results from cases with different endpoint mobility ratios and different scenarios of observed data from the IFPT. The observed pressure data from the IFPT is generated from the reservoir simulator based on the model parameters in Table 6.1 by adding uncorrelated Gaussian noise of mean zero and standard deviation 0.25 psi. The true relative permeability curves are defined by Eq. 6.1. The pressure data after 0.5 hours in each period are used for nonlinear regression.

Estimate Based on Pressure Data from the IFPT $\hat{M} = 7.9$: This test is based on the pressure data from all three periods from this 24 hour IFPT with endpoint mobility ratio $\hat{M} = 7.9$. Fig. 6.15 and Fig. 6.16 show the pressure data match and the estimate of relative permeability obtained by nonlinear regression. In Fig. 6.15, the predicted pressure data generated using our estimate of model parameters (solid curve) match the observed data (the triangular data) very well. As shown in Fig. 6.16, our estimate of relative permeability curves (circle data points) also is in good agreement with the true relative permeability curves (solid curves). The estimates of absolute permeability and skin variables are $k = 373.7$ md, $k_s = 74.5$ md and $s = 5.14$ compared to the true values of $k = 372.0$ md, $k_s = 74.4$ md and $s = 5.14$. Compared with the results from cases based on injection/falloff test, the estimate of relative permeability curves and other model parameters using the pressure data from the IFPT are more accurate.

We also did nonlinear regression based on using the monotonic B-spline curve to represent the relative permeabilities. In this case, we also using 7 knots for each relative permeability curve. Fig. 6.17 shows the pressure data match. Our predicted pressure data (solid curve) match the observed pressure data (circle data) very well. The initial guesses of pressure data (squared data) are far from the observed pressure data and our predicted

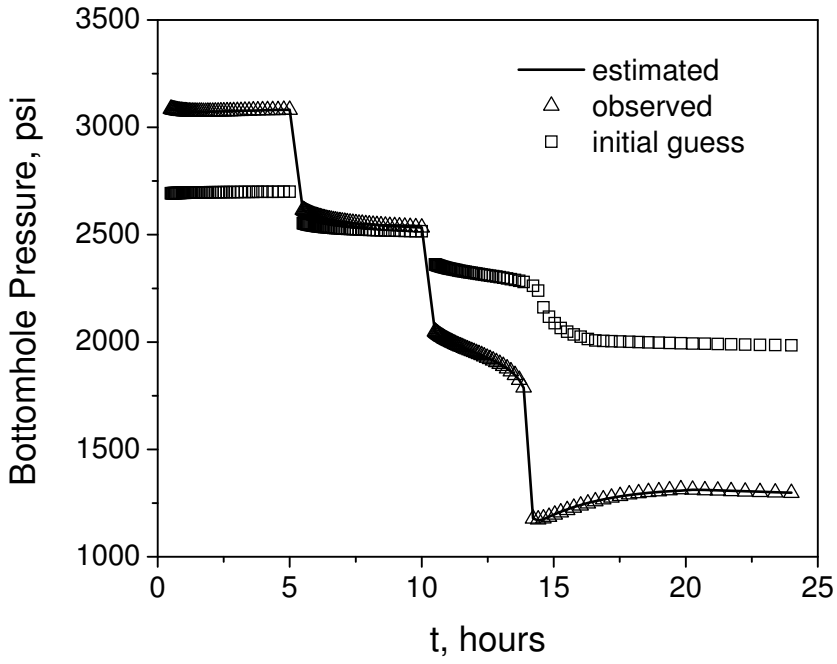

Figure 6.15: Match of bottomhole pressure based on 5-hour injection, 5-hour falloff and 14 hour production with observed pressure data after 0.5 hours for each period with convex B-spline model, $\hat{M} = 4.0$.

data. Fig. 6.18 compares the estimate of relative permeability curves (circled curves) and the true curves (solid curves). They are in very good agreement. The true relative permeability curves are convex (concave up). We can note that estimate of water phase relative permeability curve id not convex between saturations $S_w = 0.3$ and $S_w = 0.6$ in this case. The estimate of the endpoint value of water phase relative permeability curve is $a_w = 0.386$ compared with the true value $a_w = 0.405$. The estimates of absolute permeability and skin variables are $k = 372.6$ md, $k_s = 74.4$ md and $s = 5.15$ compared to the true values of $k = 372.0$ md, $k_s = 74.4$ md and $s = 5.14$.

Estimate Based on Pressure Data from the IFPT ($\hat{M} = 0.53$): This test is also based on the pressure data from the 24 hour IFPT. In this case, oil viscosity is $\mu_o = 0.8$ cp and water viscosity is $\mu_w = 1.0$ cp, and the other model parameters same as those given in Table 6.1. The true relative permeability curves are still the polynomial equations defined by Eq. 6.1. The true endpoint values of oil and water phase relative permeability

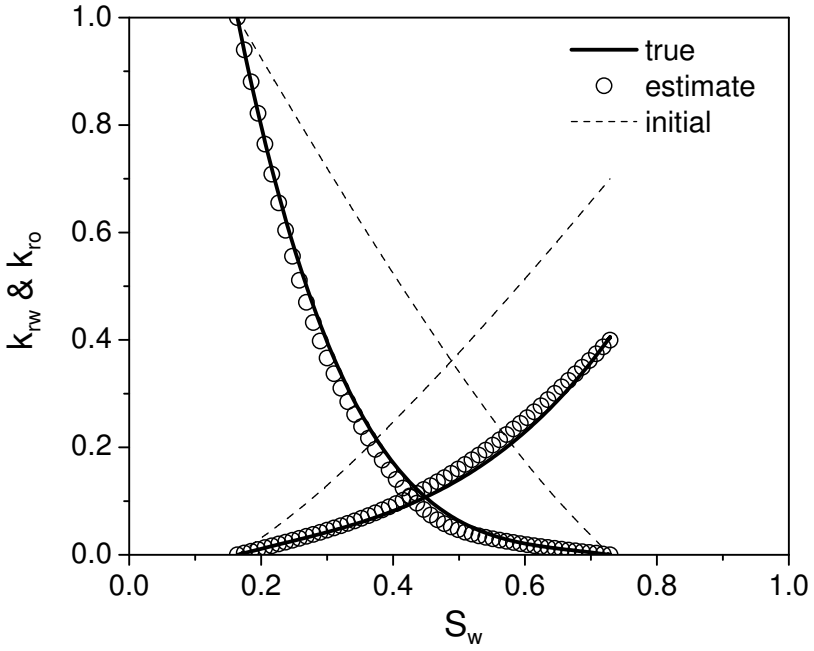

Figure 6.16: Estimate of relative permeability curves based on 5-hour injection, 5-hour falloff and 14 hour production with observed pressure data after 0.5 hours for each period with convex B-spline model, $\hat{M} = 4.0$.

curves are 1.0 and 0.405, respectively. The endpoint mobility ratio is $\hat{M} = 0.51$. During the production period, oil is displacing the injected water so a favorable mobility during injection results in an unfavorable mobility ratio when oil is displacing water. Fig. 6.19 and Fig. 6.20 show the pressure data match and the estimate of relative permeability obtained by nonlinear regression, respectively. In Fig. 6.19, the predicted pressure data based on our estimate of model parameters (solid curve) match the observed data (the triangular data) very well. As shown in Fig. 6.20, our estimate of relative permeability curves (circle data points) also are in good agreement with the true relative permeability curves (solid curves) again. The estimate of the endpoint value for water phase relative permeability curves is $a_w = 0.391$ compare with the true value $a_w = 4.06$. The estimates of absolute permeability and skin variables are $k = 382.8$ md, $k_s = 76.5$ md and $s = 5.14$ compared to the true values of $k = 372.0$ md, $k_s = 74.4$ md and $s = 5.14$.

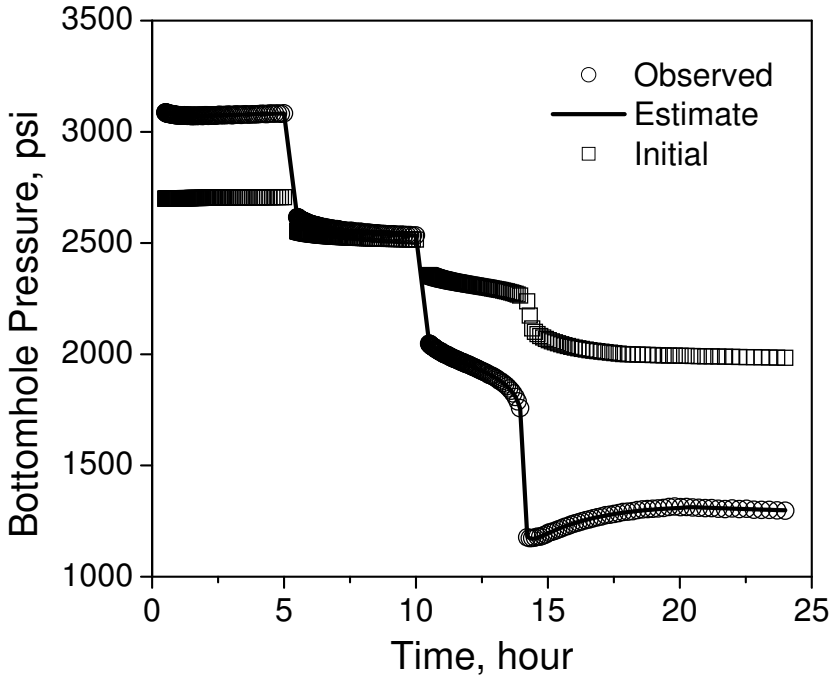

Figure 6.17: Match of bottomhole pressure based on pressure data from 5-hour injection, 5-hour falloff and 14 hour production with monotonic B-spline model, $\hat{M} = 4.0$.

Estimate Based on Only Falloff and Production: In this case, the total number of observed pressure data from the falloff and flowback periods combined is 126 and the number of observed cumulative oil production data from the flow back period is 63. For this synthetic case, we added the noise to cumulative oil with $\sigma_{Q,min} = 0.1$ RB/Day and $\sigma_{Q,max} = 5$ RB/day as we stated in Chapter 5. Fig. 6.21 and Fig. 6.22 show the pressure match of data from the falloff and production periods and cumulative oil data match during production, respectively. Our predicted data from estimates of model parameters match the observed data very well both on the pressure data and the cumulative oil data. From the results of Fig. 6.23, we see that the B-spline approximations of the relative permeability curves are in excellent agreement with the true curves. The estimates of absolute permeability and skin are $k = 371.6$ md and $s = 5.11$ compared to the true values of $k = 372.0$ md and $s = 5.14$.

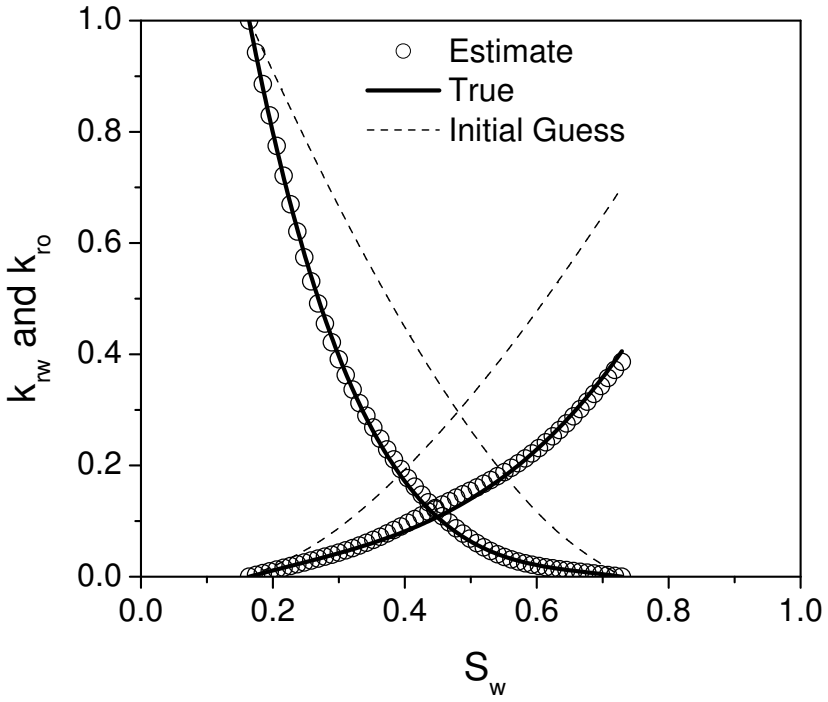

Figure 6.18: Estimate of relative permeability curves based on pressure data from 5-hour injection, 5-hour falloff and 14 hour production with monotonic B-spline model, $\hat{M} = 4.0$.

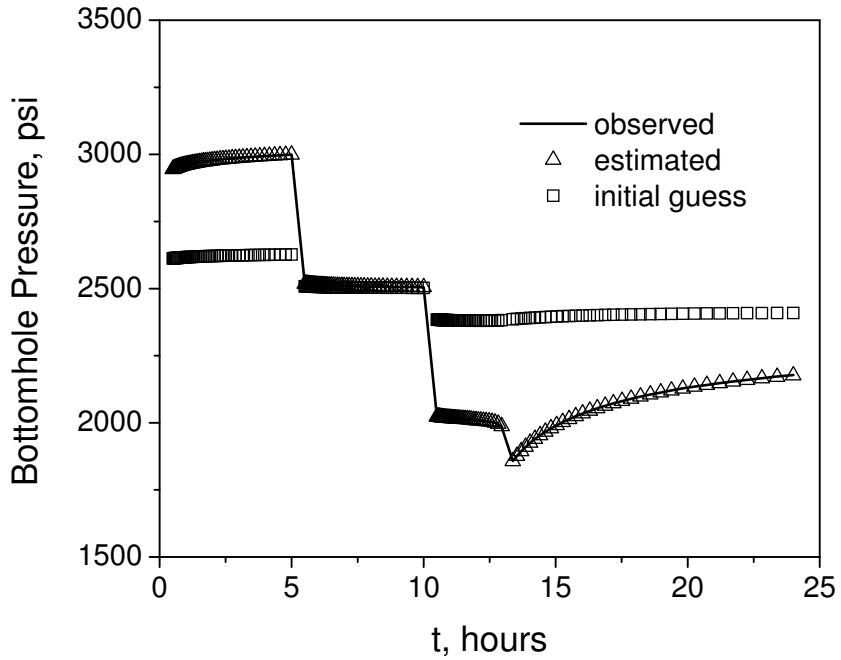

Figure 6.19: Match of bottomhole pressure based on 5-hour injection, 5-hour falloff and 14 hour production with observed pressure data after 0.5 hours for each period, $\hat{M} = 0.53$.

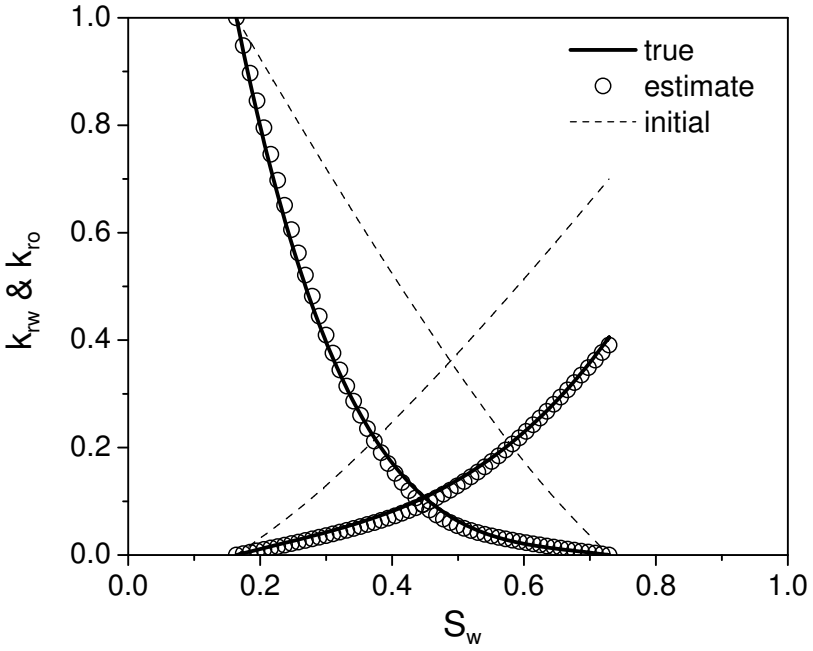

Figure 6.20: Estimate of relative permeability curves based on 5-hour injection, 5-hour falloff and 14 hour production with observed pressure data after 0.5 hours for each period, $\hat{M} = 0.53$.

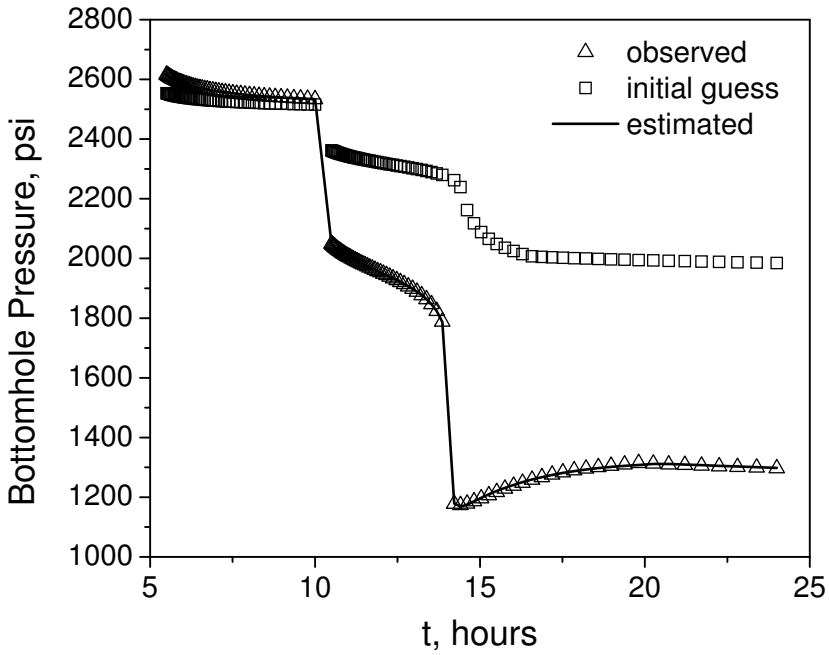

Figure 6.21: Match of bottomhole pressure based on the IFPT with observed pressure data during falloff/production periods and cumulative oil data during production period, $\hat{M} = 4.0$.

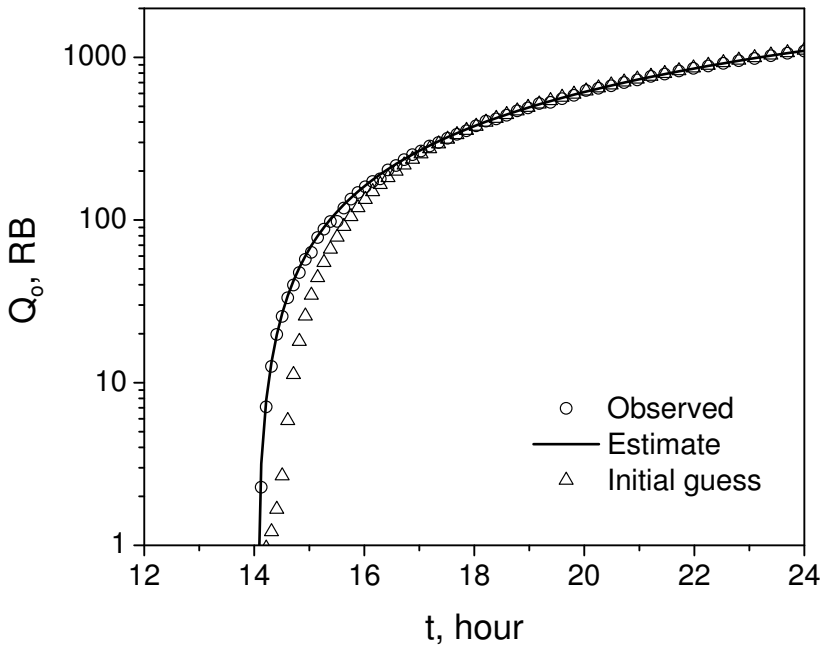

Figure 6.22: Match of cumulative oil based on the IFPT with observed pressure data during falloff/production periods and cumulative oil data during production period, $\hat{M} = 4.0$.

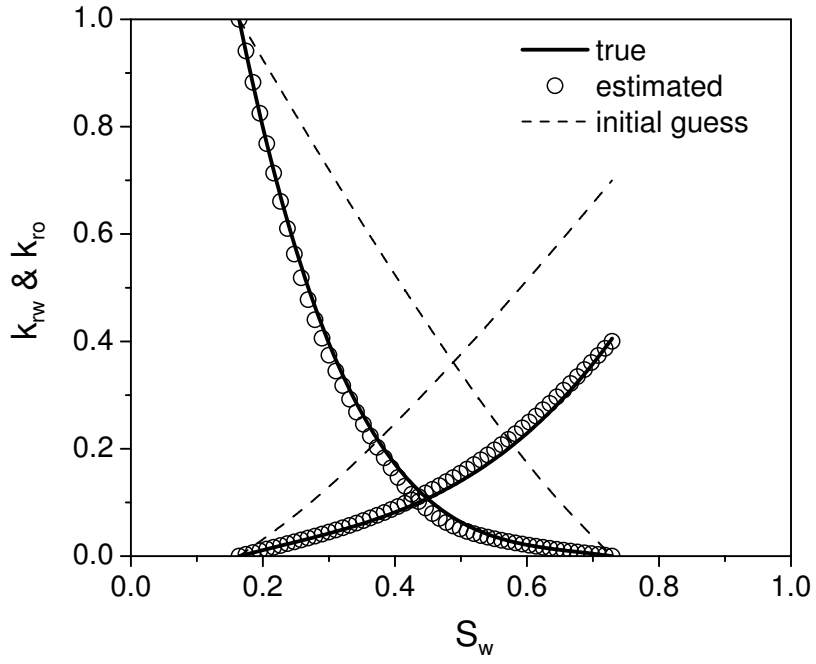

Figure 6.23: Estimate of relative permeability curves based on the IFPT with observed pressure data during falloff/production periods and cumulative oil data during production period, $\hat{M} = 4.0$.

Estimate of S_{iw} and S_{or}: In the previous section, we obtained good estimates of S_{iw} and S_{or}. As we stated before, it seems clear that both endpoint saturation cannot generally be resolved without additional information. Our limited computational experiments suggest that in general, we can only expect the sum $S_{or} + S_{iw}$ to be accurately resolved by test data. However, in some cases we fortuitously obtain good estimates of all parameters even when S_{iw} and S_{or} are included as model parameters. Fig. 6.24 displays such a case. This the same case that gave the results of Fig. 6.16 except now we estimate S_{iw} and S_{or} also. Note that reasonable estimates of the true relative permeability were obtained. The estimates of other parameters are $k = 375.6$ md, $s = 5.19$, $S_{iw} = 0.161$ and $S_{or} = 0.244$ compared to the true values of $k = 372$ md, $s = 5.14$, $S_{iw} = 0.164$ and $S_{or} = 0.271$.

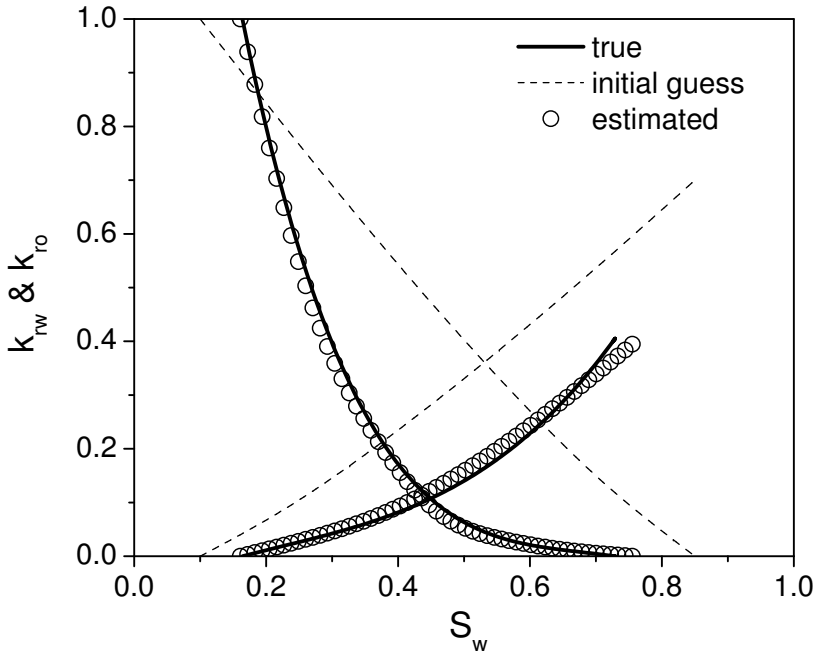

Figure 6.24: Estimate of relative permeability curves based on concave B-spline relative permeability curves, endpoint saturations also estimated by matching injection/falloff/production data, $\hat{M} = 4.0$.

6.3 Analysis Based on Approximate Analytical Solution (No Capillary Pressure)

6.3.1 Estimate Based on the Injection/Falloff Test

Based on the steady state theory of Thompson and Reynolds, the Buckley-Leverett theory, the front tracking method and the solution of Peres and Reynolds, we presented in Chapter 2, our approximate analytical solution for the pressure response during the IFPT without capillary pressure effects. Using our approximate analytical solution as the forward model in nonlinear regression, we also estimated relative permeabilities and other model parameters. Here, we give some examples to show the validity of using our approximate analytical solution in nonlinear regression. The observed data were generated from the reservoir simulator IMEX based on the simulation parameters shown in Table 6.4. The true relative permeability curves for reservoir simulation are the power

Property	Value	
q_{inj}	3000	RB/Day
h	60	ft
r_w	0.350	ft
r_e	6800	ft
r_s	1.2279	ft
Number of rings	6000	
k	300	md
k_s	60	md
μ_o	3.0	cp
μ_w	0.5	cp
$\hat{\lambda}_w$	1.0	
$\hat{\lambda}_o$	0.333	
S_{iw}	0.1	
S_{or}	0.25	
p_i	2500	psi
ϕ	0.22	
B_o	1.003	RB/STB
B_w	1.002	RB/STB
c_o	8.0×10^{-6}	psi^{-1}
c_w	3.02×10^{-6}	psi^{-1}
c_r	5.0×10^{-6}	psi^{-1}

Table 6.4: Reservoir, rock and fluid properties for simulation and analytical solution.

law model given by Eqs. 4.1 and 4.2 with endpoint values of water and oil phase relative permeabilities given by $a_w = 0.5$ and $a_o = 1.0$, and exponent values of water and oil phases are $n_w = 2.0$ and $n_o = 2.0$, respectively. Endpoint mobility ratio is $\hat{M} = 3.0$. We use both the power law and B-spline model to estimate relative permeabilities in the nonlinear regression. From an IFPT with 16-hour injection, 16-hour falloff and 24-hour production, bottomhole pressure data are used as the observed data. The observed data were obtained by adding to the true data, generated from the simulator, uncorrelated Gaussian noise with mean zero and a standard deviation of 0.1 psi. The observed pressure data that we used for nonlinear regression are also after 0.5 hours for each period.

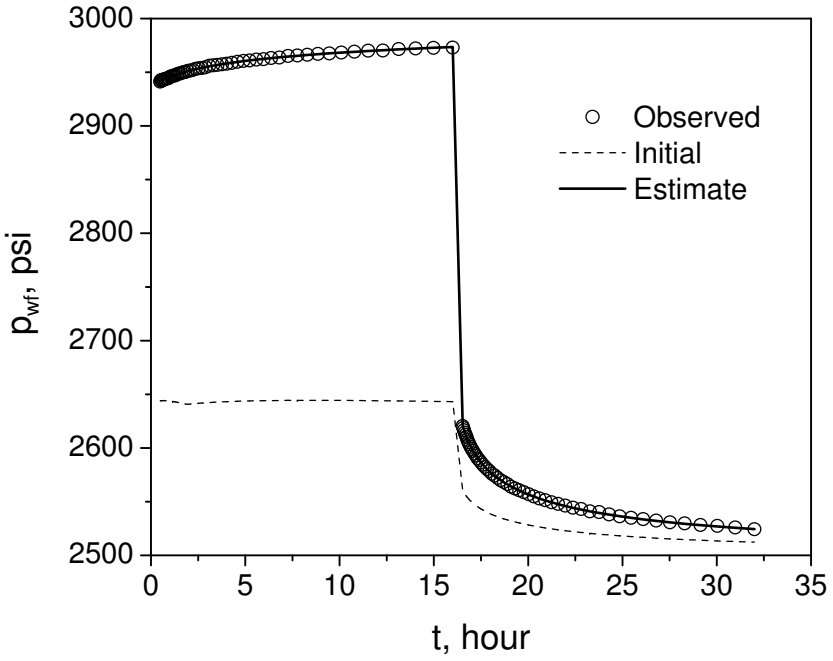

Figure 6.25: Bottomhole pressure match based on approximate analytical solution of the injection/falloff test, power law model ($\hat{M} = 3.0$).

Fig. 6.25–Fig. 6.27 display the results obtained by matching the observed pressure data from the injection and falloff periods test using the power law model. Fig. 6.25 shows that we have a good match between our predicted pressure (solid curve) and the observed pressure (circle points). Diagnostic plot of injection, Fig. 6.26, shows that the derivative of the predicted pressure (solid curve) reaches a constant value of 11.7 representing the water property given by Eq. 1.4 at late time of injection, although the derivative of

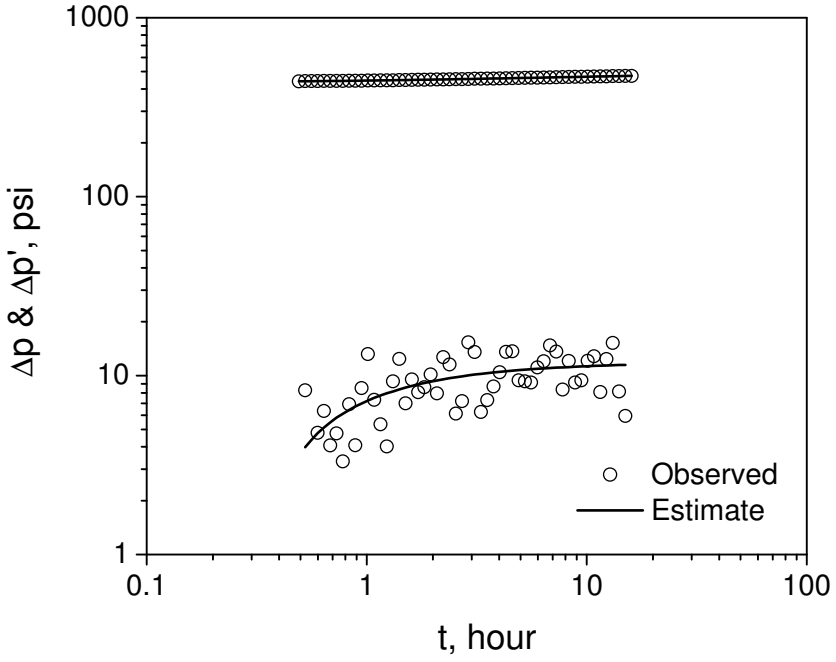

Figure 6.26: Diagnostic plot of injection based on approximate analytical solution of injection/falloff, power law model test ($\hat{M} = 3.0$).

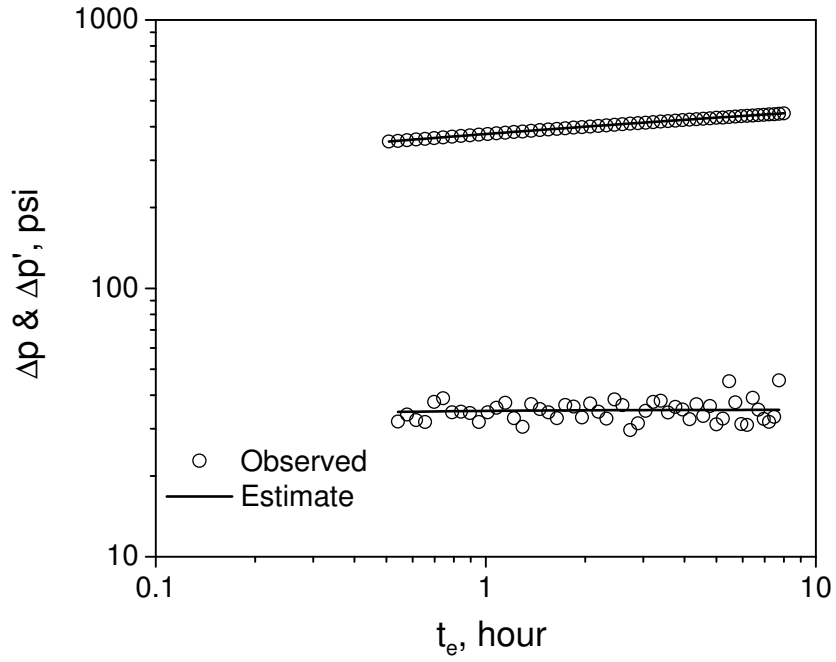

Figure 6.27: Diagnostic plot of falloff based on approximate analytical solution of injection/falloff test, power law model ($\hat{M} = 3.0$).

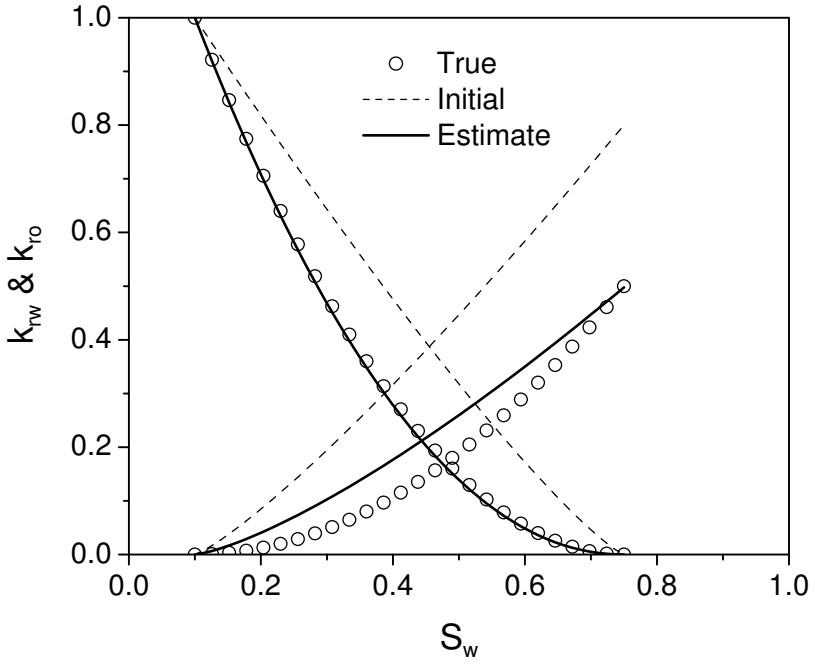

Figure 6.28: Estimate of relative permeabilities based on approximate analytical solution of injection/falloff test, power law model ($\hat{M} = 3.0$).

observed pressure data is highly oscillatory because of the noise. In the diagnostic plot (Fig. 6.27) of falloff data, the derivative of the estimated pressure difference (solid curve) si essentially constant and equal to 35.5 reflects endpoint oil mobility according to Eq. 6.2. Figs .6.25–6.27 show that we obtained a good match of bottomhole pressure. However, we did not obtain a good estimate of relative permeability curves by matching the observed data from the injection and falloff periods. As shown in Fig. 6.28, our estimate of relative permeability curves (solid curves) can not match the true relative permeability curve of water phase, except the endpoint value of water phase $a_w = 0.49$ compared with true value $a_w = 0.5$. The result also shows that a good estimate of absolute permeability is achieved as shown in Table 6.5.

parameter	k, md	Skin Factor	$k_{rw}(1-S_{or})$	n_w	n_o
True	300	5.0	0.5	2.0	2.0
Initial Guess	600	0	0.8	1.2	1.2
Injection/Falloff (Power Law)	299.8	5.05	0.49	1.34	2.09
IFPT (Power Law)	300.0	4.8	0.48	2.07	1.98
IFPT (B-spline)	300.0	5.1	0.49	-	-

Table 6.5: Estimates of model parameters based on the approximate analytical solution without capillary pressure effect.

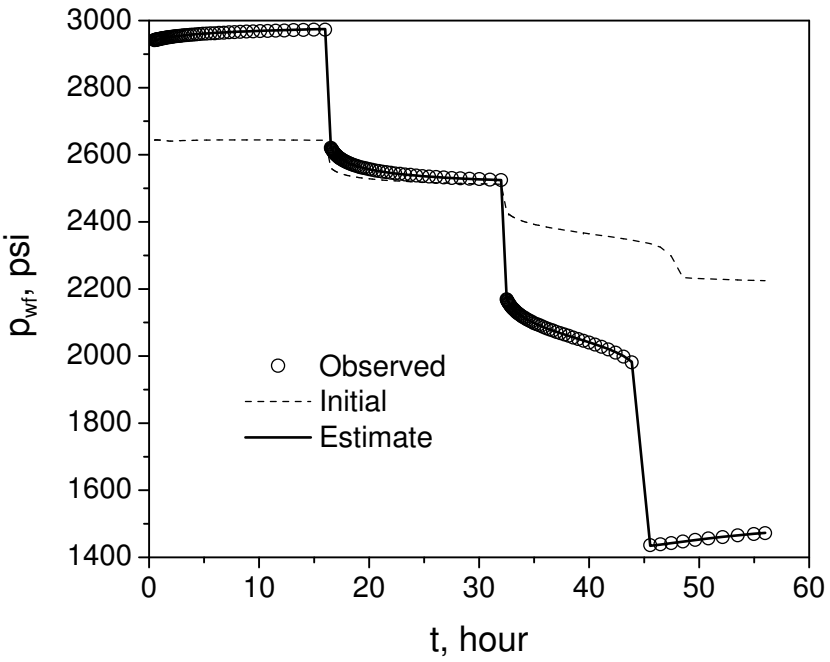

Figure 6.29: Bottomhole pressure match based on approximate analytical solution of the IFPT, power law model ($\hat{M} = 3.0$).

6.3.2 *Estimate Based on the IFPT*

The results from the preceding case show that the pressure injection/falloff data alone cannot provide enough information to resolve the shape of the relative permeability curves. Next, we show the results from two cases after nonlinear regression by using pressure data from all three periods. Fig. 6.29 and Fig. 6.30 display the bottomhole pressure

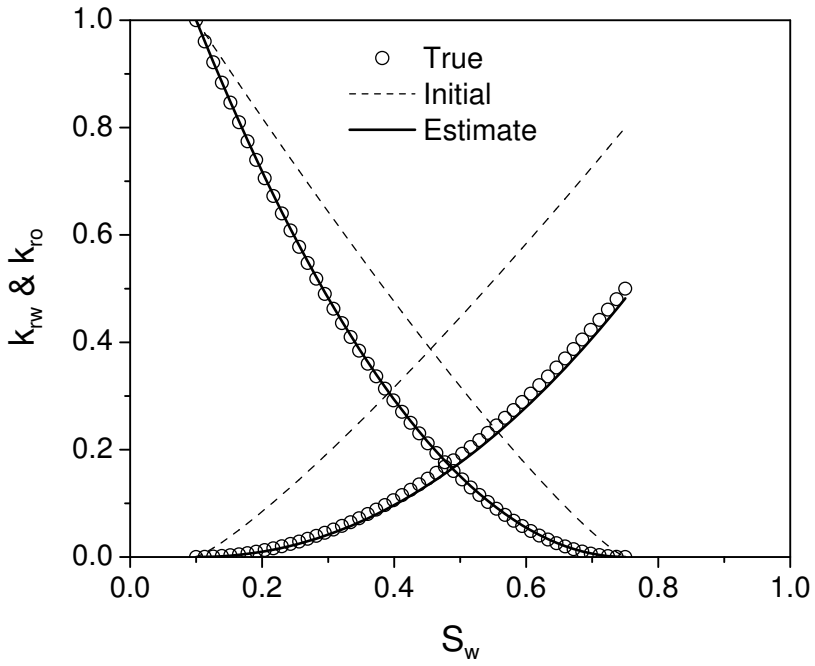

Figure 6.30: Estimate of relative permeabilities based on approximate analytical solution of the IFPT, power law model ($\hat{M} = 3.0$).

response calculated from the estimated parameters and the estimate of the relative permeability curves, respectively. The estimated were obtained from nonlinear regression by matching the pressure data from the IFPT based on the power law relative permeabilities. We obtained a good estimate pressure data again. As shown in Fig. 6.29, our estimate of pressure response (the solid curve) mirrors the observed data (circle points). In Fig. 6.30, our estimate of the relative permeability curves (solid curves) have a good agreement with the true relative permeability curves (circle point curves). We also obtained good estimates of other model parameters as shown in Table 6.5.

From the cases in previous section, we found that it is difficult to obtain good estimate of polynomial relative permeability curves using the power law model if the true

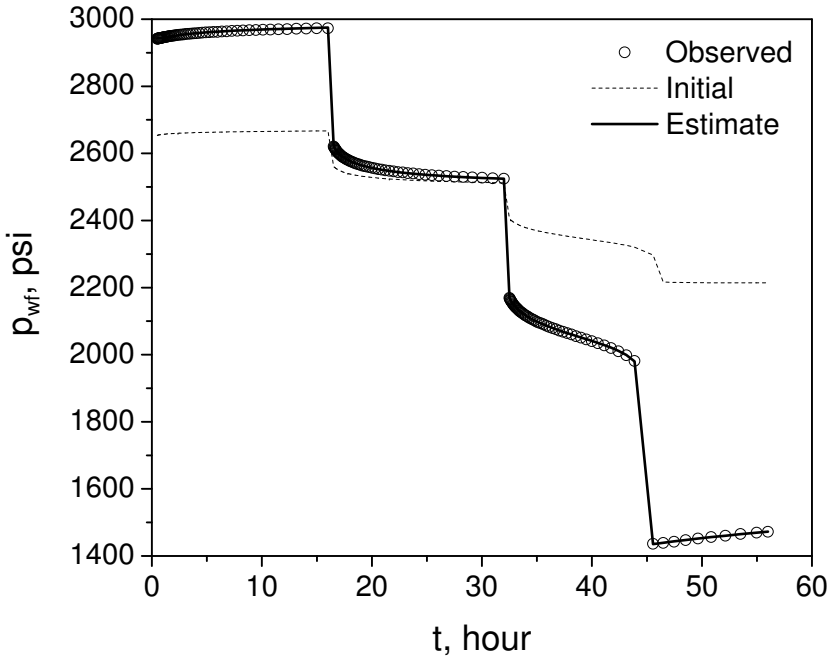

Figure 6.31: Bottomhole pressure match based on approximate analytical solution of the IFPT, B-spline model ($\hat{M} = 3.0$).

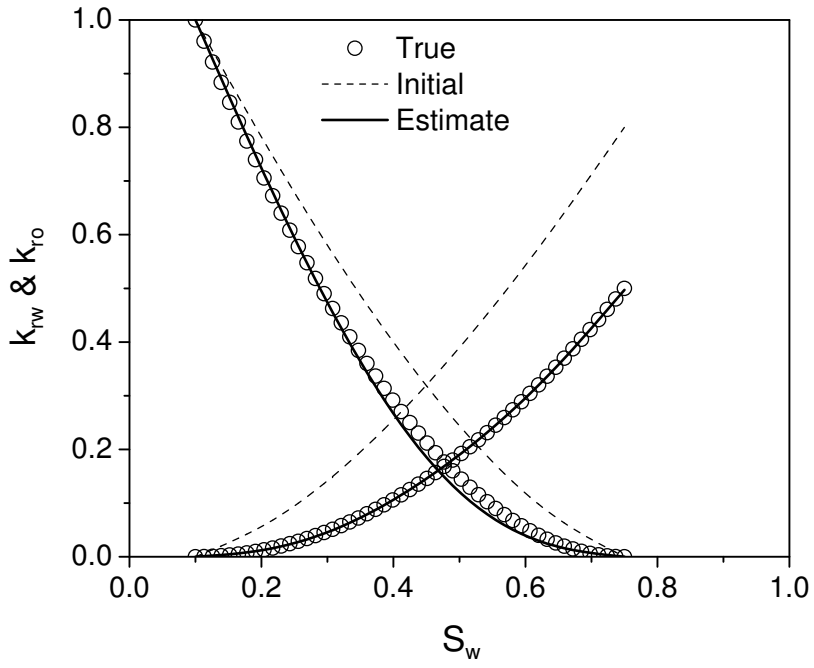

Figure 6.32: Estimate of relative permeabilities based on approximate analytical solution of the IFPT, B-spline model ($\hat{M} = 3.0$).

curves cannot be well approximated by the power law model. The B-spline representation is more flexible than power law model in describing the local shape of the relative permeability curves. Here, we also used the convex B-spline model to estimate the true power law model relative permeability curves. Fig. 6.31 and Fig. 6.32 show the results obtained using B-splines to estimate the power law relative permeability curves. In Fig. 6.31, predicted bottomhole pressure obtained from our approximate analytical solution based on the parameter estimate (solid curve) matches the observed bottomhole pressure (circle points) very well. Fig. 6.32 shows that our estimated relative permeability curves (solid curves) are in good agreement again with the true relative permeability curves (circle points). As shown in Table 6.5, we also obtained good estimates of absolute permeability $k = 300$ md, skin factor $s = 5.1$ and endpoint value of water phase relative permeability $a_w = 0.49$ compared with their true values of 300 md, 5.1 and 0.5, respectively.

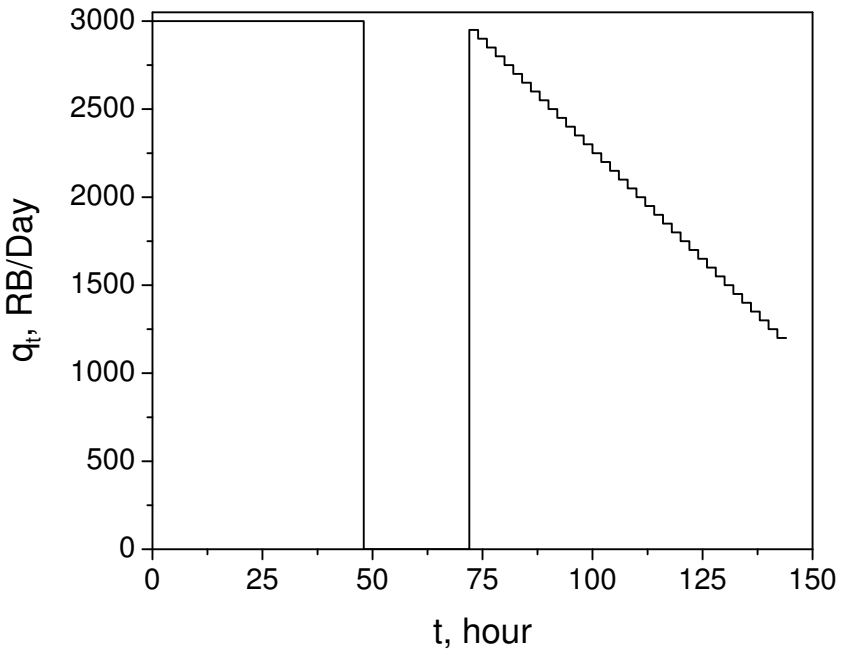

Figure 6.33: Total flow rate for case of 48-hour injection, 24-hour falloff and 72-hour production ($\hat{M} = 3.0$).

6.3.3 Estimate Based on the IFPT with a Multirate Production

In this section, we estimate model parameters from an example of an IFPT for the

case of multirate production. In Chapter 2, we have stated that our analytical solution matches results from the reservoir simulation. The following cases also employed the IFPT with 48-hour injection, 24-hour falloff and 72 hour production. During production, there are 36 uniform time interval multirate steps as shown in Chapter 2 and reproduced here as Fig. 6.33. We also used power law relative permeabilities with $k_{rw}(S_w = 1 - S_{or}) = 0.5$ and $n_w = n_o = 2.0$ as the true relative permeabilities. Other true model parameter are shown in Table 6.6 and the parameters for the reservoir simulator are shown in Table 6.4. The viscosities of oil and water are, respectively, $\mu_w = 0.5$ cp and $\mu_o = 3.0$ cp. We used the pressure data from the IFPT after 0.5 hours for each period as we used before. Fig. 6.34 and Fig. 6.35 show the results using power law relative permeabilities. After nonlinear regression, as we expected, Fig. 6.34 shows that there is a good match of bottomhole pressure. Our estimate of bottomhole pressure (solid curve) exactly covers the observed pressure data (dashed curve) and our initial pressure (squared data points) is far from the observed pressure. Fig. 6.35 shows that our estimated relative permeability curves (solid curves) are in good agreement with the true relative permeability curves (circle points). Our estimate of the endpoint value of water-phase relative permeability is 0.48 compared with the true value of 0.5. We also obtained good estimates of absolution permeability $k = 300.6$ md and skin factor $s = 4.6$ compared with true values of $k = 300$ md and $s = 5.0$, as shown in Table 6.6.

parameter	k, md	Skin Factor	$k_{rw}(1 - S_{or})$	n_w	n_o
True	300	5.0	0.5	2.0	2.0
Initial Guess	600	0	0.8	1.2	1.2
IFPT (Power Law)	300.6	4.68	0.48	2.08	2.01
IFPT (B-spline)	300.3	4.99	0.48	-	-

Table 6.6: Estimates of model parameters based on the approximate analytical solution without capillary pressure effect for the IFPT with a multirate production.

Fig. 6.36 shows the estimate of relative permeability curves based on the B-spline model. As shown in Fig. 6.36, we obtained a good match between our estimate of the relative permeabilities (solid curve) and the true relative permeabilities (circle points). Table 6.6 shows that we also obtained good estimates of absolution permeability $k = 300.6$

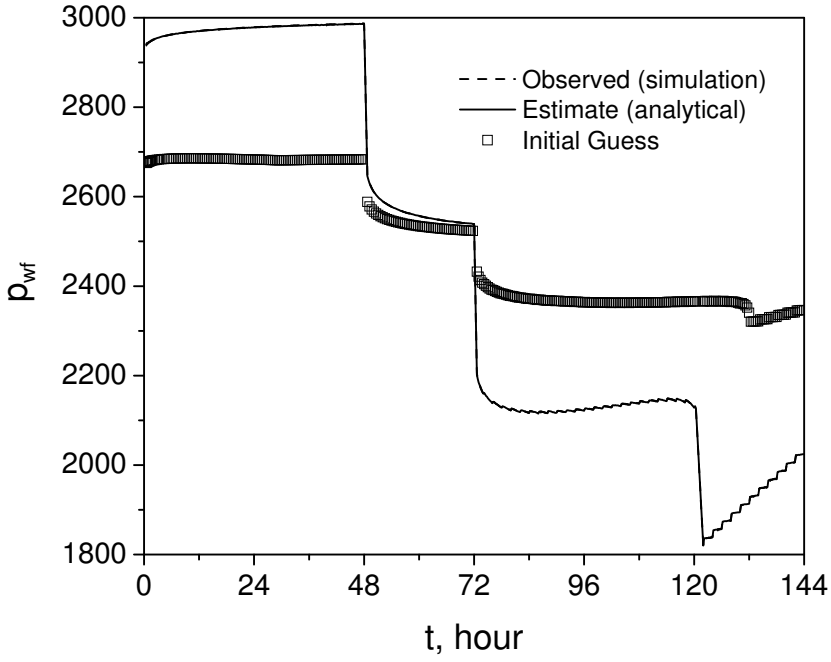

Figure 6.34: Bottomhole pressure match based on approximate analytical solution of the IFPT with multirate production, power law relative permeability ($\hat{M} = 3.0$).

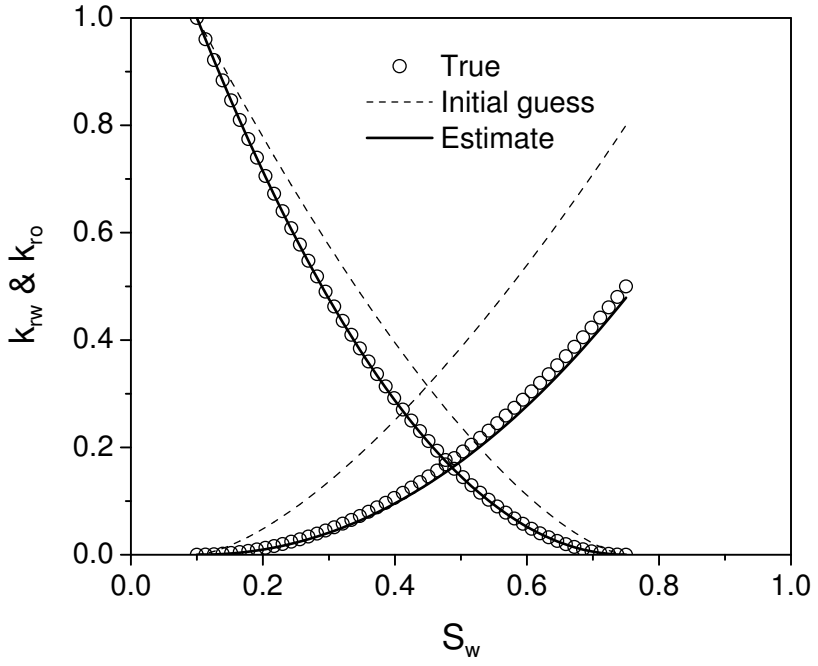

Figure 6.35: Estimate of relative permeabilities based on approximate analytical solution of the IFPT with multirate production, power law relative permeability ($\hat{M} = 3.0$).

md and skin factor $s = 4.6$ compared with true values of $k = 300$ md and $s = 5.0$.

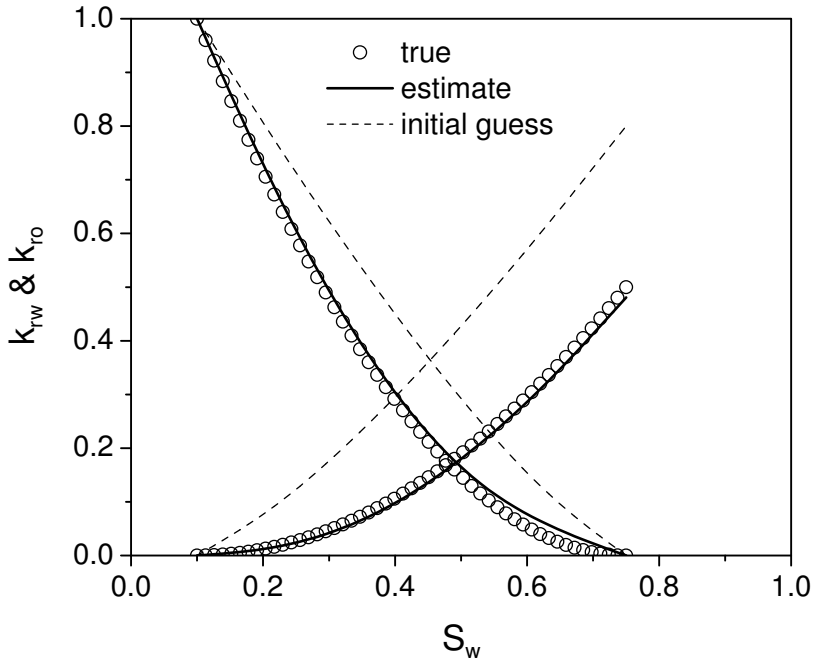

Figure 6.36: Estimate of relative permeabilities based on approximate analytical solution of the IFPT with multirate production, B-spline relative permeability ($\hat{M} = 3.0$).

6.4 Estimate of Relative Permeabilities Including Capillarity

In this section, we use the nonlinear regression to estimate both the relative permeability curves and the capillary pressure curve based on the model set up between capillary pressure and relative permeabilities stated in the Chapter 4. In this case, the true (noise free) pressure data is generated by running the reservoir simulator IMEX based on the parameters in Table 6.4. The observed pressure generated by adding noise to the true data where the noise is simulated from a Gaussian with zero mean and a standard deviation of 0.25 psi. The true capillary pressure and relative permeabilities are generated by Eq. 4.44, Eq. 4.46 and Eq. 4.47, respectively, with the true model parameters shown in Table 6.7. In this case, we fixed irreducible water saturation, S_{iw}, and residual oil saturation, S_{or} to their true values, respectively, as shown in Table 6.7, in which "fixed" means the corresponding parameter value is fixed to the true value. In this case, the forward models of capillary pressure and relative permeabilities defined by Eqs. 4.44, 4.46

and 4.46, respectively, are used to resolve our analytical solution. The pressure response is based on generated the saturation profile during production analytically and the applying the analytical solution of Eq. 2.81. We refer to this as the Numerical-analytical solution. After nonlinear regression, a good match of bottomhole pressure is obtained as shown in Fig. 6.37. Fig. 6.38 shows the estimate of capillary pressure. Our esti-

parameter	k, md	Skin Factor	a_w	p_e	λ	S_{iw}	S_{or}
True	300	5.0	0.8	1.0	2.0	0.1	0.25
Initial Guess	600	0	0.5	2.0	5.0	0.1	0.25
Estimate (IFPT)	308.1	5.2	0.78	0.98	2.05	fixed	fixed

Table 6.7: Estimates of model parameters for from capillary pressure to relative permeability.

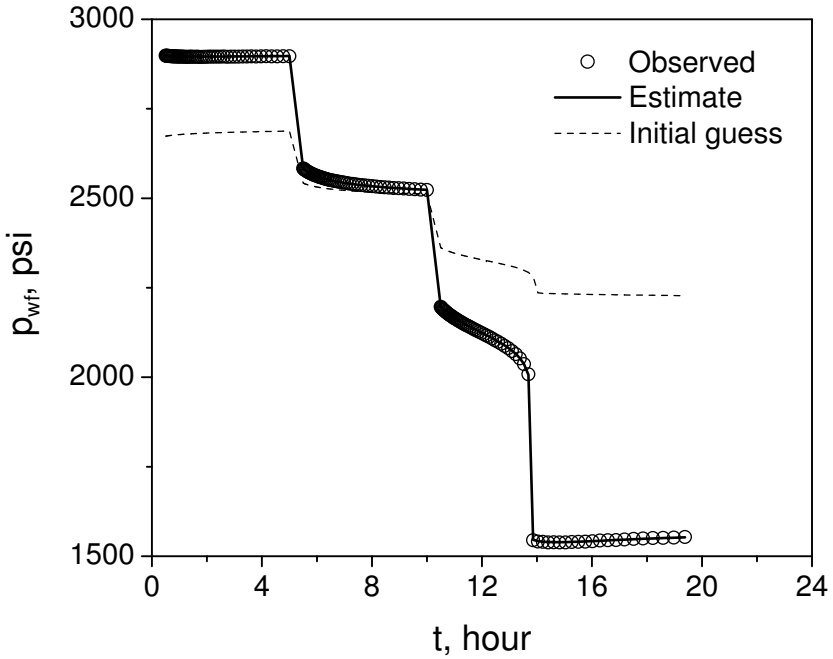

Figure 6.37: Bottomhole pressure match based on approximate Numerical-analytical solution with capillary pressure effects ($\hat{M} = 3.0$).

mate of capillary pressure (solid curve) has a good agreement with the true capillary pressure (circled points). Fig. 6.39 shows that we also is in good estimate of the relative permeability curves. Our estimate (solid curves) almost mirror the true (circled points). Compared with the true values, the other estimates of model parameters are also good.

The estimates are: the endpoint value of water relative permeability $a_w = 0.78$, absolute permeability $k = 308.1$ md, skin factor $s = 0.5$, entry capillary pressure $p_e = 0.1$ and pore size distribution index $\lambda = 2.05$ as shown in Table 6.7.

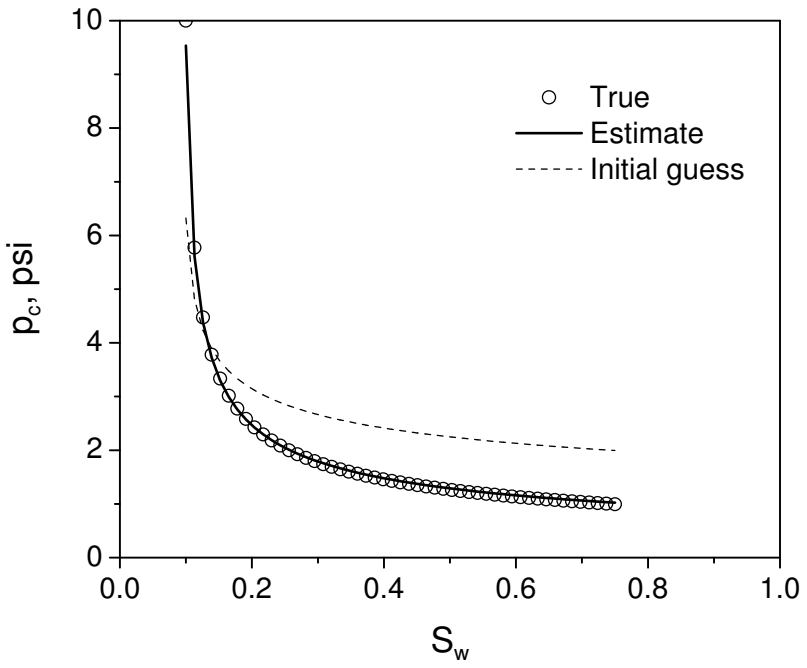

Figure 6.38: Estimate of capillary pressure based on approximate Numerical-analytical solution considering capillary pressure effects ($\hat{M} = 3.0$).

Fig. 6.40 and Fig. 6.41 show the results from analyzing data using the analytical solution which neglects capillary pressure effect. We used the flexible B-spline representing the relative permeability curves. After the nonlinear regression, Fig. 6.40 shows that the predicted pressure data (solid curves) are in good agreement with the observed pressure data (circle points). However, we did not obtain a good agreement of relative permeability curves between our estimate (solid curves) and the true curves (circle points) as shown in Fig. 6.41. Table 6.8 shows that we only have good estimates of absolute permeability, $k = 308.8$ md, and skin factor, $s = 4.6$, compared with the true values of $k = 300$ md and $s = 5.0$, respectively. The estimate of endpoint value of water relative permeability is $a_w = 0.665$ compared with the true of $a_w = 0.8$.

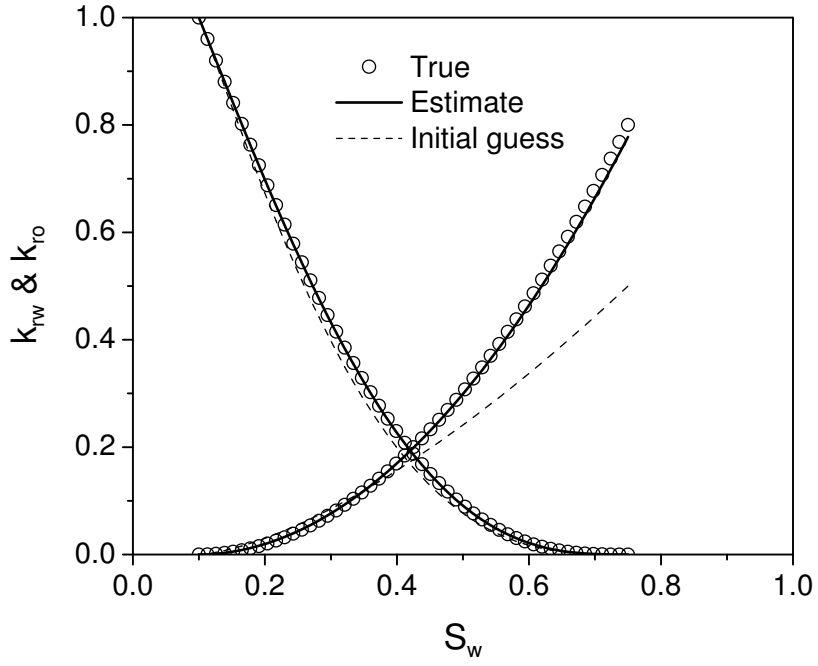

Figure 6.39: Estimate of relative permeabilities based on approximate Numerical-analytical solution with capillary pressure effects ($\hat{M} = 3.0$).

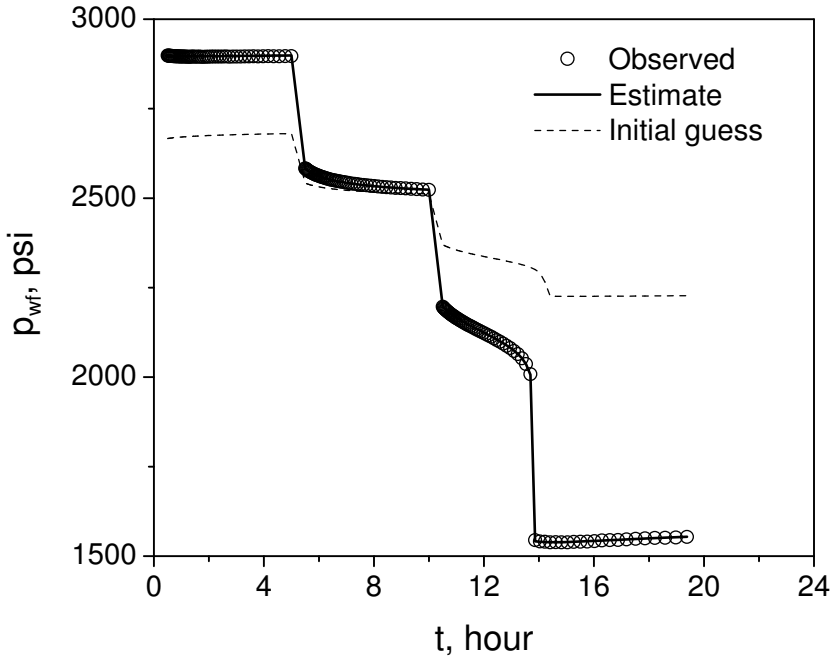

Figure 6.40: Bottomhole pressure match based on analytical solution neglecting capillary pressure effects matching pressure data with capillary pressure effects, B-spline relative permeability curves; IFPT ($\hat{M} = 3.0$).

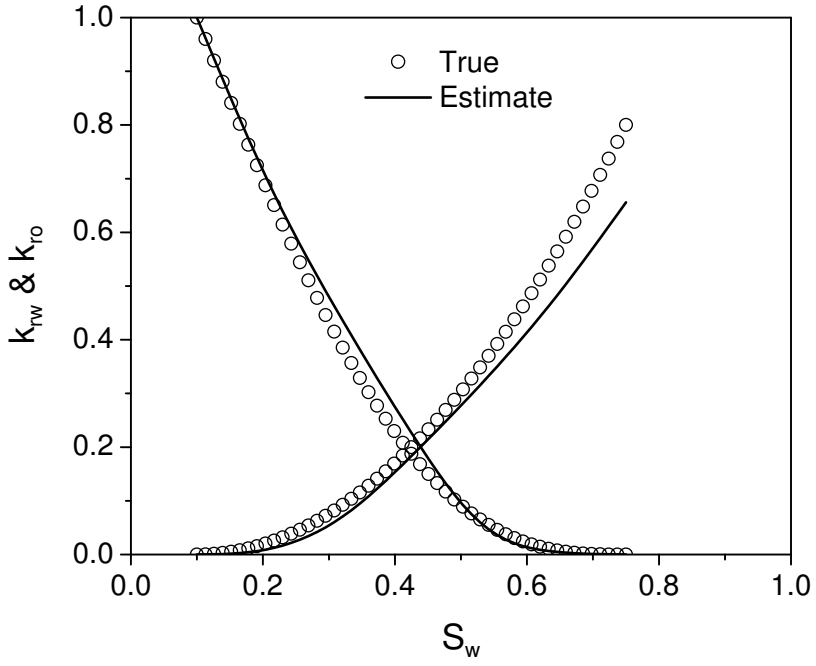

Figure 6.41: Estimate of relative permeabilities based on analytical solution neglecting capillary pressure effects matching pressure data with capillary pressure effects; B-spline relative permeability curves; IFPT ($\hat{M} = 3.0$).

parameter	k, md	Skin Factor	a_w	p_e	λ	S_{iw}	S_{or}
True	300	5.0	0.8	1.0	2.0	0.1	0.25
Initial Guess	600	0	0.5	–	–	0.1	0.25
Estimate (IFPT)	308.8	4.6	0.66	–	–	fixed	fixed

Table 6.8: Estimates of model parameters based on analytical solution neglecting capillary pressure effects matching pressure data with capillary pressure effects; B-spline relative permeability curves; IFPT ($\hat{M} = 3.0$).

6.5 Comments on Hysteresis, Heterogeneity and Flow Rate Fluctuation

In practice, observed data would be affected by some factors such as reservoir heterogeneity, hysteresis and non-constant flow rate. In the following, we give some discussions on hysteresis and show some results from synthetic cases related to heterogeneity and flow rate fluctuation.

6.5.1 Hysteresis Effect

During this special test, the IFPT, the directions of flow are difference during water injection and oil flowing back to the well and hence involve two different processes, imbibition and drainage. Thus there is a question as to whether we need to incorporate hysteresis effect in the estimated relative permeabilities.

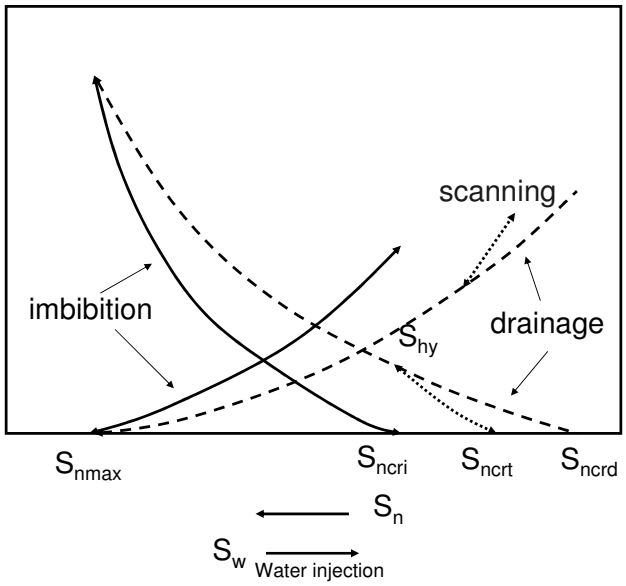

Figure 6.42: Hysteresis of relative permeability curves (Kilough's model).

Many authors have proposed some models to deal with hysteresis [33, 18, 31, 13, 6]. Experiments show that the hysteresis of the wetting phase relative permeability curve is generally small. This fact is used by many hysteresis models (see references [18, 6]), which assumes no hysteresis on the wetting phase relative permeability curves, although Killough [31] model (Fig. 6.42) considers hysteresis on both wetting and non-wetting phase relative permeability curves. For the non-wetting phase relative permeability curves, hysteresis models generally assume that the scanning curves are reversible, and this assumption has some theoretical rationale [13]. As shown in Fig. 6.42, generally, we assume that the oil originally reached the reservoir by a drainage process assuming water is the wetting phase. The saturation change follows the drainage curves, and non-wetting oil phase saturation increases to its maximum saturation $S_{nmax} = 1 - S_{iw}$ at the end of this process

in the reservoir. The oil relative permeability is at end point value assuming water now is at irreducible saturation ($S_{iw} = 1 - S_{nmax}$). So the process of injecting water into the reservoir is an imbibition process and the oil flow will follow the same imbibition relative permeability curves. After water injection, wetting phase (water) saturation distribution is between $S_{iw} = 1 - S_{nmax}$ and $1 - S_{ncri}$, where S_{ncri} is the residual non-wetting phase saturation. Because of the reversibility of the hysteresis model on the non-wetting phase (oil in our case), the oil flow during production (drainage process) will follow the imbibition relative permeability curve that was followed during water injection for oil saturation between S_{nmax} and S_{ncri}. For the non-wetting phase (oil) between saturation S_{ncri} and S_{ncrd}, oil relative permeability will follow the scanning curves (the dotted curves, like the on shown in Fig. 6.42) first, then follow the primary drainage curves. We know that all non-wetting phase (oil) saturations are between $S_{iw} = 1 - S_{nmax}$ and $1 - S_{ncri}$, so all these saturations will follow the special scanning curves - the imbibition curves. Therefore, with many relative permeability hysteresis models, the injection/falloff/production test sequence is not affect by the hysteresis.

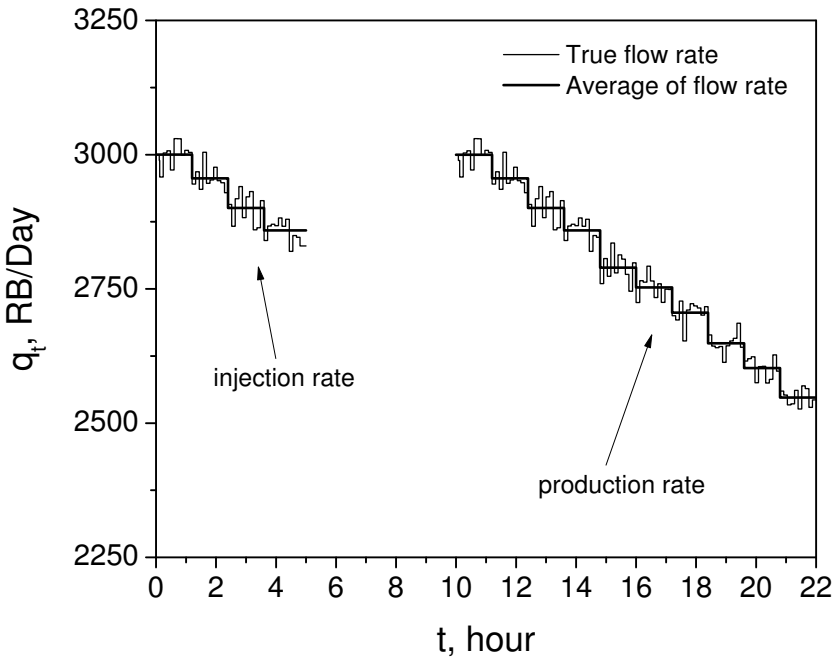

Figure 6.43: Injection rate and production for case of flow rate fluctuation, $\hat{M} = 4.0$.

6.5.2 Flow Rate Fluctuation Effect

During water injection and oil production, it is hard to keep a constant flow rate for a long time. In this work, the effect of a nonconstant flow rate is investigated using a synthetic case with a sequence of 5-hour injection, 5-hour falloff and 14-hour production. The true parameters and parameters for the reservoir simulator are shown in Table 6.1. In Fig. 6.43, the observed injection rate and production flow rate are represented by the finer solid lines which are constant on each 0.12 hours time interval. The observed flow rates were generated by adding noise to specified rates which are constant on each 1.2 hours interval as shown by the thicker solid lines in Fig. 6.43. The standard deviation of the added noise is 25 RB/Day. The flow rate difference between two neighboring 1.2 hour rates is 50 RB/Day. The noisy observed data give the same cumulative water injected during injection and the same cumulative oil and water production during the flow back period. The observed data, we use are pressure data generated from the noisy flow rates. We also added an additional noise simulating Gaussian distribution with mean zero and a standard deviation of 0.25 psi to the pressure data. We use, however, the step

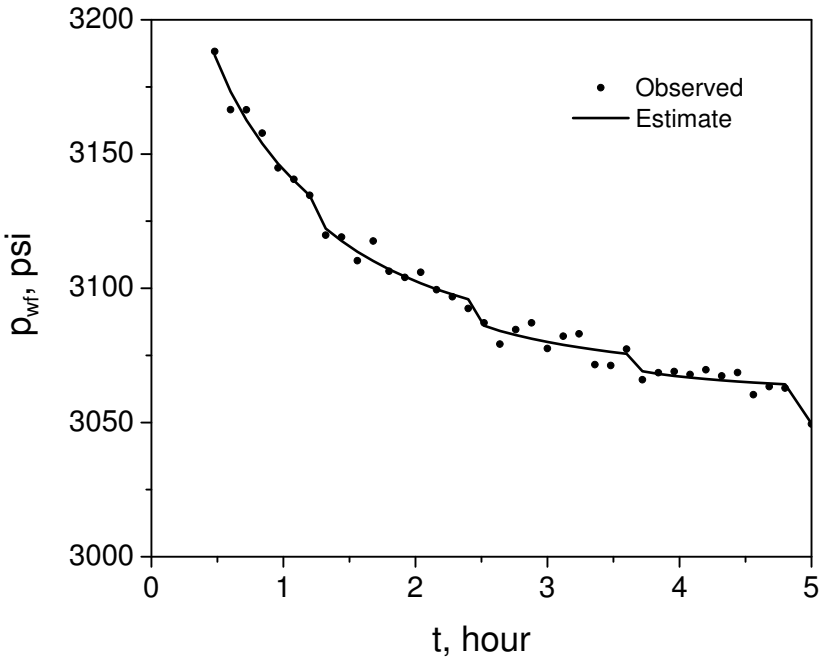

Figure 6.44: Injection pressure match, multirate problem, $\hat{M} = 4.0$.

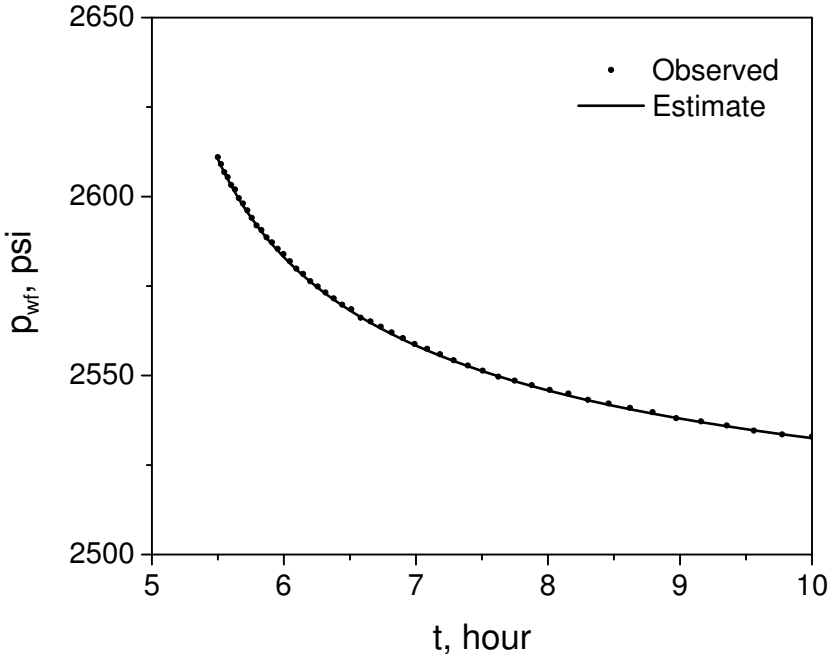

Figure 6.45: Falloff pressure match for case of flow rate fluctuation effect, $\hat{M} = 4.0$.

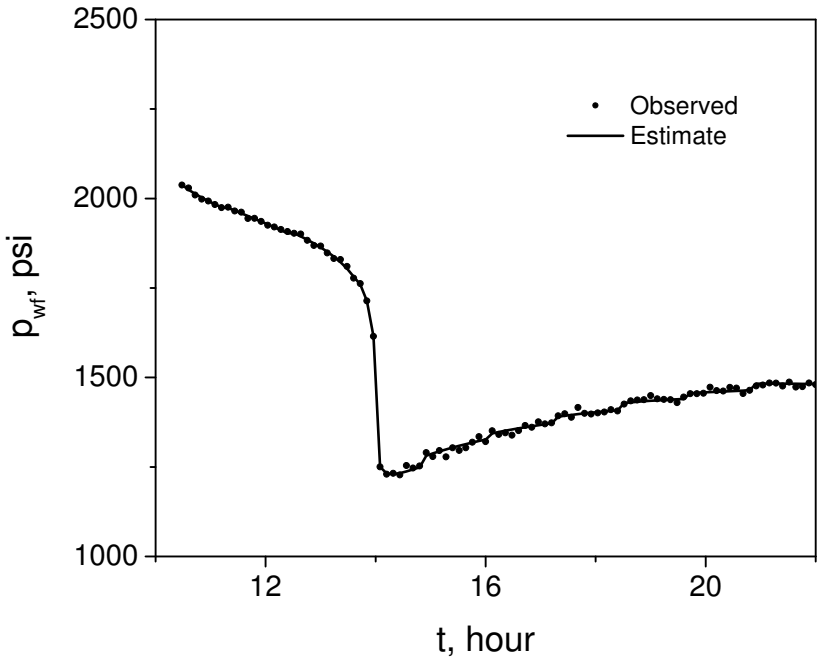

Figure 6.46: Production pressure match for case of flow rate fluctuation effect, $\hat{M} = 4.0$.

flow rates that are constant on each 1.2 hours interval during the estimation of relative permeabilities and other model parameters. Fig. 6.44 shows the pressure data match

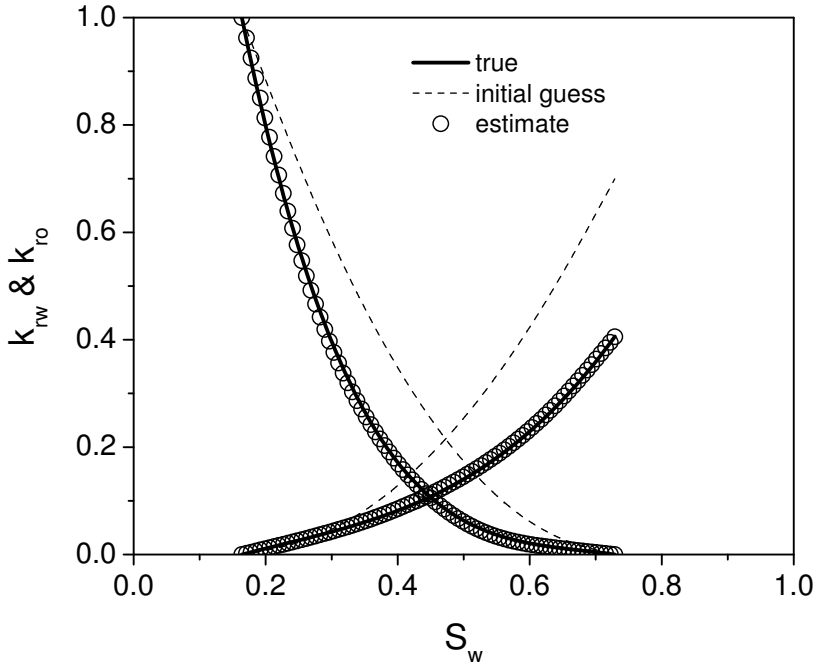

Figure 6.47: Estimate of relative permeability curve for case of flow rate fluctuation effect, $\hat{M} = 4.0$.

during injection. The estimate of pressure response (the solid curve) traces the oscillated observed pressure (the dotted data) very well. In Fig. 6.46, which shows the pressure data match during production, the pressure response, the solid curve, from the estimates based on the flow rate steps is in good agreement with the pressure response with oscillations corresponding to the noise in the measured flow rates. Fig. 6.45 shows that the predicted pressure data (solid curve) and observed pressure data (solid dots) are in good agreement during falloff. Because of zero flow rate, pressure data are smoother than the pressure data during injection and production periods. The estimate of relative permeability curves almost mirror the true relative permeability curves as shown in Fig. 6.47. The estimates of other parameters are $k = 373.7$ md and $s = 5.13$ compared to the true values of $k = 372$ md and $s = 5.14$. This case can tell us that the estimates of relative permeabilities and other model parameters are stable for fluctuations flow rates, at lease if the rate variations are not too large.

6.5.3 Heterogeneity Effect

Reservoir rock is always heterogeneous to some extent. Permeability heterogeneity affects the estimate of relative permeabilities based on our homogeneous model of the permeability field. In order to investigate the permeability heterogeneity effect, we specified different permeabilities in the different locations of the grid rings and generated a symmetric heterogeneous permeability field using sequential Gaussian simulation with a correlation length of 50 ft. The permeability has a mean $\ln k = 5.95$ (383.8 md) and a standard deviation of 0.25. We finally constructed the heterogeneous permeability field by averaging the permeability within some selected zones as shown in Fig. 6.48, which only shows the permeability field within 600 ft. The IFPT is a short time test; for this case, the water bank around wellbore after water injection is around 18 ft. The heterogeneity near the wellbore should have more effect than that far from the wellbore. Thus we actually introduced a higher heterogeneity in locations closer to the wellbore as shown in Fig. 6.48. The smallest heterogeneous zone around the well is 5 ft, except for the skin zone, which is 1.264 ft. Fig. 6.49 shows we obtained a good estimate of relative permeability curves. The estimate of absolute permeability of reservoir is $k = 378.5$ md, which is close to the true average permeability we expected $k = 383.8$ md. The estimate of skin is $s = 5.4$ compared to the true value of $s = 5.5$. In this work we did not consider the vertical heterogeneity.

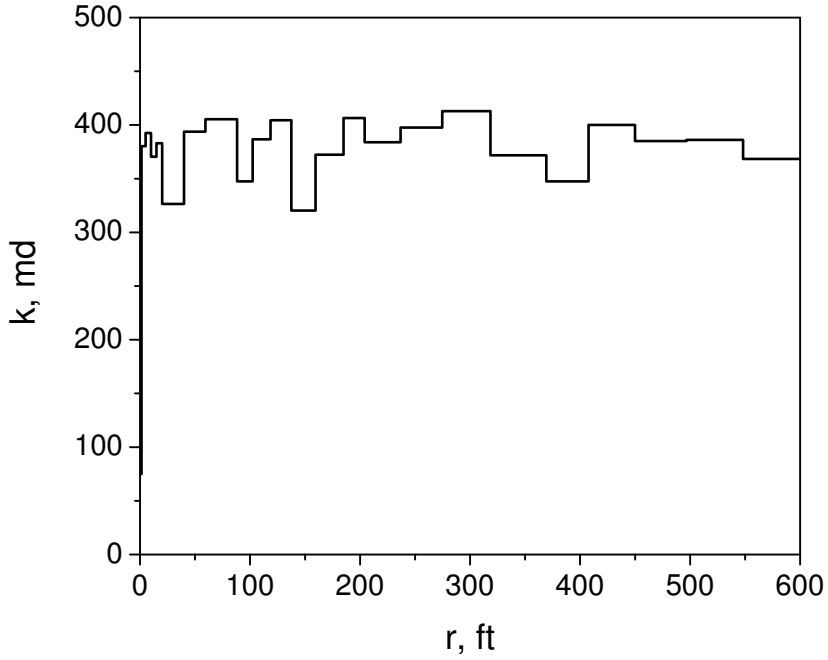

Figure 6.48: Heterogeneous permeability field.

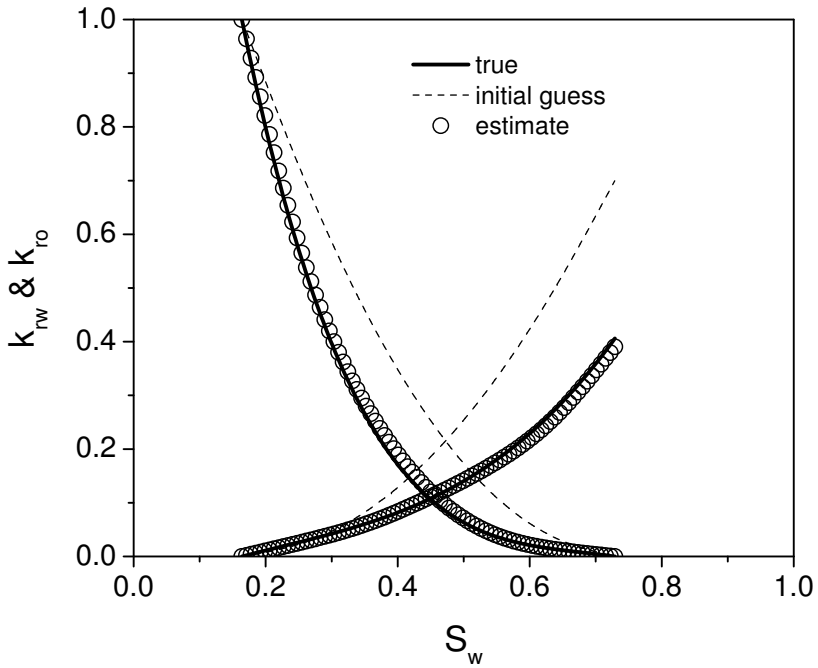

Figure 6.49: Estimate of relative permeability curve for case of permeability heterogeneity effect.

CHAPTER 7

DISCUSSION AND CONCLUSIONS

7.1 Conclusions

A novel two-phase pressure transient test – injection/falloff/production test (IFPT) is presented in this research. The IFPT has been applied to estimate relative permeability curves, absolute reservoir permeability and skin factor successfully for a wide variety of synthetic cases.

Through the theoretical study of the IFPT and the investigations of results from synthetic cases, we found that data from different periods of the IFPT provide specific information for estimating the relative permeabilities and other model parameters. The early time pressure data and the late time pressure data during water injection provide information representing oil properties and water properties, respectively. As envisioned, the injection period is relatively short, so most of the falloff data reflects oil mobility in that uninvaded zone. Thus the falloff data typically can only resolve endpoint oil mobility. During production, when oil flows back to the wellbore, the sandface is exposed to a wide range of saturation and total mobility changes, and thus pressure data provide significant information for estimating the shape of relative permeability curves. The results from cases in this research show that we can obtain a good estimate of endpoint value of water phase relative permeability, but we cannot obtain very good estimate of the shape of relative permeability curves when we use data from only the injection/falloff particularly if the injection period is short. If we use data from the production period, we can achieve a good estimate of relative permeability curves as well as other model parameters in all cases.

B-spline relative permeability curves are more flexible than power law relative permeability curves for representing arbitrary relative permeability curves. Our algorithm

based on the logarithm transform provides an efficient way to control monotonic or convex (concave up) relative permeability curves.

We presented an accurate analytical model describing the saturation evolution during production based on Buckley-Leverett [15] theory and the front tracking method without capillary pressure effect. Using the steady-sate theory of Thompson and Reynolds [55], the pressure response solution of Peres and Reynolds [46, 8], and our model of saturation evolution during production, we derived approximate analytical solutions for the pressure response during production, and showed that it is accurate by comparing the responses during production with results from the commercial reservoir simulator IMEX. Because of the assumption of the steady-state during production, which assumes a constant flow rate in the water bank immediately after a new period starts, our analytical solutions for pressure responses during the flow back period is not accurate at the very early times of this flow period. Falloff with rate superposition is accurate. Therefore, the larger the water bank, the longer this non-accurate period is. But the results from the nonlinear regression show that, for injection period of two days or longer, our analytical solution is valid for most of the flow period.

Capillary pressure causes some small smearing at the water front during production. During falloff, the flow rate is zero and capillarity diffusion is the dominant term, so the smearing around the water front becomes much more significant during falloff. The capillary smearing effect results in an earlier oil "breakthrough" time than for the case where there is no capillary effect. When the capillary force is strong, analyzing data using the analytical solution which neglects capillary pressure effects may yield inaccurate estimates of model parameters. Based on the finite difference method, our numerical solution of saturation evolution with effects of capillary pressure are accurate compared with the results from the reservoir simulator. Correspondingly, the approximate analytical solution considering capillary pressure effects is also valid to represent the pressure response and to estimate the relative permeabilities, absolute permeability and skin factor. During production, we noted that an oil front (shock) exists when oil flows back to the wellbore for both cases with and without capillary pressure effect. The shock causes a sharp change

in pressure response when it reaches the well because of the singularity in total mobility at the oil front (the location of shock).

Through the analysis of different hysteresis models, we found that the IFPT would not be affected by hysteresis when we assume a water wet reservoir. Imbibition relative permeability curves are always obtained. Second, simulating a flow rate fluctuation during water injection and production periods respectively by a synthetic case, we found that the estimates of relative permeabilities and other model parameters based on the IFPT with flow rate fluctuations are reasonable at least when rate fluctuations are not sever. Considering horizontal heterogeneity in reservoir absolute permeability, the results from a synthetic case show that analysis of IFPT data also results in good estimates of relative permeability curves and a reasonable estimate of average permeability.

7.2 Practical Comments

Despite the theoretical advantages of the injection/falloff/production test, a legitimate question exists as to whether this test can be run in practice. Although we can not provide a definite answer, we do provide some suggestions as to how such a test might be run.

7.2.1 Bottom-Hole Tool Assembly

The envisioned tool is a standard cased well testing tool string (packer, annular operated bottom-hole valve with accurate pressure and temperature gauges in real time mode or memory type gauges, circulating valves, etc.) plus a stationary bottom-hole hold-up measurement tool (optical/resistivity tool) similar to ones currently used in open hole wireline formation testers (WFT) and cased hole logging tools. Permanent pressure gauges and gradio sensors could be used to provide more accurate measurements of total flow rate water and water cut.

7.2.2 Surface Facilities

The simulated cases shown earlier in this paper indicate that during the backflow period the well initially produces essentially 100 per cent water for a time period that

may last a few hours followed by a very rapidly decreasing water cut. This behavior poses a real challenge to obtain an efficient and controlled fluid separation at the surface. Standard well testing three phase separators may not give reliable results for rapidly varying phase rates which would adversely affect flow rate measurements. Even though we are relying on bottom-hole hold-up measurements to constraint the relative permeability optimization problem, surface measurements are necessary to estimate total flow rate as well as provide an independent check on cumulative fluid production. Thus, a carefully designed surface well test plan to achieve accurate flow measurements and to comply to regulatory disposal standards is critical if the test proposed in this paper is to be run in practice. Such a plant might include, among other components, a heater (especially for viscous oil), highly efficient burners and fluid tanks for fluid metering calibration, storage and disposal and chemical injection pumps for foam control. In-line multiphase flow meters before separation and cyclone separators could be considered as well.

7.2.3 Other Important Concerns

Although we have illustrated that the test and analysis of data are applicable under reasonable fluctuations in flow rate, large rapid changes in flow rates could reduce the accuracy of the parameter estimates. Thus, we recommend trying to maintain a fairly stable total flow rate during the flow back period. Perhaps the best procedure to control production is to install an artificial lift system, such as an electrical submersible pump, in the test string. For a deepwater offshore well such a pump installed at subsea X-tree may prove sufficient to keep the total flow rate fairly constant.

NOMENCLATURE

B_j = B-spline basis function

c_o = oil compressibility

c_o = water compressibility

c_r = rock compressibility

c_t = total compressibility

C_o^i = control point of oil relative permeability curve

C_w^i = control point of water relative permeability curve

C_D = covariance matrix

d_{obs} = observed data

d_{pred} = data predicted based on estimated model parameters

$f_w(S_w)$ = water fractional flow

$f_w^{'}$ = derivative of water fractional flow

$f_o(S_o)$ = oil fractional flow

$F_w = \dfrac{q_w}{q_t}$, total fraction flow with capillary pressure effect

G = sensitivity coefficient

I = identical matrix

H = Hessian matrix

J = Jacobian matrix

h = reservoir thickness

k = absolute permeability, md

k_s = absolute permeability of damaged zone, md

k_{rw} = water relative permeability

k_{ro} = oil relative permeability

m = model parameter

$\hat{M}$ = mobility ratio

$O(m)$ = objective function based on model parameter m

p_c = capillary pressure, psi

$p_c^{'}$ = derivative of capillary pressure with respect to water saturation

Δp = pressure difference, psi

p_e = entry pressure for capillary pressure, psi

p_i = initial reservoir pressure, psi

p_{wf} = wellbore pressure, psi

$p_{wf,s}$ = final injection pres sure, psi

$p_{wf,f}$ = final falloff pressure, psi

$p_{\text{pred}}(m)$ = predicted pressure data based on model parameter m

q_{inj} = water injection rate, RB/Day

q_s = single phase oil flow rate, RB/Day

q_t = total wellbore production rate, RB/Day

$Q_{\text{pred}}(m)$ = predicted cumulative oil production

Q_{obs} = observed cumulative oil production

r_w = wellbore radius

r_s = radius of damaged zone

r_{wf} = radius of water front during injection/falloff

r_{of} = radius of oil front during production

s = skin factor

S_w = water saturation

S_o = oil saturation

S_{wD} = dimensionless water saturation

S_{iw} = irreducible water saturation

S_{or} = residual oil saturation

t_e = Agarwal's equivalent time

u_j = knot of B-spline

GREEK

α = unit conversion constant, in oil field units

$\alpha = 141.2$

β = unit conversion constant, in oil field units

$\beta = 2.637 \times 10^{-4}$

σ_p = standard deviation of pressure measurement error, psi

σ_Q = standard deviation of measurement error in cumulative oil production, STD

$\hat{\lambda}_w$ = endpoint water mobility at $S_w = 1 - S_{or}$

$\hat{\lambda}_o$ = endpoint oil mobility at $S_w = S_{iw}$

$\hat{\lambda}_o^{'}$ = derivative of oil mobility with respect to water saturation

λ_t = total mobility

μ_o = oil viscosity

μ_w = water viscosity

ϕ = porosity

θ = unit conversion constant, in oil field units

$\theta = 5.6146/24$

BIBLIOGRAPHY

[1] Y. Abacioglu, D. S. Oliver, and A. C. Reynolds. Efficient reservoir history matching using subspace vectors. *Computational Geosciences*, 5(2):151–172, 2001.

[2] M. Abbaszadeh and M. Kamal. Pressure-transient testing of water injection wells. *SPE Reservoir Engineering*, 4(1):115–124, 1989.

[3] Ram G. Agarwal. A new method to account for producing time effects when drawdown type curves are used to analyze pressure buildup and other test data. *SPE9289*, 1980.

[4] J. S. Archer and S. W. Wong. Use of a reservoir simulator to interpret laboratory waterflood data. *Soc. Petrol. Eng. J*, 12(6):343–347, 1973.

[5] Khalid Aziz and A. Settari. *Petroleum Reservoir Simulation*. Elsevier Applied Science Publishers, London, 1979.

[6] P. Bedrikovetsky, D. Marchesin, and P.R. Ballin. Mathematical model for immiscible displacement honouring hysteresis. *SPE-36132*, 1996.

[7] A. Boughrara and A. C. Reynolds. Injection/falloff testing of restricted-entry vertical wells. *TUPREP Research Report 22*, pages 10–58, 2005.

[8] A. A. Boughrara, A. M. M. Peres, S. Chen, A. A. V. Machado, and A. C. Reynolds. Approximate analytical solutions for the pressure response at a water injection well). *SPE Journal*, 12(1):19–34, 2007.

[9] Amina Boughrara. *Injection/Falloff Testing of Vertical and Horizontal Wells*. PhD thesis, U. of Tulsa, 2007.

[10] F. Bratvedt, K. Bratvedt, C.F. Buchholz, L. Holden, and H. Holden. A new front-tracking method for reservoir simulation. *SPE Reservoir Engineering*, pages 107–116, 1992.

[11] F. Bratvedt, T. Gimse, and C. Tegnander. Streamline computations for porous media flow including gravity. *Transport in Porous Media*, 25(1):63–85, 1996.

[12] R. B. Bratvold and R. N. Horne. Analysis of pressure-falloff tests following cold water injection. *SPE Formation Evaluation*, 5(3):293–302, 1990.

[13] E.M. Braun and R.R. Holland. Relative permeability hysteresis: Laboratory measurements and a conceptual model. *SPE Reservoir Engineering*, pages 222–228, August 1995.

[14] R. H. Brooks and A. T. Corey. Properties of porous media affecting fluid flow. *J. of Irrig. Drain. Div.*, 219, 1966.

[15] S.E. Buckley and M.C. Leverett. Mechanism of fluid displacement in sands. *Trans. AIME*, 146:107–116, 1942.

[16] R. L. Burden, J. D. Faires, and A. C. Reynolds. *Numerical Analysis*. Prindle, Weber & Schmidt, Boston, 1978.

[17] N. T. Burdine. Relative permeability calculations from pore size distribution data. *Trans. AIME*, 198, 1953.

[18] Francis M. Carlson. Simulation of relative permeability hysteresis to the nonwetting phase. *SPE 10157*, 1981.

[19] Shi Chen, Gaoming Li, Peres A. M. M, and A. C. Reynolds. A well test for in situ determination of relative permeability curves. In *2004 SPE Annual Technical Conference and Exhibition*, 2005.

[20] Shi Chen, Gaoming Li, and A. C. Reynolds. An in situ test for the estimation of relative permeabilities: An approximate analytical solution for the wellbore pressure. In *TUPREP Research Report 23*. The University of Tulsa, 2006.

[21] Shi Chen and A. C. Reynolds. Numerical well testing for multiphase flow problems. *TUPREP Research Report 21*, pages 310–355, 2004.

[22] A. T. Corey. The interrelation between gas and oil relative permeabilities. *Prod. Mon.*, 19, 1954.

[23] C. Dafermos. Polygonal approximation of solutions of the initial value problem for a conservation law. *J. Math. Anal.*, 38:33–41, 1972.

[24] Carl de Boor. *A Practical Guide to Splines*. Springer, New York, New York, 1978. 392 p.

[25] Dimitry Eydinov, Shi Chen, Guohua Gao, and A. C. Reynolds. Estimating relative permeabilities by history matching field data. In *TUPREP Research Report 22*. The University of Tulsa, 2005.

[26] Roger Fletcher. *Practical Methods of Optimization*. John Wiley & Sons, New York, second edition, 1987.

[27] Guohua Gao and A. C. Reynolds. An improved implementation of the LBFGS algorithm for automatic history matching. *SPE Journal*, 11(1):5–17, 2006.

[28] M. F. Jr. Hawkins. A note on the skin effect. *Trans. AIME*, 207:356–357, 1956.

[29] R. Juanes and T.W. Patzek. Analytical solution to the riemann problem of three-phase flow in porous media. *Transport in Porous Media*, 55:47–70, 2004.

[30] P. D. Kerig and A. T. Watson. Relative-permeability estimation from displacement experiments: An error analysis. *SPE Res. Eng.*, 1(1):175–182, 1986.

[31] J. E. Killough. Reservoir simulation with history-dependent saturation functions. *SPEJ*, 37:37–48, 1976.

[32] K. N. Kulkarni and Akhil Datta-Gupta. Estimating relative permeability from production data: A streamline approach. *SPE Journal*, 5(4):402–411, 2000.

[33] C. E. Land. Calculation of imibition relative permeability for two- and three-phase flow from rock properties. *SPEJ*, June 1968.

[34] Jefrey M. Lane and Richard F. Reisenfeld. A geometric proof for the variation diminishing property of B-spline approximation. *Journal of Approximation Theory*, 37(1):1–4, 1983.

[35] Tai-Yong Lee and John H. Seinfeld. Estimation of absolute and relative permeabilities in petroleum reservoirs. *Inverse Problems*, 3(4):711–728, 1987.

[36] Kenneth Levenberg. A method for the solution of certain non-linear problems in least squares. *Quarterly of Applied Mathematics*, 2:164–168, 1944.

[37] Michael. M. Levitan. Application of water injection/falloff tests for reservoir appraisal: New analytical solution method for two-phase variable rate problems (SPE 77532). *SPE J.*, 8(2):147–159, 2002.

[38] Kewen Li. Generalized capillary pressure and relative permeability model inferred from fractal. *SPE-89874*, 2004.

[39] Kewen Li and Roland N. Horne. Numerical simulation with input consistency between gapillary pressure and relative permeability. *SPE-79716*, 2003.

[40] Ruijian Li, Albert C. Reynolds, and Dean S. Oliver. Sensitivity coefficients for three-phase flow history matching. *J. Canadian Pet. Tech.*, 42(4):70–77, 2003.

[41] Donald W. Marquardt. An algorithm for least-squares estimation of nonlinear parameters. *J. Soc. Indust. Appl. Math.*, 11(2):431–441, 1963.

[42] Jorge Nocedal. Theory of algorithms for unconstrained optimization. In *Acta Numerica (1991), Cambridge University Press, London*, pages 199–244, 1992.

[43] Jorge Nocedal and Stephen J. Wright. *Numerical Optimization*. Springer, New York, 1999.

[44] Donald W. Peaceman. *Fundamentals of Numerical Reservoir Simulation*. Elsevier Scientific Publishing Company, 1977.

[45] A. M. M. Peres, A. Boughrara, and A. C. Reynolds. Rate superposition for generating pressure falloff solutions for vertical and horizontal wells (SPE-90907). *TUPREP Research Report 21*, pages 268–309, 2004.

[46] A. M. M. Peres and A. C. Reynolds. Theory and analysis of injectivity tests on horizontal wells. *SPE J.*, 8(2):147–159, 2003.

[47] T.S. Ramakrishnan and D.T. Wasan. The relative permeability function for two-phase flow in porous media: Effect of capillary number. *SPE12693 SPE/DOE Fourth Symposium on Enhanced Oil Recovery*, 1984.

[48] T.S. Ramakrishnan and D.J. Wilkinson. Water-cut and fractional flow logs from array-induction measurements. *SPE Reservoir Eval. & Eng.*, 2:85–94, February 1999.

[49] Albert C. Reynolds, Ruijian Li, and Dean S. Oliver. Simultaneous estimation of absolute and relative permeability by automatic history matching of three-phase flow production data. *J. Canadian Pet. Tech.*, 43(3):37–46, 2004.

[50] David Salomon. *Computer Graphics and Geometeric Modeling*. Springer., New York, New York, 1999.

[51] P. M. Sigmund and F. G. McCaffery. An improved unsteady-state procedure for determining the relative-permeability characteristics of heterogeneous porous media. *Soc. Petrol. Eng. J.*, 19(1):15–28, 1979.

[52] K. Sovold, D.T. Rian, and A. Sandivk. Front tracking applied to simulation of water flodding in a braided river system. *SPE 21084*, October 1990.

[53] R. K. M. Thambynayagam. Analytical solutions for pressure buildup and falloff analysis of water injection tests of partially penetrating wells: Non-unit mobility ratios (SPE-12951). *Society of Petroleum Engineers Unsolicited Manuscript*, 1983.

[54] L. G. Thompson and A. C. Reynolds. Pressure transient analysis for gas condensate reservoirs. *In Situ*, 21(2):101–144, 1997.

[55] L. G. Thompson and A. C. Reynolds. Well testing for radially heterogeneous reservoirs under single and multiphase flow conditions. *SPE Formation Evaluation*, 12(1):57–64, 1997.

[56] N. N. Verigin. On the pressurized forcing of binder solutions into rocks in order to increase the strength and imperviousness to water of the foundations of hydrotechnical installations, (in Russian). *Akademija Nauk SSR Izvestija Odt. Tehn. Nauk*, 5:674–687, 1952.

[57] A. Ted Watson, J. H. Seinfeld, G. R. Gavalas, and P. T. Woo. History matching in two-phase petroleum reservoirs. *Soc. Petrol. Eng. J.*, 20(12):521–532, 1980.

[58] H.J. Welge. A simplified method for computing oil recoveries by gas or water drive. *Trans. AIME*, 195:91–98, 1952.

[59] Zhan Wu. *Conditioning Geostatistical Models to Two-Phase Flow Production Data*. PhD thesis, University of Tulsa, 1999.

[60] Pin-Huel Yang and A. Ted Watson. A Bayesian methodology for estimating relative permeability curves. *SPE Reservoir Engineering*, 6(2):259–265, 1991.

[61] Murat Zeybek, T.S. Ramakrishnan, Saud S. Al-Otaibi, Salam P. Salamy, and F.J. Kuchuk. Estimating multiphase-flow properties from dual-packer formation-tester interval tests and openhole array resistivity measurements. *SPE Reservoir Evaluation & Engineering*, pages 40–46, 2004.

[62] F. Zhang, A. C. Reynolds, and D. S. Oliver. Optimization algorithms for history matching. In *TUPREP Research Report 18*, pages 144–171. The University of Tulsa, 2001.

APPENDIX A

B-SPLINE MODEL OF RELATIVE PERMEABILITY CURVES

B-splines provide a very flexible way to define a parametric representation of a curve. Assuming the curve lies in the $x-y$ plane, we wish to define the x and y coordinates of points on the curve in terms of the parameter u so the curve is represented by $\overrightarrow{C}(u) = (x(u), y(u))$ for $u_{\min} \leq u \leq u_{max}$. Note $\overrightarrow{C}(u)$ is a two dimensional vector. To represent $\overrightarrow{C}(u)$ in terms of B-splines, we wish to define B-spline basis functions. For this purpose, we define discrete points (knots) on the u-domain by $u_0 < u_1 < u_2 < u_3 < \cdots < u_m$. Although it is sometimes advantageous to consider multiple knots which allows for the possibility that $u_j = u_{j+1}$ for some j's, in our application we only consider the case where $u_j < u_{j+1}$ for all j. Given the knots, the B-spline basis function $B_{j,p}$ is nonzero only on the interval $[u_j, u_{j+p+1}]$ and on each subinterval $[u_i, u_{i+1}]$ for $i = j, j+1, \cdots, j+p$, $B_{j,p}$ is a polynomial of degree p. Thus, $B_{j,p}$ is referred to as a B-spline basis function of degree p. Moreover, $B_{j,p}$ is in $C^{p-1}[u_0, u_m]$, i.e., has $p-1$ continuous derivatives on the whole u-domain. Thus, any linear combination of these basis function is a polynomial of degree p on each subinterval $[u_j, u_{j=1}]$ and has $p-1$ continuous derivatives on the whole u domain. We will refer to any linear combination of the basis functions as a B-spline.

For cubic B-splines (p=3), each $B_{j,3}$ has two continuous derivatives on $[u_0, u_m]$. As on each subinterval $[u_i, u_{i+1})$ for $i = j, j+1, \cdots, j+3$, $B_{j,3}$ is a cubic polynomial and hence infinitely differentiable, $\mathbb{C}^2$ continuity means that second derivatives exist and are continuous at the knots.

The basis functions $B_{j,p}$ are conveniently defined by the Cox-deBoor recursion

formulas, [24]. Specifically,

$$B_{j,0}(u) = \begin{cases} 1 & \text{if } u_j \leq u < u_{j+1} \\ 0 & \text{elsewhere,} \end{cases} \tag{A.1}$$

and

$$B_{j,p}(u) = \frac{(u-u_j)B_{j,p-1}(u)}{u_{j+p}-u_j} + \frac{(u_{j+p+1}-u)B_{j+1,p-1}(u)}{u_{j+p+1}-u_{j+1}}. \tag{A.2}$$

When $p = 1$, Eq. A.2 gives

$$\begin{aligned} B_{j,1}(u) &= \frac{u-u_j}{u_{j+1}-u_j}B_{j,0}(u) + \frac{u_{j+2}-u}{u_{j+2}-u_{j+1}}B_{j+1,0}(u) \\ &= \begin{cases} \frac{u-u_j}{u_{j+1}-u_j}, & u_j \leq u \leq u_{j+1}, \\ \frac{u_{j+2}-u}{u_{j+2}-u_{j+1}}, & u_{j+1} \leq u \leq u_{j+2}, \\ 0, & \text{elsewhere.} \end{cases} \end{aligned} \tag{A.3}$$

For the case of interest to us, we will use uniform knots, i.e., for some positive constant Δu, we will require that $u_{j+1} - u_j = \Delta u$ for all j. As noted in more detail later, this makes it quite easy to evaluate a function which is a linear combination of B-spline basis functions. The basis functions of the first, second and third degrees for the case of uniform knots are shown in Fig. A.1.

We assume that we wish to approximate a function defined on the interval $[a, b]$ by a B-spline. To define a B-spline requires that we define knots. For the case of uniform knots, we let $\Delta u = (b-a)/m$, where m is an arbitrary positive integer; larger values of m lead to more accurate approximations so ideally, m should be chosen as the smallest possible integer so that function of interest can be approximated sufficiently accurately with a B-spline based on m knots. Also, one expects, that we will need larger values of m if we use linear approximating B-splines than if we use cubic approximating B-splines.

We first define knots by $u_0 = a$ and $u_j = u_{j-1} + \Delta u$ for $j = 1, 2, \cdots m$. We focus on the cubic B-spline case. Any function which is a cubic B-spline on $[u_0, u_m]$ has two continuous derivatives on this interval and is a cubic polynomial on each subinterval

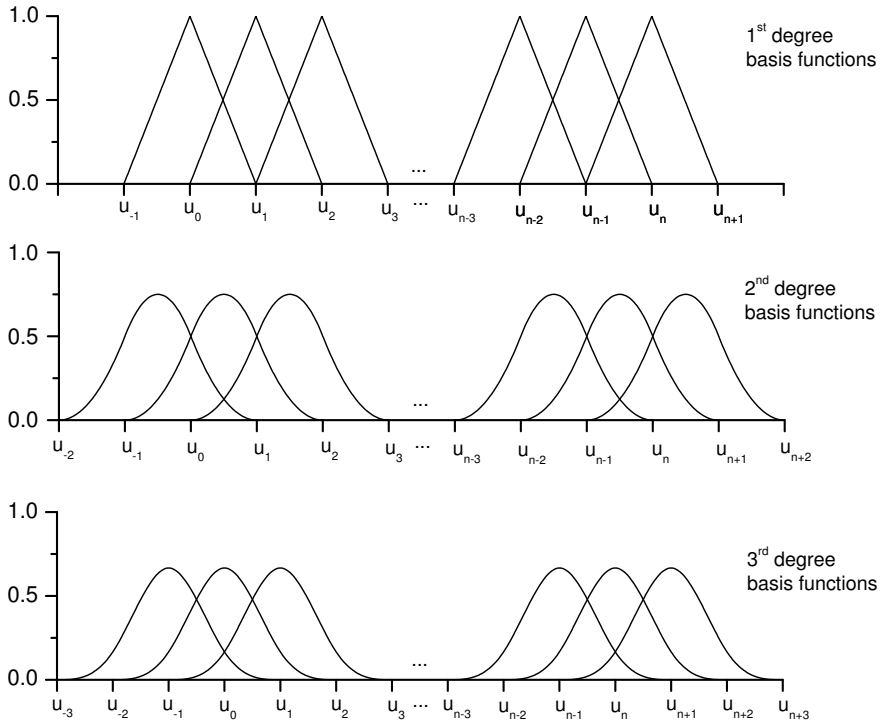

Figure A.1: Uniform B-spline basis functions.

.

$[u_j, u_{j+1}]$ for $j = 0, 1, \cdots, m-1$. These knots, however, are sufficient to define only the functions, $B_{j,3}$ for $j = 0, 1, \cdots m-4$. For example to define $B_{m-1,3}$, which is nonzero on the interval $[u_{m-1}, u_{m+3}]$ we need to define knots u_{m+1}, u_{m+2} and u_{m+3}. If we only wish to represent the function for $u \leq u_m = b$, the basis function $B_{m,3}$ does not need to be defined since it would be zero for $u \leq u_m = b$. For our purposes we define these additional knots to the right of b by $u_{m+i} = u_{m+i-1} + \Delta u$ for $i = 1, 2, 3$. At this point, the knots are sufficient to define the cubic B-splines basis functions, $B_{j,3}$ for $j = 0, 1, \cdots m-1$. These basis functions are not sufficient to form a basis for the set of all B-spline functions, however. This can be seen easily by noting that only one of these basis functions ($B_{0,3}$) is nonzero on $[u_0, u_1]$. Thus, we do not have enough basis functions to represent an arbitrary cubic function on $[u_0, u_1]$ and thus we need to add three additional basis functions. Defining three additional knots, $u_j = u_0 + j\Delta u$ for $j = -1, -2, -3$, we now have a set of basis functions, $B_{j,3}$ for $j = -3, -2, \cdots m-1$ and any B-spline, $P(u)$ defined on $[u_0, u_m]$ can be written as a linear combination of the basis B-splines, i.e., there exist constants a_j such

that for all u in $[u_0, u_m]$

$$P(u) = \sum_{j=-3}^{m-1} a_j B_{j,3}(u). \tag{A.4}$$

Note the number of knots, $(m+7)$ is equal to the number of basis functions $(m+3)$ in the sum plus the degree of the spline (3) + 1. More generally, letting n_k denote the number of knots, p the degree of the spline and n_c the number of spline basis functions, we must always have

$$n_k = n_c + p + 1, \tag{A.5}$$

in order to define a basis for the set of splines of degree p defined on the interval $[a, b]$ where $a = u_0 < u_1 < \cdots u_m = b$.

If the spline $P(u)$ defined in Eq. A.4 is to be an approximation to a function $f(u)$, the question becomes how to determine the a_j's. There is more than one method to do this, e.g., interpolation, least-squares. Also we can define the a_j's as control points. The latter is the method we will use. If $P(u)$ is the cubic interpolating spline for $f(u)$ on $[u_0, u_m]$, we require that P agree with f at the knots, i.e.,

$$P(u_j) = \sum_{j=-3}^{m-1} a_j B_{j,3}(u_j). \tag{A.6}$$

for $0 \leq j \leq m$. Note Eq. A.6 represents $m+1$ equations in $m+3$ unknowns (the a_j's) so we need two more conditions to obtain a system of $m+3$ equations in $m+3$ unknowns. Free boundary conditions refer to the case where we require that the second derivative of $P(u)$ is zero at u_0 and u_m and clamped boundary conditions refer to the case where we require that

$$\frac{dP(u_j)}{du} = \frac{df(u_j)}{du}\,, \text{ for } j = 0 \text{ and } j = m; \tag{A.7}$$

see, for example (see [16]). Note both sets of conditions refer to specifying derivatives at the endpoints of the interval of interest. When we use control points, the terminology clamped boundary conditions is used to refer to the case where the approximating spline passes through the first and last control points.

First degree B-splines are somewhat simpler in that we only need to define two

additional knots, u_{-1} and u_{m+1} to define $B_{j,1}$ $j = -1, 0, 1, \cdots m-1$ and then any linear B-spline defined on $[a, b] = [u_0, u_m]$ can be written as

$$P(u) = \sum_{j=-1}^{m-1} a_j B_{j,1}(u). \tag{A.8}$$

for $u_0 < u < u_m$. Here $n_k = m + 3$, $n_c = m + 1$ and $p = 1$ so Eq. A.5 holds. The linear interpolating spline of a function $f(u)$ defined on $[a, b]$ must now satisfy $P(u_j) = f(u_j)$ for $j = 0, 1, \cdots m$, i.e.,

$$\sum_{j=-1}^{m-1} a_j B_{j,1}(u_j) = f(u_j), \tag{A.9}$$

for $0 \leq j \leq m$. Note Eq. A.9 give $m + 1$ equations in the $m + 1$ unknowns and can be solved for the a_j's. In fact, because of the local nature of the linear B-spline basis functions (see Fig. A.1), we must have

$$a_j = f(u_j) \text{ for } j = 0, 1, 2 \ldots m. \tag{A.10}$$

Typical relative permeability curves can be accurately approximated by a linear B-spline if we use a sufficient number of knots. Cubic B-splines would require less knots to accurately approximate such curves. Moreover, if relative permeability curves are represented by smooth curves which have well defined continuous first and second derivatives, then it should be more appropriate to approximate a relative function with a B-cubic spline. Although, we will present results for both approaches, only the cubic B-spline case is discussed in detail.

Our objective is to estimate (or generate realizations of) relative permeability curves by history matching production data. For this purpose, we must parameterize the relative permeability curves. The parameters then will be estimated (or stochastically simulated) by history matching production data. Relative permeability curves should be monotonic functions and it appears that they are often (if not always) convex (concave up) functions. Unfortunately, if we approximate a relative permeability curve by an interpolating cubic spline of the form given in Eq. A.8 using the a_j's as parameters to

be adjusted in the history matching process, there appears to be no easy way to ensure that $P(u)$ is monotonic or that $P(u)$ is convex. If instead, we use an approximating B-spline based on control points with the control points representing parameters to be estimated (or stochastically simulated) by conditioning to production data, then it can be shown that the approximating B-spline is monotonic if the control points are monotonic and the approximating B-spline is convex if the control points are convex. A major contribution of this work is that we have been able to devise a simple method to constrain the control points to be monotonic or convex. (If the control points are convex, they are also monotonic.)

We started with the problem of constructing a parametric representation of curve using B-splines. Based on the same knot system described above, we can generate our approximate curve for $u_0 = u_{\min} \leq u \leq u_{\max} = u_m$ as

$$\overrightarrow{C}(u) = \sum_{j=-p}^{m-1} \overrightarrow{C}_{j+p-1} B_{j,p}(u), \tag{A.11}$$

where p is the degree. For cubic B-splines, $p = 3$ and for linear $p = 1$. These are the only two cases considered, when using B-splines to approximate relative permeability curves. The $\overrightarrow{C}_j$'s are specified control points and by specifying them one defines the parametric curve $\overrightarrow{C}(u) = (x(u), y(u))$. Denoting the number of control points by n_c, the number of knots is $n_k = m + 2p + 1$ and the number of controls points, denoted by n_c is given by $n_c = m + p$. This illustrates that Eq. A.5 holds where n_c denotes the number of control points which is identical to the number of B-spline basis functions in Eq. A.11. Note the control points are two-dimensional and can be written as $\overrightarrow{C}_j = (c_{x,j}, c_{y,j})$ and then the x and y coordinates, respectively, of points on the curve can be written as

$$x(u) = \sum_{j=-p}^{m-1} c_{x,j+p-1} B_{j,p}(u), \tag{A.12}$$

and

$$y(u) = \sum_{j=-p}^{m-1} c_{y,j+p-1} B_{j,p}(u). \tag{A.13}$$

In this notation, the total set of knots is given by $u_{j-p}, u_{j-p+1}, \cdots u_{m+p}$. For cubic B-splines, $p = 3$ and the $m + 3$ control points involved in Eqs. A.11 are $\overrightarrow{C_\ell}$, $\ell = -1, 0, 1, \cdots m, m+1$ The reason for using the different indexing for the spline basis functions and the control points will become apparent when we consider the representation of relative permeability curves.

In Fig. A.2 the control points $\overrightarrow{C}_j$, $j = 0, 1, \cdots, 7$ are represented by points connected by line segments and the curve represents the cubic B-spline curve defined by Eq. A.11 (the approximating B-spline) for values of u from u_0 to u_m. In this case, we have applied conditions, which are discussed later, to ensure that the curve passes through the first and last control point. Note the curve does not pass through any of the other control points but is "attracted" to these control points. Also note the control points are monotonically increasing, i.e., the curve defined by the connected line segments through control points (the control polyline) is monotonically increasing. As discussed in more detail, monotonic control points ensures the B-spline curve of Eq. A.11 is monotonic and convex control points ensures the B-spline curve is convex. This is the principle reason for using approximating B-splines defined by control points. On the other hand, interpolating B-splines are not necessarily monotonic and convex even, if the interpolation points satisfy these conditions. Fig. A.2 shows an interpolating B-spline which passes through the interpolating points (circles). The interpolation points are monotonic but note the B-spline is not; see the curve segment between interpolation points C_5 and C_6.

A.1 Evaluation of a Linear B-Spline

For the linear case, Eq. A.13 gives that

$$y(u) = \sum_{j=-1}^{m-1} c_{y,j} B_{j,p}(u), \tag{A.14}$$

for $u_0 \leq u \leq u_m$. If we wish to evaluate y at some u in $[u_0, u_m]$, we first find the subinterval

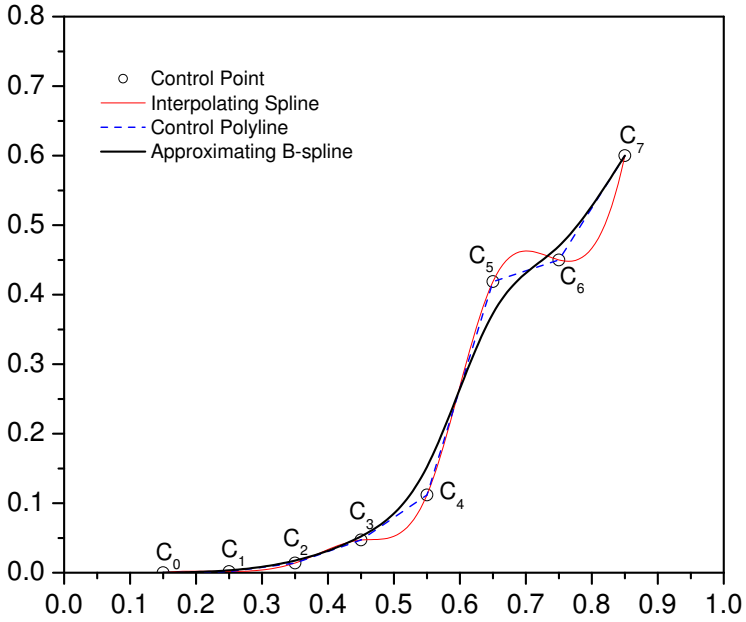

Figure A.2: Interpolating B-spline curve.

.

$[u_k, u_{k+1})$ that contains u. On this subinterval, all basis functions except $B_{k-1,1}$ and $B_{k,1}$ are nonzero and Eq. A.14 gives

$$y(u) = c_{y,k-1}B_{k-1,1}(u) + c_{y,k}B_{k,1}(u). \tag{A.15}$$

For $u_k \leq u < u_{k+1}$, Eq. A.3 gives

$$B_{k-1,1}(u) = \frac{u_{k+1} - u}{u_{k+1} - u_k}, \tag{A.16}$$

as well as

$$B_{k,1}(u) = \frac{u - u_k}{u_{k+1} - u_k}. \tag{A.17}$$

Using the values obtained from Eqs. A.16 and A.17 in Eq. A.15 gives $y(u)$. The value of $x(u)$ can be obtained in a similar manner. For linear B-splines, this procedure provides a reasonable way to evaluate the point $x(u)$ and $y(u)$. However, for higher degree splines

defined using uniform knots, it is convenient to use a transformation to evaluate a B-spline. For the linear case, the procedure simple defines

$$t = \frac{(u - u_k)}{u_{k+1} - u_k} = \frac{u - u_k}{\Delta u}, \tag{A.18}$$

so that

$$u = u_k + t\Delta u. \tag{A.19}$$

Note $u_k \leq u < u_{k+1}$ implies $0 < t < 1$. In terms of t Eq. A.17 is

$$B_{k,1}(u) = B_{k,1}(t) = t, \tag{A.20}$$

and Eq. A.16 is

$$B_{k-1,1}(u) = B_{k-1}(t) = 1 - t. \tag{A.21}$$

Defining $b_0(t) = 1 - t$ and $b_1(t) = t$, Eq. A.15 gives

$$y(u) = y(t) = c_{y,k-1}b_0(t) + c_{y,k}b_1(t). \tag{A.22}$$

Thus to evaluate $y(u)$ and $x(u)$ for any u, we need only compute t from Eq. A.18 for the appropriate value of k and then apply Eq. A.22.

A.2 Evaluation of a Cubic B-Spline

Using the Cox-deBoor recursion formula, basis function of degree p can be expressed as,

$$B_{j,p}(u) = \frac{(u - u_j)B_{j,p-1}(u)}{u_{j+p} - u_j} + \frac{(u_{j+p+1} - u)B_{j+1,p-1}(u)}{u_{j+p+1} - u_{j+1}}. \tag{A.23}$$

the zero degree basis function, $p = 0$, is given by

$$B_{j,0}(u) = \begin{cases} 1, & u_j \leq u < u_{j+1} \\ 0, & \text{otherwise.} \end{cases} \tag{A.24}$$

Eq A.24 indicates that the zero degree basis function is a piecewise constant function which is zero except on the interval. Based on Eqs. A.23 and A.24, when $p = 1$, we have, for $u_{j-1} \leq u < u_j$, $B_{j-1,0} = 1$ and $B_{j,0} = 0$ so that

$$\begin{aligned} B_{j-1,1}(u) &= \frac{u - u_{j-1}}{u_j - u_{j-1}} B_{j-1,0}(u) + \frac{u_{j+1} - u}{u_{j+1} - u_j} B_{j,0}(u) \\ &= \frac{u - u_{j-1}}{u_j - u_{j-1}}. \end{aligned} \tag{A.25}$$

For, $u_{j-1} \leq u < u_j$, we have,

$$\begin{aligned} B_{j-1,1}(u) &= \frac{u - u_{j-1}}{u_j - u_{j-1}} B_{j-1,0}(u) + \frac{u_{j+1} - u}{u_{j+1} - u_j} B_{j,0}(u) \\ &= \frac{u_{j+1} - u}{u_{j+1} - u_j}. \end{aligned} \tag{A.26}$$

So, when $p = 1$, the basis function based on uniform knots can be expressed as,

$$B_{j-1,1}(u) = \begin{cases} \frac{u - u_{j-1}}{u_j - u_{j-1}}, & u_{j-1} \leq u < u_j \\ \frac{u_{j+1} - u}{u_{j+1} - u_j}, & u_j \leq u < u_{j+1} \\ 0 & \text{otherwise.} \end{cases} \tag{A.27}$$

Similarly, the expression for $B_{j,1}(u)$, which will be used in calculation of basis function for $p = 2$, is given by

$$B_{j,1}(u) = \begin{cases} \frac{u - u_j}{u_{j+1} - u_j}, & u_j \leq u < u_{j+1} \\ \frac{u_{j+2} - u}{u_{j+2} - u_{j+1}}, & u_{j+1} \leq u < u_{j+2} \\ 0 & \text{otherwise.} \end{cases} \tag{A.28}$$

Basis functions for the first degree uniform B-spline, $B_{j,1}(u)$, is shown as in Fig. A.1. Note $B_{j,1}(u)$ is zero outside of the interval $[u_j, u_{j+2})$. We should note that by uniform B-spline, we mean that the B-spline is based on uniform knots.

When $p = 2$, we have, for $u_{j-1} \le u < u_j$,

$$\begin{aligned} B_{j-1,2} &= \frac{u - u_{j-1}}{u_{j+1} - u_{j-1}} B_{j-1,1}(u) + \frac{u_{j+2} - u}{u_{j+2} - u_j} B_{j,1}(u) \\ &= \frac{u - u_{j-1}}{u_{j+1} - u_{j-1}} \frac{u - u_{j-1}}{u_j - u_{j-1}} + \frac{u_{j+2} - u}{u_{j+2} - u_j} \cdot 0 \\ &= \frac{u - u_{j-1}}{u_{j+1} - u_{j-1}} \frac{u - u_{j-1}}{u_j - u_{j-1}}; \end{aligned} \tag{A.29}$$

for $u_j \le u < u_{j+1}$, we find

$$\begin{aligned} B_{j-1,2} &= \frac{u - u_{j-1}}{u_{j+1} - u_{j-1}} B_{j-1,1}(u) + \frac{u_{j+2} - u}{u_{j+2} - u_j} B_{j,1}(u) \\ &= \frac{u - u_{j-1}}{u_{j+1} - u_{j-1}} \frac{u_{j+1} - u}{u_{j+1} - u_j} + \frac{u_{j+2} - u}{u_{j+2} - u_j} \frac{u - u_j}{u_{j+1} - u_j}; \end{aligned} \tag{A.30}$$

and for $u_{j+1} \le u < u_{j+2}$,

$$\begin{aligned} B_{j-1,2} &= \frac{u - u_{j-1}}{u_{j+1} - u_{j-1}} B_{j-1,1}(u) + \frac{u_{j+2} - u}{u_{j+2} - u_j} B_{j,1}(u) \\ &= \frac{u - u_{j-1}}{u_{j+1} - u_{j-1}} \cdot 0 + \frac{u_{j+2} - u}{u_{j+2} - u_j} \frac{u_{j+2} - u}{u_{j+2} - u_{j+1}} \\ &= \frac{u_{j+2} - u}{u_{j+2} - u_j} \frac{u_{j+2} - u}{u_{j+2} - u_{j+1}}. \end{aligned} \tag{A.31}$$

So, generally, when $p = 2$, we have

$$B_{j-1,2}(u) = \begin{cases} \frac{u-u_{j-1}}{u_{j+1}-u_{j-1}} \frac{u-u_{j-1}}{u_j-u_{j-1}}, & u_{j-1} \le u < u_j \\ \frac{u-u_{j-1}}{u_{j+1}-u_{j-1}} \frac{u_{j+1}-u}{u_{j+1}-u_j} + \frac{u_{j+2}-u}{u_{j+2}-u_j} \frac{u-u_j}{u_{j+1}-u_j}, & u_j \le u < u_{j+1} \\ \frac{u_{j+2}-u}{u_{j+2}-u_j} \frac{u_{j+2}-u}{u_{j+2}-u_{j+1}}, & u_{j+1} \le u < u_{j+2} \\ 0 & \text{otherwise,} \end{cases} \tag{A.32}$$

and

$$B_{j,2}(u) = \begin{cases} \frac{u-u_j}{u_{j+2}-u_j}\frac{u-u_j}{u_{j+1}-u_j}, & u_j \le u < u_{j+1} \\ \frac{u-u_j}{u_{j+2}-u_j}\frac{u_{j+2}-u}{u_{j+2}-u_{j+1}} + \frac{u_{j+3}-u}{u_{j+3}-u_{j+1}}\frac{u-u_{j+1}}{u_{j+2}-u_{j+1}}, & u_{j+1} \le u < u_{j+2} \\ \frac{u_{j+3}-u}{u_{j+3}-u_{j+1}}\frac{u_{j+3}-u}{u_{j+3}-u_{j+2}}, & u_{j+2} \le u < u_{j+3} \\ 0 & \text{otherwise.} \end{cases} \tag{A.33}$$

When $p = 3$, we have, for $u_{j-1} \le u < u_j$,

$$\begin{aligned} B_{j-1,3}(u) &= \frac{u-u_{j-1}}{u_{j+2}-u_{j-1}}B_{j-1,2}(u) + \frac{u_{j+3}-u}{u_{j+3}-u_j}B_{j,2}(u) \\ &= \frac{u-u_{j-1}}{u_{j+2}-u_{j-1}}\frac{u-u_{j-1}}{u_{j+1}-u_{j-1}}\frac{u-u_{j-1}}{u_j-u_{j-1}}; \end{aligned} \tag{A.34}$$

for $u_j \le u < u_{j+1}$, we find

$$\begin{aligned} B_{j-1,3}(u) &= \frac{u-u_{j-1}}{u_{j+2}-u_{j-1}}B_{j-1,2}(u) + \frac{u_{j+3}-u}{u_{j+3}-u_j}B_{j,2}(u) \\ &= \frac{u-u_{j-1}}{u_{j+2}-u_{j-1}}\left(\frac{u-u_{j-1}}{u_{j+1}-u_{j-1}}\frac{u_{j+1}-u}{u_{j+1}-u_j} + \frac{u_{j+2}-u}{u_{j+2}-u_j}\frac{u-u_j}{u_{j+1}-u_j}\right) \\ &\quad + \frac{u_{j+3}-u}{u_{j+3}-u_j}\frac{u-u_j}{u_{j+2}-u_j}\frac{u-u_j}{u_{j+1}-u_j} \end{aligned} \tag{A.35}$$

for $u_{j+1} \le u < u_{j+2}$,

$$\begin{aligned} B_{j-1,3}(u) &= \frac{u-u_{j-1}}{u_{j+2}-u_{j-1}}B_{j-1,2}(u) + \frac{u_{j+3}-u}{u_{j+3}-u_j}B_{j,2}(u) \\ &= \frac{u-u_{j-1}}{u_{j+2}-u_{j-1}}\frac{u_{j+2}-u}{u_{j+2}-u_j}\frac{u_{j+2}-u}{u_{j+2}-u_{j+1}} \\ &\quad + \frac{u_{j+3}-u}{u_{j+3}-u_j}\left(\frac{u-u_j}{u_{j+2}-u_j}\frac{u_{j+2}-u}{u_{j+2}-u_{j+1}} + \frac{u_{j+3}-u}{u_{j+3}-u_{j+1}}\frac{u-u_{j+1}}{u_{j+2}-u_{j+1}}\right) \end{aligned} \tag{A.36}$$

for $u_{j+2} \le u < u_{j+3}$

$$
\begin{aligned}
B_{j-1,3}(u) &= \frac{u-u_{j-1}}{u_{j+2}-u_{j-1}}B_{j-1,2}(u) + \frac{u_{j+3}-u}{u_{j+3}-u_j}B_{j,2}(u) \\
&= \frac{u_{j+3}-u}{u_{j+3}-u_j}\frac{u_{j+3}-u}{u_{j+3}-u_{j+1}}\frac{u_{j+3}-u}{u_{j+3}-u_{j+2}};
\end{aligned}
\tag{A.37}
$$

for all $u \notin [u_{j-1}, u_{j+3})$, $B_{j-1,3}(u) = 0$.

As long as we use uniform knots, all the basis functions are similar. In fact, they have exactly the same shape, and the only difference is that each basis function $B_{j,3}(u)$ has its support on the interval $[u_j, u_{j+4})$ and as j changes the support changes. We wish to make use of this fact to simplify our calculations. For that purpose, we introduce a general algorithm for calculation of a point on a B-spline curve, Eq. A.11, for an arbitrary $u \in [u_j, u_{j+1})$. The universal method can be applied for the function evaluation at any point on the domain of interest. For uniform knots, $u_{j+1} - u_j = \Delta u$, for all j. We consider the function evaluation on the interval $[u_j, u_{j+1})$; for all the other intervals, we employ the same method. There are four non-zero basis functions on the interval $[u_j, u_{j+1})$, namely,

$$
B_{j-3,3}(u) = \left(\frac{u_{j+1}-u}{3\Delta u}\right)\left(\frac{u_{j+1}-u}{2\Delta u}\right)\left(\frac{u_{j+1}-u}{\Delta u}\right);
\tag{A.38}
$$

$$
\begin{aligned}
B_{j-2,3}(u) = \left(\frac{\Delta u + u_{j+1}-u}{3\Delta u}\right)&\left[\left(\frac{u-u_j-\Delta u}{2\Delta u}\right)\left(\frac{u_{j+1}-u}{\Delta u}\right)+\left(\frac{\Delta u+u_{j+1}-u}{2\Delta u}\right)\left(\frac{u-u_j}{\Delta u}\right)\right] \\
&+ \left(\frac{u-u_j+2\Delta u}{3\Delta u}\right)\left(\frac{u_{j+1}-u}{2\Delta u}\right)\left(\frac{u_{j+1}-u}{\Delta u}\right);
\end{aligned}
\tag{A.39}
$$

$$
\begin{aligned}
B_{j-1,3}(u) = \left(\frac{u-u_j+\Delta u}{3\Delta u}\right)&\left[\left(\frac{u-u_j+\Delta u}{2\Delta u}\right)\left(\frac{u_{j+1}-u}{\Delta u}\right)+\left(\frac{\Delta u+u_{j+1}-u}{2\Delta u}\right)\left(\frac{u-u_j}{\Delta u}\right)\right] \\
&+ \left(\frac{2\Delta u+u_{j+1}-u}{3\Delta u}\right)\left(\frac{u-u_j}{2\Delta u}\right)\left(\frac{u-u_j}{\Delta u}\right);
\end{aligned}
\tag{A.40}
$$

$$
B_{j,3}(u) = \left(\frac{u-u_j}{3\Delta u}\right)\left(\frac{u-u_j}{2\Delta u}\right)\left(\frac{u-u_j}{\Delta u}\right).
\tag{A.41}
$$

To eliminate the knots u_j's from expressions for the basis functions we introduce additional

parameter t, that ranges from 0 to 1 on the given interval

$$t = \frac{u - u_j}{u_{j+1} - u_j}. \tag{A.42}$$

Then we may rewrite the basis functions in Eqs. A.38-A.41 as functions of t as

$$\begin{aligned} B_{j-3,3}(t) &= \frac{1}{3}(1-t)\frac{1}{2}(1-t)(1-t) \\ &= \frac{1}{6}(-t^3 + 3t^2 - 3t + 1) = b_0(t), \end{aligned} \tag{A.43}$$

$$\begin{aligned} B_{j-2,3}(t) &= \frac{1}{6}(t^3 - 3t + 2) + \frac{1}{6}(2-t)(-2t^2 + 2t + 1) \\ &= \frac{1}{6}(t^3 - 3t + 2 - 4t^2 + 4t + 2 + 2t^3 - 2t^2 - t) \\ &= \frac{1}{6}(3t^3 - 6t^2 + 4) = b_1(t), \end{aligned} \tag{A.44}$$

$$\begin{aligned} B_{j-1,3}(t) = \frac{1}{3}(1+t)\left[\frac{1}{2}(t+1)(1-t) + \frac{1}{2}(1+1+t)t\right] \\ + \frac{1}{3}(2+1-t)\frac{1}{2}t \cdot t = \frac{1}{6}(-3t^3 + 3t^2 + 3t + 1) = b_2(t), \end{aligned} \tag{A.45}$$

$$B_{j,3}(t) = \frac{t}{3} \cdot \frac{t}{2} \cdot t \quad = \frac{1}{6}t^3 = b_3(t). \tag{A.46}$$

The four basis functions b_0, b_1, b_2 and b_3 at some given interval are shown in Fig. A.3. On each subinterval of the domain this local basis is exactly the same. So for any given value of $\overline{u} \in [u_0, u_m)$ we can use very simple expression to find the point on the curve $\overrightarrow{C}(\overline{u})$ which is in general given by

$$\overrightarrow{C}(\overline{u}) = \sum_{j=-3}^{m-1} \overrightarrow{C}_{j+2} B_{j,3}(\overline{u}). \tag{A.47}$$

We find the interval $[u_j, u_{j+1})$, such that $\overline{u} \in [u_j, u_{j+1})$. As the only cubic B-spline basis functions which are nonzero on this interval, are $B_{k,3}(u)$, for $k = j-3, j-2, j-1, j$. Eq. A.47 gives

$$\overrightarrow{C}(\overline{u}) = \sum_{k=j-3}^{j} \overrightarrow{C}_{k+2} B_{k,3}(\overline{u}). \tag{A.48}$$

and we calculate the point on the B-spline curve as

$$\overrightarrow{C}(\overline{t}) = \sum_{k=0}^{3} \overrightarrow{C}_{j+k-1} b_k(\overline{t}), \tag{A.49}$$

where

$$\overline{t} = \frac{\overline{u} - u_j}{u_{j+1} - u_j}. \tag{A.50}$$

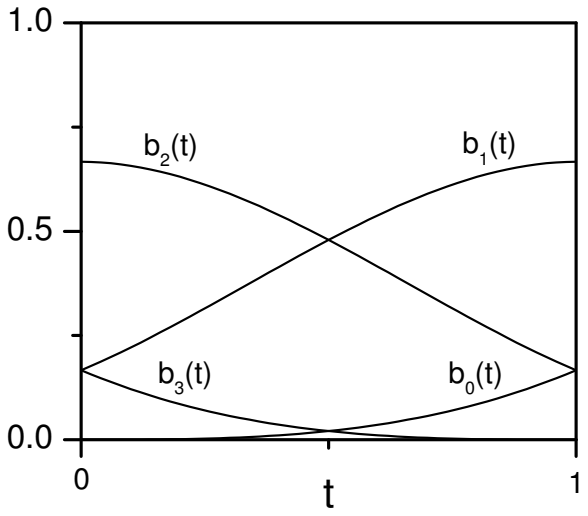

Figure A.3: Weight functions of uniform cubic B-spline on a knot interval.

A.2.1 Endpoints

We can force the cubic B-spline curve of Eq. A.11 to pass through the control point C_0 when $u = u_0$, and through the control point C_m when $u = u_m$ by requiring that

$$\overrightarrow{C}_0 = \overrightarrow{C}(u_0) = \sum_{j=-3}^{-1} \overrightarrow{C}_{j+2} B_j(u_0) \tag{A.51}$$

and

$$\overrightarrow{C}_m = \overrightarrow{C}(u_m) = \sum_{j=m-3}^{m-1} \overrightarrow{C}_{j+2} B_j(u_m). \tag{A.52}$$

Note here we used the fact that $B_{j,3}(u_0) = 0$ for $j \geq 0$, and $B_{j,3}(u_m) = 0$ for $j \leq m-4$.

A curve that passes through the first and the last control points is referred to as *clamped* B-spline curve. In general, multiple knots are used to force the B-spline curve to pass through a control point. But in the case of multiple knots we obviously do not have have a uniform distribution of knots, which complicates calculations. In our work, we propose an alternative method to ensure the uniform cubic B-spline passing through the first and the last control points. Using Eqs. A.49, A.51 and A.52 we can show that

$$\overrightarrow{C}_0 = \frac{1}{6}(\overrightarrow{C}_{-1} + 4\overrightarrow{C}_0 + \overrightarrow{C}_1), \qquad \overrightarrow{C}_m = \frac{1}{6}(\overrightarrow{C}_{m-1} + 4\overrightarrow{C}_m + \overrightarrow{C}_{m+1}), \tag{A.53}$$

We wish to define $\overrightarrow{C}_{-1}$ and $\overrightarrow{C}_{m+1}$ so that we can get a clamped curve. Those points are beyond the domain of interest ($[u_0, u_m]$) and are actually introduced to generate a clamped curve. From Eqs. A.53, it follows that

$$\overrightarrow{C}_{-1} = 2\overrightarrow{C}_0 - \overrightarrow{C}_1, \tag{A.54}$$

and

$$\overrightarrow{C}_{m+1} = 2\overrightarrow{C}_m - \overrightarrow{C}_{m-1}. \tag{A.55}$$

For the given set of control points $(\overrightarrow{C}_0, \overrightarrow{C}_1, \ldots, \overrightarrow{C}_m)$, in case if the knots are uniformly spaces, we will always obtain the curve that passes through the control points C_0 and C_m if we define $(\overrightarrow{C}_{-1})$ and $(\overrightarrow{C}_{m+1})$ by Eqs. A.54 and A.55

A.2.2 Monotonic and Convex Curves

In this section we establish the main properties of B-spline curves we need for the representation of relative permeability curves. The curve connecting all the control

points in order of their indexes is referred to as *the control polyline*. We show that B-spline approximating curve is always monotonic (convex) if a control polyline is monotonic (convex).

Suppose the control polyline is monotonic. Mathematically, this means that if $\overrightarrow{C}_j = (c_{x,j}, c_{y,j})$ and $c_{x,0} < c_{x,1} < \cdots < c_{x,m}$, then $c_{y,0} < c_{y,1} < \cdots < c_{y,m}$. We wish to prove that the B-spline approximating curve based on the given set of control points is a monotonic function. To prove that, we make use of one remarkable property of B-spline curves, the so called *variation diminishing property*: no straight line intersects a B-spline curve more times than it intersects the curve's control polyline (see [34]). First of all, note that the clamped curve cannot be monotonically decreasing. If it could, it would never pass through the both endpoints. Note also that the B-spline curve is always contained in the control polygon $C_0C_1C_2...C_{n-1}C_nC_0$. If it had a segment that lies above that line we could find a straight line, that intersects the curve, but does not intersect the control polyline, which would contradict the variation diminishing property. So the curve is always above the control polyline and below the straight line C_0C_n.

Suppose the B-spline curve we obtain based on the given set of control points is non-monotonic and monotonically increasing on some subdomain, i.e. it has a local extremum (for example a local maximum) of c_y on the domain as depicted by the curve labelled approximation curve in Fig. A.4.

Let l_1 be the straight line tangent to the approximation curve at the extremum point of c_y. It intersects the approximation curve as well as the control polyline one time. Consider a straight line l_2, which is parallel to the l_1 and lies below this line. We always can find some curve l_2 so that it has two intersection points with the approximation curve and only one with the control polyline. But this conflicts with the variation diminishing property, which means there exists no extremum points of the B-spline curve on the domain. Therefore, the curve is monotonic.

Next, we show that if the control polyline is convex in $x-y$ plane then the B-spline approximation curve is also convex. Convexity of the control polyline can be expressed as

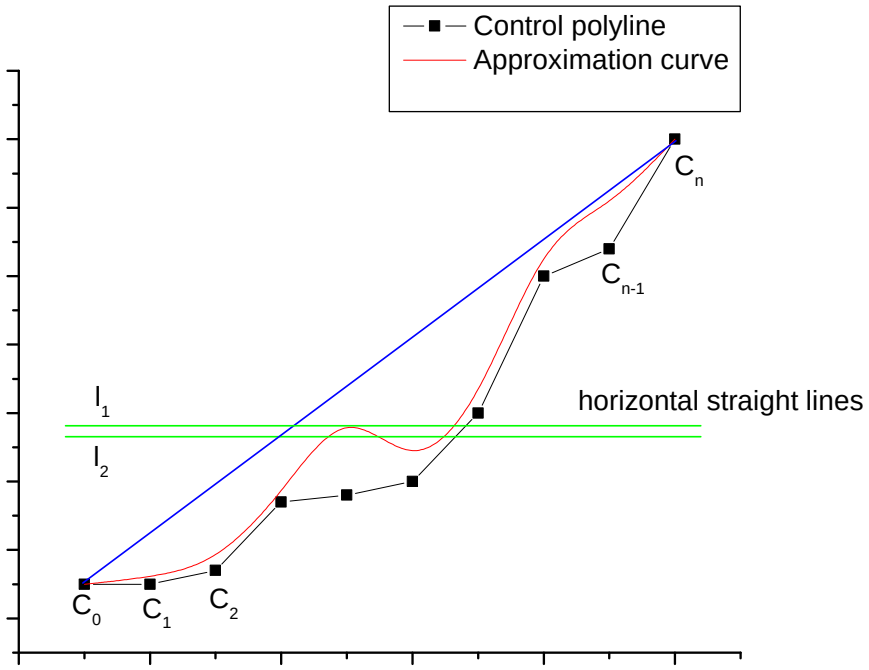

Figure A.4: Monotonic polyline.

.

$$\frac{c_{y,j} - c_{y,j-1}}{c_{x,j} - c_{x,j-1}} < \frac{c_{y,j+1} - c_{y,j}}{c_{x,j+1} - c_{y,j}}. \tag{A.56}$$

Suppose the approximating B-spline curve changes its curvature, i.e. it has a point of inflection as shown by the curve labelled approximation curve in Fig. A.5.

First we note that a clamped B-spline curve cannot be concave everywhere on the domain. If it were concave everywhere it could not pass through the control points C_0 and C_n, because it has be below the line C_0C_n. Let l_1 be the line tangent to the approximation curve at the inflection point, see Fig. A.5. This line intersects the control polyline two times at maximum. Consider a straight line l_2, which also passes through the inflection point and has a small angle with the l_1. This straight line intersects the approximation curve at least three times, while it intersect the control polyline no more than two times. This contradicts the variation diminishing property. Therefore the curve has no points of inflection, and hence it is convex on the domain.

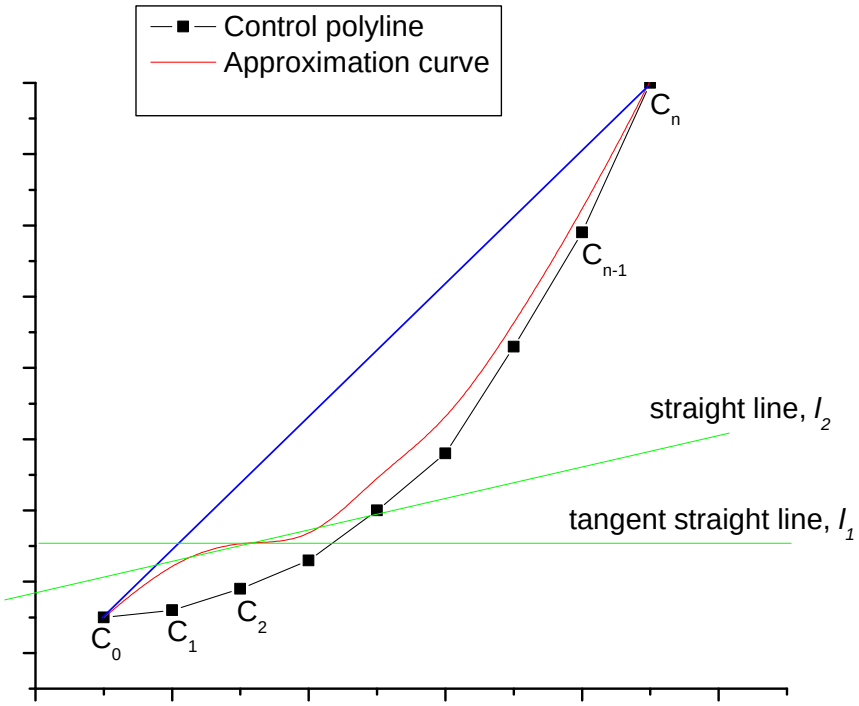

Figure A.5: Convex polyline.

.

A.2.3 Representation of Relative Permeability Curves with B-splines

To simplify the calculations, we reduce the approximation of relative permeability curves to a one dimensional problem. In general, the control points have two coordinates $\overrightarrow{C}_j = (c_{x,j}, c_{y,j})$, which represent values of saturation, S, and relative permeability, K_r, respectively. We wish to relate the x coordinate to the parameter u directly, so that the control points coordinates are expressed as $\overrightarrow{C}_j = (c_{x,j}(\overrightarrow{u}), c_{y,j})$, where $\overrightarrow{u}$ is the knot vector.

We are free to define any set of knots, the only thing we require is that the knots are uniform. We can define the knots on the dimensionless saturation domain, which gives $S_{wd} = u$. More specifically we divide the dimensionless saturation domain $S_{wd} \in [0, 1]$ into m equal subintervals of length

$$\Delta S_{wd} = (1 - 0)/m = \frac{1}{m}, \tag{A.57}$$

and define the knots as

$$u_j = j\Delta S,\ j = -3, \ldots, m+3. \tag{A.58}$$

Recall that we need additional knots $u_{-3}, u_{-2}, u_{-1}, u_{m+1}, u_{m+2}$ and u_{m+3} to define a full basis on the domain of interest.

We will show that for the given set of knots, the component $c_x(u)$ of the B-spline approximating curve is always equal to u on the domain. Let $\overline{u}$ be some point within the interval $[u_j, u_{j+1}]$. From Eq. A.49 we have

$$c_x(\bar{t}) = \sum_{k=0}^{3} c_{x,j+k-1} b_k(\bar{t}), \tag{A.59}$$

where t is the parameter given by Eq. A.50. Note that the control points involved in calculations for this case are

$$\begin{aligned} c_{x,j-1} &= u_j - \Delta u, \\ c_{x,j} &= u_j, \\ c_{x,j+1} &= u_{j+1}, \\ c_{x,j+2} &= u_{j+1} + \Delta u. \end{aligned} \tag{A.60}$$

Substituting the basis functions from Eqs. A.42-A.46 and the control points from Eq. A.60 we have

$$\begin{aligned} c_x(\bar{t}) &= \frac{1}{6}\Big[(-\bar{t}^3 + 3\bar{t}^2 - 3\bar{t} + 1)(u_j - \Delta u) + (3\bar{t}^3 - 6\bar{t}^2 + 4)(u_j) \\ &\qquad +(-3\bar{t}^3 + 3\bar{t}^2 + 3\bar{t} + 1)(u_{j+1}) + (\bar{t}^3)(u_{j+1} + \Delta u)\Big] \\ &= \frac{1}{6}\Big[\bar{t}^3(2u_j - 2u_{j+1} + 2\Delta u) + \bar{t}^2(-3u_j + 3u_{j+1} - 3\Delta u) \\ &\qquad +\bar{t}(-3u_j + 3u_{j+1} - 3\Delta u) + (5u_j + u_{j+1} - \Delta u)\Big]. \end{aligned} \tag{A.61}$$

Note that $u_{j+1} = u_j + \Delta u$. Thus,

$$c_x(\bar{t}) = \bar{t}\Delta u + u_j = \overline{u}. \tag{A.62}$$

This means that the two dimensional approximation curve always has the component $c_x(u) = u$. So we can define one dimensional control points, which are nothing but relative permeability values, and approximate a curve as follows

$$K_r(S) = K_r(u) = \sum_{j=-p}^{m-1} C_{j+p-1} B_{j,p}(u), \tag{A.63}$$

where the jth control point is defined as a relative permeability value at the given saturation, i.e.

$$C_j = K_r(j\Delta S_{wd}),\ j = 0, ..., m. \tag{A.64}$$

Although the notation of Eq. A.64 is convenient we should keep in mind that the resulting B-spline approximation to the relative permeability curve is only guaranteed to pass through C_0 and C_m.